

PART - I

**SYNTHESIS, CHARACTERIZATION
AND CORROSION INHIBITION
STUDIES OF HETEROCYCLIC
SCHIFF BASES**



CHAPTER 1

INTRODUCTION AND REVIEW

Corrosion is a universal phenomenon, omnipresent and omnipotent, which can affect directly or indirectly the economy. Corrosion is the deterioration of metals and alloys by chemical or electrochemical means. It is an extremely dangerous problem leads to the collapse of bridges and buildings, breaking of oil pipelines, leakage of chemical plants etc. In 1983, three peoples were killed by the collapse of the Mianus river bridge and in West Virginia, the collapse of the Silver bridge resulted in the death of 46 people. In both cases the corrosion was the main reason. Corrosion also makes threaten to the disposal of radioactive waste, which stored in containers for thousands of years. Corroded electrical contacts may results fires and corroded medical implants may cause health problems. Metals such as iron, aluminum and copper are highly susceptible to corrosion. Not only metals, materials like polymers and ceramics are also vulnerable to corrosion. Corrosion can make adverse effects on the properties of materials such as strength and appearance. In industrial fields, de-scaling, pickling etc which are commonly employed for the metal surface cleaning, demand enormous amount of HCl and lead to metal disintegration [1]. Corrosion problems have always acquired considerable attention from corrosion engineers and therefore they are continuously engaged in the processes of reducing corrosion rate.

Corrosion is an electrochemical process, and is possible by the electrons flow through the conductive metals from the anodic to the cathodic sites in the presence of oxygen and water. A corrosion system can be considered as an

electrochemical cell and the possible reactions are given in equations 1 to 4.

Mechanism of corrosion is represented in the Figure 1.1.

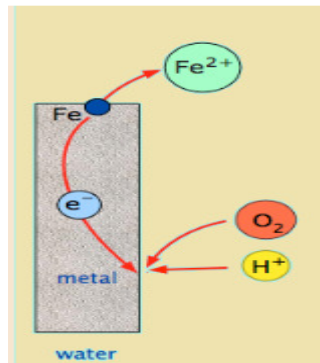
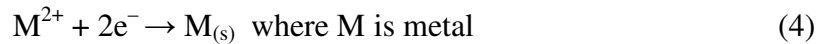
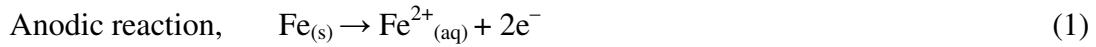


Figure 1.1: Mechanism of corrosion

Corrosion process can be classified as different forms based on three factors mainly, mechanism of corrosion, appearance of the corroded metal and nature of the corrodent. Some of the most common forms of corrosion are diagrammatically represented in the following Figure 1.2.

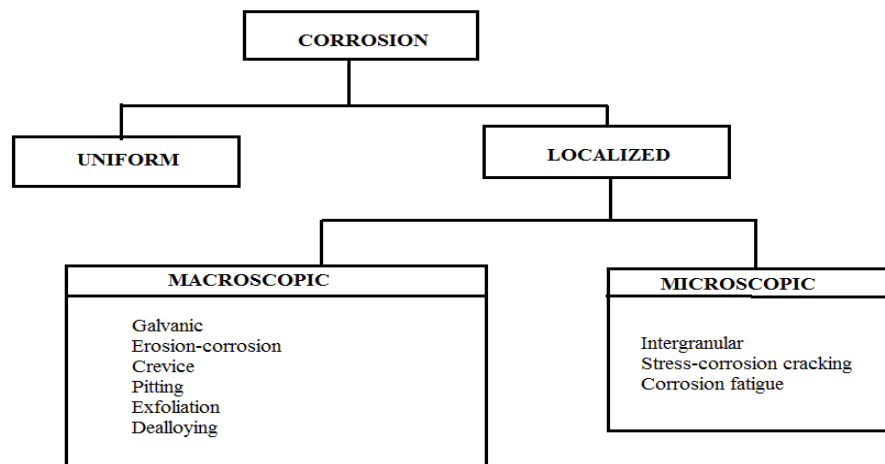


Figure 1.2: Common forms of corrosion

Generally corrosion is considered as two types, uniform corrosion and localized corrosion.

Uniform corrosion: It is a type of corrosion attack, which is more uniformly distributed over the exposed metal surface. Since uniform corrosion is easier to predict, it is not considered as a serious form of corrosion [2].

Localized corrosion: It is defined as the metal deterioration at small regions. Here corrosion takes place with some destructive process like erosion, stress and other chemical attack. It can be classified as macroscopic corrosion and microscopic corrosion.

Macroscopic corrosion: It occurs at macroscopic level on the corroding surface and can be identify by naked eyes [3]. According to the nature of corrosion mechanism, macroscopic corrosion is divided into 6, galvanic corrosion, erosion-corrosion, crevice corrosion, pitting corrosion, exfoliation corrosion and dealloying corrosion.

1. **Galvanic corrosion:** It is an electrochemical process in which one metal preferentially corrodes when it is electrically contacted with another metal, in the presence of an electrolyte [4].
2. **Erosion-corrosion:** It is a degradation of metal surface by the mechanical actions such as abrasion by slurry, fast flowing liquid or gas containing suspended particles, droplets etc.
3. **Crevice corrosion:** It refers to the corrosion takes place in confined regions to which the working fluid from the environment is limited. These regions are generally called crevices [5].
4. **Pitting corrosion:** It is an extremely localized corrosion that causes to the formation of small holes on the metal surface [6].

5. ***Exfoliation corrosion:*** It is a type of corrosion, which increases the surface grains from metal by the formation of corrosion products at grain boundaries.
6. ***Dealloying corrosion:*** It is a type of corrosion occurring in some solid solution alloys, when a component of the alloys is preferentially leached from the material in suitable conditions. It is also called selective leaching.

Microscopic corrosion: This type corrosion generally occurs at the corroding materials at microscopic level and can be identify only by the help of special types of microscopes such as optical microscope, electron microscope, etc [7]. Based on corrosion mechanism, microscopic corrosion is mainly divided into three intergranular corrosion, stress corrosion cracking and corrosion fatigue.

1. ***Intergranular corrosion:*** It is a form of corrosion where the boundaries of crystals of the material are more liable to corrosion than bulk.
2. ***Stress-corrosion cracking:*** Here there is crack formation in the presence of the corrosive environment and lead to unexpected breaking of metals when subjected to a tensile stress.
3. ***Corrosion fatigue:*** It is the mechanical degradation of a metal by the combined action of corrosion and cyclic loading.

Corrosion causes countless issues and makes threats to the environment and human being. Thus development of effective preventing methods should be inevitable for the proper and thorough control of corrosion in various fields.

Generally five methods are employed to control corrosion.

Material selection: All metals and alloys possess unique corrosion behaviour and its corrosion preventing ability depends on the exposed environment. If the corrosion resistance of the material increases for a given corrosive environment, the rate of corrosion decreases. There are many competing materials available that have the capacity to meet the corrosion requirements and the material selection becomes the most economical solution for the corrosion control.

Coatings: Applying a coating of more noble metal on the active metal surface makes use of greater corrosive resistance of the noble metal. Coatings can be divided into two groups, organic coatings and inorganic coatings. Organic coatings are paints or powders which require several layers to inhibit corrosion. Inorganic coatings are those that have silicate like coating.

Cathodic protection: Cathodic protection method protects the metal surface from corrosion by suppressing the corrosion current [8].

Design: Corrosion mainly occurs in more corrosive crevices or dead spaces and these areas can be eliminated or controlled in this process.

Inhibitors: A compound which can be added to a metal to reduce its corrosion rate is called corrosion inhibitor [9].

Corrosion inhibitors

A compound which can be added to a metal to reduce its corrosion rate is called corrosion inhibitor. The application of chemical inhibitors to resist the corrosion is quite diverged. In the industry of oil extraction and processing,

inhibitors have considered as the first step of defence to prevent the corrosion process.

Corrosion inhibition due to inhibitors generally occurs by three mechanisms:

- The inhibitor is adsorbed on the metal surface and generating a thin protective film.
- The inhibitor makes a metal itself to generate a protective film of metal oxides and leads to improve its resisting capacity.
- The inhibitor protects the corrosive substance in the water.

There are mainly four types of corrosion inhibitors.

Anodic inhibitors: The chemical substances react with oxygen and generate a protective film on the surface of metal and resist the metal corrosion process. They decrease the corrosion potential of the metal by oxidizing a surface layer which reacts slightly with corrosive elements. Anodic inhibitors are also called as passivators because they change the anodic reactions and force the surface of metals to the passive region. The concentration of anodic inhibitors and corrosion rates are related. The mechanism of anodic corrosion inhibitor involves the blocking of anodic sites and depends on concentration of the inhibitor. At low concentrations, the inhibitor activity is relatively weak. When concentration rises, inhibitors undergo reaction with strong anodes and form a passive layer to reduce the corrosion rates. The important examples of anodic inhibitors are chromates, molybdates, nitrites, orthophosphates, etc.

Cathodic inhibitors: They can retard the cathodic reaction or decrease the diffusion of more reductive elements like hydrogen or oxygen to the surface of metal. They are also described as chemical substances which decrease the corrosion rate of

a metal. The efficiency of cathodic inhibitors depends on the water quantity, flow regime, and the fluid composition. The mechanism involves a passivation layer formation to prevent the diffusion of the corrosive substance to the metal. Inhibition takes place by different mechanisms like cathodic poisons, oxygen scavengers and cathodic precipitates.

1. ***Cathodic poisons:*** These are used to suppress the cathodic reduction process to balance the anodic reaction [10]. The metal has a susceptibility to hydrogen-induced cracking and liable to cathodic inhibition process because the metals have the capacity to absorb hydrogen during the time of cathodic charging. In low-pH conditions some reduced hydrogen may diffuse into the metal as atomic hydrogen instead of forming the gas. Actually this is happening during pickling or electroplating of the metal. The common cathodic poisons are antimony, arsenic, sulfur, tellurium, selenium and cyanide ions, which prevent the formation of hydrogen gas from hydrogen.
2. ***Oxygen scavengers:*** These are the chemical substances, which reduce corrosion by reacting with the dissolved oxygen. Sulfite and bi-sulfite ions are the important examples. Cobalt or nickel is used as catalyst for this redox reaction.
3. ***Cathodic precipitates:*** These involve the precipitation of certain metals like zinc, calcium, magnesium, etc on cathodic metal surfaces in order to form a protective layer on corroding metal.

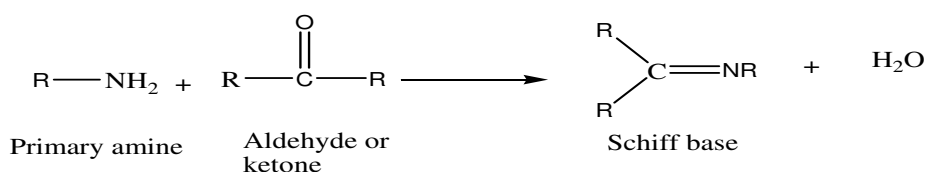
Mixed inhibitors: They form a thin film or precipitate to decrease both the anodic and cathodic reactions. The main examples are sodium phosphates and silicates used in domestic water softener to prevent rust.

Volatile corrosion inhibitors- They are delivered to the corrosion site in a closed environment and form a protective film to resist the corrosion. For example, volatile compounds such as hydrazine or morpholine are carried with steam to resist the corrosion process in condenser tubes.

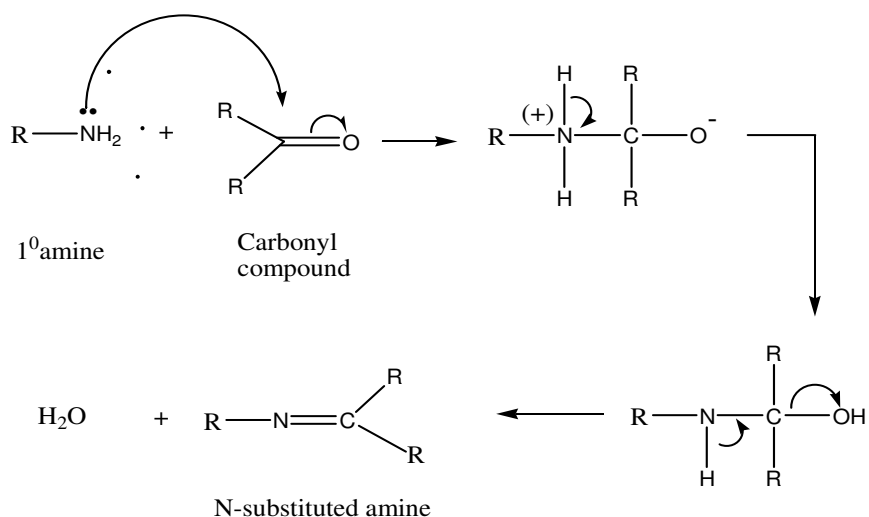
According to the nature of the compounds corrosion inhibitors are classified as two types, organic inhibitors and inorganic inhibitors. Molybdate anion, calcium nitrite, zinc phosphate, chromate, rare earth metals salts etc are used as common inorganic inhibitors. Because of the efficiency at wide range of temperatures, low costs, good solubility in water, and less toxicity, organic inhibitors are predominantly employed as corrosion inhibitors. Most of the organic compounds containing hetero atoms such as nitrogen, oxygen, sulphur generally act as good corrosion inhibitors. In addition, compounds with multiple bonds behave as efficient inhibitors due to the availability of π electrons for interaction with the metal surface. Schiff bases with $-\text{CH}=\text{N}-$ linkage have the above features combined with their structure which make them effective potential corrosion inhibitors.

Schiff bases are the condensation products of primary amines with carbonyl compounds gaining importance day by day. A Schiff base is considered as a nitrogen occurring analogue of an aldehyde or ketone where $\text{C}=\text{N}$ group replaces the carbonyl group. Schiff bases exhibit useful applications such as strong coordination agents, biological applications, analytical agents, catalysts, pharmaceuticals and corrosion inhibitors. Thus they have received continuous attention from researchers who recognized the properties and applications of novel Schiff bases in various fields, which influence the fast development of chemistry. In the field of coordination chemistry, the study of Schiff bases as ligands has eccentric scope and

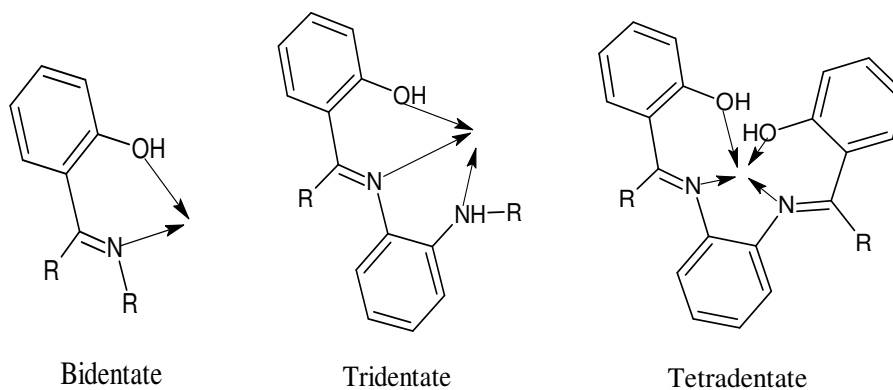
practical applications. Schiff bases are formed by the condensation reaction of an aldehyde or ketone with aliphatic or aromatic amines.



Generally aryl substituents containing Schiff bases are considered as more stable than alkyl substituents, which are easily polymerizable. The mechanism of Schiff base formation can be explained by the nucleophilic addition of amines to the carbonyl group. At the initial step of the mechanism, the ketone or aldehyde reacts with amine to form a very unstable compound called carbinolamine and loses water. The Schiff base formation from ketones or aldehydes is a reversible reaction catalyzed by acid or base, or upon heating.



Schiff bases commonly occur as bidentate, tridentate, tetradentate or polydentate ligands and are capable to form stable compounds with transition as well as inner transition metals. They mainly act as coordinating ligands and react with metal ions to form five or six membered ring.

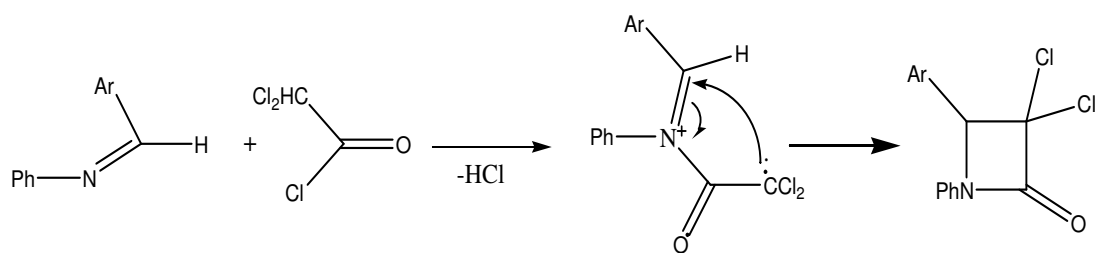


Schiff bases have numerous applications in the field of organic chemistry [12-14]. They are generally used as dyes, pigments, catalysts, polymer stabilisers and intermediates in synthetic organic chemistry. Schiff bases exhibit many biological activities [15-18] involving antibacterial, antitumor, antimalarial, antiviral, antifungal, antipyretic and anti-inflammatory properties [19-21]. Among many common organic compounds, Schiff bases have eminent characteristics, comparatively effortless preparation method, structural resemblance with naturally occurring biological substances [22] and synthetic flexibility. Schiff bases have a predominant role in the field of coordination chemistry as they easily form very stable complexes with transition metal ions. Synthetic organic chemistry consists of the reactions of Schiff bases involving carbon-nitrogen bond formation [23] and they are widely exerted in agrochemical and pharmaceutical industry [24-26]. Chiral Schiff bases are considered as initial substrates of the asymmetric synthesis of amino acids [27]. The Schiff bases derived by the condensation reaction of carbonyl compounds and aryl amines are considered as intermediates in the formation of compounds such as arene diazonium nitrates, N-arylarene carboxamide, cyanamides and β -lactams [28]. Schiff bases are also used as precursors for the oxidative ring closure reaction of polycyclic compounds like quinoline and isoquinoline by the influence of ultraviolet light. The role of Schiff base compounds for the production

of macrocyclic and acyclic compounds like coronates, cryptats, and podates are very important [29]. Schiff base compounds are also involved in the reaction between an amino acid and ninhydrin to form Ruhemann's purple, which is commonly used in the fingerprint detection [30].

Another important action of Schiff base compounds is in transamination catalysed by enzymes known as transaminases [31]. These enzymes are generally occurring in eukaryotic cells and mitochondria. A Schiff base reaction is associated with the chemistry of vision, where amino group of the opsin protein reacts with aldehyde group of 11-cis-retinal and vision become possible. Besides these biological activities, photochromism and solid-state thermochromism are other characteristics of these compounds resulting to their application in the field of materials science [32, 33].

Acylation reaction of Schiff bases using acyl cyanides, acid anhydrides and acid chlorides is initiated by the reaction at the nitrogen atom, results to the addition of the acylating reagent to the C=N bond and this type of reaction has eminent role in the natural products synthesis. Various enzymatic reactions are mainly based on the Schiff base intermediate. One of the best examples is the formation of Schiff base by the condensation reaction of an amine group in an enzyme of a lysine residue, with carbonyl group of the substrate. The condensation reaction of N-aryldimines with acetyl chlorides having at least one α hydrogen and an electron withdrawing group takes place by acylation reaction at the N atom and form β lactams, which have great role in penicillin chemistry [28,34].



The Schiff base compounds are good chelating agents [35, 36] and can be easily synthesized and characterized. However their use for analytical purposes will limit to basic conditions because of two reasons. They easily decompose in acidic solutions and are insoluble in aqueous solutions. Many Schiff base compounds are used as chelating agents for the identification and quantitative estimations of metal ions. Complex formation is the important step which depends on cation size, pH, ligand structure and the temperature. Schiff bases have an important role in fluourometry [37]. Sabry synthesized a Schiff base from 2-acetylbutyrolactone and investigated it's fluorescence properties. In the case of primary amines, 2-acetylbutyrolactone has been used as a fluorogenic agent for the spectrofluorimetric analysis [38]. This reagent undergo reaction with primary amines in DMF and makes Schiff base compounds having strong fluorescent properties. From 1930's the application of potentiometric membrane sensors in various fields are very important. Many Schiff base compounds are used in these sensors as cation carriers because of their stability, sensitivity and selectivity for particular metal ions [39-43]. Schiff base compounds are also used as solvent extraction reagents [44-47]. The macro cyclic Schiff bases containing thiophene or phenol groups have marked effect on the liquid- liquid extraction process of bivalent transition metal ions. In the last few years, different types of Schiff base compounds such as hydrazones, dithiocarbamates and dithiazonates are used in high performance liquid chromatography (HPLC) technique also [48].

Recently Schiff base compounds are commonly employed as synthons in the synthesis of different biologically and industrially important compounds like benzoxazines, formazans etc via cycloaddition reactions, replacement reactions and ring closure reactions [49]. Thus the application of Schiff base compounds in various fields has encouraged the researchers to develop new eco-friendly heterocyclic and aryl Schiff bases [50-52].

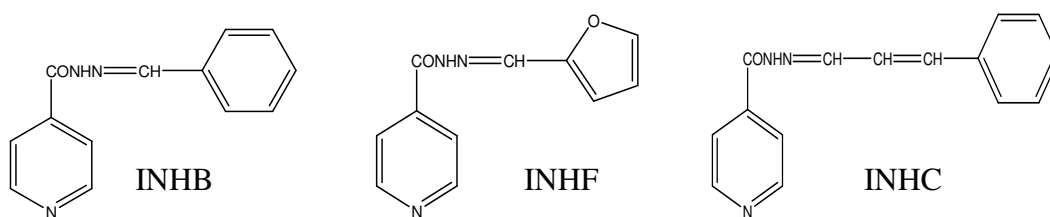
Schiff base corrosion inhibitors – A Review

Literature survey indicates that many researchers synthesized different type of Schiff base compounds and studied their various applications in different areas particularly in corrosion protection fields. In 1998, H. Shokry *et.al.*, investigated the corrosion inhibition efficacy of Schiff base compounds obtained from *o*-methoxy, *o*-hydroxy aromatic aldehydes and diamines namely N,N'-bis (salicylaldehyde)-1,8-diaminooctane and N,N'-bis (salicylaldehyde) -1,12 -diaminododecane on mild steel by weight loss studies, electrochemical and surface analysis methods in different solutions like HCl and tap water [53]. The maximum inhibition efficiency of 93% was measured for N,N'-bis (salicylaldehyde)-1,12-diaminododecane in HCl.

In 1999, S. L. Li *et.al.*, revealed the inhibition efficiency of various Schiff base compounds N-2-hydroxyphenyl-(3-methoxy-salicylideneimine) (V–bso), N,N'-*o*-phenylen-*bis*(3-methoxy-salicylideneimine) (V–oph–V), N-4-phenylcarbazide-(3-methoxy-salicylideneimine) (V–psd), N-4-phenylcarbazide-(salicylideneimine) (S–psd), N,N'-*p*-phenylen-*bis*(salicylideneimine) (S–pph–S) and N,N'-*o*-phenylen-*bis*(salicylideneimine) (S–oph–S) on the copper metal corrosion in 1M NaCl by potentiostatic polarization and impedance techniques [54]. All investigated Schiff base compounds were very effective in 1M NaCl. The highest inhibition efficiency was obtained for N, N'-*o*-phenylen-*bis*(3-methoxy-salicylideneimine).

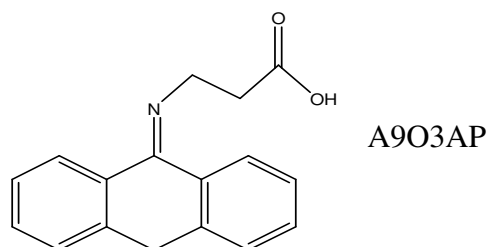
In 2003, Kaan C *et.al.*, studied the corrosion inhibition properties of Schiff bases synthesized from salicylaldehyde and amine by various electrochemical methods on MS [55]. *N*-(2-methyl phenyl)salicylaldimine compound exhibited maximum inhibition efficiency. The mechanism of adsorption process of *N*-(2-methoxyphenyl)salicylaldimine and *N*-(2-methyl phenyl)salicylaldimine compounds obeyed the Temkin isotherm and *N*-(2-hydroxyphenyl)salicylaldimine obeyed the Langmuir isotherm.

In 2009, Ishtiaque Ahamad *et.al.*, synthesized four Schiff bases by the condensation of isonicotinohydrazide and appropriate aldehydes such as benzaldehyde (INHB), furfural (INHF) and crotonaldehyde (INHC) [56]. They studied their inhibition efficiency on mild steel corrosion in 1M HCl by gravimetric analysis, electrochemical analysis and quantum chemical calculations. All the prepared Schiff bases showed above 90% efficacy and their activation energy of corrosion and thermodynamic parameters were evaluated to explain the corrosion inhibition mechanism.



In 2012, Shaju, K. S *et.al.*, reported that KI has synergistic effect on the corrosion inhibition efficiency of polynuclear Schiff base compound anthracene 9(10H)-one-3-aminopropanoic acid (A9O3AP) on steel in 0.5M sulphuric acid solution [57]. They studied the efficiency using gravimetric measurements, potentiodynamic polarization analysis and EIS spectroscopy. The inhibition efficiencies rise with increase in concentration of the inhibitor molecule and was

enhanced on the addition of KI because of synergism. The adsorption mechanism of inhibitor and inhibitor + KI on the corroding surface of the metal obeyed Freundlich and Langmuir isotherm models respectively.



In 2013, Carla Marins Goulart *et.al.*, studied the inhibition efficacy of some thiosemicarbazones and semicarbazones on carbon steel corrosion in 1M HCl using molecular modeling, potentiodynamic polarization and EIS studies [58]. Polarization curves established that all synthesized Schiff base inhibitors acted as mixed type. EIS plots implied that the R_{ct} values rise due to the presence of inhibitors and lead to improve the inhibition capacity. The mechanism of inhibition was verified by the adsorption studies and the inhibitors followed the Langmuir adsorption isotherm. The quantum mechanical study data established that the thiosemicarbazones have more inhibition efficiency than the semicarbazones.

Heterocyclic Schiff base corrosion Inhibitors – A Review

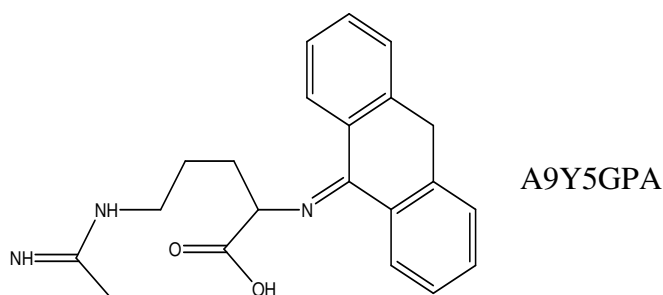
A number of active Schiff bases containing heterocyclic ring have been synthesized and studied by many researchers. In 2004, A. Yurt *et.al.*, synthesized some heterocyclic Schiff bases such as 2-((1Z)-1-aza-2-(2-pyridyl)vinyl)pyrimidine, 2-((1E)-2-aza-2-pyrimidine-2-ylvinyl)thiophene, 2-((1Z)-1-aza-2-(2-thienyl)vinyl)benzothiazole and 2-((1E)-2-aza-2-(1,3-thiazol-2-yl)vinyl)thiophene [59]. Potentiodynamic polarisation and EIS studies were conducted to measure the inhibition efficacy on carbon steel corrosion in 1M HCl solution. Polarization studies revealed that the examined Schiff base inhibitors

essentially acted as anodic type. The difference of inhibitive efficiency mainly depends on the substituents in the inhibitor. Electrochemical investigation implied that the adsorption of Schiff bases on the surface of metal obeys Temkin's isotherm. The values of free energies of adsorption, equilibrium constant and activation parameters were also calculated.

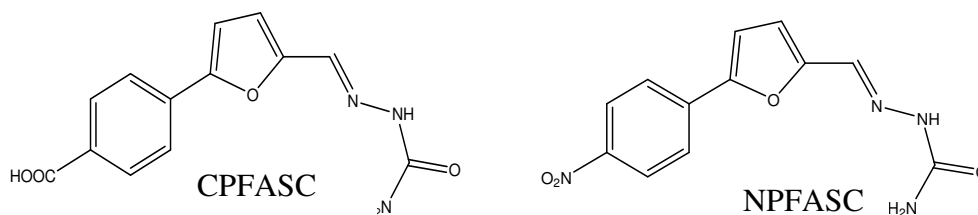
In 2005, Kaan C. Emregül *et.al.*, synthesized a heterocyclic Schiff base and studied its corrosion inhibition efficiency on steel [60]. They prepared 4-[(4-hydroxy-3-hydroxymethyl-benzylidene)-amino]-1,5-dimethyl-2-phenyl-1,2-dihydro-pyrazol-3-one (phv), by the reaction between 4-amino-1,5-dimethyl-2-phenyl-1,2-dihydro-pyrazol-3-one (phz) and 4-hydroxy-3-methoxy-benzaldehyde (vn), and measured its inhibition efficiency in 2M HCl by weight loss studies, EIS and polarization methods. Even if vn and phz were found to decrease the corrosion rate, the derivatives of vn and phz displayed more inhibition efficiency. The activation energies and other thermodynamic parameters were also derived.

In 2008, M. Behpour *et.al.*, studied the inhibition efficiency of 3 heterocyclic Schiff bases, 2-[(2-sulfanylphen-yl)ethanimidoyl]phenol (A) 2-[(2-1-(methylphenyl)methylidene]amino}-1-benznethiol (B), and 2-[(2-sulfanylphenyl)imino]methyl}}phenol (C) on mild steel corrosion in 15% HCl by weight loss studies, polarization and EIS methods [61]. The results indicated that the Schiff bases B and C have an efficiency of 99% at a concentration of 200 mg/L. The efficiency of inhibitors was explained due to the mechanism of adsorption on the surface of metal and followed the Langmuir isotherm. Thermodynamic adsorption parameters and activation parameters were evaluated by the corrosion currents.

In 2013, K. S. Shaju *et.al.*, synthesized an active polynuclear Schiff base (s)-2-(anthracene-9-(10H)-ylidene amino)-5-guanidinopentanoic acid (A9Y5GPA) and studied the inhibition efficiency on carbon steel corrosion in 1M HCl by different methods like gravimetric analysis, EIS and potentiodynamic polarization techniques [62]. The results revealed that the efficiency gradually increases with the rise in the inhibitor concentration and the adsorption process was obeyed the Langmuir isotherm model. Surface morphological analysis of the metal with and without of inhibitor was conducted by SEM.



In 2016, Vinod P Raphael *et.al.*, synthesized two novel heterocyclic semicarbazones (E)-2-((5-(4-nitrophenyl)furan-2-yl)methylene)hydrazine carboxamide (NPFASC) and (E)-4-(5-((2-carbamoylhydrazano)methyl)furan-2-yl)benzoic acid (CPFASC) and investigated their inhibition ability on carbon steel corrosion in 1M HCl medium [63]. The unexpected result elucidated that the non-planar NPFASC possess more inhibition efficiency than CPFASC due to the tendency of NO₂ group in the NPFASC to change into NH₂ group when it approach the surface of metal. This transformation leads to the more suitable geometry change of the compound for corrosion inhibition. The corrosion investigations were performed by gravimetric studies, polarization and EIS techniques. Surface morphological analysis was carried out by AFM, SEM and IR spectroscopy.



Schiff bases derived from various class of compounds such as pyridine carbaldehydes, indole carbaldehydes and thiophene carbaldehydes attained special attention nowadays.

Schiff base corrosion inhibitors derived from Pyridine derivatives- A Review

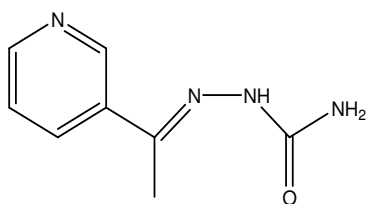
From the literature survey, it was revealed that numerous Schiff bases derived from pyridine derivatives have so many practical applications especially in the field of corrosion inhibition. In 1995 a series of Schiff base compounds such as 2-acetylpyridine-(4-methylthiosemicarbazone) (2AP4MTSC) and 2-acetylpyridine-(4-phenylthiosemicarbazone) (2AP4PTSC) were synthesized from 2-acetyl pyridine and substituted thiosemicarbazide, characterized and inhibition efficiency on mild steel corrosion in HCl was studied by U. J. Ekpe *et.al.* [64]. 2AP4PTSC exhibited maximum inhibition efficiency of 80.67%. Generally, inhibition efficiency has a tendency to improve with decrease in temperature and rise in inhibitor concentration.

In 2007, Saravana Loganathan *et.al.*, synthesized 2-acetylpyridine-N(4)-morpholine thiosemicarbazone (HAcPMTSc) and studied its corrosion inhibition efficiency on mild steel in acid media [65]. Different inhibitor concentrations were tested, and the efficiency was determined by weight loss studies, EIS and potentiodynamic polarization techniques. Chemisorption of HAcPMTSc was verified by the Langmuir isotherm model. The inhibition mechanism and surface

analysis were carried out by various techniques like SEM-EDS, FTIR, UV-visible and EPR.

In 2013, A. Dandia *et.al.*, reported five pyrazolo pyridine derivatives [66], 4-(2-chloro-6-flurpphenyl)-3-methyl-6-oxo-4,5,6,7-tetrahydro-2*H*-pyrazolo[3,4-*b*]pyridine-5-carbonitrile, 3-methyl-6-oxo-4,5,6,7-tetrahydro-2*H*-pyrazolo[3,4-*b*]pyridine-5-carbonitrile, 3-methyl-6-oxo-4-(*p*-tolyl)-4,5,6,7-tetrahydro-2*H*-pyrazolo[3,4-*b*]pyridine-5-carbonitrile, 4-(methoxyphenyl)-3-methyl-6-oxo-4,5,6,7-tetrahydro-2*H*-pyrazolo[3,4-*b*]pyridine-5-carbonitrile, and 3-methyl-6-oxo-4-(3,4,5-trimethoxyphenyl)-4,5,6,7-tetrahydro-2*H*-pyrazolo[3,4-*b*]pyridine-5-carbonitrile and their corrosion inhibition efficiency on steel in 1M HCl was studied by different techniques such as weight loss analysis, potentiodynamic polarization and EIS methods. The polarization data indicated that cathodic effect was prominent and maximum efficiency of 95.2% was obtained for 3-methyl-6-oxo-4-(3,4,5-trimethoxyphenyl)-4,5,6,7-tetrahydro-2*H*-pyrazolo[3,4-*b*]pyridine-5-carbonitrile at 100 ppm.

In 2014, Vinod. P. Raphael *et.al.*, were investigated the inhibition efficiency of 3-acetylpyridine-semicarbazide (3APSC) on steel corrosion in 1M HCl by weight loss analysis, potentiodynamic polarization and EIS measurements [67]. Even at very low concentrations, 3APSC exhibited pronounced efficiency. The adsorbed inhibitor on the metal surface obeys Langmiur isotherm model and thermodynamic parameters were also evaluated. Polarization studies indicated that 3APSC inhibitor acted as a mixed-type and metal surface morphological study was conducted by SEM.



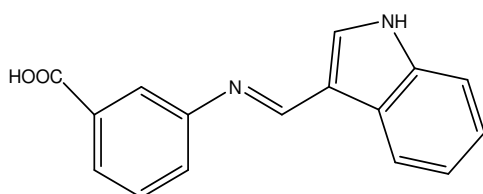
3APSC

Schiff base corrosion inhibitors derived from Indole derivatives- A Review

Some researchers studied various applications of Schiff bases derived from indole derivatives. In addition to anti corrosion activity, anti-oxidant property and cytotoxic activity of indole based Schiff bases are well established.

Ashish Kumar Singh investigated corrosion inhibition capacity of 3-(4-((Z)-Indolin-3-ylideneamino)phenylimino)indolin-2-one (PDBI) in 2012 [68]. The inhibition efficiency of the compound on mild steel corrosion in 1M HCl solution was analysed by potentiodynamic polarization studies, weight loss measurements and EIS techniques. The compound showed predominant inhibition efficiency against mild steel corrosion. The adsorption process was obeyed Langmuir isotherm model.

In 2012, Aby Paul *et.al.*, revealed the inhibition efficiency of Schiff base derived from 3-formylindole and 3-aminobenzoic acid (3FI3ABA) on mild steel corrosion in 1M HCl using weight loss analysis, EIS and potentiodynamic polarization studies [69]. At low concentrations, the Schiff bases displayed marked inhibition capacity and the efficiency rises with the concentration of inhibitors. The adsorption of inhibitor was obeyed Langmuir isotherm and thermodynamic parameters were determined.

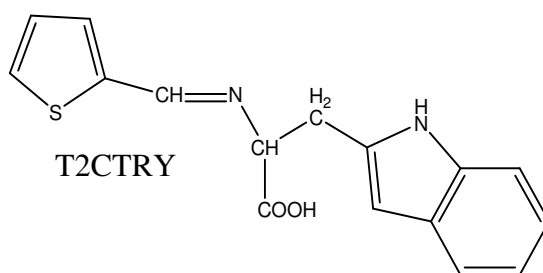


3FI3ABA

Schiff base corrosion inhibitors derived from Thiophene derivatives- A Review

Numerous potential Schiff bases derived from thiophene derivatives have been prepared by many researchers and studied their use in various fields especially in corrosion control area. In 2014, Daoud D *et.al.*, studied adsorption and corrosion inhibition properties of synthesized [70] thiophene Schiff base, (NE)-N-(thiophen-3-ylmethylidene)-4-({4-[(E)-(thiophen-2-ylmethylidene)amino] phenyl}m-ethyl) aniline on steel in 1M HCl and 1M H₂SO₄ using weight loss studies and electrochemical methods.

Nimmy Kuriakose *et.al.*, introduced and studied corrosion inhibition efficiency of a new Schiff base with thiophene moiety and derived from amino acid in 2014 [71]. They prepared thiophene-2-carbaldehyde tryptophan (T2CTRY) and measured its inhibition efficiency on mild steel in 1M HCl using weight loss analysis, EIS and potentiodynamic polarization methods. The Schiff base compound exhibited good corrosion inhibition efficiency. The inhibitor adsorption mechanism was obeyed Freundlich isotherm model and thermodynamic parameters were evaluated. A maximum efficiency of 96.2% was displayed at 1 mM concentration.

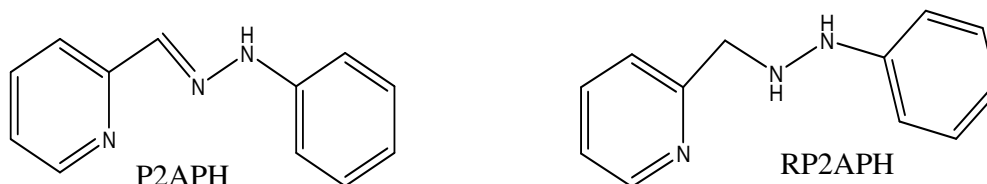


Reduced Schiff base corrosion inhibitors- A Review

The study of the corrosion inhibition activity of reduced Schiff bases is very rarely conducted. In 2009, Adriana Barbosa da Silva *et.al.*, investigated the activity of the Schiff base N,N'-bis(salicylidene)-1,2-ethylenediamine (Salen) and

its reduced form (N,N'-bis(2-hydroxybenzyl)-1,2-ethylenediamine) as inhibitors on steel corrosion in 1M HCl by potential measurements, EIS, potentiodynamic polarization and spectrophotometry study [72]. The derived data clearly established that the reduced Schiff base molecules have relatively the highest values of inhibition efficiency than others.

In 2016, Vinod P Raphael *et.al.*, synthesized a heterocyclic Schiff base phenylhydrazone 2-[(E)-(2-phenylhydrazinylidene)methyl]pyridine (P2APH) and its reduced form 2-[(2-phenylhydrazinyl)methyl]pyridine (RP2APH). They also investigated the corrosion inhibition efficiency on CS specimen in 1M HCl by the different methods such as gravimetric, electrochemical polarization, noise, surface analysis and quantum chemical studies [73]. P2APH exhibited good inhibition efficiency than RP2PPH. However the RP2PPH was stable in HCl medium and remained as a potential inhibitor for days. The evaluation of energy of LUMO, HOMO, energy difference, electronegativity and the number of transferred electrons etc were carried out by quantum chemical studies



Scope and objectives of the present investigation

The study of Schiff bases was considered as a popular and predominant research area due to their simple method of synthesis, adaptability, and wide range of applications. Thus, Schiff bases have a predominant role in the progress of coordination chemistry and possess various applications in industrial, catalytic and pharmaceutical fields as they form stable complexes with metals. Compounds with functional groups containing hetero atom, are capable to donate lone pair of

electrons, and can act as very potential corrosion inhibitors. Schiff bases are organic imines possess these features and they can act as potential inhibitors for metal deterioration. Previously many Schiff bases have been invented as inhibitors for steel, aluminium and copper corrosion in acid medium. However literature survey revealed that Schiff bases derived from heterocyclic compounds like acetyl pyridine, indole and thiophene aldehydes and ofcourse their reduced forms were not much reported as corrosion inhibitors.

The present investigation focuses to synthesize heterocyclic Schiff bases of 2-acetylpyridine and reduced form of previously reported Schiff bases derived from 3-acetylpyridine, 3-formylindole and thiophene-2-carbaldehyde and characterize by different spectroscopic techniques such as NMR, UV-vis, FTIR and mass. Various techniques like weight loss studies, electrochemical studies such as EIS, Tafel polarization and noise measurements are also proposed to find out the corrosion inhibition efficiency of compounds. It is also proposed to explain the mechanism of corrosion by plotting different adsorption isotherms. The temperature effect on corrosion inhibition efficiency was analysed to obtain the thermodynamic parameters like enthalpy, entropy and activation energy. To investigate the changes observed in the surface of the metal, surface morphological analysis was planned to conduct by taking scanning electron micrographs (SEM) of the metal surfaces. Quantum mechanical investigations are also proposed to evaluate the energy of HOMO, LUMO, their energy gap, electronegativity, hardness and number of transferred electrons.

CHAPTER 2

MATERIALS AND METHODS

This chapter contains all the details about the common reagents and the procedure used for the synthesis and corrosion study of Schiff base compounds. The techniques conducted for the purification of the compounds and various analytical methods employed for the characterization are also explained.

Reagents

The preparation of Schiff bases was carried out using analar grade samples of 2-acetylpyridine, 3-formylindole and thiophene-2-carbaldehyde procured from Fluka and other reagents such as phenylhydrazine hydrochloride, semicarbazide, thiosemicarbazide, 3- amino benzoic acid and 4- amino benzoic acid were purchased from E-Merck.

All the Schiff base preparation was conducted in ethanol medium and analar grade hydrochloric acid and sulphuric acid were used for corrosion investigations. The preparation procedure and other details of Schiff bases are given in the following chapters.

Experimental techniques

C H N analysis

Carbon, hydrogen and nitrogen percentage of the Schiff bases were measured by microanalysis using Elementar make Vario EL III model CHN analyzer.

Infrared spectra

The infrared spectra of the Schiff base compounds were recorded by KBr pellet method in the range of $4000-400\text{cm}^{-1}$ on Shimadzu model FT-IR Spectrometer

(Model IR affinity-1). The infrared spectrum contains the characteristic stretching frequencies which help to predict the functional groups present in the compounds.

Electronic spectra

The electronic spectra of the Schiff bases were recorded on a Shimadzu UV-Visible-1800 Spectrophotometer with DMSO as solvent. The spectral data gives additional evidence for the molecular structure of Schiff bases.

Mass spectra

The mass spectral studies of Schiff base compounds were carried out only after the removal of the impurities present in trace amount by chromatographic method. Mass spectra were recorded using GCMS Qp-2010 plus model.

NMR spectra

^1H nmr and ^{13}C nmr spectra of Schiff base compounds were recorded in DMSO – D_6 solvent using Bruker Avance III, 400MHz model

Corrosion inhibition studies

Corrosion inhibition studies were carried out by gravimetric analysis as mentioned by ASTM method. A further confirmation of the inhibition efficiency of the Schiff bases was obtained from electrochemical experiments such as potentiodynamic polarization, impedance studies and noise measurements.

Gravimetric analysis

Aggressive solutions

Gravimetric analysis conducted by making 150ml stock solutions of Schiff bases and their precursors having concentration of 1mM in 1M HCl and 0.5M H_2SO_4 solutions. These solutions were diluted with 1M HCl and 0.5M H_2SO_4 to obtain solutions of different concentrations 0.2 to 1mM.

Metal specimens

Mild steel metal specimens of approximate composition C, 0.42%; Mn, 0.05%; P, 0.01%; S, 0.016%; Si, 0.025% and rest Fe for the gravimetric studies were prepared as mentioned by ASTM (American Society for Testing and Materials G31-72, ASTM “Laboratory Immersion Corrosion Testing of Metals”) standards. Metal specimens of approximate dimension 1x1x0.04 cm were cut and abraded by emery papers of different grades (100, 220, 400, 600, 800, 1000, 1500 and 2000). The area of the metal specimens was measured using screw gauge and vernier calipers. The specimens were washed with methanol, acetone and with distilled water. It was dried and accurately weighed with 0.0001g accuracy. These metal specimens were immersed in inhibitor solutions of different concentrations taken in stoppered bottles in hanging position with the help of fishing lines.

Procedure

The gravimetric measurements were carried out using ASTM standard method. The weight loss happened for the metal specimens were calculated for 4 consecutive days at an interval of 24 hours. A blank measurement was also taken without inhibitor addition. For better results, duplicate experiments were conducted and the average values were noted. From weight loss measurements corrosion rate and percentage of corrosion inhibition efficiency were determined. The corrosion rate and the inhibition efficiency of compounds were calculated using equations 5 and 6 respectively.

$$\text{Rate of corrosion } W = \frac{K \times \text{wt. loss in grams}}{\text{Area in sq.cm} \times \text{time in Hrs} \times \text{Density}} \quad (5)$$

where ‘K’ = 87600 (This is a factor used to convert cm/hour into mm/year), density of MS specimen = 7.88g/cc and the density of Cu = 8.76g/cc

Percentage of inhibition or the inhibition efficiency (η) is given by

$$\eta = \frac{W-W'}{W} \times 100 \quad (6)$$

where W' & W are the corrosion rate of the MS specimen with and without the inhibitor respectively [74].

Adsorption isotherms

The mechanism of corrosion inhibition by the organic molecules on the surface of metal is not yet completely disclosed. However it is strongly convinced by the scientific researchers that the corrosion inhibition mainly occurred due to the adsorption of the molecules on the metal surface [75, 76]. Physical, chemical or both type adsorptions may happen. Adsorption isotherms have an important role in determining the corrosion inhibition mechanism [77-79]. The common adsorption isotherms are Langmiur, Temkin, Freundlich and Frumkin adsorption isotherms. All the above mentioned isotherms were tried with the help of equations given below to fit the best adsorption model.

$$\text{Langmiur adsorption isotherm} \quad \frac{C}{\theta} = \frac{1}{K_{ads}} + C \quad (7)$$

$$\text{Freundlich adsorption isotherm} \quad \theta = K_{ads}C \quad (8)$$

$$\text{Temkin adsorption isotherm} \quad e^{f\theta} = K_{ads} C \quad (9)$$

$$\text{Frumkin adsorption isotherm} \quad \frac{\theta}{1-\theta} \exp(f\theta) = K_{ads}C \quad (10)$$

where C is the inhibitor concentration, θ is the fractional surface coverage, f is the molecular interaction parameter and K_{ads} is the adsorption equilibrium constant. Among the tried isotherms, most suitable one which has the highest correlation coefficient value (R^2) was considered for explaining the adsorption mechanism.

The relation between adsorption equilibrium constant K_{ads} and the standard free energy of adsorption ΔG_{ads}^0 is given by the equation,

$$\Delta G_{ads}^0 = -RT \ln (55.5 K_{ads}) \quad (11)$$

where the constant value 55.5 is the molar concentration of water, R is the ideal gas constant and T is the temperature in Kelvin. The value of K_{ads} and ΔG_{ads}^0 were obtained from different adsorption isotherms.

Surface morphological analysis using SEM

Analysis of changes occurred in the surface morphology of the metal specimens helps to explain the inhibition mechanism by which the Schiff bases decrease the corrosion rate [80]. This was carried out by taking scanning electron micrographs (SEM) of the surfaces of bare metal, metal immersed in acid solution (24 h) and metal immersed in inhibitor solution (24 h). It was taken by JEOL model JSM-6390LV in the resolution value 2.00 x.

Temperature studies

Gravimetric analysis were carried out in the temperature range 30-60°C for evaluating different corrosion thermodynamic parameters such as entropy of corrosion (ΔS^*), enthalpy of corrosion (ΔH^*), activation energy (E_a) and Arrhenius parameter (A). The activation energy for corrosion process in the presence and absence of inhibitor was evaluated by following Arrhenius equation.

$$K = A \exp \left(\frac{-E_a}{RT} \right) \quad (12)$$

where K is the rate of corrosion, E_a is the activation energy, A is the frequency factor, T is the temperature and R is the universal gas constant. According to this equation, the plot of $\log K$ Vs $1000/T$ should be a straight line with a slope of $-E_a/2.303R$ and intercept of $\log A$.

The enthalpy and entropy of activation (ΔH^* , ΔS^*) were evaluated by the transition state theory [81], which is represented by the equation,

$$K = \left(\frac{RT}{Nh}\right) \exp\left(\frac{\Delta S^*}{R}\right) \exp\left(\frac{-\Delta H^*}{RT}\right) \quad (13)$$

where N is the Avagadro number and h is the Planck's constant. Then the above equation is changed to $y = mx + c$ form.

$$\log \frac{K}{T} = \log \frac{R}{Nh} + \frac{\Delta S}{2.303 R} - \frac{\Delta H}{2.303 RT} \quad (14)$$

The enthalpy of the reaction can be evaluated from the slope of the equation ie., $-\Delta H/2.303R$. Entropy of the reaction can be obtained from the intercept of the equation ie., $\log \frac{R}{Nh} + \frac{\Delta S}{2.303 R}$

Electrochemical corrosion investigations

Metallic corrosion is considered as the gradual deterioration of metals by an electrochemical phenomenon with their environment. Thus electrochemical methods can be used for determining corrosion rate with certainty [82-84]. Fast development of the computer technology and fundamental electrochemistry lead to arise perfect potentiostats acceptable for the investigation of rate of corrosion and help the researchers to introduce rate controlling mechanisms. Generally gravimetric analysis is time consuming investigation method for the measurement of corrosion rates, but electrochemical methods conducting with the help of computer are comparatively very fast and obtained results which are in good agreement with the gravimetric measurements.

Theoretical concept for the electrochemical corrosion investigation technique is based on the mixed potential theory. According to this theory, the total oxidation reactions rate (anodic) is equal to the total reduction reactions rate (cathodic) on the surface of corroding metal. The mixed corrosion potential derived is called the corrosion potential or open circuit potential (OCP) denoted by the symbol E_{corr} . i_{corr} is the current density called corrosion current density.

Most applicable electrochemical investigations are a) Polarization studies and b) Electrochemical Impedance Spectroscopy.

Potentiodynamic polarization analysis

Generally polarization studies are divided into two i) Linear polarization studies and ii) Tafel extrapolation studies. Polarization method associated with the change of the working electrode potential and the produced current was monitored as a function of time or potential [85-87].

Linear polarization technique

The polarization response of a metal specimen (i_{app}) is explained by the equation similar to the Butler-Volmer equation

$$i = i_{corr} \left[e^{\left(\frac{\eta}{\beta_a} \right)} - e^{\left(\frac{\eta}{\beta_c} \right)} \right] \quad (15)$$

where i = net current density across the metal electrolyte interface, i_{corr} is the corrosion current density (Acm^{-2}), η is the over potential ($E_{measured} - E_{corr}$). β_a and β_c are the anodic and cathodic constants depending on the reaction mechanism and are given by

$$\beta_a = \frac{RT}{(1-\alpha)nF} \quad (16) \quad \beta_c = -\frac{RT}{\alpha nF} \quad (17)$$

Equation 8 establishes that the slowest rate determining step in the electrochemical process of corrosion is the charge transfer process occurred at the metal-solution interface. This relationship is observed experimentally between applied electrochemical current density and the potential of a corroding electrode in the absence of competing redox reactions. The relevance of this relationship depends on single charge transfer controlled anodic and cathodic reactions. This equation deliver the base of the electrochemical polarization method as applied to the electrode which undergo corrosion and corresponding potential change.

Linear polarization method depends on the theoretical and practical verifications that the potentials are very close to E_{corr} , +/- 10mV and the applied current density is linear as function of the electrode potential. This is illustrated in the Figure 1.3.

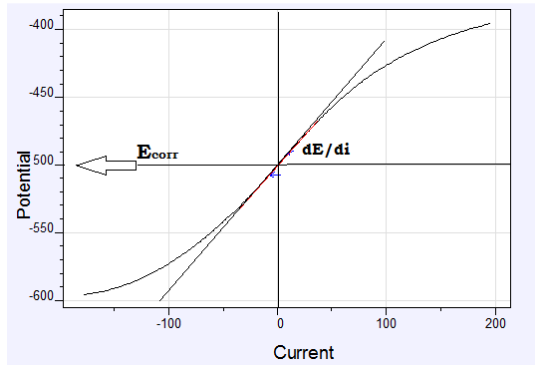


Figure 1.3: Linear polarization

dE/di is the slope and has the unit of resistance known as polarization resistance (R_p), thus this method is sometimes known as polarization resistance method. The famous Stern and Geary equation 18 is obtained by mathematical linearization of equation 15, which indicates i_{corr} is inversely related to the slope by the equation.

$$i_{\text{corr}} = \left[\frac{b_a b_b}{2.303(b_a b_b)} \right] \frac{\Delta i}{\Delta E} = \frac{B}{R_p} \quad (18)$$

where b_a and b_b are the anodic and cathodic Tafel slopes, respectively. Equation 18 helps to measure the corrosion rate as current density, i_{corr} , where B is a constant and R_p is polarization resistance. Linear polarization technique was employed for measuring corrosion inhibition efficiency in the manner that the polarization resistance (R_p) have the tendency to increase with the increase in the inhibitor concentration. The adsorption of inhibitor molecules on the corroding metal surface will lead to decrease the rate of charge transfer process. This leads to reduce the corrosion rate or to increase the polarization resistance. From the analysis of the

slope of linear polarization curves in the region of corrosion potential of blank and various concentrations of the inhibitor, the polarization resistance values were obtained [88,89].

In the present investigation the electrochemical studies were performed by Ivium compactstat-e electrochemical system. The ‘Ivium soft’ is a software which provide the R_p value directly after the analysis of linear polarization curves. The inhibition efficiency was calculated from the polarization resistance value, using the equation

$$\eta_{R_p} \% = \frac{R'_p - R_p}{R'_p} \times 100 \quad (19)$$

where R'_p and R_p are the polarization resistance with and without the inhibitor respectively.

Tafel extrapolation technique

Tafel equation reveals the correlation between the applied potential value and the logarithm of current density. For simple metal dissolution (anodic process), the current density is obtained by Tafels law:

$$I = i_{corr} e^{\left(\frac{\eta_a}{\beta_a}\right)} \quad (20)$$

The equation must satisfy the condition $\left(\frac{\eta_a}{\beta_a}\right) \gg 1$. On taking the logarithm of the equation (20),

$$\eta_a = -\beta_a \ln i_{corr} + \beta_a \ln i_a \quad (21)$$

Converting into logarithm to base 10 and defining the anodic Tafel constants a and

$$b, \text{ then } \eta_a = a_a + b_a \log i_a \quad (22)$$

where $a_a = -2.303\beta_a \log i_{corr}$ and $b_a = 2.303\beta_a$

In the same way for cathodic process $\left(\frac{\eta_b}{\beta_c}\right) \ll 1$

$$i = -i_{\text{corr}} e\left(-\frac{\eta_c}{\beta_c}\right) \quad (23)$$

$$\text{Then } \eta_c = a_c - b_c \log i_c \quad (24)$$

$$\text{where } a_c = -2.303\beta_c \log i_{\text{corr}} \quad \text{and } b_c = 2.303\beta_c \log i_c$$

The plot of electrode potential versus the logarithm of current density gives a straight line, according to equations 22 and 24 and they are known as Tafel lines. The slope of a Tafel plot, 'b' establishes the electrode process mechanism and the intercept 'a' at $\eta = 0$ provides the exchange current density and gives the information about the rate constant of the reaction.

The method of extrapolating the linear segments of potential-current density curves considered as a way to measure i_{corr} value. This procedure is based on the principle that the specimens were made to act as cathode of the electrochemical cell consisting the corrodent. The cathodic potential-current density curve is plotted over a potential range E_{corr} to E_c . Similarly the anodic potential-current density is obtained in the direction away from E_{corr} . This leads the specimen to act as anode at this moment. Both the obtained cathodic and anodic potential-current density curves include linear segments, considered as Tafel regions. By extrapolating this linear segment of cathodic and anodic curves, both Tafel lines intersect at the point of coordinates $(E_{\text{corr}}, \log i_{\text{corr}})$ and the value of corrosion current density was obtained.

Then the percentage of inhibition efficiency is measured using the equation

$$\eta_{\text{pol}} \% = \frac{i_{\text{corr}} - i'_{\text{corr}}}{i_{\text{corr}}} \times 100 \quad (25)$$

where i'_{corr} and i_{corr} are corrosion current densities with and without the inhibitors, respectively [90].

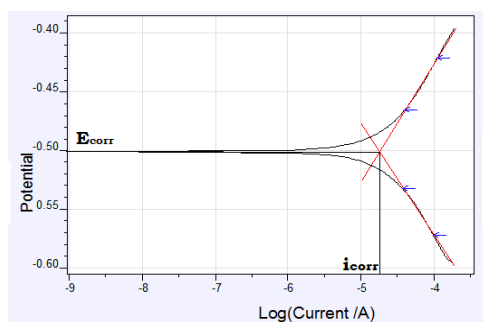


Figure 1.4: Tafel plot

In the present investigation Tafel polarization studies of mild steel in 1M HCl and 0.5M H₂SO₄ with and without inhibitor were conducted by recording both anodic and cathodic potentiodynamic polarization curves using Ivium compactstat-e electrochemical system. The exposed area of the metal specimen was taken as 1cm². Polarization plots were obtained in the electrode potential range from -250 to +250 mV Vs corrosion potential (E_{corr}) at a scan rate of 1mVsec⁻¹.

Electrochemical impedance spectroscopy (EIS)

Electrochemical impedance spectroscopy has been considered as an effective method for the study where polarization measurements failed to provide the correct values of current densities [91]. Impedance measurements also provide the kinetic and mechanistic details. So this technique is considered as an important method for the study of corrosion [92].

Electrochemical systems are attributed with respect to the equivalent electrical circuits. A simple system shown in the Figure 1.5, where R_s is the solution resistance, R_{ct} is the charge transfer resistance and C_{dl} is the double layer capacitance which forms due to the interaction of charged metal surface and the opposite charged layer distributed by the ions in the solution [93,94]. From R_{ct} values, calculation of electrochemical reaction rates became possible.

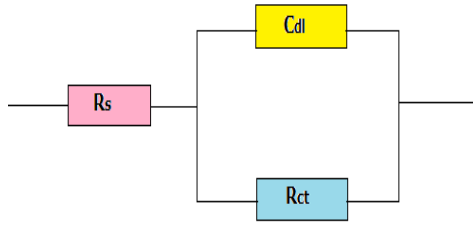


Figure 1.5: Equivalent circuit

Capacitance measurements illustrate the mechanism of the film formation at the electrode. During the electrochemical measurements it is observed that the C_{dl} value decreases and it can be explained by the decrease of its electrical capacity. The adsorption of the inhibitor molecules on the surface of electrode displaces the water molecules and other ions originally adsorbed on the surface and thereby reduce the electrical capacity. This decrease in the capacity with the rise in inhibitor concentration revealed a protective film formation on the electrode surface.

The target of EIS measurement is to confirm that the electrochemical system fits a certain equivalent-circuit model. This is experimentally done by observing the electrochemical system response to an ac excitation signal over a wide range of frequencies and the system impedance can be calculated. Impedance, Z , is a measurement of the tendency of circuit to resist the flow of an alternating electrical current [95, 96]. The EIS plot contains the real (resistance) and imaginary (capacitance) components of the system. Impedance is recorded as a complex number with real component $Z'(\omega)$ and imaginary component $Z''(\omega)$ as represented in the equation 26.

$$Z(\omega) = Z'(\omega) + iZ''(\omega) \quad (26)$$

Different type of plots can be used to obtain the impedance data. Each type provides significant advantages for establishing certain characteristics of a particular system. Commonly used plots are Nyquist plot and Bode plot.

Nyquist plot

This type of impedance plot is also called Cole-Cole plot. The imaginary component (Z'') is plotted against the real component (Z') of the impedance for all excitation frequency. R_s is the solution resistance or uncompensated resistance between the reference electrode and working electrode. R_{ct} is the charge transfer resistance or polarization resistance at the interface of electrode and solution. For high frequency values, the impedance of the system is entirely generated by the solution resistance R_s [97]. The frequency attains its highest value at the left side end of the semicircle curve, where the curve touches the x-axis and the frequency attains its lowest value at the right side end of the semicircle (Figure 1.6). Then the inhibition efficiency of a molecule can be calculated from R_{ct} values using the equation 27 [98].

$$\eta_{EIS} \% = \frac{R_{ct} - R'_{ct}}{R_{ct}} \times 100 \quad (27)$$

where R_{ct} and R'_{ct} are the charge transfer resistances of working electrode in the presence and absence of inhibitor, respectively.

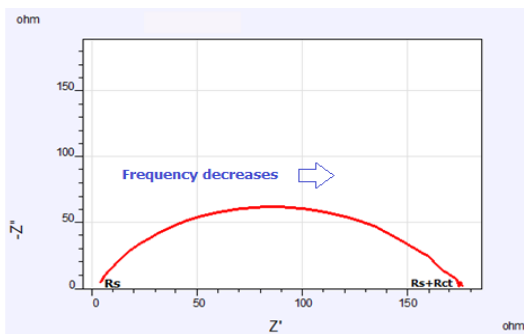


Figure 1.6: Nyquist plot

Bode plot

This type of plot helps to find out the absolute impedance Z using the equation $|Z| = \sqrt{Z'^2 + Z''^2}$ and the phase angle ' θ ' of the resultant wave form is recorded as a function of frequency. The Bode plot is a time consuming alternative

of the Nyquist plot, helps to avoid longer times for the low frequency measurements. The value of R_s and R_{ct} obtained from the curve representing $\log|Z|$ versus \log frequency (impedance plot). The break point of this curve lies on a straight line whose slope will be -1. Extrapolation of this straight line to the y-axis at $f=1$ or $\log f = 0$ results the value of C_{dl} .

$$|Z| = \frac{1}{C_{dl}} \quad (28)$$

The plot of ' θ ' versus $\log f$ shows a peak corresponding to $f \theta^{\max}$. This point represents the maximum phase shift value and from which C_{dl} can be calculated.

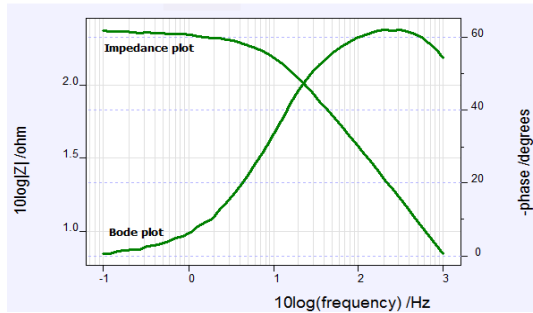


Figure 1.7: Bode and impedance plots

A three electrode cell system is commonly used for performing EIS measurements (Figure 1.8). It consists of saturated calomel electrode (SCE) as the reference electrode, Platinum electrode having 1cm^2 as counter electrode and metal specimens with an exposed area of 1cm^2 as the working electrode. The experiments were performed using a Ivium compactstat-e electrochemical system. 1M HCl and 0.5M H_2SO_4 were taken as the electrolyte and the working area of the metal specimens were exposed to the electrolyte for 30 minutes prior to the measurement. EIS measurements were recorded at constant potential (OCP) in the range of frequency from 1 KHz to 100 mHz with an excitation signal of amplitude of 10 mV [99].

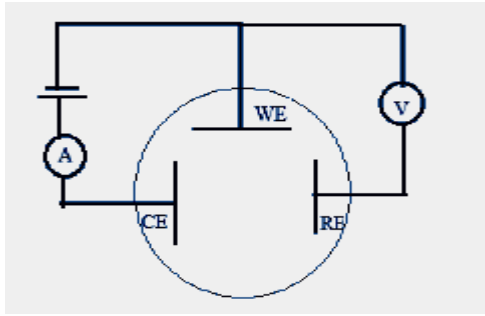


Figure 1.8: Three electrode cell system

Electrochemical noise analysis

Electrochemical noise (ECN) is the general term measures the fluctuations of potential and current associated with corrosion process and it is the result of discrete events involved during metal deterioration. ECN helps to measure the amount of localized pitting corrosion also [100-102]. Electrochemical noise (ECN) measurements were performed using a three-electrode cell system, which consists of two carbon steel electrodes of 1 cm^2 area which are used as working electrode and as counter electrode and SCE as reference electrode [103, 104]. All ECN analyses were performed for a period of 1200 sec using Ivium compactstat-e electrochemical system controlled by iviumsoft software.

Noise is an algebraic expression with random nature which describes the amplitude-time dependence of a source, indicates that noise is a non-deterministic process. Generally deterministic processes are periodic in nature and can be defined mathematically by a time varying function. Fluctuations observed in corrosion current values are random and classified as non-deterministic, which is analysed by probability and statistics rather than algebraic equation. Figure 1.9 represents the plot of noise current Vs time, and the noise current values give the idea about the corrosion protective power of sample. Figure 1.10 represents the pitting index curve of the sample and the amplitude of the curve indicates the resisting power of sample against localized pitting corrosion.

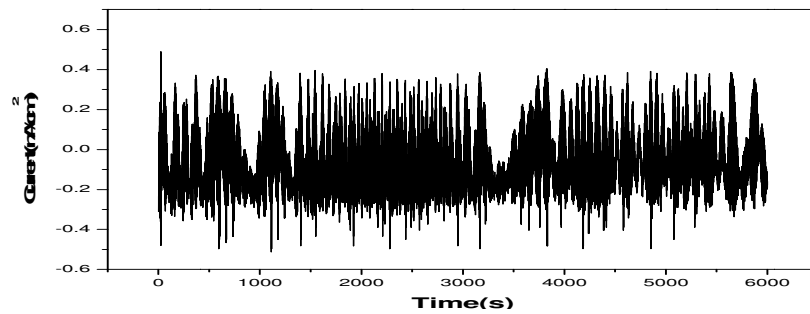


Figure 1.9: Noise current Vs time plot

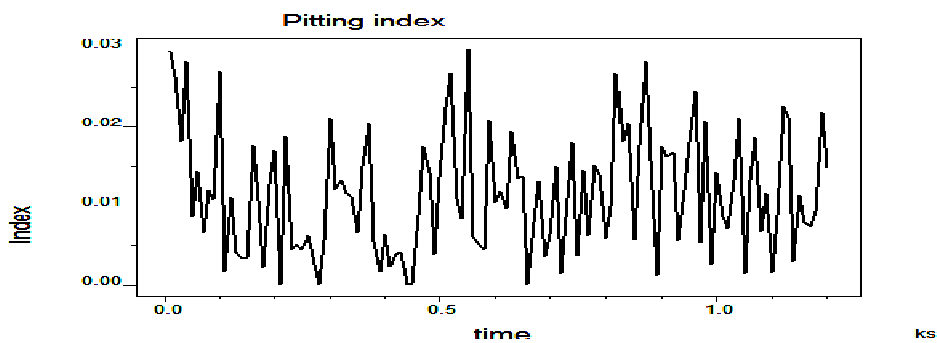


Figure 1.10: Pitting index curve

Frequency domain analysis

The basic concept about the frequency-domain analysis is established that a waveform of any complexity can be taken as the sum of numerous sinusoidal waveforms of suitable amplitude, relative phase and periodicity [105-107]. The representation of a time depending process in the frequency domain analysis is called a spectrum. The frequency domain analysis of noise measurement gave the PSD (Power Spectral Density) of systems, which is represented in the Figure 1.11. It has various applications in different branches of science and technology.

Fast Fourier Transform

Fast Fourier Transform (FFT) is a machine calculation method of the complex Fourier series, and considerably faster than traditional methods. Two major problems associated with analysis by FFT are leakage and aliasing. Aliasing is an error occurs by the too slow sampling rate and is applicable to all spectral analysis

methods. Leakage is the result from the basic presumption of the Fourier Transform that the finite time record is assumed as periodic.

Maximum Entropy Method

The analysis by Fourier Transform has been considered as a basic tool in every spectral analysis method [108]. The Fourier analysis become accurate only when there is long record length. When the record length is short, conventional spectrum estimation by smoothing may provide poor resolution. The Burg's maximum entropy method helps to improve the spectral resolution of short length records. This is achieved by the extrapolation of auto-correlation function and helps to maximize the entropy of the probability density function in each step of the extrapolation. Burg's method is data dependable method and therefore it is nonlinear. The MEM has applications in various fields in science and technology.

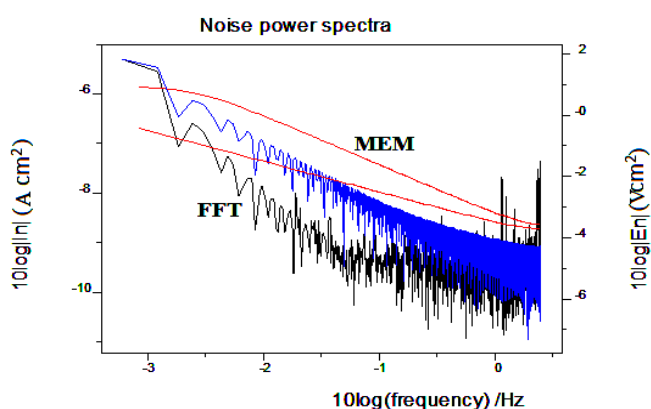


Figure 1.11: PSD plot

Quantum mechanical analysis

The corrosion inhibition properties of the newly synthesized inhibitors can also be determined by the analysis of the Frontier molecular orbital energy levels [109-111]. According to the HSAB concept, the interaction of the filled molecular orbitals of the inhibitor molecules with vacant d orbitals of different atoms present on the metal surface can be considered as a donor-acceptor type. This interaction has an

eminent role in the inhibition action of inhibitor molecules [112-114]. The strong interaction between the metal surface and inhibitor molecules is indicated by the higher E_{HOMO} values and low energy difference value between the HOMO and LUMO (ΔE). GAMMES software and DFT method are used for the determination of optimized geometry of compounds and quantum chemical evaluations. A combination of Lee–Yang–Parr nonlocal correlation functional (B3LYP) and Beck’s three parameter exchange functional was employed in DFT method. HSAB parameters such as electro negativity (χ) and chemical hardness (η) of the molecules were evaluated by the following equations,

$$\chi \approx -1/2 (E_{\text{HOMO}} + E_{\text{LUMO}}) \quad (29) \quad \eta \approx 1/2 (E_{\text{HOMO}} - E_{\text{LUMO}}) \quad (30)$$

The number of transferred electrons from donor to acceptor molecules (ΔN) is measured from the quantum chemical parameters. The chemical hardness and the electronegativity of bulk iron are assumed as 0 and 7eV respectively for the convenience. The approximate number of transferred electrons from the inhibitor molecule to the iron atoms is evaluated by the following equation,

$$\Delta N = \frac{\chi_{\text{Fe}} - \chi_{\text{inhib}}}{2(\eta_{\text{Fe}} + \eta_{\text{inhib}})} \quad (31)$$

The optimized geometry of synthesized compounds can be established by quantum mechanical software GAMMESS. Optimized geometry helps to predict the three dimensional atomic arrangement of molecules which makes them most stable with minimum energy.

CHAPTER 3

CORROSION INHIBITION STUDIES ON SCHIFF BASES DERIVED FROM 2- ACETILPYRIDINE

The scientific literature till date records extensive studies on various heterocyclic Schiff bases in which compounds derived from 2-acetylpyridine are much less in number. Two heterocyclic Schiff bases namely (E)-2-(1-(2-phenylhydrazono)ethyl)pyridine (or 2-acetylpyridine phenylhydrazone) (2APPH) and (E)-2-(1-triazylideneethyl)pyridine (or 2-acetylpyridine semicarbazone) (2APSC) were synthesized, characterized and their corrosion inhibition behaviour as well as mechanism of inhibition were investigated by different techniques. Structural characterization includes NMR, mass, IR and UV-visible spectroscopy and elemental analysis.

Corrosion inhibition behaviour of aforesaid compounds on mild steel in 1M hydrochloric acid and 0.5M sulphuric acid solutions were examined by different methods including weight loss studies, potentiodynamic polarization analysis, electrochemical impedance spectroscopic techniques and electrochemical noise measurement. The mechanism of corrosion inhibition was explored and supplemented by adsorption studies and surface morphological studies. The effect of temperature on the inhibition of corrosion process was also subjected to investigation. Quantum mechanical investigations on corrosion behaviour of compounds were carried out to get further support. This chapter is further divided into four sections which comprise the detailed explanation of the synthetic, physicochemical, corrosion inhibition and quantum mechanical evaluations on the synthesised Schiff bases mentioned earlier.

SECTION 1

SYNTHESIS AND CHARACTERIZATION OF SCHIFF BASES DERIVED FROM 2-ACETILPYRIDINE

The synthesis and characterization of two potential Schiff bases 2-acetylpyridine phenylhydrazone (2APPH) and 2-acetylpyridine semicarbazone (2APSC), for the corrosion inhibition studies are presented in this section.

Preparation of 2-acetylpyridine phenylhydrazone (2APPH)

A hot ethanolic solution of 2-acetylpyridine was added to a refluxing solution of phenylhydrazine hydrochloride in ethanol and refluxed further for 3 hours on a water bath. The resulting solution was concentrated in order to obtain orange crystals, which was collected and washed with ethanol. Recrystallization from methanol gave 80% yield of the desired product. Elemental analysis data calculated: C, 73.9%; H, 6.16%; N, 19.90%. Found: C, 73.6%; H, 6.12%; N, 19%. Melting point: 220°C.

Characterization of 2APPH

NMR spectral analysis

The ^1H nmr spectrum of the Schiff base 2APPH (Figure 1.12) exhibited nine clear peaks for nine different hydrogen atoms. The methyl protons displayed a peak at 2.19 δ as singlet. A weak broad singlet peak exhibited at 10.26 δ was due to the NH proton and the broadness of the peak can be explained by the effects of H-bonding and quadrupole broadening. The peaks appeared in the range 7.78 - 8.72 δ were assigned to the pyridine ring aromatic protons. The remaining three peaks in the range 6.926 - 7.61 δ were due to the aromatic protons on phenyl ring. All aromatic protons exhibited J values of about 7-8 Hz due to the ortho coupling. The

CH proton adjacent to nitrogen in pyridine exhibited low coupling constant value of 6.5 Hz. It can be explained by the fact that, the value of coupling constant is inversely proportional to the electronegativity of neighbouring atom.

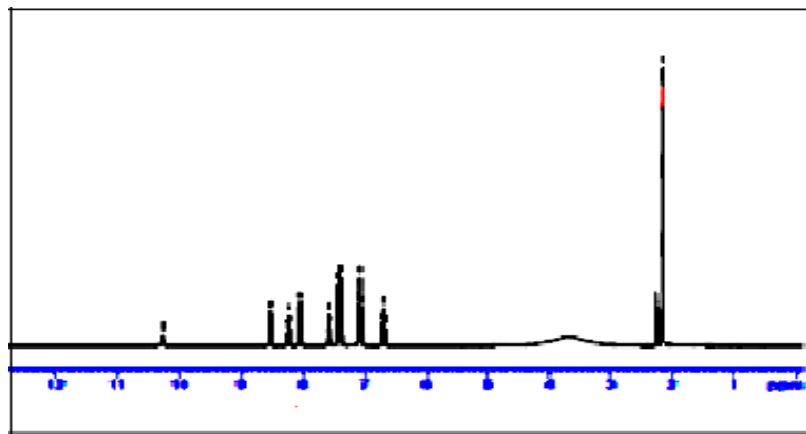


Figure 1.12: ^1H nmr spectrum of 2APPH

Table 1.1: ^1H nmr and ^{13}C nmr spectral data of 2APPH

	^1H nmr		^{13}C nmr		
	H Label	δ value	C Label	δ value	
	1	8.72(d, 1H, J=6.5Hz)	1	144	
	2	8.44(t, 1H, J=8Hz)	2	142	
	3	7.78(t, 1H, J= 7Hz)	3	122	
	4	8.25(d, 1H, J= 8Hz)	4	145	
	5	2.42(s, 3H)	5	128	
	6	10.48(sbr, 1H)	6	132	
	7	7.61(d, 1H, J=8Hz)	7	12.1	
	8	7.29(t, 1H, J=8Hz)	8	149	
	9	6.92(t, 1H, J=8Hz)	9	114	
			10	123	
			11	121	

The ^{13}C nmr spectrum is represented in the Figure 1.13. The spectrum exhibited 11 peaks corresponding to the 11 different carbon atoms and explained in the Table 1.1. A peak appeared at 12.1ppm was displayed by methyl carbon atom

and all 10 different type sp^2 hybridized carbon on aromatic ring was showed their signals in the range 114-149ppm. The details of nmr peaks are depicted in the Table 1.1.

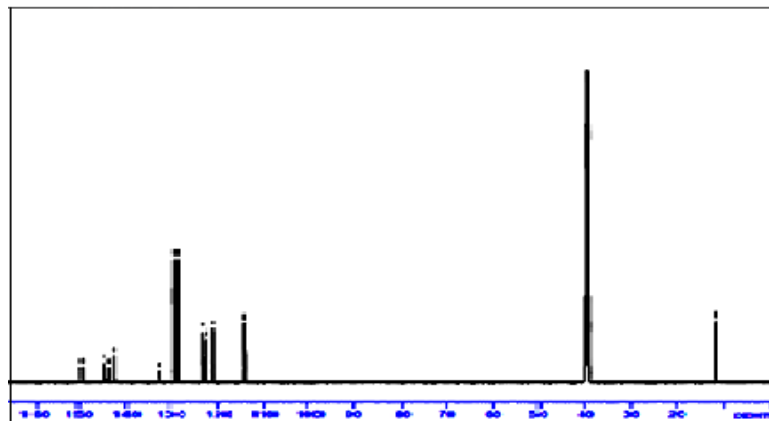


Figure 1.13: ^{13}C nmr spectrum of 2APPH

Mass spectral analysis

Mass spectrum of 2APPH is represented in the Figure 1.14. Base peak was displayed in the spectrum at m/z 211, which is exactly equal to the molecular weight of the Schiff base compound (M^+ peak). This implies the molecular stability of the compound. Also a signal was appeared at m/z 212, ($M+1$) peak which has $[M^+]:[M+1]$ intensity ratio as 100: 14 . This clearly establishes that total number of carbon atoms in the molecule is 13. The clear signals appeared at m/z 196, 194 and 106 were assigned due to the fragments $[\text{C}_{12}\text{H}_{10}\text{N}_3]^+$, $[\text{C}_{12}\text{H}_8\text{N}_3]^+$ and $[\text{C}_6\text{H}_6\text{N}_2]^+$ respectively. The signals observed at m/z 93 and 78 were due to the fragments $[\text{C}_6\text{H}_7\text{N}]^+$ and $[\text{C}_5\text{H}_4\text{N}]^+$. The secondary fragments originated from the pyridine $[\text{C}_3\text{H}_5]^+$ and $[\text{C}_4\text{H}_3]^+$ displayed the peaks at m/z 65 and 51 respectively. In GCMS, only one distinct peak was appeared which confirms the purity of the sample.

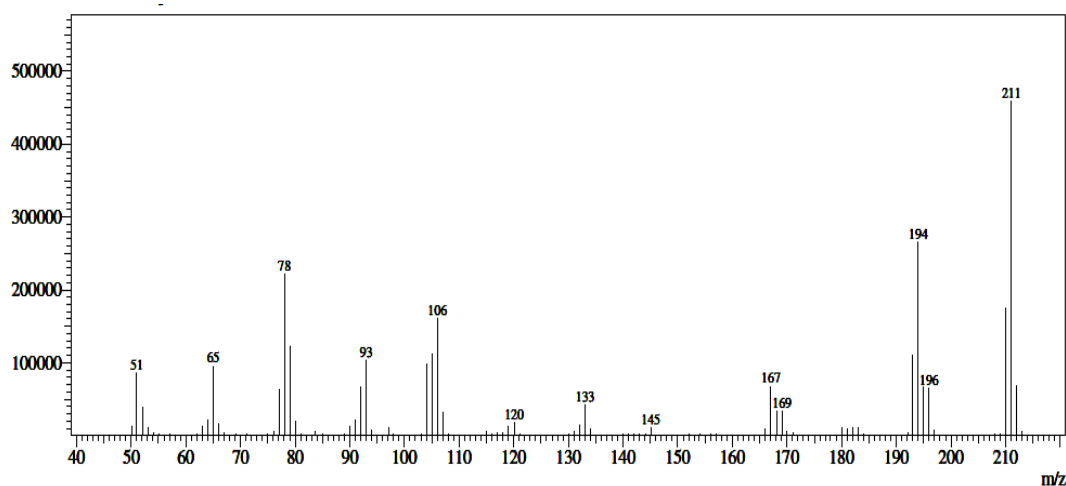


Figure 1.14: Mass spectrum of 2APPH

IR spectral analysis

The IR spectrum of the Schiff base showed the characteristic stretching and bending vibration frequencies. An intense peak observed at 1606 cm^{-1} is assigned due to the C=N stretching vibration. The vibration frequency of NH group exhibited a broad band at 3343 cm^{-1} . The peaks at 1549 cm^{-1} and 1446 cm^{-1} can be assigned to C=C vibrations of aromatic system. Stretching vibration frequency of C-N was observed at 1244 cm^{-1} and C-H vibrations were shown at $3215, 3036\text{ cm}^{-1}$. The in plane bending vibrations of pyridine ring appeared at 1097 cm^{-1} and 1037 cm^{-1} . Also the peaks obtained at 760 cm^{-1} and 630 cm^{-1} can be assigned as out of plane bending vibrations.

Electronic spectral analysis

UV-visible spectrum of the 2APPH exhibited three characteristic absorption bands at 28901 cm^{-1} , 32680 cm^{-1} and 39216 cm^{-1} , which are assigned to $n \rightarrow \pi^*$ (R-band), $\pi \rightarrow \pi^*$ (benzenoid band) and $\pi \rightarrow \pi^*$ (K band) transitions respectively.

Based on the spectral and elemental analysis, the structure of the Schiff base 2APPH was confirmed and the proposed structure is given in the Figure 1.15

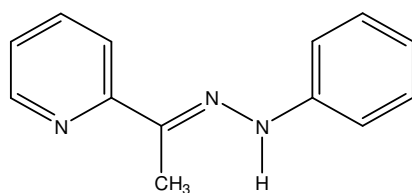


Figure 1.15: Structure of 2APPH

Preparation of 2-acetylpyridine semicarbazone (2APSC)

A hot ethanolic solution of 2-acetylpyridine was added to a refluxing solution of semicarbazide in ethanol and allowed to reflux for 3 hours on a water bath. The resulting solution was concentrated and the separated light rose coloured crystals were collected and washed with ethanol. Recrystallization from methanol gave 78% yield of the desired product. Elemental analysis data calculated: C, 53.93%; H, 5.61%; N, 31.46%; O, 8.98%. Found: C, 53.46%; H, 5.45%; N, 31.39%; O, 8.79%. Melting point: 200°C.

Characterization of 2APSC

NMR spectral analysis

The eight distinct non equivalent protons of 2APSC exhibited eight clear peaks on ^1H nmr spectrum (Figure 1.16). The three protons on sp^3 hybridized carbon atom (CH_3) showed its characteristic peak at 2.31 δ . A broad peak observed at 3.9 δ is assigned to the NH_2 protons and the broadness of the peak can be explained by the effects of H-bonding and quadrupole broadening. The NH proton exhibited a peak at 10.16 δ and the peaks appeared in the range 7.91- 8.80 δ were assigned to the aromatic protons. A very weak peak appeared at 6.18 δ can be assigned to the $-\text{OH}$ proton, which generates by tautomerism. All aromatic protons exhibited coupling constants of 8 Hz (ortho coupling) except the neighbouring $-\text{CH}$ protons of pyridine nitrogen.

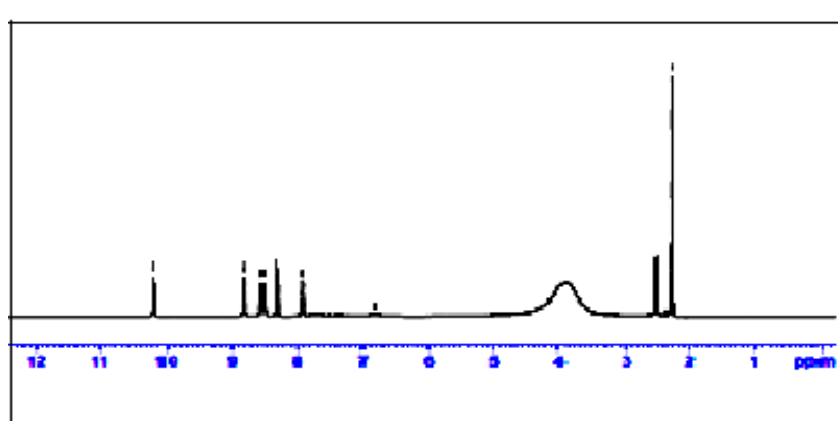


Figure 1.16: ^1H nmr spectrum of 2APSC

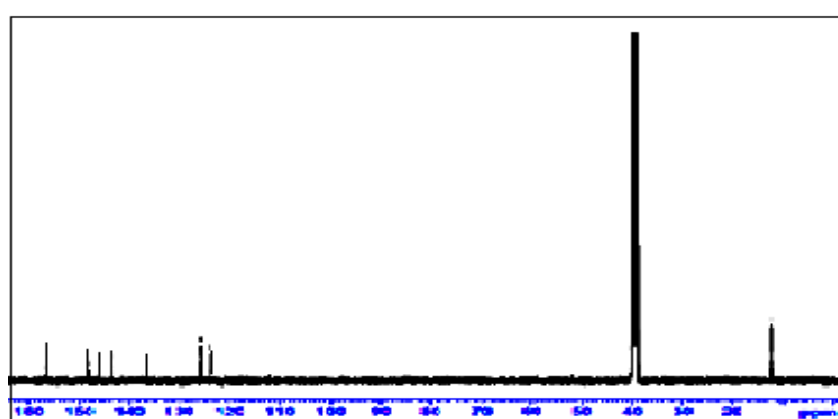


Figure 1.17: ^{13}C nmr spectrum of 2APSC

Table 1.2: ^1H nmr and ^{13}C nmr spectral data of 2APSC

	^1H nmr		^{13}C nmr		
	H Label	δ value	C Label	δ value	
	1	8.80(d, 1H, J=5Hz)	1	145	
	2	7.91(t, 1H, J=6.5Hz)	2	142	
	3	8.53(t, 1H, J=8Hz)	3	125	
	4	8.30(d, 1H, J=8Hz)	4	123	
	5	2.31(s, 3H)	5	136	
	6	10.16(S_{br} , 1H)	6	148	
	7	3.9(S_{br} , 2H)	7	12.02	
	-OH	6.815(S_{br} , 1H)	8	156	

In the ^{13}C nmr spectrum (Figure 1.17) the peaks appeared at 12.02ppm and 156ppm were displayed by methyl carbon atom and carbonyl group carbon atom respectively. The peaks of remaining carbon atoms were appeared in the range 123-148ppm. The assignment of nmr peaks are described in the Table 1.2

Mass spectral analysis

In the mass spectrum of 2APSC (Figure 1.18) molecular ion peak was displayed at m/z 178. The base peak observed at m/z 134 is assigned to the fragment $[\text{C}_7\text{H}_8\text{N}_3]^+$, which was generated by the removal of amide group from the molecular ion. The clear signals appeared at m/z 106, 78 and 51 were assigned due to the fragments $[\text{C}_7\text{H}_8\text{N}]^+$, $[\text{C}_5\text{H}_4\text{N}]^+$ and $[\text{C}_4\text{H}_3]^+$ respectively.

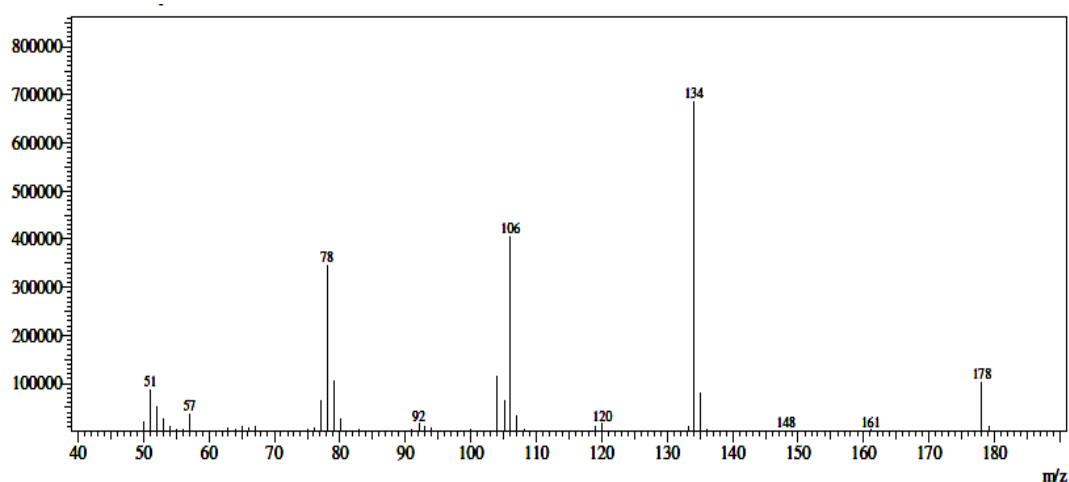


Figure 1.18: Mass spectrum of 2APSC

IR spectral analysis

The IR spectrum of 2APSC contains two intense peaks of C=O and C=N stretching vibrations at 1716 cm^{-1} and 1608 cm^{-1} respectively. The NH group vibration exhibited a band at 3176 cm^{-1} . The peaks observed at 3374 cm^{-1} and 3300 cm^{-1} represent the asymmetric and symmetric stretching vibrations of NH_2 group. The peaks at 1525 cm^{-1} and 1445 cm^{-1} can be assigned to C=C vibrations of aromatic system. Stretching vibration frequency of C-N was observed as a strong peak at 1293 cm^{-1} and C-H vibrations were shown at $3176, 3045\text{ cm}^{-1}$. The clear

peaks appeared at 1167, 1083 cm^{-1} and 760, 630 cm^{-1} can be assigned to the in plane and out of plane bending vibrations of aromatic ring system respectively.

Electronic spectral analysis

The distinct electronic transitions in the molecule was appeared at 29412 cm^{-1} , 34013 cm^{-1} and 39370 cm^{-1} , which are assigned to $n \rightarrow \pi^*$ (R-band), $\pi \rightarrow \pi^*$ (benzenoid band) and $\pi \rightarrow \pi^*$ (K band) transitions respectively.

Based on the spectral and elemental analysis the structure of the Schiff base 2APSC was confirmed and the proposed structure is given in the Figure 1.19

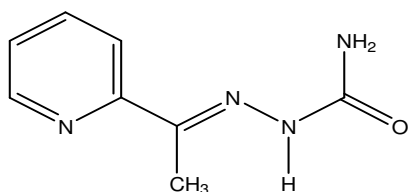


Figure 1.19: Structure of 2APSC

SECTION 2

CORROSION BEHAVIOUR OF MILD STEEL IN THE PRESENCE OF SCHIFF BASES DERIVED FROM 2-ACETILPYRIDINE IN 1M HCl

The corrosion inhibition behaviour of the prepared Schiff bases, 2-acetylpyridine phenylhydrazone (2APPH) and 2-acetylpyridine semicarbazone (2APSC) on mild steel were studied in 1M HCl by preparing the inhibitor solution of the concentrations ranging from 0.2mM-1mM

Gravimetric analysis

Weight loss analysis of mild steel were performed by immersing metal coupons of 1 cm² area in 1M HCl solution for 4 consecutive days with and without Schiff bases at different concentrations and analysing them daily in order to study the effect of Schiff bases on corrosion inhibition. The corrosion rate of the immersed mild steel was calculated in mmy⁻¹ and percentage of inhibition efficiencies of the prepared Schiff bases 2APPH and 2APSC are recorded in the Tables 1.3 and 1.4 and compared with the plots of corrosion rates and inhibition efficiency vs concentration in the Figures 1.20 and 1.21 respectively.

From the analytical studies conducted, it is evident that there is significant decrease in the corrosion rate with the introduction of inhibiting Schiff bases of different concentrations in the corroding 1M HCl solution for the mild steel examined. Thus the prepared Schiff bases under study have the capacity to efficiently inhibit the metallic disintegration of mild steel in the acidic medium even at very low concentration and the efficiency of inhibition increases with Schiff base concentration. The inhibiting Schiff bases 2APPH and 2APSC exhibited more than

80% inhibition efficiency at all examined concentrations as evident from the experimental results. However, inhibitor 2APPH performed marginally higher efficiency at all concentrations and a maximum inhibition efficiency of 95.64% was achieved at 1mM concentration

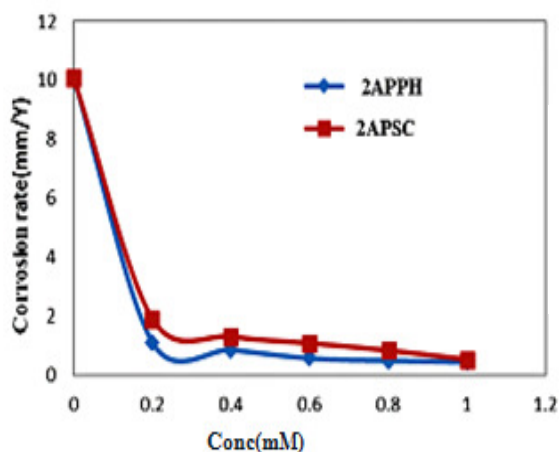


Figure 1.20: Change of corrosion rates of MS with different concentrations of Schiff bases 2APPH and 2APSC in 1M HCl for 24 hours.

Table 1.3: Corrosion rates of MS in the presence and absence of 2APPH and 2APSC in 1M HCl for 4 days

Schiff Base	Conc (mM)	Corrosion rate(mmy ⁻¹)			
		24 hr	48 hr	72 hr	96 hr
2APPH	0	10.080	7.1845	6.2124	5.7850
	0.2	1.1098	1.2742	1.4866	1.7161
	0.4	0.8634	1.1306	1.3910	1.5315
	0.6	0.5727	0.8399	1.0881	1.4030
	0.8	0.4949	0.7226	0.9965	1.2301
	1	0.4390	0.7062	0.9543	1.1088
2APSC	0.2	1.9029	1.8930	2.1408	2.3737
	0.4	1.3119	1.5553	1.8013	1.9150
	0.6	1.0853	1.5073	1.6445	1.7535
	0.8	0.8422	1.1556	1.5058	1.6551
	1	0.5322	1.0236	1.3171	1.5866

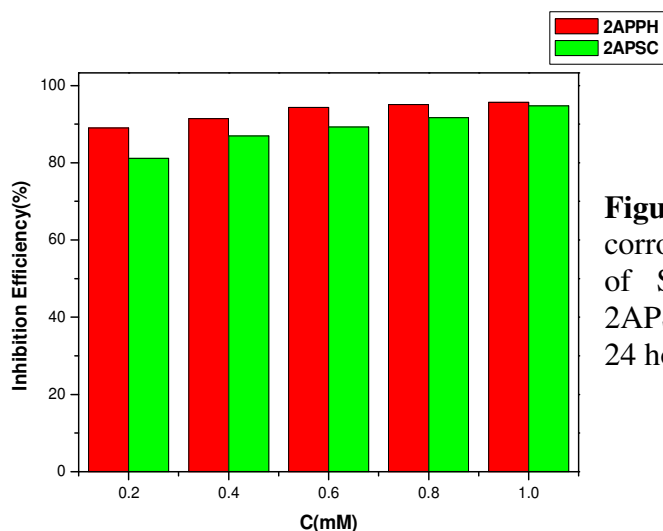


Figure 1.21: Comparison of corrosion inhibition efficiencies of Schiff bases 2APPH and 2APSC on MS in 1M HCl for 24 hours

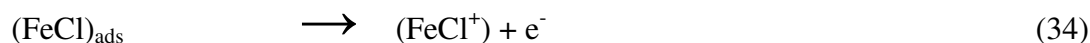
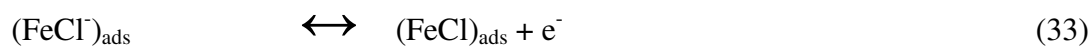
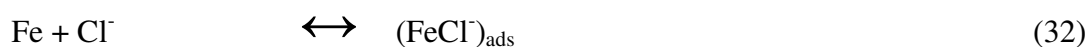
Table 1.4: Inhibition efficiency of MS in the presence and absence of 2APPH and 2APSC in 1M HCl for 4 days

Schiff Base	Conc (mM)	Inhibition efficiency (%)			
		24 hr	48 hr	72 hr	96 hr
2APPH	0.2	88.99	82.26	76.07	70.33
	0.4	91.43	84.26	77.60	73.52
	0.6	94.31	88.30	82.48	75.74
	0.8	95.09	89.94	83.95	78.73
	1	95.64	90.16	84.63	80.83
2APSC	0.2	81.12	73.65	65.53	58.96
	0.4	86.98	78.35	71.00	66.89
	0.6	89.23	79.01	73.52	69.68
	0.8	91.64	83.91	75.56	71.38
	1	94.71	85.75	78.79	72.57

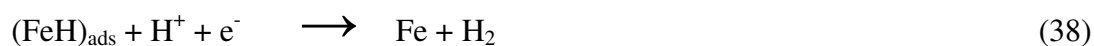
Metal surface tend to have positively charged nature in acidic media. The adsorption of negatively charged Cl^- ion in the corrosion media used here will lead to the distribution of more and more negative charge and facilitate the adsorption of the protonated Schiff bases on the same and thereby preventing further Fe to Fe^{2+} oxidation. Inhibition efficiency of the compounds under study can be attributed to

various factors as mentioned earlier. In this case the binding of the compound on the metallic surface can be associated with the presence of the heteroatom containing lone pair electrons, pi- electron cloud containing aromatic rings, azomethine moiety etc. It can be also ascribed to the molecular geometry of the two Schiff bases prepared 2APPH and 2APSC as their derived molecular structures by minimum energy calculation indicated that 2APPH acquired a perfect planar geometry and the presence of two aromatic ring systems having a high pi-electron cloud facilitates strong binding interaction to the metallic surface under consideration in addition to binding from the azomethine moiety. The aforesaid mechanism of interaction is illustrated in the Figure 1.22.

The following reactions are suggested as mechanism for anodic dissolution of iron in HCl.



The mechanism of hydrogen evolution at cathode can be illustrated as follows:



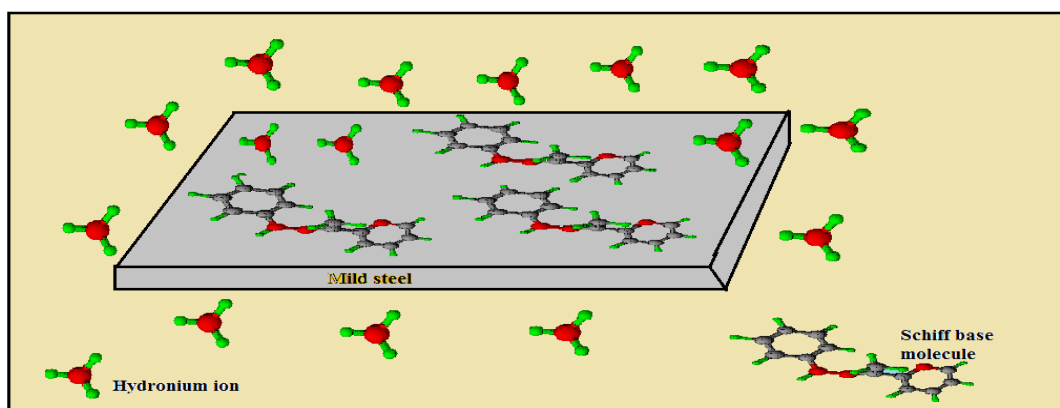


Figure 1.22: Corrosion inhibition mechanism of Schiff base molecules on metallic surface

Variation of corrosion rate and inhibition efficiency with immersion time

Gravimetric analysis of steel specimens was conducted in different concentrations of Schiff base inhibitors for 4 consecutive days to determine the variation of the rate of corrosion and efficiency of inhibition with the variation in immersion time. The results obtained were tabulated and graphically plotted in the Figures 1.23 and 1.24. The analytical observations reveal the remarkable increase in the corrosion efficiency and decrease in the inhibition efficiency with time. It can be explained due to the higher susceptibility of azomethine moiety in the synthesised Schiff bases towards acid hydrolysis.

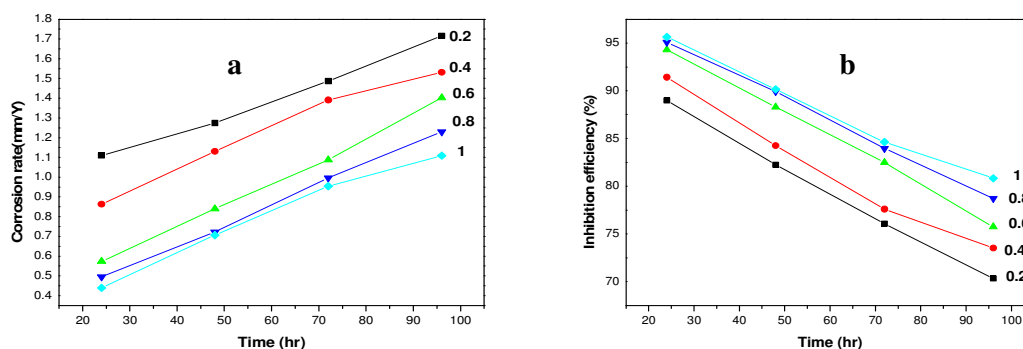


Figure 1.23: Variation of a) rate of corrosion and b) inhibition efficiency on MS with immersion time in the presence and absence of 2APPH in 1M HCl

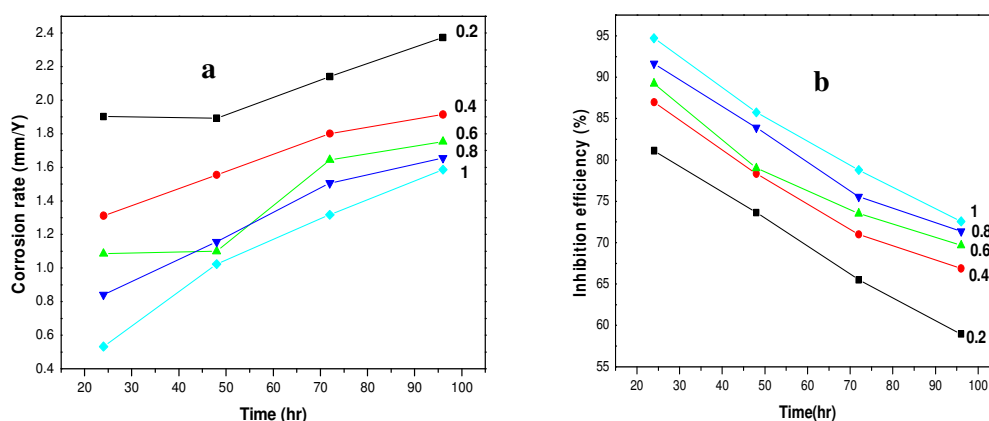


Figure 1.24: Variation of **a)** rate of corrosion and **b)** inhibition efficiency on MS with immersion time in the presence and absence of 2APSC in 1M HCl

Comparison between the inhibition efficiency of Schiff base and its parent compounds

Gravimetric analysis of steel specimens was also conducted in 1mM concentrations of parent compounds in order to find their inhibition efficiency for comparison with the same exhibited by Schiff bases. The results are tabulated and graphically represented in the Table 1.5 and Figure 1.25 respectively, as a comparative analysis of the Schiff bases under study and their parent compounds. From the observations it is evident that both Schiff bases exhibits remarkably high inhibition efficiencies in comparison with those exhibited by their corresponding parent compounds. This substantiates the significant aspect of the azomethine (C=N) moiety exists in the Schiff bases which inhibit the mechanism of corrosion on the metal surface.

The gravimetric analysis using the parent compounds 2-acetylpyridine (2AP), phenylhydrazine hydrochloride (PH), and semicarbazide (SC) shows that 2-acetylpyridine have the properties for corrosion inhibition whereas the parent amines exhibited negative corrosion inhibition efficiency. This indicates that the parent amines act as corrosion accelerators in the experimental media. The corrosion

inhibition efficiency exhibited by 2-acetylpyridine can be explained due to the presence of heteroatom containing aromatic ring.

Table 1.5: Corrosion inhibition efficiencies of parent compounds at 1mM concentration

Parent compound	Inhibition efficiency (%)
2AP	25
PH	-34
SC	-20

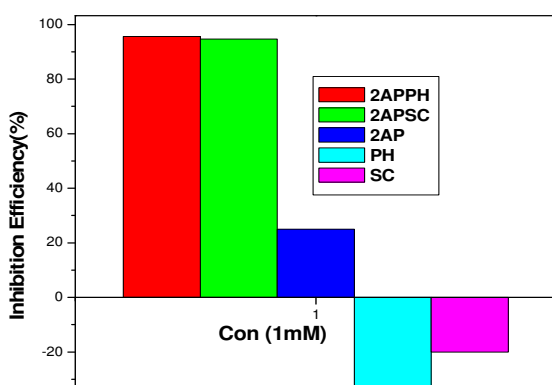


Figure 1.25: Comparison of corrosion inhibition efficiencies of Schiff bases 2APPH and 2APSC and their parent compounds 2AP, PH and SC on MS in 1M HCl

Adsorption studies

The mechanism of inhibition of the Schiff bases under study can be explained by adsorption process and the resultant surface modifications on the metallic surface under consideration. The mechanism of adsorption of organic compounds and their surface modifications can be described by invoking suitable adsorption isotherms in which the commonly used ones are Langmuir, Temkin, Frumkin and Freundlich isotherms. The evaluation of thermodynamic parameters was done by selecting the best fit isotherm model assisted by the correlation coefficient (R^2). Figure 1.26 represents the adsorption isotherms for the compounds 2APPH and 2APSC in 1M HCl. The adsorption behaviour of both 2APPH and 2APSC on MS specimens in 1M HCl was obtained from Langmuir adsorption

isotherm and it can be expressed as

$$\frac{C}{\theta} = \frac{1}{K_{ads}} + C$$

where C is the concentration of inhibitor, θ is the fractional surface coverage and K_{ads} is the value of adsorption equilibrium constant.

This adsorption equilibrium constant, K_{ads} mainly depends on the standard free energy of adsorption ΔG_{ads}^0 , by the relation

$$\Delta G_{ads}^0 = -RT \ln (55.5 K_{ads})$$

where 55.5 is the molar concentration of water, R is the ideal gas constant and T is the temperature in Kelvin. Adsorption parameter values derived are listed in the Table 1.6

Table 1.6: Adsorption parameters of Schiff bases for the adsorption on MS surface in 1M HCl

Adsorption parameter	2APPH	2APSC
K_{ads}	33333.3	20000
ΔG_{ads}^0 (kJ/mol)	-36.13	-34.85

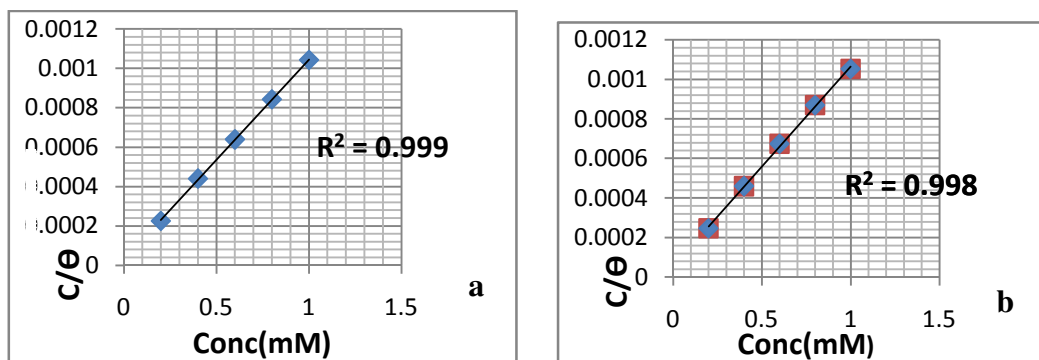


Figure 1.26: Langmuir adsorption isotherms for a) 2APPH and b) 2APSC on MS in 1M HCl

The adsorption equilibrium constant K_{ads} represents the measurement of the adsorption taking place on the corresponding surface. The above data show that 2APPH has comparatively high K_{ads} value than 2APSC which indicates that the efficacy of adsorption of 2APPH is greater than that of 2APSC. The ΔG_{ads}^0 values up to -20kJ mol^{-1} indicates clearly the electrostatic attraction or physisorption between a charged molecule and metal surface whereas those more negative than

-40kJ mol⁻¹ indicate the strong adsorption of the inhibitors on metallic surface through strong co-ordinate bonds or chemisorptions [115]. In the case of investigated inhibitors ΔG_{ads}^0 value ranges between -34kJmol⁻¹ and -36kJmol⁻¹ for MS specimens implies that the adsorption of all these compounds involves both physisorption and chemisorption.

Temperature studies

The effect of temperature on the corrosion inhibition property of the synthesized Schiff bases were analysed in the range of 30-60°C. The energy of activation for corrosion in the presence and absence of inhibitor was evaluated by the following Arrhenius equation.

$$K = A \exp \left(\frac{-E_a}{RT} \right)$$

where K is the corrosion rate, E_a is the activation energy, A is the frequency factor, T is the temperature and R is the gas constant. Arrhenius plots were acquired by plotting log K versus 1000/T for the Schiff bases and are given in the Figures 1.27 and 1.28. The value of regression coefficients of obtained straight lines which are very near to unity reveals that the corrosion process on MS in HCl medium can be attributed by simple kinetic model.

Enthalpy and entropy of activation (ΔH^* , ΔS^*) were evaluated by the transition state theory, which is represented by the equation,

$$K = \left(\frac{RT}{Nh} \right) \exp \left(\frac{\Delta S^*}{R} \right) \exp \left(\frac{-\Delta H^*}{RT} \right)$$

where N is the Avogadro number and h is the Planck's constant. When plot log(K/T) Vs 1/T, straight lines are obtained for the corrosion of MS in 1M HCl with and without of Schiff bases (Figures 1.27 and 1.28)

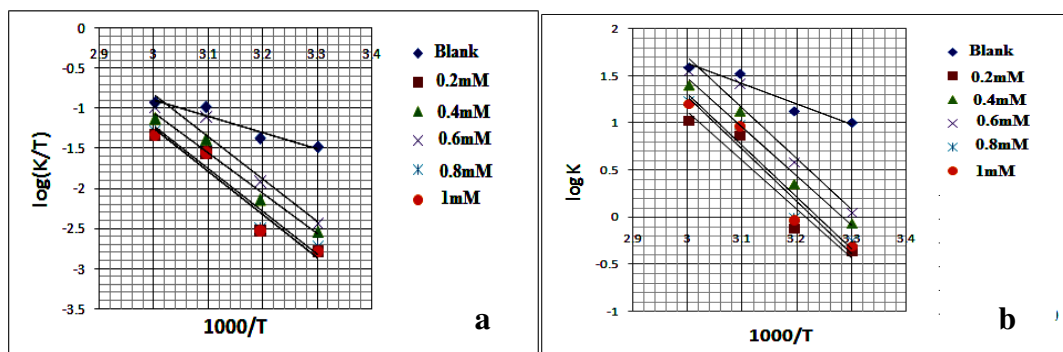


Figure 1.27: a) Arrhenius plots and b) $\log(K/T)$ Vs $1000/T$ plots for the corrosion of MS in the presence and absence of 2APPH in 1M HCl.

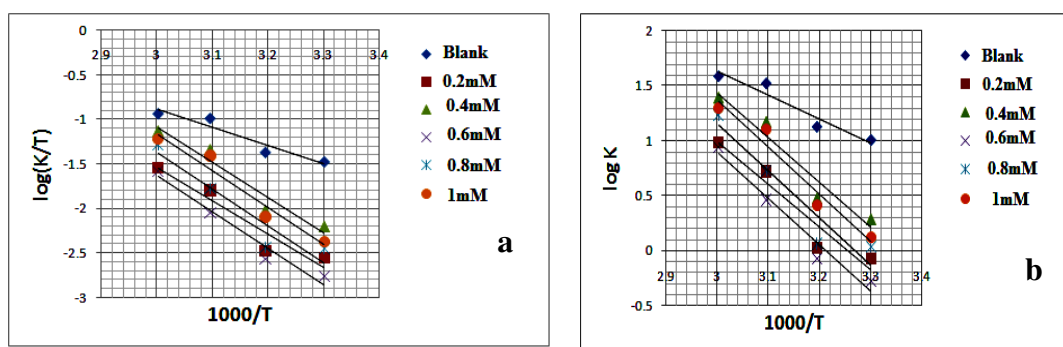


Figure 1.28: a) Arrhenius plots and b) $\log(K/T)$ Vs $1000/T$ plots for the corrosion of MS in the presence and absence of 2APSC in 1M HCl.

The values of activation energy and thermodynamic parameters in the absence and presence of Schiff base compounds are tabulated in the Table 1.7. The derived data is a clear implication of the increase in the activation energy for metal disintegration with increase in the inhibitor concentration which in turn points to the resistant nature of the metallic surface against corrosion. The resultant positive enthalpy values point towards the fact that the corrosion process is endothermic in nature and higher inhibitor concentration makes the metallic disintegration at the surface obviously sluggish. Both the activation energy and enthalpy of corrosion increased continuously with inhibitor concentration for both Schiff bases 2APPH and 2APSC.

Table 1.7: Thermodynamic parameters of corrosion of MS in the presence and absence of inhibitors 2APPH and 2APSC in 1M HCl

Schiff bases	Conc (mM)	E _a (kJ mol ⁻¹)	A	ΔH* (kJ mol ⁻¹)	ΔS* (J mol ⁻¹ K ⁻¹)
2APPH	0	41.70	1.48 x 10 ⁸	39.1	-90.42
	0.2	98.60	3.63x10 ¹⁶	96	70.33794
	0.4	99.54	1.17 x 10 ¹⁷	96.9	79.91151
	0.6	103.14	7.08 x 10 ¹⁷	101	95.03775
	0.8	104.33	4.47 x 10 ¹⁷	102	91.01685
	1	106.03	7.76 x 10 ¹⁷	103	95.61217
2APSC	0.2	74.21	4.07 x 10 ¹²	71.6	5.33156
	0.4	77.90	4.37 x 10 ¹³	75.3	14.23682
	0.6	80.30	2.95 x 10 ¹³	77.7	10.98181
	0.8	81.75	9.12 x 10 ¹³	79.1	20.36391
	1	81.79	1.51 x 10 ¹⁴	79.2	24.57628

When we compare the values of E_a and ΔH* it is evident that these values are high in the presence of 2APPH at higher concentration of 1mM. This can be considered as a strong evidence for the argument that the adsorption efficiency on the metallic surface for 2APPH molecules is higher than that of 2APSC. From the Table 1.7, it was observed that the values of ΔS* increased with inhibitor concentration whereas for blank and low inhibitor concentrations entropy of activation was comparatively small, which suggests a decrease in disorder in the rate determining step. When the reactants transform to the activated complex state, a further increase in inhibitor concentration was noted and was reflected in corresponding higher values for ΔS*.

Electrochemical corrosion investigations

Electrochemical investigations were carried out using a three electrode system, which consists of saturated calomel electrode (SCE) as reference electrode, platinum electrode of 1cm² area as counter electrode and mild steel specimen with

an area of 1cm^2 as working electrode. Electrochemical investigations including AC impedance analysis and potentiodynamic polarization studies were performed by Ivium Compactstat-e electrochemical system.

EIS analysis

The corrosion behaviour of MS in 1M HCl with and without of inhibitor was examined using impedance spectroscopic analysis at 30°C . Figures 1.29 and 1.30 represent the Nyquist plots and Bode plots of two Schiff bases 2APPH and 2APSC respectively. The impedance parameters including double layer capacitance (C_{dl}), solution resistance (R_s) and percentage of inhibition efficiency ($\eta_{\text{EIS}}\%$) were evaluated from the values of charge transfer resistance (R_{ct}) and tabulated in the Table 1.8. The percentage of inhibition efficiency was evaluated from R_{ct} values using the following equation.

$$\eta_{\text{EIS}} \% = \frac{R_{ct} - R'_{ct}}{R_{ct}} \times 100$$

where R_{ct} and R'_{ct} are the working electrode charge transfer resistances in the presence and absence of inhibitor respectively.

At both higher and lower frequencies, the capacitance loop intercepts the real axis. These intercepts at the high frequency end represent the solution resistance (R_s) and at the other lower frequency end represent the sum of R_s and R_{ct} . The difference between these intercepts can be calculated to find out R_{ct} which is a measure of the electron transfer that takes place on the exposed metallic surface area under analysis and is inversely proportional to the corrosion rate of the surface.

The study of impedance behaviour was carried out by electric models which helped to evaluate numerical measurements for the chemical and physical properties of the corresponding electrochemical system under investigation. The equivalent circuit that exactly fit to the EIS curves generally consists of

a solution resistance R_s , double layer capacitance C_{dl} and charge transfer resistance R_{ct} (Figure 1.31).

Table 1.8: Electrochemical impedance data of MS corrosion in the presence and absence of Schiff bases 2APPH and 2APSC in 1M HCl

Schiff base	Conc (mM)	R_{ct} (Ωcm^2)	C_{dl}	η_{EIS} %
2APPH	0	59.7	98.9	
	0.2	342	94.1	82.54
	0.4	359	77.9	83.30
	0.6	395	77.6	84.88
	0.8	445	66.9	86.58
	1	826	54.5	92.70
2APSC	0.2	231	102	74
	0.4	267	85.2	77.64
	0.6	317	84.7	81.16
	0.8	413	82.4	85.54
	1	470	81.6	87.29

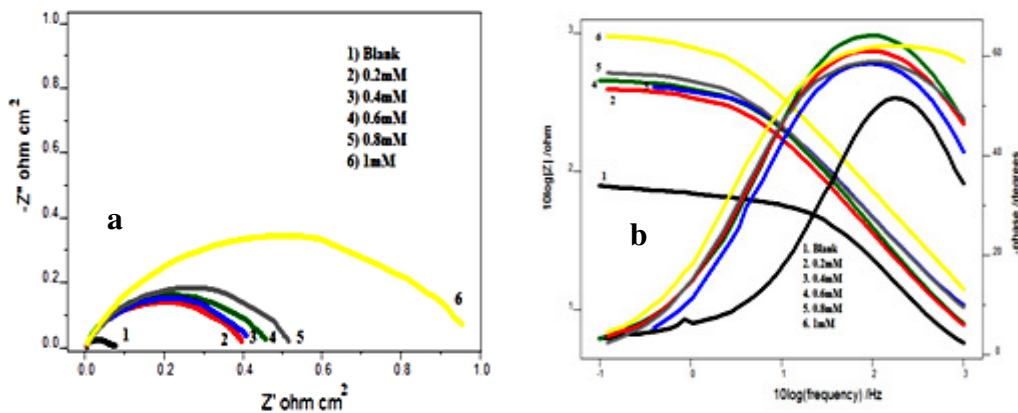


Figure 1.29: a) Nyquist plots and b) Bode plots of MS corrosion in the presence and absence of 2APPH in 1M HCl.

Generally, all the Nyquist plots were observed in semicircles and showed some irregularities which can be ascribed to the non-homogeneous nature or roughness of the metal surface. From the Table 1.8, it was observed that along with the increasing concentration of the inhibitor, C_{dl} values were decreased and R_{ct} values were increased in the case of both inhibitors. The variation in R_{ct} values

can be explained by the adsorption process by which the inhibition mechanism takes place.

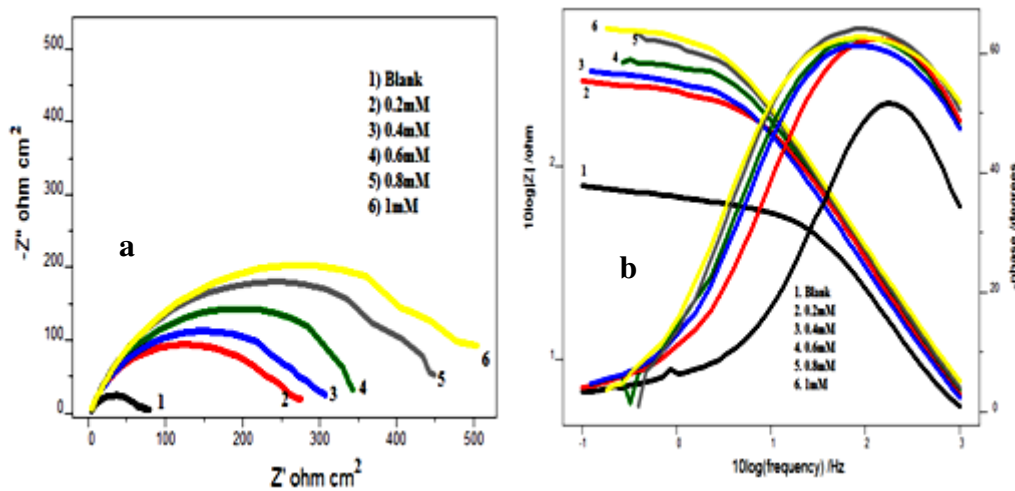


Figure 1.30: a) Nyquist plots and b) Bode plots of MS corrosion in the presence and absence of 2APSC in 1M HCl

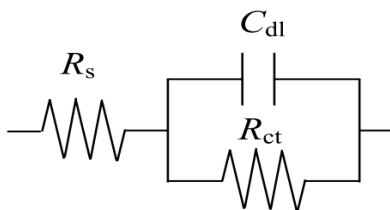


Figure 1.31: Equivalent circuit fitted for EIS measurements

As the inhibitor concentration increases there would be a considerable increase in the amount of adsorption process which is the result of the prevention of the charge transfer of the metal atoms on the metallic surface and solution by adsorbed molecules. The lowering of C_{dl} values with increase in the inhibitor concentration can be associated with the reduction of local dielectric constant values and rise in the thickness of electrical double layer [116,117]. These observations testify the inhibitor action at the solution–metal interface.

From the data it is obvious that both Schiff bases 2APPH and 2APSC acted as potential corrosion inhibitors in hydrochloric acid media. Both of them exhibited above 70% efficiency of corrosion inhibition and a maximum efficiency of 92.7% was obtained for 2APPH at concentration of 1mM. The efficiency of inhibition of

the two Schiff bases derived from 2-acetylpyridine obeys the order 2APPH > 2APSC which is in good correlation with the data received from weight loss studies.

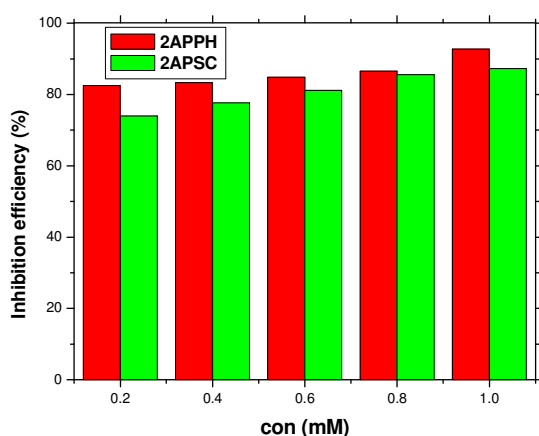


Figure 1.32: Comparison of corrosion inhibition efficiencies ($\eta_{EIS}\%$) of Schiff bases 2APPH and 2APSC on MS corrosion in 1M HCl

Potentiodynamic polarization analysis

Tafel extrapolation analysis and linear polarization studies were conducted to establish the impact of Schiff base compounds towards the polarization of metal specimens by the determination of polarization resistance, corrosion current density and the percentage of inhibition efficiencies. The percentage of inhibition efficiency was calculated from the values of polarization resistance using the equation

$$\eta_{Rp} \% = \frac{R'_p - R_p}{R'_p} \times 100$$

where, R'_p and R_p are the polarization resistances with and without inhibitor respectively. From corrosion current densities, inhibition efficiency was calculated using,

$$\eta_{pol} \% = \frac{i_{corr} - i'_{corr}}{i_{corr}} \times 100$$

where, i_{corr} and i'_{corr} are corrosion current densities in the absence and presence of inhibitor respectively.

Tafel polarization curves and linear polarization curves obtained for the different Schiff bases concentrations are represented in the Figures 1.33 and 1.34

and their corrosion parameters -corrosion potential (E_{corr}), corrosion current density (i_{corr}), polarization resistance (R_p) and inhibition efficiency percentage ($\eta_{\text{pol}} \%$) are listed in the Table 1.9.

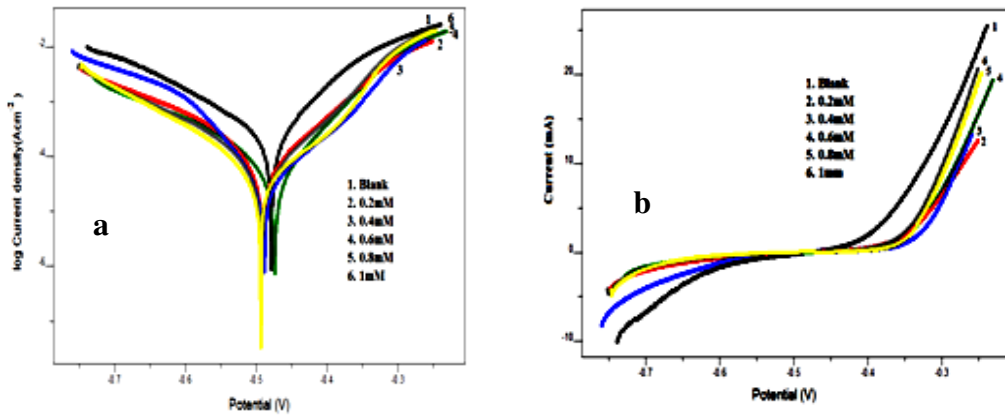


Figure 1.33: a) Tafel plots and b) linear polarization curves for MS corrosion in the presence and absence of 2APPH in 1M HCl

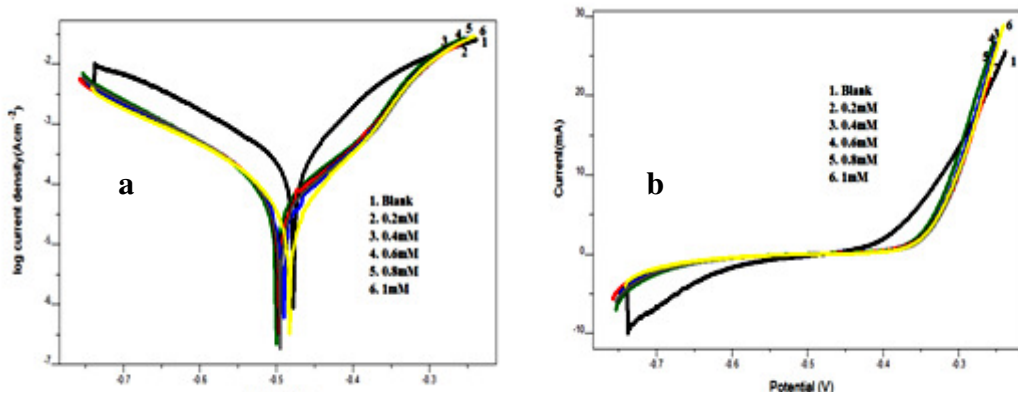


Figure 1.34: a) Tafel plots and b) linear polarization curves for MS corrosion in the presence and absence of 2APSC in 1M HCl.

Tafel data analysis pointed out that the values obtained for corrosion current density (i_{corr}) were significantly decreased and high inhibition efficiencies were obtained in presence of both inhibitors in 1M HCl even at low concentrations. A closer examination clarified that the Schiff base 2APPH displayed more efficiency on MS surface as compared to 2APSC and a maximum inhibition efficiency of 85% achieved by 2APPH at 1mM concentration.

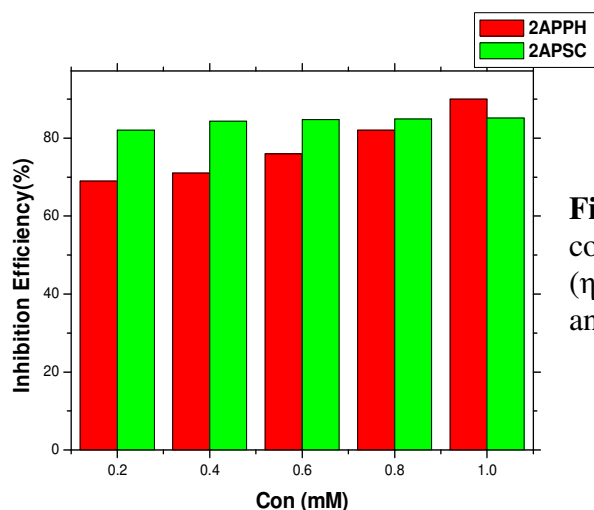


Figure 1.35: Comparison of corrosion inhibition efficiencies ($\eta_{pol}\%$) of Schiff bases 2APPH and 2APSC on MS in 1M HCl

Table 1.9: Polarization data for MS corrosion in the presence and absence of inhibitors 2APPH and 2APSC in 1M HCl

Schiff Bases	Tafel Data					Polarization Data		
	Conc (mM)	E_{corr} (mV/SCE)	I_{corr} ($\mu\text{A}/\text{cm}^2$)	b_a (mV/dec)	$-b_c$ (mV/dec)	η_{pol} %	R_p (ohm)	η_{Rp} %
2APPH	0	-498	360	122	150	-	83.23	-
	0.2	-456	66.6	71	163	81.5	321.6	74.1
	0.4	-451	56.2	64	155	84.3	351.8	76.3
	0.6	-460	55	66	144	84.7	358.4	76.7
	0.8	-453	54.2	67	150	84.9	370.4	77.5
	1	-448	34.4	62	162	90.4	542.8	84.6
2APSC	0.2	-458	110.8	86	188	69.4	232	64.1
	0.4	-425	103.9	75	166	71.1	215.4	61.3
	0.6	-455	87	81	191	75.8	282.8	70.5
	0.8	-460	66.4	72	164	81.5	327.8	74.6
	1	-450	53.2	61	143	85.2	367.7	77.7

In the cases of both Schiff bases 2APPH and 2APSC the E_{corr} value were not altered (>85) with respect to E_{corr} of blank experiment and there was no appreciable change in anodic or cathodic slopes for both the Schiff bases suggesting that in 1M HCl, they are mixed type inhibitors for MS.

Surface morphological analysis

To verify the inhibition mechanism of investigated Schiff base compounds on the MS surface, morphological studies were conducted by taking SEM images of steel surfaces [118, 119]. Figure 1.36 represents the SEM images of bare sample, metal immersed in 1M HCl, and metal immersed in 1M HCl containing 1mM 2APPH. On close examination of figures it was evident that the MS surface was highly corroded in blank HCl solution. Small cracks and pits on the bare metal surface generated by the surface polishing were totally disappeared on the metal surface dipped in acid solution in the absence of Schiff base due to the occurrence of severe corrosion. The comparison of figures established that the surface damaging was appreciably decreased in the presence of 2APPH, which indicates that the corrosion tendency was considerably suppressed due to the formation of a protective film of 2APPH through adsorption.

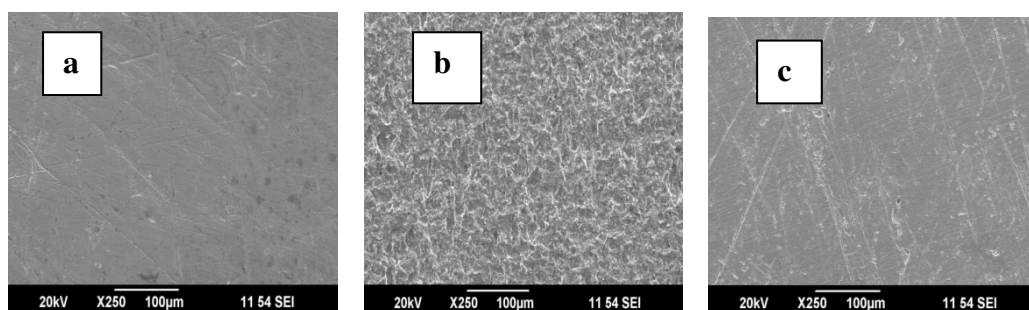


Figure 1.36: SEM images of **a)** bare sample **b)** metal immersed in 1M HCl **c)** metal immersed in 1M HCl containing 1mM 2APPH

Quantum mechanical analysis

The corrosion inhibition efficacy of various compounds can be correlated with the Frontier molecular orbital energies. The HSAB concept (donor-acceptor interaction) between the vacant orbitals of Fe atoms and the filled molecular orbitals of the inhibitor compounds has an important role in the prevention mechanism of metal disintegration. The lowest $E_{LUMO} - E_{HOMO}$ (ΔE) value of inhibitors is the

essential quantum mechanical parameter which helps them to bind on the metal surface strongly. Quantum mechanical evaluations were carried out using DFT method by GMMES software. Calculated quantum mechanical parameters like E_{HOMO} , E_{LUMO} , ΔE , electronegativity (χ), hardness (η) and number of transferred electrons (ΔN) for the investigated inhibitors are tabulated in the Table 1.10 and the HOMO and LUMO of the inhibitors are represented in the Figure 1.37 and 1.38 respectively. The ΔE between HOMO and LUMO is comparably low for 2APPH than 2APSC, which imply that 2APPH has predominant inhibition efficiency. These data indicate that the energy required to move electrons from HOMO of 2APPH to the vacant orbitals of Fe is very low. The ΔN from donor to acceptors are also evaluated from these quantum mechanical parameters which provide the information about interaction with the metal atoms. Optimized geometry of compounds established quantum mechanically is represented in the Figure 1.39. The calculations were conducted using following equations,

$$\chi \approx -1/2 (E_{\text{HOMO}} + E_{\text{LUMO}}) \qquad \eta \approx 1/2 (E_{\text{HOMO}} - E_{\text{LUMO}})$$

$$\Delta N = \frac{\chi_{\text{Fe}} - \chi_{\text{inhib}}}{2(\eta_{\text{Fe}} + \eta_{\text{inhib}})}$$

Table 1.10: Quantum mechanical parameters of inhibitor compounds on MS

Molecule	$E_{\text{HOMO}}(\text{eV})$	$E_{\text{LUMO}}(\text{eV})$	ΔE (eV)	χ	η	ΔN
2APPH	-3.2653	1.0612	4.3265	1.1020	2.1632	1.36
2APSC	-3.5919	1.1156	4.7075	102381	2.3537	1.22

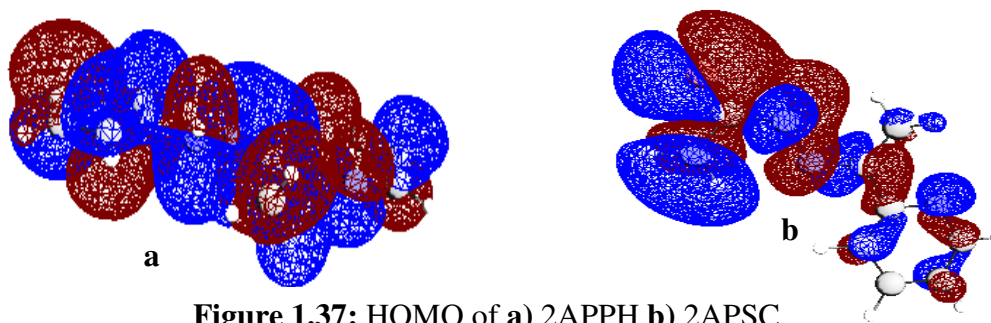


Figure 1.37: HOMO of a) 2APPH b) 2APSC

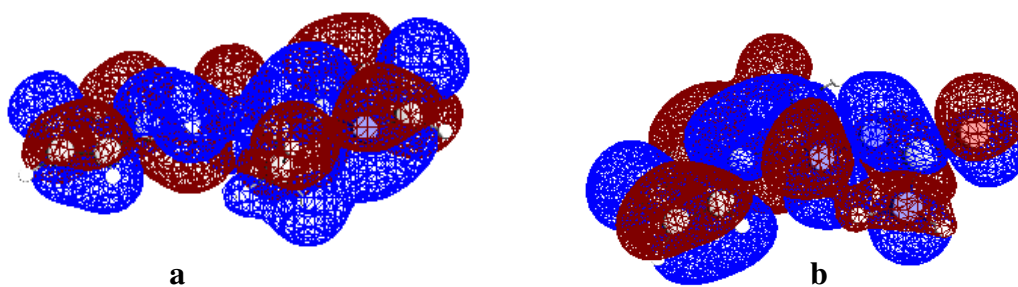


Figure 1.38: LUMO of a) 2APPH b) 2APSC

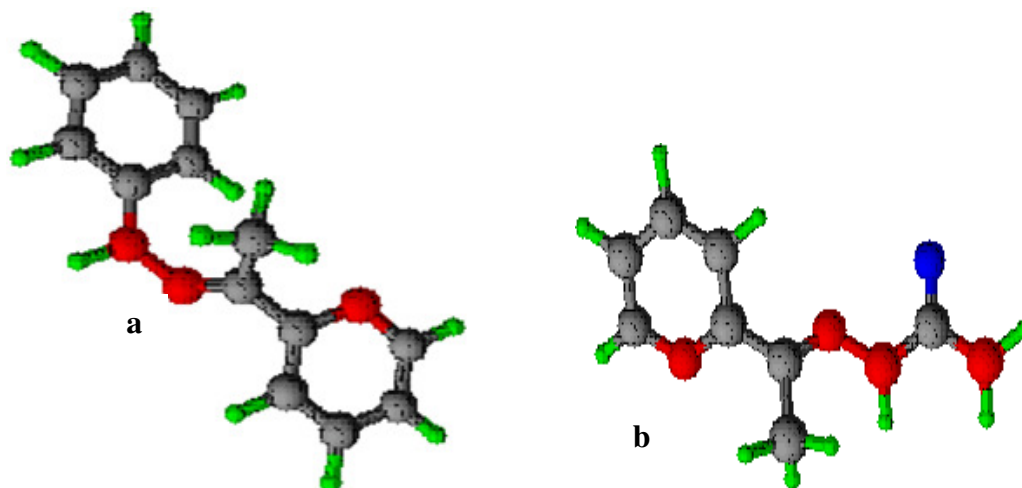


Figure 1.39: Optimized geometry of a) 2APPH b) 2APSC

SECTION 3

CORROSION BEHAVIOUR OF MILD STEEL IN THE PRESENCE OF SCHIFF BASES DERIVED FROM 2-ACETILPYRIDINE IN 0.5M H₂SO₄

The characteristics of corrosion inhibition by two Schiff bases, 2-acetylpyridine phenylhydrazone (2APPH) and 2-acetylpyridine semicarbazone (2APSC) were studied in 0.5M H₂SO₄ using the inhibitor solution of the concentration range 0.2mM-1mM.

Gravimetric analysis

Weight loss analysis of MS coupons were performed by immersing metal coupons of 1cm² area in 0.5M H₂SO₄ solution for 24 hours in the presence and absence of the prepared Schiff bases and analysing them for the study of effectiveness of Schiff bases on corrosion inhibition. The corrosion rate of the immersed MS is calculated in mmy⁻¹. Efficiency of inhibition of the prepared inhibitor molecules 2APPH and 2APSC are recorded in the Table 1.11 and compared with the plot of inhibition efficiency vs concentration in the Figure 1.40.

These experimental analysis and data clearly indicate that the corrosion rate of MS specimen in sulphuric acid medium in the presence of the synthesised Schiff base inhibitors decreases significantly. In contrary to the expected results based on the previous experiment with HCl, 2APSC exhibited more corrosion inhibition efficiency in H₂SO₄ whereas 2APPH showed higher corrosion efficiency in HCl.

Table 1.11: Corrosion rates and inhibition efficiency of MS in the presence and absence of 2APPH and 2APSC in 0.5M H₂SO₄ at 24hrs

Conc (mM)	2APPH		2APSC	
	Corrosion rate (mmy ⁻¹)	Inhibition Efficiency (%)	Corrosion rate (mmy ⁻¹)	Inhibition efficiency (%)
0	16.26	-	16.26	-
0.2	10.19	37.32	8.14	49.89
0.4	8.19	49.59	6.11	62.41
0.6	6.79	58.18	4.67	71.24
0.8	5.54	65.91	3.58	77.93
1	5.02	69.12	3.50	78.42

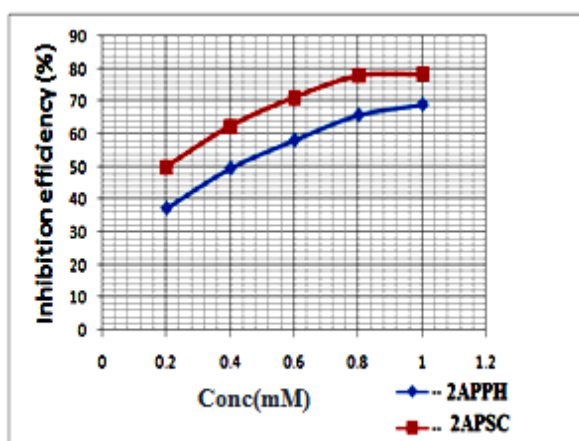


Figure 1.40: Comparison of corrosion inhibition efficiency of MS with different concentration of Schiff bases 2APPH and 2APSC in 0.5M H₂SO₄ for 24 hours

According to the data, 2APSC exhibited higher inhibition efficiency, compared to that of 2APPH and achieved a maximum efficiency of 78% at 1mM concentration. The inhibition of corrosion on MS surface by Schiff bases in H₂SO₄ medium is comparatively low than in HCl medium, which can be explained by the mechanism that at initial stages, the inhibitor molecules get strongly adsorbed on the metallic surface which are surrounded by a number of hydronium ions due to their polar nature. It is leading to the hydrolysis of the molecules which ultimately results in their desorption from the metal surface. Generally, the interaction of hydronium ions with metal atoms is facilitated only by the replacement of adsorbed water molecules from the metal surface. However, here, the inhibitor molecules facilitate

higher possibility for the hydronium ions to reach the metal surface which leads to the reduction of the corrosion inhibition efficiency of these bases in H₂SO₄ medium.

Adsorption studies

Corrosion inhibition mechanism of Schiff bases on metallic surface is mainly explained by the adsorption process. The mechanism of adsorption and surface modifications by the organic compounds can be easily described by invoking suitable adsorption isotherms from which a best fit isotherm model is selected with the assistance of correlation coefficient (R^2) and the thermodynamic parameters evaluated.

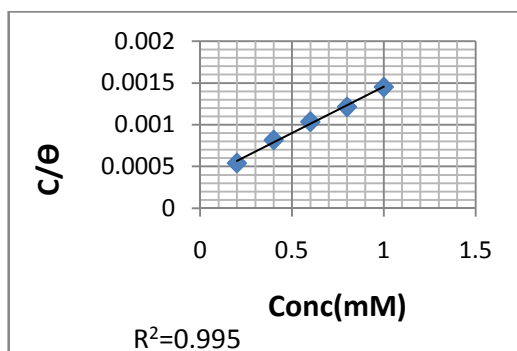


Figure 1.41: Langmuir adsorption isotherm for 2APPH on MS in 0.5M H₂SO₄

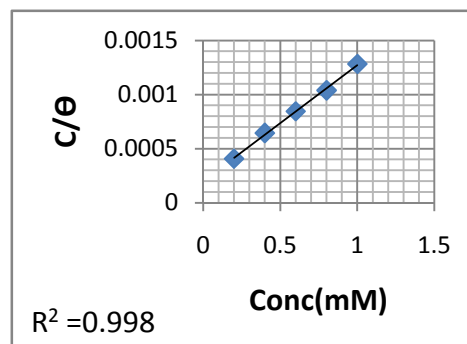


Figure 1.42: Langmuir adsorption isotherm for 2APSC on MS in 0.5M H₂SO₄

Figures 1.41 and 1.42 represent the adsorption isotherms for 2APPH and 2APSC in 0.5M H₂SO₄ respectively. From attempts on various isotherms, the adsorption behaviour of 2APPH and 2APSC can be described by Langmuir isotherm with regression coefficient values 0.995 and 0.998 respectively.

Table 1.12: Adsorption parameters of Schiff bases for the adsorption on MS surface in 0.5M H₂SO₄

Adsorption Parameter	2APPH	2APSC
K_{ads}	10000	20000
ΔG_{ads}^0 (kJ/mol)	-33.12	-34.85

The adsorption equilibrium constant K_{ads} , which is a measure of adsorption for 2APSC, is comparatively higher than 2APPH, suggesting the more efficient adsorption of 2APSC on the metallic surface. Both compounds have ΔG_{ads}^0 value between -34 and -33 kJmol^{-1} which indicate the involvement of both physisorption and chemisorption and the negative sign explains the spontaneity of the process.

Electrochemical corrosion investigations

Electrochemical investigations were carried out using a three electrode system, which consists of saturated calomel electrode (SCE) as reference electrode, platinum electrode as counter electrode and MS specimen with 1cm^2 area as working electrode. Electrochemical investigations including AC impedance analysis and potentiodynamic polarization studies were performed by Ivium Compactstat-e electrochemical system.

EIS analysis

The corrosion behaviour of MS in 0.5M H_2SO_4 in the presence and absence of inhibitor was examined using impedance spectroscopic analysis at 30°C . Figures 1.43 and 1.44 represent the Nyquist plots and Bode plots of two Schiff bases 2APPH and 2APSC respectively. The impedance parameters such as solution resistance (R_s), capacitance of double layer (C_{dl}) and percentage of inhibition efficiency ($\eta_{\text{EIS}}\%$) were evaluated from the charge transfer resistance (R_{ct}) values and are noted in the Table 1.13. The percentage of inhibition efficiency was evaluated from R_{ct} values from equation.

$$\eta_{\text{EIS}} \% = \frac{R_{\text{ct}} - R'_{\text{ct}}}{R_{\text{ct}}} \times 100$$

where R_{ct} and R'_{ct} are the working electrode charge transfer resistances in the presence and absence of Schiff bases respectively.

Table 1.13: Electrochemical impedance data of MS corrosion in the presence and absence of Schiff bases 2APPH and 2APSC in 0.5M H₂SO₄

Schiff base	Conc (mM)	R _{ct} (Ωcm ²)	C _{dl}	η _{EIS} %
	0	13.3	67.1	
2APPH	0.2	56.1	70.8	76.29
	0.4	57.8	76.2	76.98
	0.6	65	81.2	79.53
	0.8	65.1	79.3	79.56
	1	98.9	63	86.5
2APSC	0.2	20.1	48.8	33.83
	0.4	25.5	52.9	47.84
	0.6	28	50.8	52.50
	0.8	43.1	51.2	69.14
	1	84.9	43.3	84.33

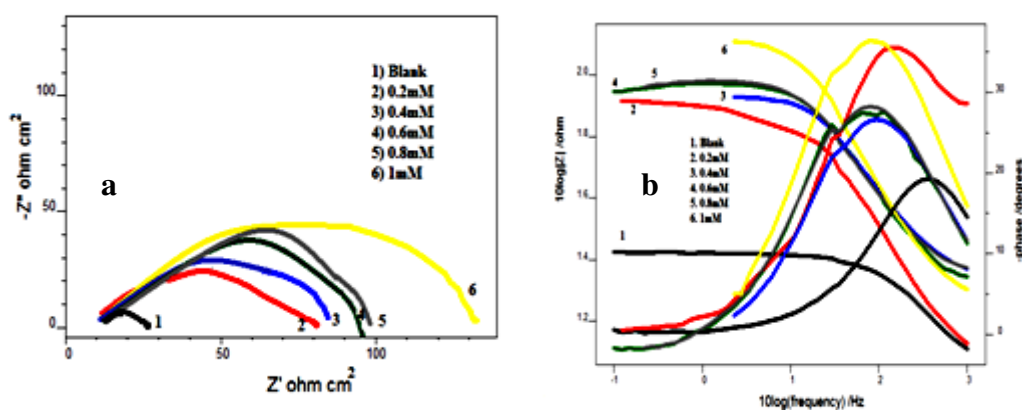


Figure 1.43: a) Nyquist plots and b) Bode plots of MS corrosion in the presence and absence of 2APPH in 0.5M H₂SO₄

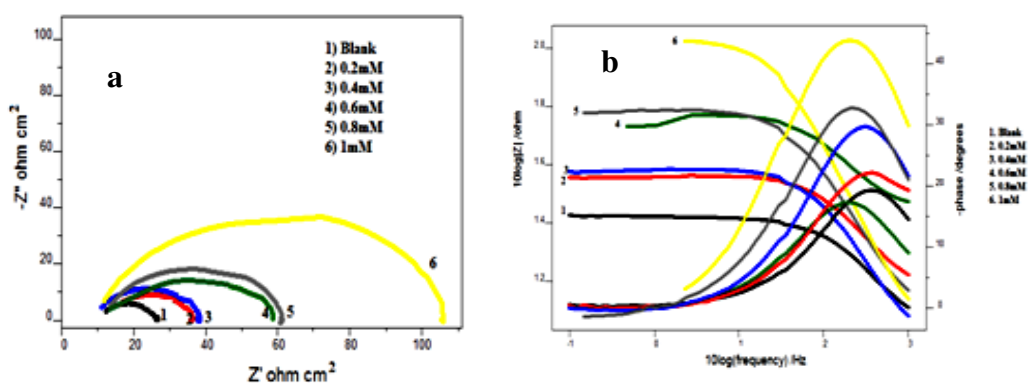


Figure 1.44: a) Nyquist plot and b) Bode plot of MS corrosion in the presence and absence of 2APSC in 0.5M H₂SO₄

From the experimental and analytical data it was observed that:

- a) Among the Schiff bases studied, 2APPH showed comparatively good efficiency at all concentrations and a maximum efficiency of 86.5% was obtained at 1mM concentration.
- b) 2APSC exhibited a minimum efficiency at lower concentrations but acted as a good inhibitor at higher concentrations achieving 84% efficiency at 1 mM concentration.
- c) Both Schiff bases 2APPH and 2APSC exhibited less inhibition efficiency when compared to those in HCl medium in 30 minutes.

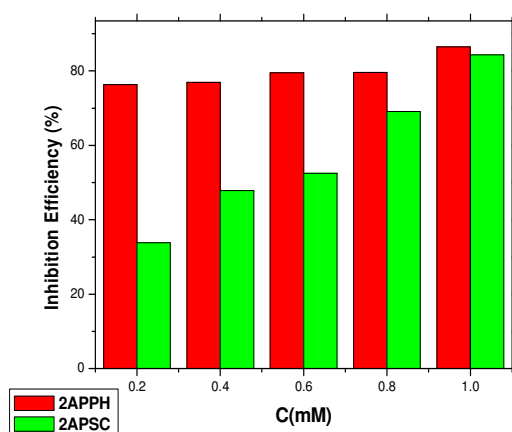


Figure 1.45: Comparison of corrosion inhibition efficiencies ($\eta_{EIS}\%$) of Schiff bases 2APPH and 2APSC on MS corrosion in 0.5M H_2SO_4

Potentiodynamic polarization analysis

Tafel extrapolation analysis and linear polarization studies were conducted to establish the impact of Schiff base compounds towards the polarization of metal specimens by the determination of corrosion current density, polarization resistance and the percentage of inhibition efficiencies. The percentage of inhibition efficiency was obtained from the values of polarization resistance.

$$\eta_{R_p} \% = \frac{R'_p - R_p}{R'_p} \times 100$$

where, R_p' and R_p are the polarization resistances with and without inhibitor respectively. Inhibition efficiency was calculated from corrosion current densities using the equation,

$$\eta_{\text{pol}} \% = \frac{i_{\text{corr}} - i'_{\text{corr}}}{i_{\text{corr}}} \times 100$$

where, i_{corr} and i'_{corr} are corrosion current densities in the absence and presence of inhibitor respectively. Comparison of corrosion inhibition efficiencies of Schiff bases is represented in the Figure 1.46.

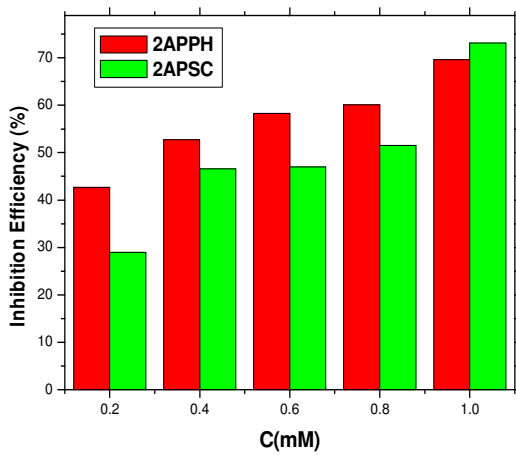


Figure 1.46: Comparison of corrosion inhibition efficiencies ($\eta_{\text{pol}}\%$) in the presence and absence of Schiff bases 2APPH and 2APSC on MS in 0.5M H_2SO_4

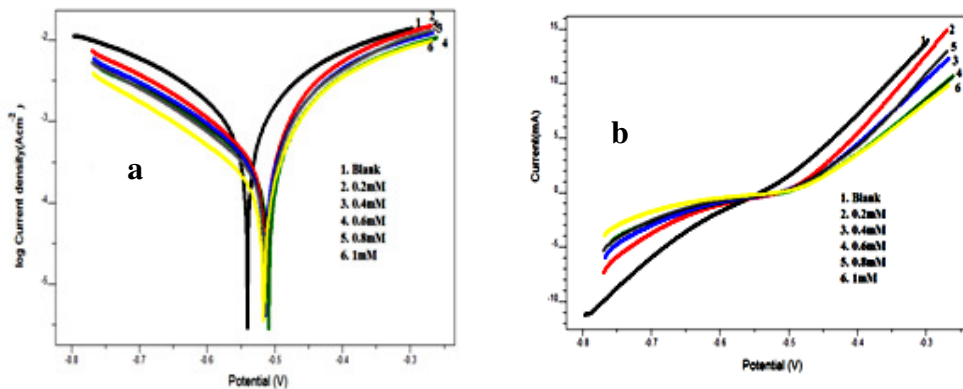


Figure 1.47: a) Tafel plots and b) linear polarization curves for MS corrosion in the presence and absence of 2APPH in 0.5M H_2SO_4

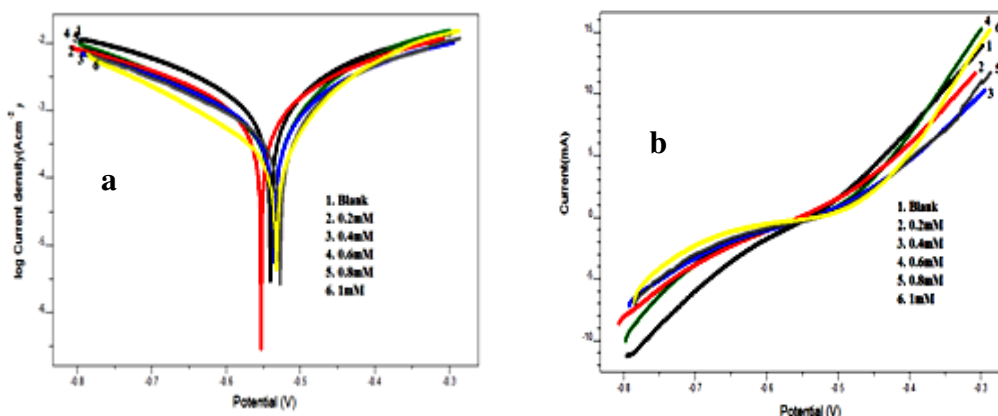


Figure 1.48: a) Tafel plots and b) linear polarization curves for MS corrosion in the presence and absence of 2APSC in 0.5M H₂SO₄

Tafel curves and linear polarization curves obtained for the different Schiff base concentrations are represented in the Figures 1.47 and 1.48 and their corrosion parameters such as corrosion potential (E_{corr}), corrosion current density (i_{corr}), polarization resistance (R_p) and inhibition efficiency percentage ($\eta_{\text{pol}} \%$) are listed in the Table 1.14. The Tafel data analysis revealed moderate inhibition efficiency of both compounds in 0.5M H₂SO₄ at all inhibitor concentrations on the MS surface and a maximum efficiency of 73.1% was achieved by 2APSC at 1mM concentration which is slightly different from the data obtained in EIS measurements. In the cases of both Schiff bases 2APPH and 2APSC, there was no appreciable change in cathodic and anodic slopes which is a clear evidence for the action of these inhibitor molecules on both the cathodic and anodic sites. Furthermore, the E_{corr} value was not altered (>85) with respect to E_{corr} of blank experiment in both cases suggesting that they act as mixed type inhibitors for MS in 0.5M H₂SO₄.

Table 1.14: Polarization data for MS corrosion in the presence and absence of 2APPH and 2APSC in 0.5M H₂SO₄

Schiff Bases	Tafel Data					Polarization Data		
	Conc (mM)	E _{corr} (mV/SCE)	I _{corr} (μA/cm ²)	b _a (mV/dec)	-b _c (mV/dec)	η _{pol} %	R _p (ohm)	η _{Rp} %
2APPH	0	-560	1468	236	232	-	34.62	-
	0.2	-572	841	216	192	42.7	52.45	-34
	0.4	-570.4	694	214	200	52.7	64.67	46.4
	0.6	-568	611	221	202	58.3	72.97	52.5
	0.8	-576.4	586	206	189	60.1	74.98	54
	1	-586.2	445	210	187	69.6	96.85	64.2
2APSC	0.2	-563.3	1040	217	244	29	47.92	27.7
	0.4	-559.5	783	211	225	46.6	52.38	34
	0.6	-566.4	778	181	195	47	60.42	42.7
	0.8	-571	712	215	205	51.5	63.98	46
	1	-532.9	395	156	169	73.1	89.12	67.2

Electrochemical noise analysis

Electrochemical noise (ECN) measurements were done using a three-electrode cell system, which consists of two carbon steel electrodes of area 1cm² used as working electrode and as counter electrode and SCE as reference electrode. All ECN analyses were performed for a period of 1200 seconds using Ivium Compactstat-e electrochemical system controlled by Iviumsoft software. Figure 1.49 represents the noise current of metal specimen dipped in acid solution in the presence and absence of Schiff bases. From the figure it is evident that the noise current in the presence of Schiff bases have very low value than the blank metal specimen, which indicates the corrosion protective power of Schiff bases.

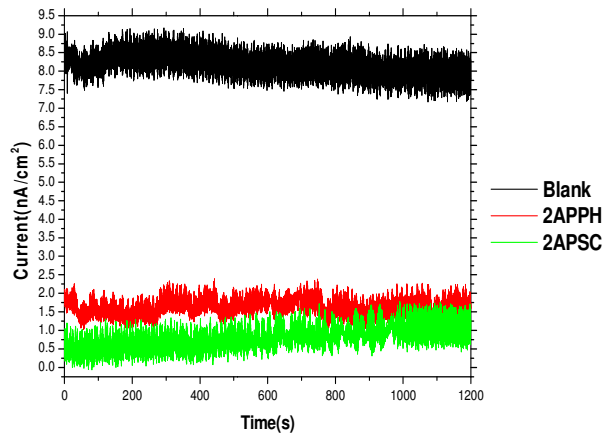


Figure 1.49: Noise current for MS in the presence and absence of 2APPH and 2APSC (1mM) in 0.5M H₂SO₄ solution.

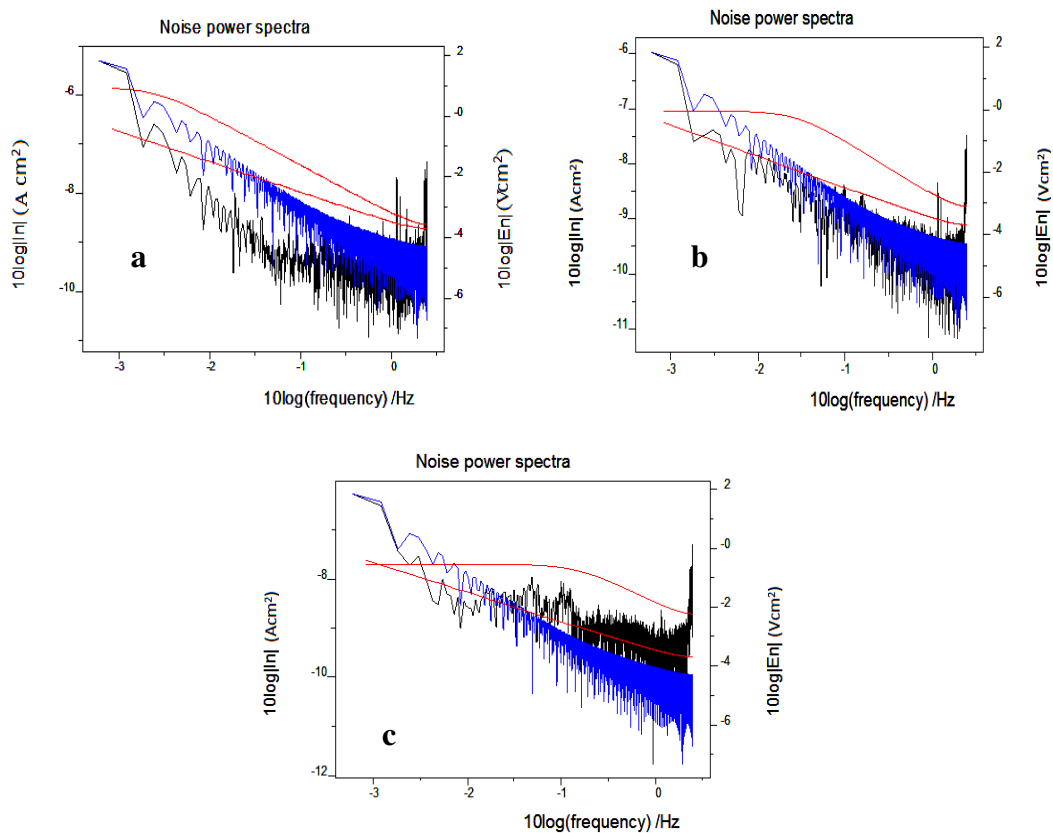


Figure 1.50: PSD curve of MS in 0.5M H₂SO₄ a) blank b) 2APPH (1mM) c) 2APSC (1mM)

The frequency domain analysis of noise measurement gave the PSD (Power Spectral Density) of different systems, which is represented in the Figure 1.50. On close examination of PSD plots, it is understandable that at all frequencies the values of current noise are comparatively large for blank metal specimen than the metal dipped in the acid solution in the presence of 2APPH and 2APSC which is

a clear implication of the occurrence of localized corrosion on MS surface in the absence of Schiff base compounds. The measurement of the resisting power to localised pitting corrosion is indicated as pitting index or Pitting Resistance Equivalent Number (PREN). On analysing the pitting index curves represented in the Figure 1.51, obviously established that the amplitude of pitting index curves corresponding to the blank metal specimen is lower than the metal specimen treated with Schiff base containing solution indicating the higher resistance of Schiff base adsorbed surface towards pitting corrosion.

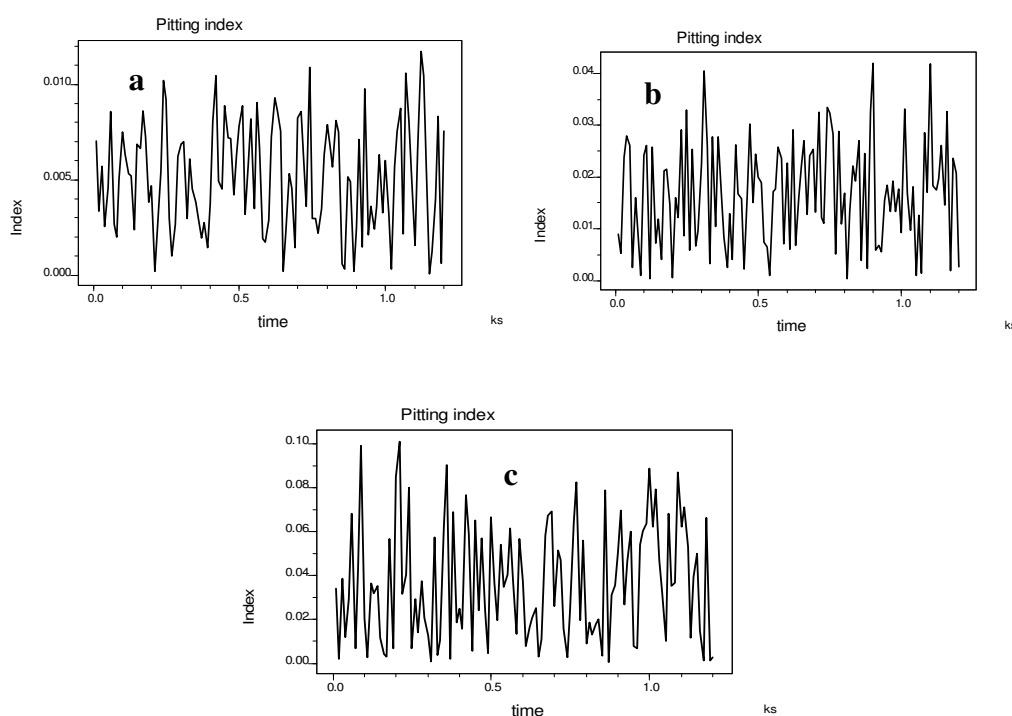


Figure 1.51: Pitting index curves of MS in 0.5M H₂SO₄ a) blank b) 2APPH (1mM) c) 2APSC (1mM)

Surface morphological analysis

To verify the inhibition mechanism of investigated Schiff base compounds on the MS surface, morphological studies were conducted by taking SEM images of steel surfaces. Figure 1.52 represents the SEM images of bare sample, metal immersed in 0.5M H₂SO₄, and metal immersed in 0.5M H₂SO₄ containing

1mM 2APPH. On close examination it was evident that the MS surface was highly corroded in blank H_2SO_4 solution. Small cracks and pits on the bare metal surface generated by the surface polishing were totally disappeared on the metal surface dipped in acid solution in the absence of Schiff base due to the occurrence of corrosion. The comparison of figures established that the surface damaging was appreciably decreased in the presence of 2APPH, which indicates that the corrosion tendency was considerably suppressed due to the formation of a protective film of 2APPH through adsorption.

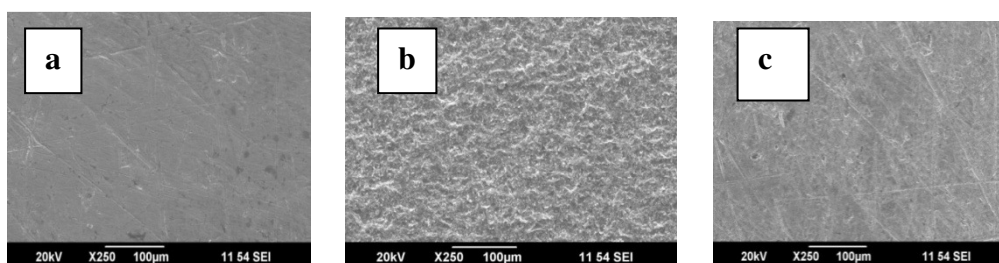


Figure 1.52: SEM images of **a)** bare sample **b)** metal immersed 0.5M H_2SO_4 **c)** metal immersed in 0.5M H_2SO_4 containing 1mM 2APPH

CHAPTER 4

CORROSION INHIBITION STUDIES ON REDUCED SCHIFF BASES DERIVED FROM 3- FORMYLINDOLE, 3-ACETILPYRIDINE AND THIOPHENE-2-CARBALDEHYDE

Scientific reports cite that Schiff base compounds derived from heterocyclic compounds have remarkable applications in various fields. Numerous investigations were carried out on Schiff bases derived from various aldehydes and ketones as reported in the literature. But the applications of reduced form of Schiff bases are not much reported.

This chapter mainly focus on the synthesis, characterization and corrosion inhibition behaviour of reduced form of Schiff bases derived from 3-formylindole, thiophene-2-carbaldehyde and 3-acetylpyridine namely 3-(((1H-indole-3yl) methyl) amino) benzoic acid (or reduced 3-formylindole-3-amino benzoic acid) (R3FI3ABA), 4-(((1H-indole-3yl) methyl) amino) benzoic acid (or reduced 3-formylindole-4-amino benzoic acid) (R3FI4ABA), 3-((thiophen-2-ylmethyl) amino) benzoic acid (or reduced thiophene-2-carbaldehyde-3-amino benzoic acid) (RT2C3ABA) and 2-(1-(pyridine-3-yl) ethyl) hydrazine carbithioamide (or reduced 3-acetylpyridine thio- semicarbazide) (R3APTSC). These compounds were synthesized and characterized by different techniques such as NMR, Mass, UV-visible and IR spectroscopy as well as elemental analysis.

The investigation of their corrosion inhibition behaviour on mild steel in 1M HCl and 0.5M H₂SO₄ were studied by different methods such as weight loss studies, potentiodynamic polarization studies, electrochemical impedance spectroscopic

techniques and electrochemical noise measurements. Insights to the corrosion inhibition mechanism of these inhibitors were provided by adsorption studies and further verification was done by surface morphological studies. The effect of temperature on the rate of corrosion in the presence and absence of these compounds were investigated at a temperature range of 30-60°C. Detailed explanations of synthesis, characterization and corrosion inhibition properties of these Schiff bases are documented in this chapter as four sections.

SECTION 1

SYNTHESIS AND CHARACTERIZATION OF REDUCED SCHIFF BASES

Schiff bases formed from thiophene-2-carbaldehyde, 3-acetylpyridine and 3-formylindole were already investigated for their anticorrosion activity whereas studies on their reduced form were not reported. The detailed study of investigations on the synthesis and structural aspects of four reduced Schiff bases are presented in this section.

Preparation of RT2C3ABA

A hot ethanolic solution of thiophene-2-carbaldehyde was added to a refluxing solution of 3-amino benzoic acid in ethanol and the mixture was allowed to reflux on a water bath for 3 hours. It was then concentrated and cooled in ice bath to afford the precipitate (T2C3ABA) which was collected, washed with ethanol and dried.

5 mM of T2C3ABA was dissolved in 1:1 ethanol-water mixture and cooled in ice bath and an ethanolic solution of NaBH_4 was added slowly with constant stirring until the colour of the solution was disappeared. The mixture was concentrated in order to separated out the product RT2C3ABA which was then washed with small quantities of water-ethanol mixture and dried. Yield was 72%. MP = $>300^\circ\text{C}$. Elemental analysis data calculated: C, 61.47%; H, 4.69%; N, 5.97%; O, 13.66%; S, 0.52%. Found: C, 62.32%; H, 4.78%; N, 5.99%; O, 14.51; S, 0.54%.

Characterization of RT2C3ABA

The structure of RT2C3ABA is well established by various spectroscopic methods such as NMR, mass, IR and UV-visible spectroscopy.

NMR spectral analysis

The ^1H nmr spectrum of the Schiff base RT2C3ABA (Figure 1.53) exhibited 11 peaks. The COOH group and $-\text{CH}_2$ group displayed their characteristic peaks at 12.10 δ and 4.41 δ respectively. The broad peak observed at 4.8 δ is assigned to the NH protons and the aromatic protons appeared in the range 6.05 - 7.33 δ . A very weak peak appeared at 6.05 δ is due to the $-\text{SH}$ proton, which is generated by tautomerism. The details of ^1H nmr peaks are depicted in the Table 1.15

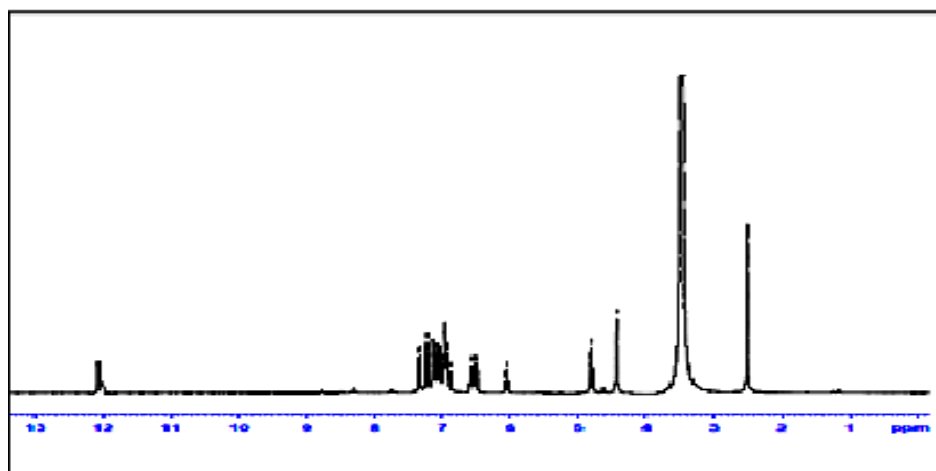
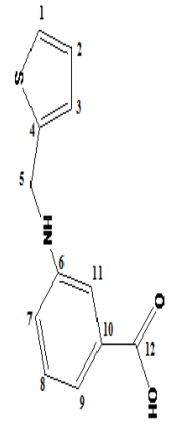


Figure 1.53: ^1H nmr spectrum of RT2C3ABA

The ^{13}C nmr spectrum is represented in the Figure 1.54 and tabulated in the Table 1.15. The peaks appeared at 42.17ppm and 170ppm were displayed by $-\text{CH}_2$ carbon and COOH carbon respectively. The remaining aromatic carbon atoms exhibiting their peaks in the range 112-147ppm.

Table 1.15: ^1H nmr and ^{13}C nmr spectral data of RT2C3ABA

^1H nmr			^{13}C nmr		
H Label	δ value	C Label	δ value		
1	6.89(d,1H)	1	117		
2	6.53(t,1H)	2	112		
3	6.92(d,1H)	3	113		
4	4.41(s,2H)	4	115		
5	4.8(s, 1H)	5	42.17		
6	7.11(d, 1H)	6	144		
7	7.08(t, 1H)	7	127		
8	7.23(d, 1H)	8	124		
9	7.33(s, 1H)	9	126		
10	12.1(s,1H)	10	147		
-SH	6.05(s,1H)	11	140		
		12	170		

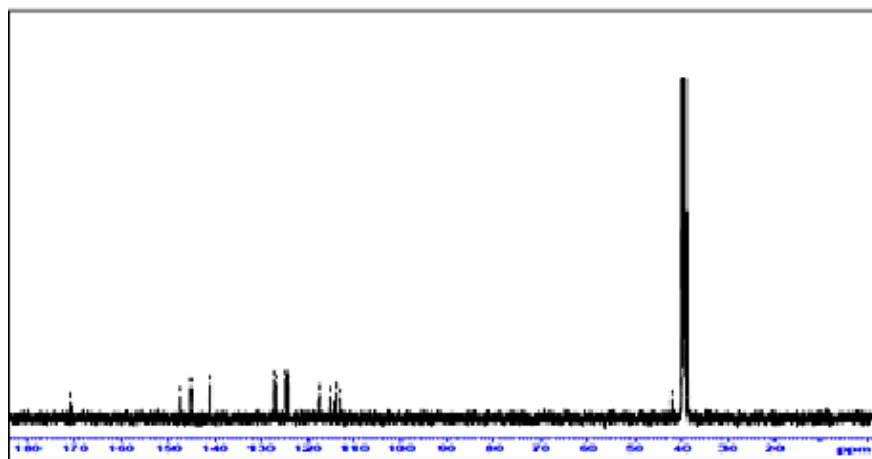


Figure 1.54: ^{13}C nmr spectrum of RT2C3ABA

Mass spectral analysis

Mass spectrum of RT2C3ABA (Figure 1.55) contains a very weak M^+ peak at m/z 233, which is exactly equal to the molecular weight of the reduced Schiff base compound. The $[\text{M}+2]$ peak originated by the presence of sulphur is observed

at m/z 235 and the base peak observed at m/z 137 is assigned to the fragment $[C_7H_7NO_2]^+$. The clear signals appeared at m/z 120 and 97 were assigned due to the fragments $[C_7O_2]^+$ and $[C_5H_5S]^+$ respectively.

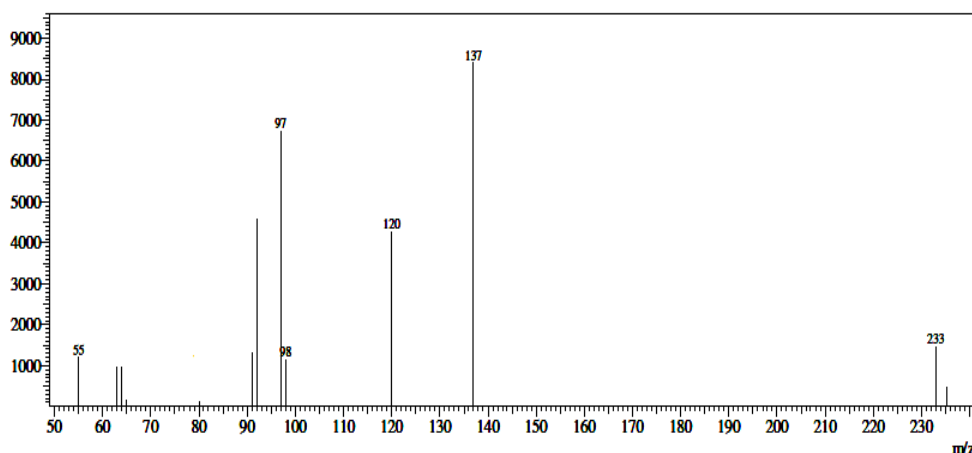


Figure 1.55: Mass spectrum of RT2C3ABA

IR spectral analysis

The IR spectrum of the reduced Schiff base compound RT2C3ABA exhibited a scalloped peak at 3406 cm^{-1} corresponding to $-OH$ group vibration which was merged with $-NH$ vibration peak. The vibrational frequency of sp^2 hybridized C-H bond exhibited a peak at 3020 cm^{-1} . The asymmetric stretching vibration frequency of carboxylic group displayed a peak at 1689 cm^{-1} . The intense peak observed at 1760 cm^{-1} is assigned due to C=O stretching vibration and the peaks at 1558 cm^{-1} , 1516 cm^{-1} and 1406 cm^{-1} can be assigned to C=C vibrations of aromatic system. Stretching vibration frequency of C-N was observed at 1293 cm^{-1} and C-H vibrations were shown between $3176 - 3045\text{ cm}^{-1}$. The in plane bending vibrations of aromatic ring appeared at $1020, 991\text{ cm}^{-1}$ and out of plane bending vibrations observed at $767, 696\text{ cm}^{-1}$.

Electronic spectral analysis

The different electronic transitions in the molecule were appeared at 32362 cm^{-1} and 39062 cm^{-1} , which may be assigned to $n \rightarrow \pi^*$ (R-band) and $\pi \rightarrow \pi^*$ (benzenoid band) transitions respectively.

Based on the spectral and elemental analysis the structure of the reduced Schiff base RT2C3ABA was confirmed and the proposed structure is given in the Figure 1.56

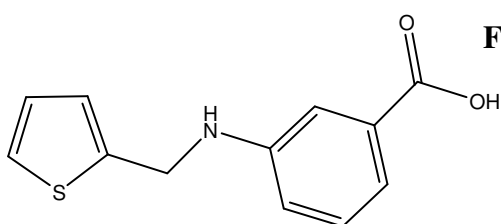


Figure 1.56: Structure of RT2C3ABA

Preparation of R3APTSC

A hot ethanolic solution of 3-acetylpyridine was added to a refluxing solution of thiosemicarbazide in ethanol and the mixture was allowed to reflux further for 3 hours. Then the solution was concentrated and cooled. The precipitate formed (3APTSC) which was collected, washed with ethanol and dried.

5 mM of 3APTSC was dissolved in 1:1 ethanol-water mixture and cooled. An ethanolic solution of NaBH_4 was added slowly with constant stirring until the disappearance of the colour. The mixture was then concentrated and the resulted product (R3APTSC) was separated, washed with small quantities of water-ethanol mixture and dried. Yield was 80%. MP= 220⁰C. Elemental analysis data calculated: C, 48.90%; H, 6.1%; N, 28.53%; S, 16.30%. Found: C, 49.32%; H, 6.4%; N, 29.1%; S, 17.12%.

Characterization of R3APTSC

The structure of R3APTSC is well established by various spectroscopic methods such as NMR, mass, IR and UV-visible spectroscopy.

NMR spectral analysis

In the ^1H nmr spectrum of the Schiff base R3APTSC (Figure 1.57) an intense singlet peak observed at 2.13 δ arises due to the presence of methyl protons. A highly intense peak appeared at 3.51 δ was originated by the merging of two peaks corresponding to the methylene proton on sp^3 hybridized carbon and terminal NH_2 group. The peaks of two $-\text{NH}$ proton also undergo merging and appeared as a broad peak at 7.96 δ . The broadness of this peak is due to the combined effects of H-bonding and quadrupole broadening. The protons of thiophene ring appeared in the range 7.39- 9.08 δ . A very weak peak appeared at 6.32 δ is due to the $-\text{SH}$ proton, resulted by tautomerism. The details of ^1H nmr peaks are depicted in the Table 1.16

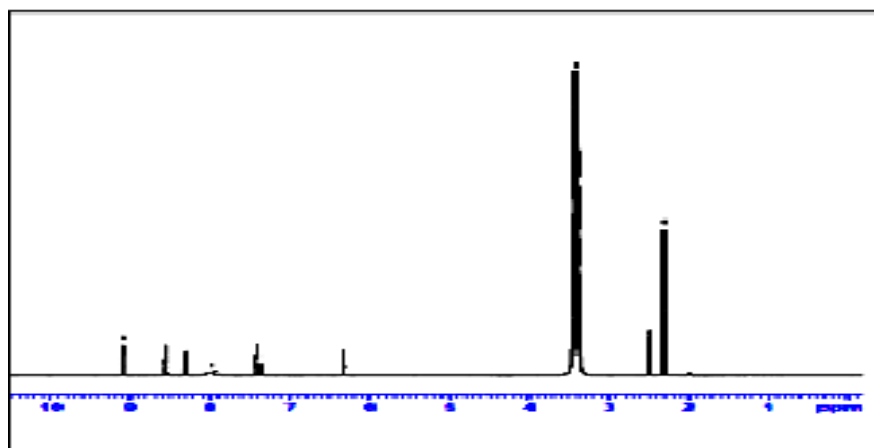
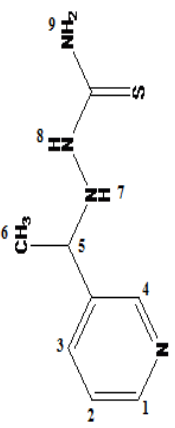


Figure 1.57: ^1H nmr spectrum of R3APTSC

In the ^{13}C nmr spectrum (Figure 1.58) the methyl carbon atom displayed its characteristic peak at 13.65ppm. The aromatic pyridine ring carbon atoms were resonated in the range 133.45-149.51ppm. The peak observed at 123.22ppm was due to the carbon atom near to the N atom. The $-\text{C}=\text{S}$ group containing carbon atom

exhibited a peak at 179.34ppm. ^{13}C nmr data and the assignments are given in the Table 1.16

Table 1.16: ^1H nmr and ^{13}C nmr spectral data of R3APTSC

	^1H nmr		^{13}C nmr	
	H Label	δ value	C Label	δ value
	1	9.080(d, 1H)	1	147.62
	2	7.39(t, 1H)	2	133.45
	3	8.30 (d, 1H)	3	133.71
	4	8.542(s, 1H)	4	145.31
	5&9	3.51(s, 3H)	5	149.51
	6	2.137(s, 3H)	6	123.22
	7&8	7.96(s, 2H)	7	13.65
	-SH	6.322(s, 1H)	8	179.34

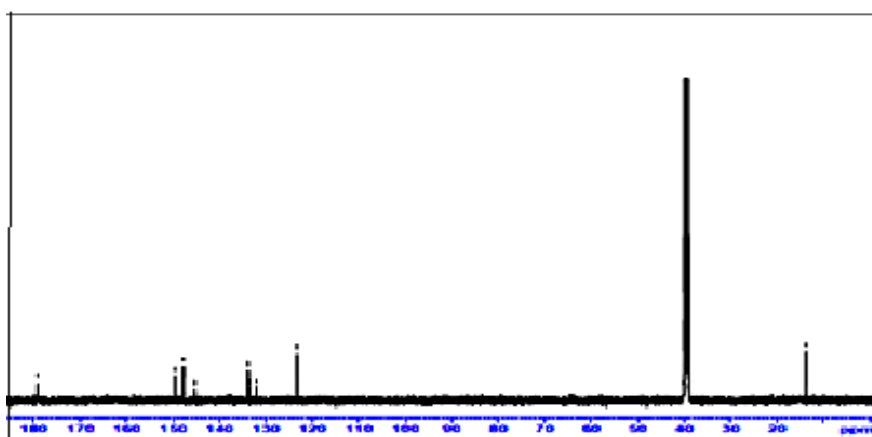


Figure 1.58: ^{13}C nmr spectrum of R3APTSC

Mass spectral analysis

Mass spectrum of R3APTSC (Figure 1.59) contains a very weak M^+ peak at m/z 196, which is exactly equal to the molecular weight of the reduced Schiff base. A very weak $[\text{M}+2]$ peak originated by the presence of sulphur is observed at m/z 198 and the base peak observed at m/z 194 is considered as $[\text{M}-2]$ peak. The peak appeared at m/z 179 is assigned to the fragment $[\text{C}_7\text{H}_7\text{N}_4\text{S}]^+$. The peak observed at

m/z 161 was shown by the removal of $-\text{CH}_3$ group from $[\text{M}-2]$ molecule. The other prominent peaks appeared at m/z 134, 120 and 93 were assigned due to the fragments $[\text{C}_7\text{H}_8\text{N}_3]^+$, $[\text{C}_7\text{H}_8\text{N}_2]^+$, and $[\text{C}_6\text{H}_7\text{N}]^+$ respectively. The stable pyridine fragment $[\text{C}_5\text{H}_4\text{N}]^+$ gives an intense peak at m/z 78. The clear peaks displayed at m/z 60 and 51 were corresponding to the fragments $[\text{CSNH}_2]^+$ and $[\text{C}_4\text{H}_3]^+$ respectively.

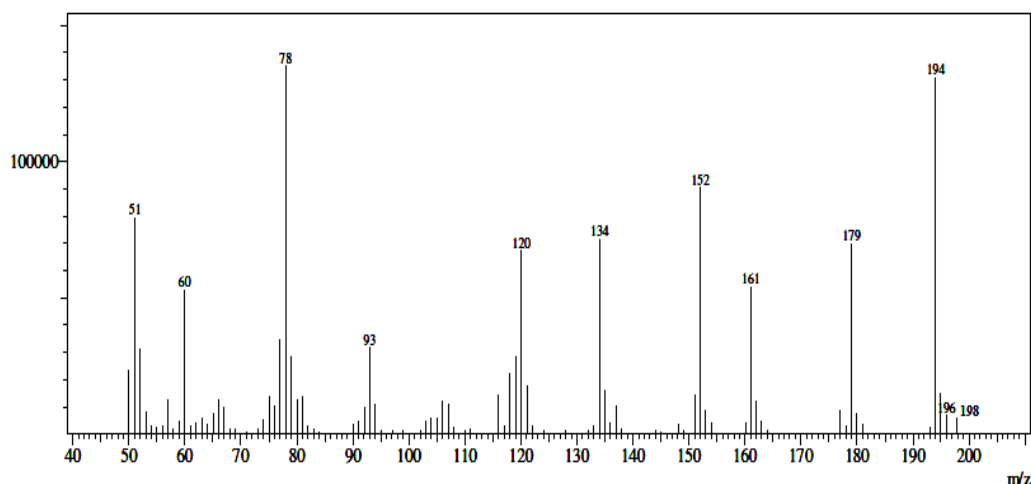


Figure 1.59: Mass spectrum of R3APTSC

IR spectral analysis

The IR spectrum of the R3APTSC contains an intense peak at 3259 cm^{-1} corresponding to NH group stretching vibration. The peaks observed at 3034 cm^{-1} and 3456 cm^{-1} were corresponding to the symmetric and asymmetric stretching frequencies of $-\text{NH}_2$ group. A prominent vibrational coupling is possible for nitrogen containing thiocarbonyl compounds and three strong bands appeared at the range of $1315 - 1595\text{ cm}^{-1}$, $1261 - 1419\text{ cm}^{-1}$ and $970 - 1089\text{ cm}^{-1}$ were due to the mixed vibrations. A very weak peak observed at 2360 cm^{-1} is assigned to the vibrational frequency of $-\text{SH}$ bond, which generated by tautomerism. The peaks at 1419 cm^{-1} , 1473 cm^{-1} and 1502 cm^{-1} can be assigned to $\text{C}=\text{C}$ vibrations of aromatic system and $\text{C}=\text{S}$ shown its characteristic peak at 852 cm^{-1} . Stretching vibration frequency of $\text{C}-\text{N}$ was observed at 1293 cm^{-1} and $\text{C}-\text{H}$ vibrations were shown

between 3180- 3050 cm^{-1} . The in plane bending vibrations of pyridine ring appeared at 1018, 970 cm^{-1} and out of plane bending vibrations observed at 756, 700 cm^{-1} .

Electronic spectral analysis

The various electronic transitions in the molecule were appeared at 31810 cm^{-1} , 31670 cm^{-1} and 25480 cm^{-1} which are assigned to $n \rightarrow \pi^*$ (R-band), $\pi \rightarrow \pi^*$ (benzenoid band) and $\pi \rightarrow \pi^*$ (K band) transitions respectively.

On the basis of above mentioned data, the structure of the reduced Schiff base R3APTSC was confirmed and the proposed structure is given in the Figure 1.60

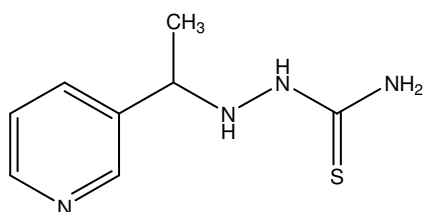


Figure 1.60: Structure of R3APTSC

Preparation of R3FI3ABA

A hot ethanolic solution of 3-formylindole was added to a refluxing solution of 3-amino benzoic acid in ethanol and the mixture was allowed to reflux on a water bath for 4 hours. It was then concentrated and cooled so as to get the precipitate of 3FI3ABA which was collected, washed with ethanol and dried.

5 mM of 3FI3ABA was dissolved in 1:1 ethanol-water mixture, cooled in ice bath and an ethanolic solution of NaBH_4 was added slowly with constant stirring until the colour of the solution disappeared. The mixture was concentrated and the precipitate formed (R3FI3ABA) was washed with small quantities of water-ethanol mixture and dried. Yield was 76%. The product has a tendency to decompose around 200 $^{\circ}\text{C}$ and undergo charring. Elemental analysis data calculated: C, 72.14%; H, 5.26%; N, 10.52%; O, 12.02%. Found: C, 73.6%; H, 6.02%; N, 11.63; O, 13.1%.

Characterization of R3FI3ABA

According to the $^1\text{Hnmr}$ spectrum, the reduced Schiff base R3FI3ABA (Figure 1.61) contains 13 non equivalent protons. The resonance of carboxylic acid group containing proton exhibited a peak at 11.01 δ . The NH proton in the indole system appeared at 5.64 δ and other $-\text{NH}$ proton displayed a peak at 4.81 δ . The peak at 4.37 δ is corresponding to $-\text{CH}_2$ group. Peaks due to aromatic protons of indole and benzenoid ring system were appeared in the range 6.50 – 7.63 δ . The $^{13}\text{Cnmr}$ spectrum is represented in the Figure 1.62. The peak observed at 170ppm was due to the carboxylic acid carbon and the peak at 65ppm was assigned to methylene group. The carbon atoms on aromatic rings were resonated in the range 112-147ppm. Mass spectrum of R3FI3ABA is represented in the Figure 1.63. The base peak observed at m/z 137 was due to the fragment $[\text{C}_7\text{H}_7\text{O}_2\text{N}]^+$. The molecular ion peak was absent in the spectrum. The other prominent peaks appeared at m/z 117 and 92 were assigned due to the fragments $[\text{C}_8\text{H}_7\text{N}]^+$ and $[\text{C}_6\text{H}_6\text{N}]^+$ respectively.

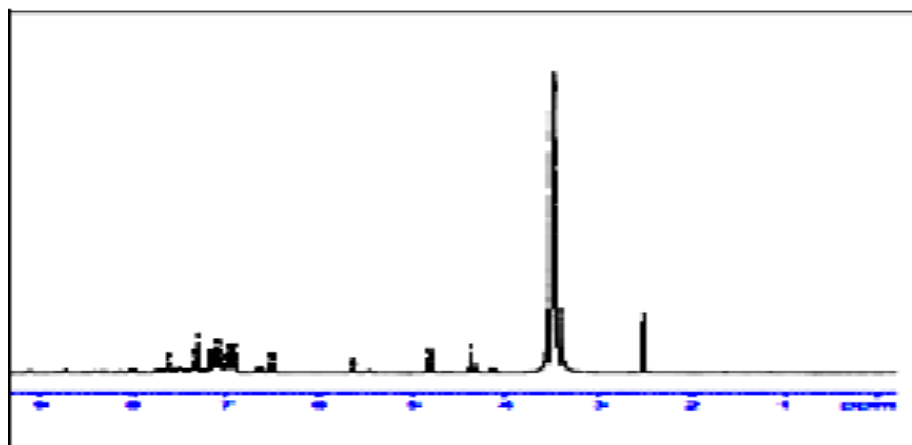


Figure 1.61: $^1\text{Hnmr}$ spectrum of R3FI3ABA

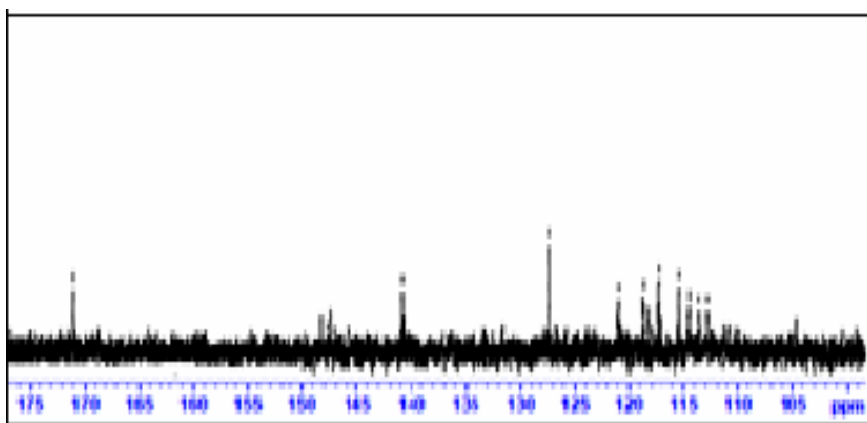


Figure 1.62: ¹³Cnmr spectrum of R3FI3ABA

The IR spectrum exhibited –OH stretching vibration frequency of the carboxylic acid part at 3404 cm⁻¹. Stretching vibration frequency of C-N was observed at 1290 cm⁻¹ and C-H vibrations were shown between 3200-2860 cm⁻¹. The asymmetric and symmetric stretching vibration frequencies of the -COOH group were displayed at 1498 cm⁻¹ and 1676 cm⁻¹ respectively. An intense peak at 1392 cm⁻¹ was occurred due to the C-O bond stretching. The various electronic transitions in the molecule appeared at 34483 cm⁻¹, 35461 cm⁻¹ and 39063 cm⁻¹, which are assigned to n→π* (R-band), π→π* (benzenoid band) and π→ π* (K band) transitions respectively.

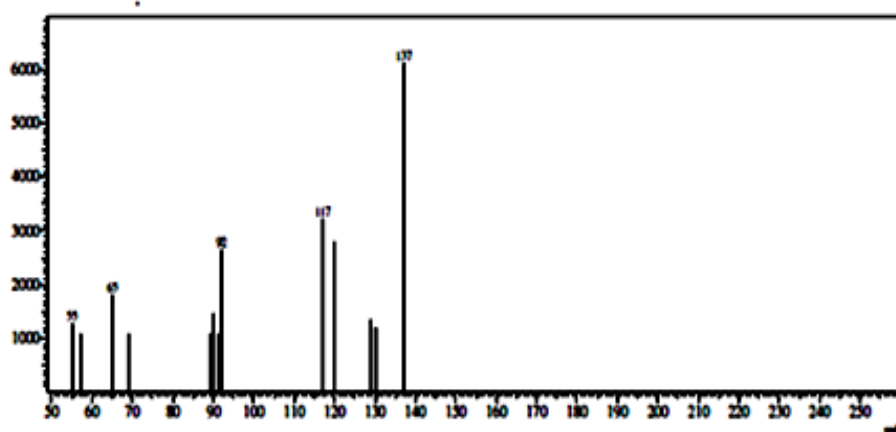


Figure 1.63: Mass spectrum of R3FI3ABA

On the basis of above mentioned data, the structure of the reduced Schiff base R3FI3ABA was confirmed and the proposed structure is given in the Figure 1.64

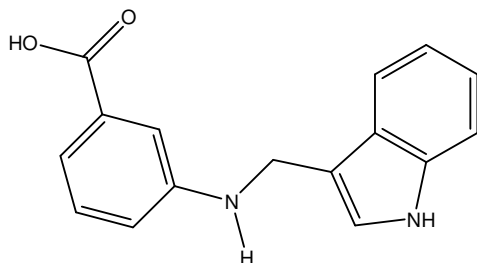


Figure 1.64: Structure of R3FI3ABA

Preparation of R3FI4ABA

A hot ethanolic solution of 3-formylindole was added to a refluxing solution of 4-amino benzoic acid in ethanol and the mixture was allowed to reflux on a water bath for 4 hours. It was then concentrated and cooled to obtain the precipitate of 3FI4ABA which was collected, washed with ethanol and dried.

5 mM of 3FI4ABA was dissolved in 1:1 ethanol-water mixture and cooled in ice bath and an ethanolic solution of NaBH_4 was added slowly with constant stirring until the colour of the solution was disappeared. The mixture was then concentrated and the separated product (R3FI4ABA) was washed with small quantities of water-ethanol mixture and dried. Yield was 74%. The product has a tendency to decompose around 200°C and undergo charring. Elemental analysis data calculated: C, 72.14%; H, 5.26%; N, 10.52%; O, 12.02%. Found: C, 73.9%; H, 6.08%; N, 11.48%; O, 13.52%.

Characterization of R3FI4ABA

The $^1\text{Hnmr}$ spectrum of the Schiff base R3FI3ABA (Figure 1.65) exhibited 11 clear peaks. The resonance of carboxylic proton exhibited a peak at 11δ . The NH proton in the indole system appeared at 5.27δ and other NH proton displayed a broad peak at 3.94δ . The broadness of this peak can be explained by the effects of

H-bonding and quadrupole broadening. The peak at 4.3δ is corresponding to $-\text{CH}_2$ group. All aromatic protons of indole and benzenoid ring system appeared in the range $7.13 - 8.11\delta$. In the ^{13}C nmr spectrum (Figure 1.66) the peak observed at 184ppm was due to the carboxylic acid carbon and the peak appeared at 70ppm was displayed by $-\text{CH}_2$ group. The carbon atoms in the aromatic rings were resonated in the range 112-150ppm. Mass spectrum of R3FI4ABA is represented in the Figure 1.67. The base peak observed at m/z 137 was due to the fragment $[\text{C}_7\text{H}_7\text{O}_2\text{N}]^+$. The molecular ion peak is absent in the spectrum. The other prominent peaks appeared at m/z 120 and 92 were assigned to the fragments $[\text{C}_7\text{H}_4\text{O}_2]^+$ and $[\text{C}_6\text{H}_6\text{N}]^+$ respectively.

The IR spectrum exhibited $-\text{OH}$ stretching vibration frequency of the carboxylic acid part at 3390 cm^{-1} . Stretching vibration frequency of C-N was observed at 1241 cm^{-1} and C-H vibrations were shown between $3200-2870\text{ cm}^{-1}$. An intense peak at 1637 cm^{-1} was occurred due to the C=O bond stretching. The various electronic transitions in the molecule were appeared at 34364 cm^{-1} , 36630 cm^{-1} and 39370 cm^{-1} , which can be assigned to $n\rightarrow\pi^*$ (R-band), $\pi\rightarrow\pi^*$ (benzenoid band) and $\pi\rightarrow\pi^*$ (K band) transitions respectively.

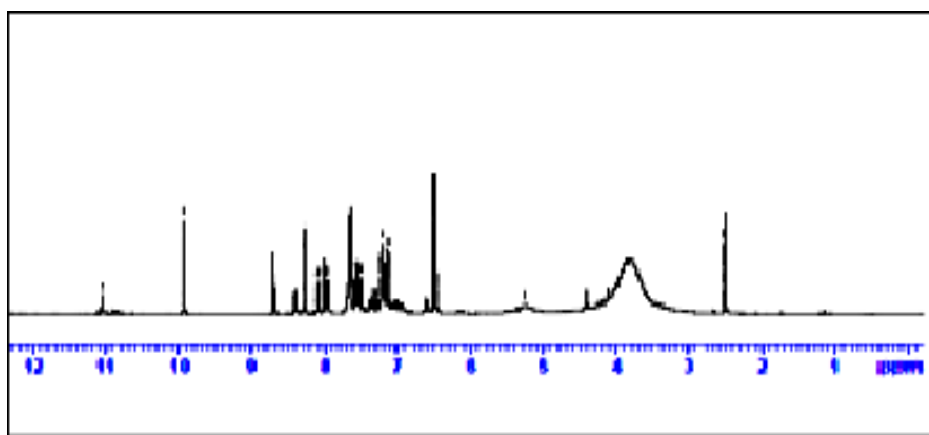


Figure 1.65: ^1H nmr spectrum of R3FI4ABA

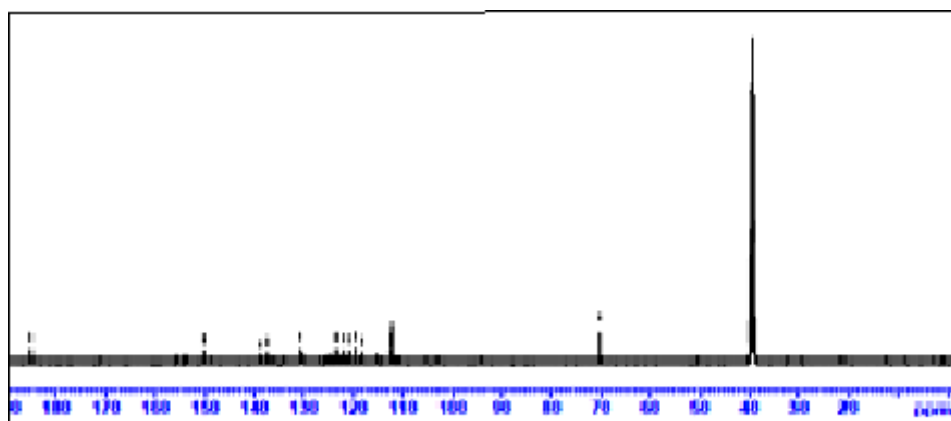


Figure 1.66: ¹³Cnmr spectrum of R3FI4ABA

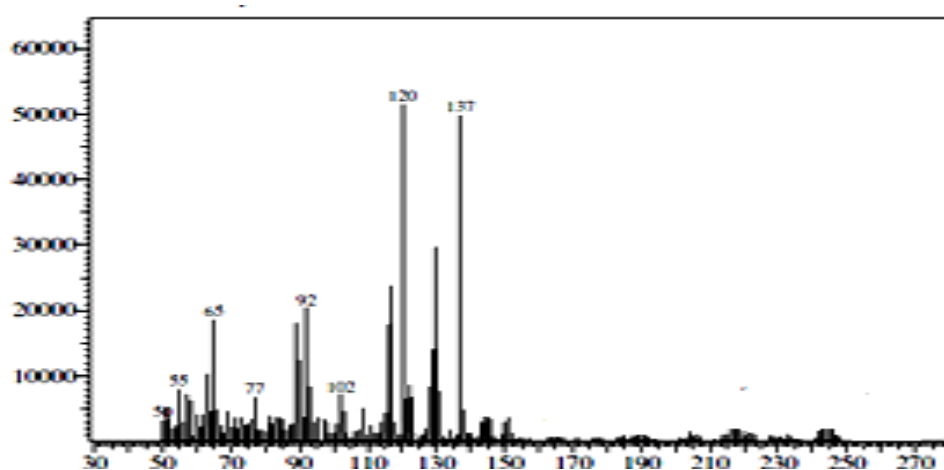


Figure 1.67: Mass spectrum of R3FI4ABA

On the basis of above mentioned data, the structure of the reduced Schiff base R3FI4ABA was confirmed and the proposed structure is given in the Figure 1.68

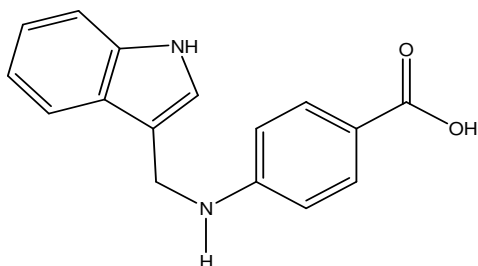


Figure 1.68: Structure of R3FI4ABA

SECTION 2

CORROSION BEHAVIOUR OF MILD STEEL IN THE PRESENCE OF REDUCED SCHIFF BASES IN 1M HCl

The corrosion inhibition behaviour of four reduced Schiff bases R3FI3ABA, R3FI4ABA, RT2C3ABA and R3APTSC were studied in 1M HCl using inhibitor solutions of the concentration range 0.2mM - 1mM.

Gravimetric analysis

Weight loss analysis of mild steel were performed by immersing metal coupons of 1cm² area in 1M HCl solution and recorded readings for consecutive 4 days with and without the reduced Schiff bases at different concentrations and analysed them daily in order to study the effect of reduced Schiff bases on corrosion inhibition. The corrosion rate in mmy⁻¹ and percentage of inhibition efficiencies of reduced Schiff bases are represented in the table 1.17 and table 1.18 respectively. The plots of corrosion rates and inhibition efficiency Vs concentration are given in Figures 1.69 and 1.70 respectively.

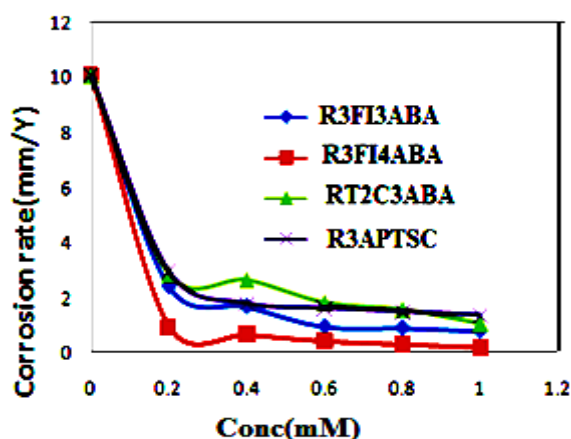


Figure 1.69: Corrosion rates of MS in the presence and absence of reduced Schiff bases in 1M HCl for 24 hours.

Table 1.17: Corrosion rates of MS in the presence and absence of reduced Schiff bases in 1M HCl for 4 days

Schiff Base	Conc (mM)	Corrosion rate (mmy ⁻¹)			
		24 hr	48 hr	72 hr	96 hr
R3FI3ABA	0	10.080	7.1845	6.2124	5.7850
	0.2	2.4025	1.7548	1.6429	1.6323
	0.4	1.6789	1.2418	1.1505	1.1346
	0.6	0.9382	0.7449	0.7739	0.7672
	0.8	0.8901	0.7124	0.6749	0.6818
	1	0.7798	0.6462	0.5804	0.6211
R3FI4ABA	0.2	0.9602	0.7442	0.7353	0.7383
	0.4	0.6801	0.5148	0.4686	0.5051
	0.6	0.4372	0.4238	0.3667	0.3689
	0.8	0.3200	0.2870	0.3101	0.3350
	1	0.2170	0.2148	0.1888	0.2170
RT2C3ABA	0.2	2.8474	2.1638	1.9881	2.0115
	0.4	2.6295	2.0264	1.8157	1.7514
	0.6	1.8015	1.4185	1.3644	1.2897
	0.8	1.5512	1.1759	1.1403	1.1094
	1	1.0421	0.8750	0.8289	0.8607
R3APTSC	0.2	2.9337	2.1264	1.8485	1.7318
	0.4	1.7836	1.3045	1.2031	1.1692
	0.6	1.6120	1.1492	1.0194	0.9883
	0.8	1.4870	1.1437	0.9945	0.9796
	1	1.3572	0.9889	0.9018	0.87186

From the tables and figures it is evident that corrosion rates of mild steel specimens significantly decreased in the presence of reduced Schiff bases. Even at low concentrations, all the four reduced Schiff bases decrease the rate of corrosion of mild steel appreciably, compared to the rate of corrosion of the metal specimens immersed in the absence of the inhibitor (blank).

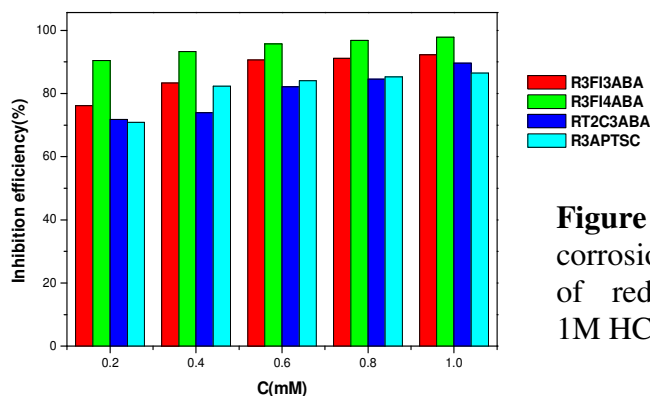


Figure 1.70: Comparison of corrosion inhibition efficiencies of reduced Schiff bases in 1M HCl

After 24 hours, rate of corrosion of mild steel specimen in the absence of inhibitor was 10.080 mmy^{-1} , whereas the lowest corrosion rate value of 0.217 mmy^{-1} was obtained for the inhibitor solution of R3FI4ABA at 1 mM concentration. Data resulted from the corrosion inhibition studies indicate that all the reduced Schiff bases under study acted as potential corrosion inhibitors on MS in 1M HCl and percentage of efficiency of inhibition increased with rise in inhibitor concentration. This can be explained by the fact that the surface of the metal was covered by the inhibitor molecules through adsorption process, which increased with increase in concentration. All of the reduced Schiff base compounds displayed inhibition efficiency $>70\%$ even at low concentrations. On close examination of the values from the Table 1.18 and the Figure 1.70, it is understood that the percentage of inhibition efficiency of the two reduced Schiff bases R3FI3ABA and R3FI4ABA were significantly greater than the other two reduced compounds RT2C3ABA and R3APTSC at 24 hours and follows the order $\text{R3FI4ABA} > \text{R3FI3ABA} > \text{RT2C3ABA} > \text{R3APTSC}$. A maximum inhibition efficiency of 97.84% was achieved by R3FI4ABA at 1 mM concentration.

Table 1.18: Inhibition efficiency of MS in the presence and absence of reduced Schiff bases in 1M HCl for 4 days

Reduced Schiff Base	Conc (mM)	Inhibition efficiency (%)			
		24 hr	48 hr	72 hr	96 hr
R3FI3ABA	0.2	76.16	75.57	73.55	71.78
	0.4	83.34	82.71	81.48	80.38
	0.6	90.69	89.63	87.54	86.73
	0.8	91.16	90.08	89.13	88.21
	1	92.26	91.00	90.65	89.26
R3FI4ABA	0.2	90.47	89.64	88.16	87.23
	0.4	93.25	92.83	92.45	91.26
	0.6	95.66	94.10	94.09	93.62
	0.8	96.82	96.00	95.00	94.20
	1	97.84	97.00	96.96	96.24
RT2C3ABA	0.2	71.75	69.88	67.99	65.22
	0.4	73.91	71.79	70.77	69.72
	0.6	82.12	80.25	78.03	77.70
	0.8	84.61	83.63	81.64	80.82
	1	89.66	87.82	86.65	85.12
R3APTSC	0.2	70.89	70.40	70.24	70.06
	0.4	82.30	81.84	80.63	79.78
	0.6	84.00	84.00	83.59	82.91
	0.8	85.24	84.08	83.99	83.06
	1	86.53	86.23	85.48	84.92

The predominant corrosion inhibition ability of R3FI4ABA, R3FI3ABA and RT2C3ABA is due to the interaction of these compounds on the surface of the metal through two aromatic ring systems as compared to R3APTSC, which contains only one aromatic ring. The inhibition efficiency of RT2C3ABA and R3APTSC can also attribute to the presence of more polarisable sulphur atom which is responsible for strong interactions with the metal surface. Even though RT2C3ABA contains two

aromatic ring systems, they show little bit low efficiency in comparison with 3-formylindole derivatives which may be due to the divergence from the coplanarity in molecular structure. Even though the molecule contains active inhibition centres; the puckered nature of the compound prevents the interaction with the metal surface and thus decreases the inhibition efficiency.

Figures 1.71 to 1.74 represent the effect of time on the percentage of corrosion inhibition efficiency. From the plot it is revealed that the straight lines corresponding to the inhibition efficiency of reduced Schiff bases have less steep nature and didn't have appreciable change as the days progressed. This can be explained by the fact that the reduced form of Schiff bases are free from the azomethine moiety and is not susceptible to the hydrolysis process and showed eminent inhibition efficiency. Generally, the stability of the molecules is very important if it is to be recommended as corrosion inhibitors for a prolonged use. The result of gravimetric corrosion studies derived to the conclusion that reduced Schiff base compounds have prolonged corrosion inhibition efficiency.

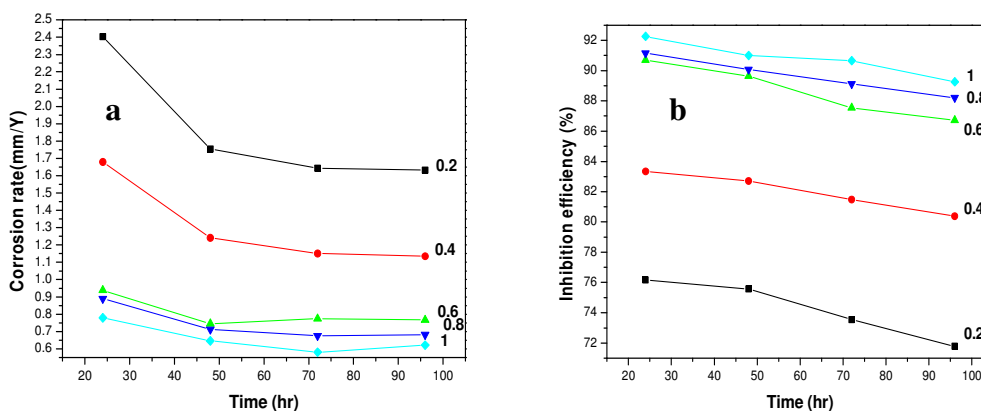


Figure 1.71: Variation of **a)** corrosion rate and **b)** inhibition efficiency of MS with immersion time in the presence and absence of R3FI3ABA in 1M HCl

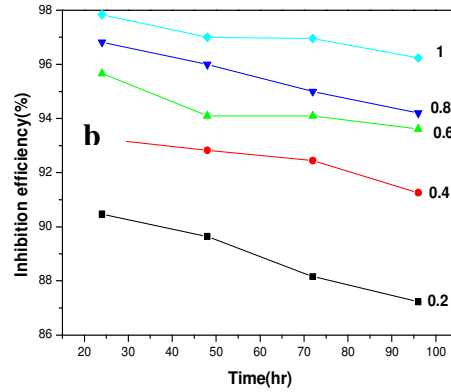
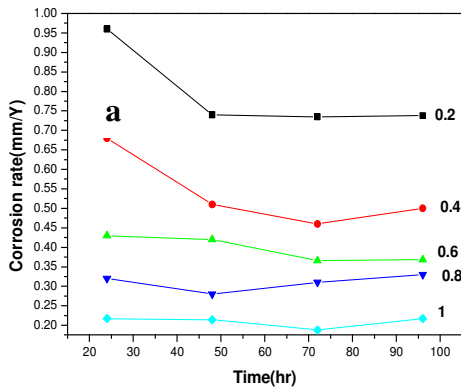


Figure 1.72: Variation of a) corrosion rate and b) inhibition efficiency of MS with immersion time in the presence and absence of R3FI4ABA in 1M HCl

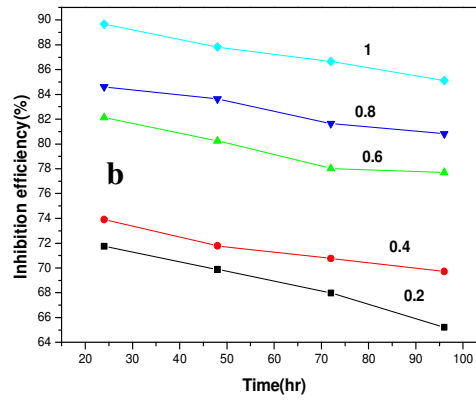
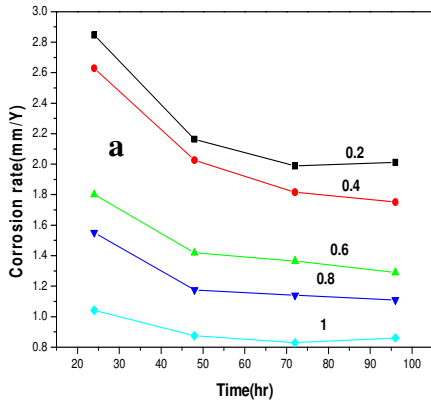


Figure 1.73: Variation of a) corrosion rate and b) inhibition efficiency of MS with immersion time in the presence and absence of RT2C3ABA in 1M HCl

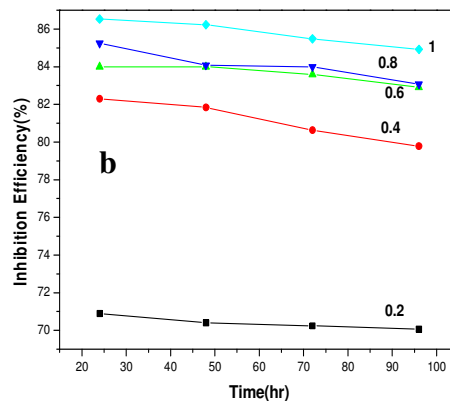
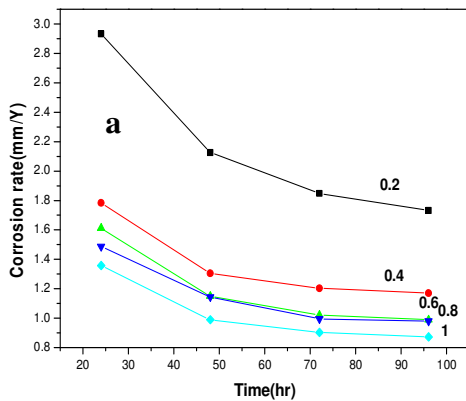


Figure 1.74: Variation of a) corrosion rate and b) inhibition efficiency of MS with immersion time in the presence and absence of R3APTSC in 1M HCl

Comparison between the inhibition efficiency of reduced Schiff bases and their parent Schiff bases

To compare the inhibition efficiencies of reduced Schiff bases R3FI3ABA, R3FI4ABA, RT2C3ABA and R3APTSC with their corresponding parent Schiff bases (3FI3ABA, 3FI4ABA, T2C3ABA, 3APTSC), gravimetric analysis of parent compounds were also conducted for 4 consecutive days. Table 1.19 and Figure 1.75 represent and compare the corrosion inhibition efficiencies of Schiff bases and their corresponding parent compounds at 1mM concentration.

Table 1.19: Corrosion inhibition efficiencies of parent Schiff bases (1mM) for consecutive 4 days

Schiff base	Inhibition efficiency (%)			
	24 hr	48 hr	72 hr	96hr
3FI3ABA	94	85	73	64
3FI4ABA	98.3	87	79	68
T2C3ABA	94	83	70	61
3APTSC	92	79	65	58

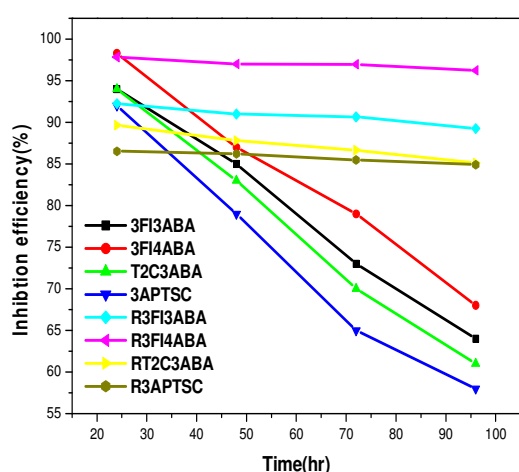


Figure 1.75: Comparison of inhibition efficiency of reduced Schiff bases with their parent Schiff base

For a period of 24 h, the parent Schiff bases showed more inhibition efficiency than their reduced form at all concentrations which can be described by the presence of strong azomethine linkage in Schiff base compounds and the planar geometry of the molecules. The Figure 1.75 indicated that the decrease in the inhibition efficiency percentage for Schiff base compounds was steeper than that of its reduced forms as the days progressed which was due to the slow hydrolysis of Schiff base molecules in HCl medium. The azomethine moiety (C=N) present in the molecules can easily undergo hydrolysis whereas the reduced forms of these Schiff bases are free from the azomethine linkage and are not susceptible to hydrolysis and provide good inhibition efficiency for prolonged days. From the gravimetric results it is evident that reduced Schiff bases have prolonged corrosion inhibition efficiency.

Adsorption studies

The inhibition mechanism of reduced Schiff bases is mainly explained by the adsorption process and their adsorption parameters can be evaluated by the selection of the best fit isotherm model with the assistance of correlation coefficient (R^2). Figures 1.76 to 1.79 represent the adsorption isotherms for studied reduced Schiff bases in 1M HCl. From the attempt of various isotherms, the adsorption behaviour of all reduced Schiff bases are explained by Langmuir isotherm with $R^2=0.999$. The adsorption parameters are given in the Table 1.20.

Table 1.20: Adsorption parameters of reduced Schiff bases for the adsorption on MS surface in 1M HCl

Adsorption parameter	R3FI3ABA	R3FI4ABA	RT2C3ABA	R3APTSC
K_{ads}	16666	33333	16000	10000
ΔG_{ads}^0 (kJ/mol)	36.13	-38.88	-34.40	-32.80

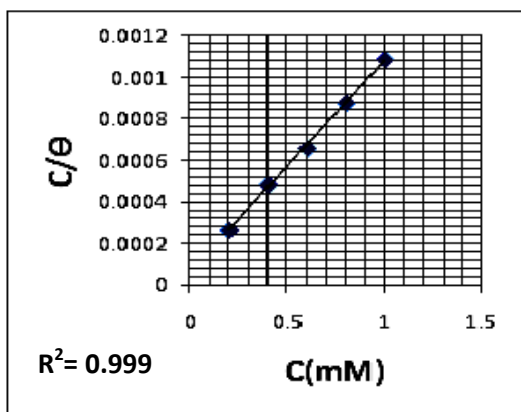


Figure 1.76: Langmuir isotherm for R3FI3ABA on MS in 1M HCl.

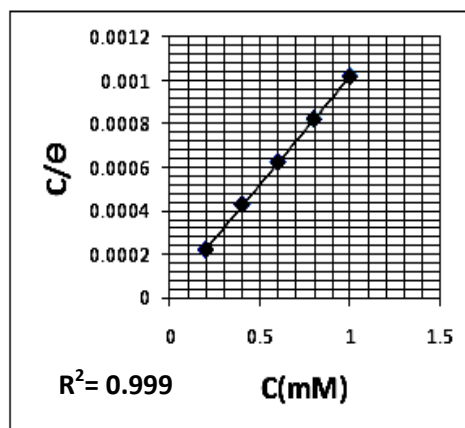


Figure 1.77: Langmuir isotherm for R3FI4ABA on MS in 1M HCl

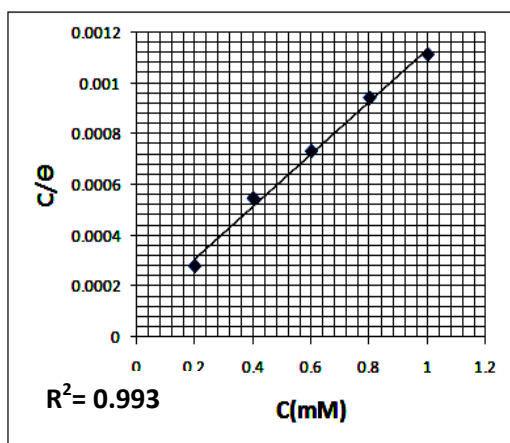


Figure 1.78: Langmuir isotherm for RT2C3ABA on MS in 1M HCl.

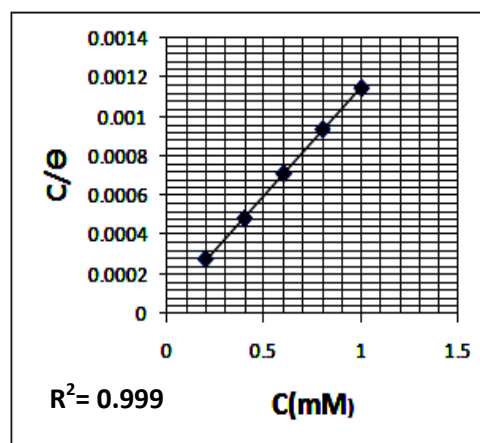


Figure 1.79: Langmuir isotherm for R3APTSC on MS in 1M HCl.

From the Table 1.20, it is clear that R3FI4ABA has comparatively high K_{ads} , value than all other reduced Schiff bases, suggesting that R3FI4ABA is adsorbed more efficiently on MS surface than others. ΔG_{ads}^0 for all reduced Schiff bases have negative values showing the spontaneity of the process. In the present study, all compounds have ΔG_{ads}^0 value between -34kJmol^{-1} and -38kJmol^{-1} pointing out the fact that the adsorption process involves both physisorption and chemisorption.

Temperature studies

The effect of temperature on corrosion was examined by conducting the weight loss measurements of four reduced Schiff bases in the temperature range

30-60°C. The activation energy for corrosion process in the presence and absence of inhibitor was evaluated by following Arrhenius equation.

$$K = A \exp\left(\frac{-E_a}{RT}\right)$$

where K is the corrosion rate, E_a is the activation energy, A is the frequency factor, T is the temperature and R is the gas constant.

Arrhenius curves were acquired by plotting $\log K$ Vs $1000/T$ for reduced Schiff bases and are given in the Figures 1.80 to 1.83. The value of regression coefficients of the straight lines derived which are very close to unity, reveals that the corrosion process on MS in HCl medium can be explained by simple kinetic model. Enthalpy and entropy of activation (ΔH^* , ΔS^*) were evaluated by the transition state theory and can be represented by the equation,

$$K = \left(\frac{RT}{Nh}\right) \exp\left(\frac{\Delta S^*}{R}\right) \exp\left(\frac{-\Delta H^*}{RT}\right)$$

where N is the Avagadro number and h is the Planck's constant. When plotted $\log(K/T)$ Vs $1/T$, straight lines were obtained for the corrosion of MS in 1M HCl with and without Schiff bases (Figures 1.80 to 1.83)

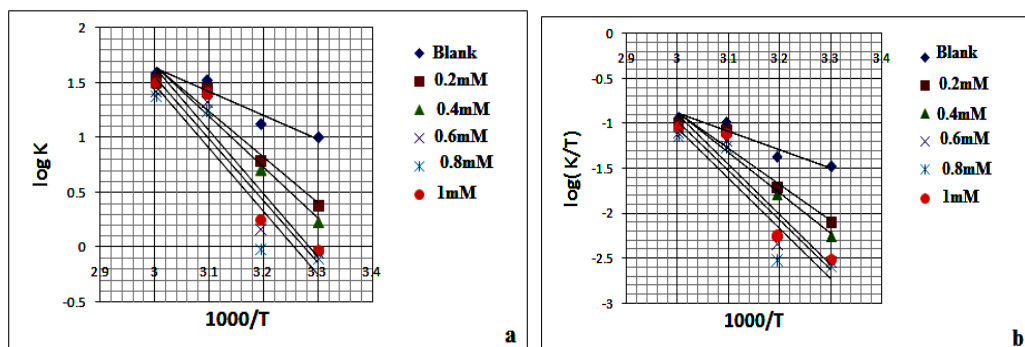


Figure 1.80: a) Arrhenius plot and b) $\log(K/T)$ Vs $1000/T$ plot for the MS corrosion in the presence and absence of R3FI3ABA in 1M HCl

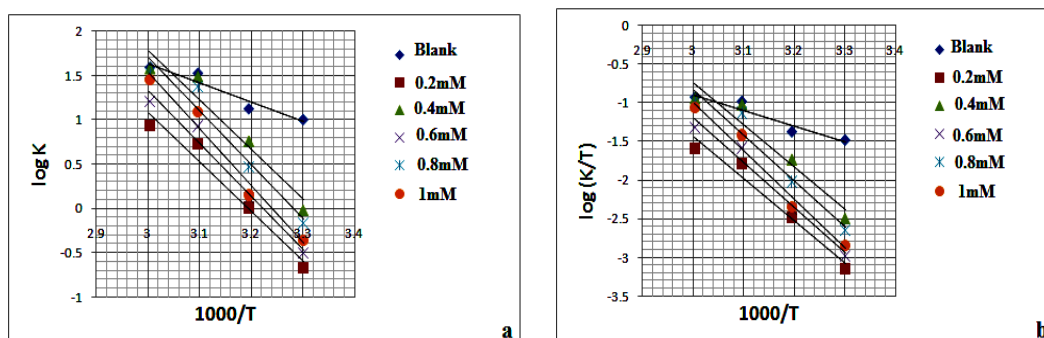


Figure 1.81: a) Arrhenius plot and b) $\log (K/T)$ Vs $1000/T$ plot for the MS corrosion in the presence and absence of R3FI4ABA in 1M HCl

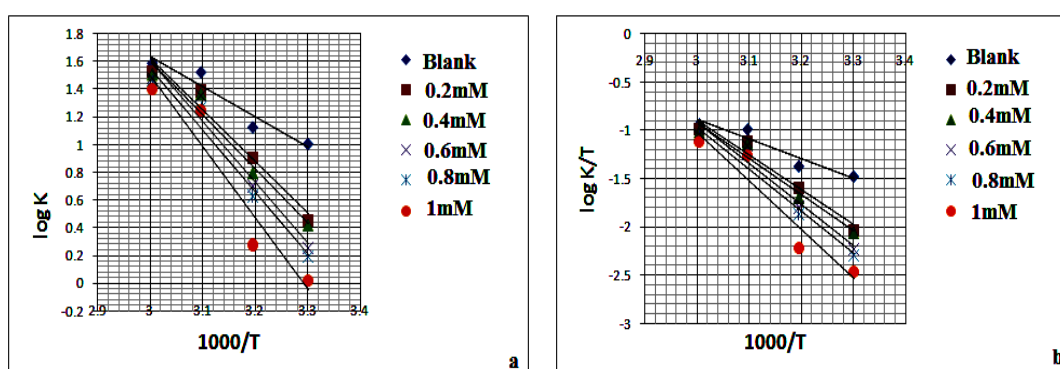


Figure 1.82: a) Arrhenius plot and b) $\log (K/T)$ Vs $1000/T$ plot for the MS corrosion in the presence and absence of RT2C3ABA in 1M HCl

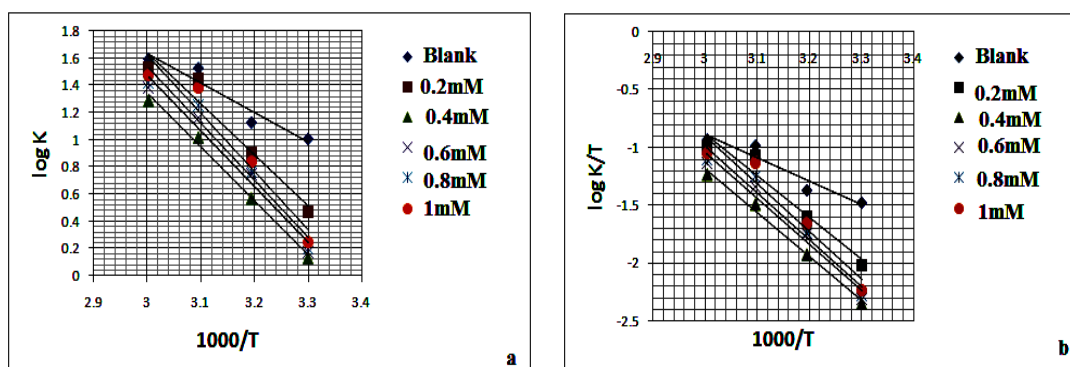


Figure 1.83: a) Arrhenius plot and b) $\log (K/T)$ Vs $1000/T$ plot for the MS corrosion in the presence and absence of R3APTSC in 1M HCl

Electrochemical corrosion investigations

Electrochemical investigations were carried out using a three electrode system, which consists of saturated calomel electrode (SCE) as reference electrode,

platinum electrode of 1cm² area as counter electrode and mild steel specimen with an area of 1cm² as working electrode. Electrochemical investigations including AC impedance analysis and potentiodynamic polarization studies were performed by Ivium Compactstat-e electrochemical system.

EIS analysis

The corrosion behaviour of MS in 1M HCl with and without inhibitor was studied using impedance spectroscopic analysis at 30⁰C. Figures 1.85 to 1.88 represent the Nyquist plots and Bode plots of reduced Schiff bases R3FI3ABA, R3FI4ABA, RT2C3ABA and R3APTSC respectively. The impedance parameters such as solution resistance (R_s), double layer capacitance (C_{dl}), charge transfer resistance (R_{ct}) and inhibition efficiency percentage (η_{EIS}%) were evaluated from the values of R_{ct} and are documented in the Table 1.21. The percentage of inhibition efficiency was evaluated from R_{ct} values using the following equation

$$\eta_{\text{EIS}} \% = \frac{R_{\text{ct}} - R'_{\text{ct}}}{R_{\text{ct}}} \times 100$$

where R_{ct} and R'_{ct} are the charge transfer resistances of working electrode in the presence and absence of inhibitor respectively.

Impedance parameters calculated show that the values of charge transfer resistance (R_{ct}) for all the studied reduced Schiff bases increased with concentration. This trend indicated that all reduced Schiff bases have a strong tendency to prevent the rate controlling charge transfer process of corrosion.

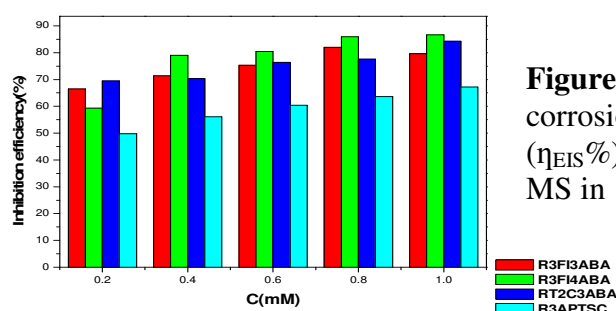


Figure 1.84: Comparison of corrosion inhibition efficiencies (η_{EIS}%) of reduced Schiff bases on MS in 1M HCl.

Table 1.21: Electrochemical impedance data of MS corrosion in the presence and absence of reduced Schiff bases in 1M HCl

Reduced Schiff base	Conc (mM)	R_{ct} (Ωcm^2)	C_{dl}	η_{EIS} %
	0	59.7	98.9	-
R3FI3ABA	0.2	178	77.3	66.46
	0.4	209	108	71.43
	0.6	242	88.5	75.33
	0.8	332	92.1	82.01
	1	293	83.4	79.62
		0.2	147	107
R3FI4ABA	0.4	285	85.3	79.05
	0.6	305	91.0	80.42
	0.8	427	74.9	86.01
	1	447	66.2	86.64
		0.2	196	68.5
RT2C3ABA	0.4	201	88.6	70.29
	0.6	253	111	76.40
	0.8	266	78.8	77.55
	1	381	78	84.33
		0.2	119	59.5
R3APTSC	0.4	136	73.9	56.10
	0.6	151	82.7	60.46
	0.8	164	62.6	63.59
	1	182	62	67.19

On examining the Table 1.21, the following points are obtained.

1. All the studied reduced Schiff bases can be used as effective corrosion inhibitors.
2. Even though all compounds exhibited moderate efficiency at lower concentration, they displayed better efficiency at higher concentrations.

- Among the studied reduced Schiff bases, R3FI4ABA acts as good corrosion inhibitor as compared with others.
- For R3FI3ABA, the maximum efficiency of 82% was obtained at 0.8mM concentration.
- R3FI4ABA exhibited only 59% efficiency at low concentration and the efficiency increased with rise in concentration and attained a saturation value of 86% at 0.8mM concentration. Beyond this concentration a significant increase in the inhibition efficiency was not attained.
- 3-formylindole derivatives exhibited maximum inhibition efficiency at 0.8mM concentration while other inhibitors show highest activity at 1mM concentration.
- The inhibition efficiency of studied reduced Schiff bases follows the order R3FI4ABA > R3FI3ABA > RT2C3ABA > R3APTSC, which is in good correlation with the data resulted from gravimetric analysis for 24 h.

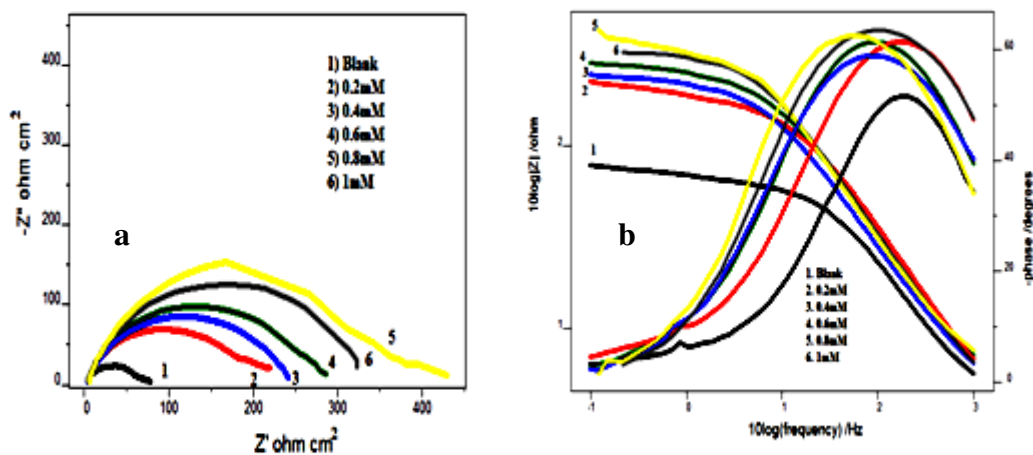


Figure 1.85: a) Nyquist plots and b) Bode plots of MS corrosion in the presence and absence of R3FI3ABA in 1M HCl

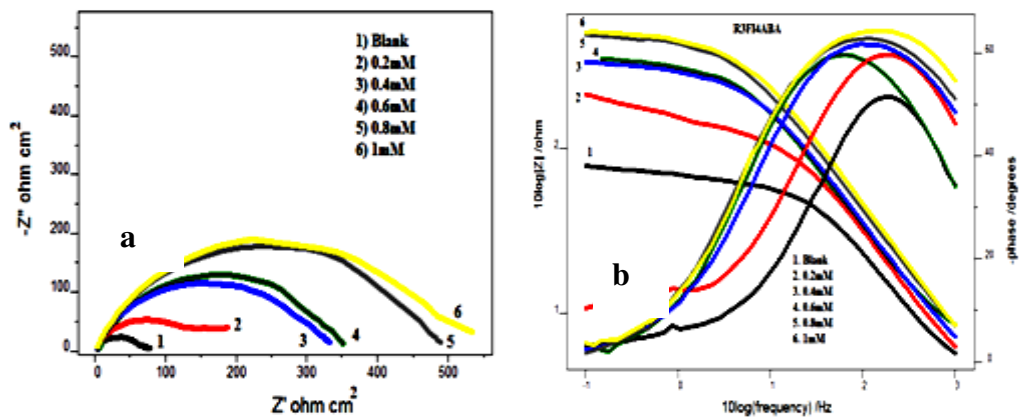


Figure 1.86: a) Nyquist plots and b) Bode plots of MS corrosion in the presence and absence of R3FI4ABA in 1M HCl

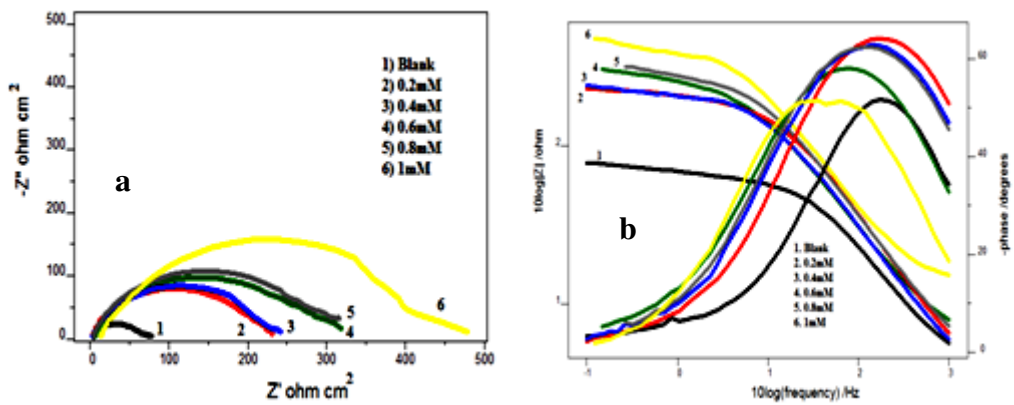


Figure 1.87: a) Nyquist plots and b) Bode plots of MS corrosion in the presence and absence of RT2C3ABA in 1M HCl

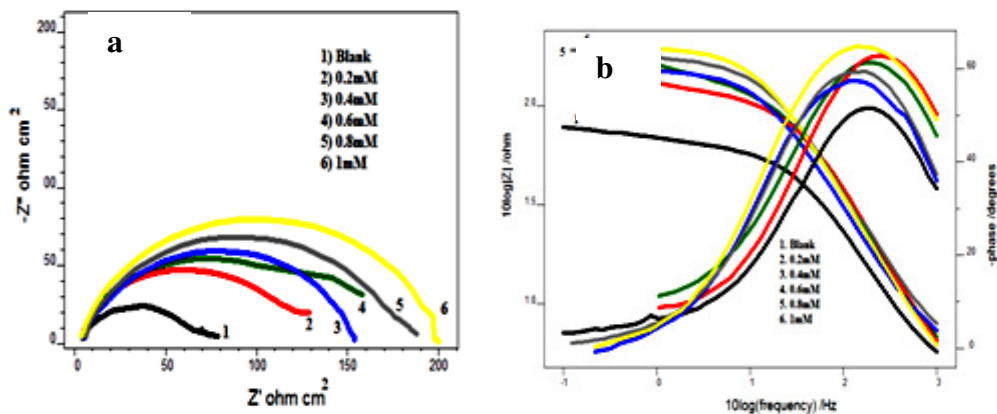


Figure 1.88: a) Nyquist plots and b) Bode plots of MS corrosion in the presence and absence of R3APTSC in 1M HCl

Potentiodynamic polarization analysis

Tafel extrapolation analysis and linear polarization studies were conducted to establish the impact of reduced Schiff base compounds towards the polarization of metal specimens by the determination of corrosion current density, polarization resistance and the percentage of inhibition efficiencies. The percentage of inhibition efficiency was calculated from the polarization resistance using the equation

$$\eta_{R_p} \% = \frac{R'_p - R_p}{R'_p} \times 100$$

where R'_p and R_p are the polarization resistance with and without inhibitor respectively. From corrosion current densities, percentage of inhibition efficiency can be derived using the relationship,

$$\eta_{pol} \% = \frac{i_{corr} - i'_{corr}}{i_{corr}} \times 100$$

where i_{corr} and i'_{corr} are uninhibited and inhibited corrosion current densities respectively.

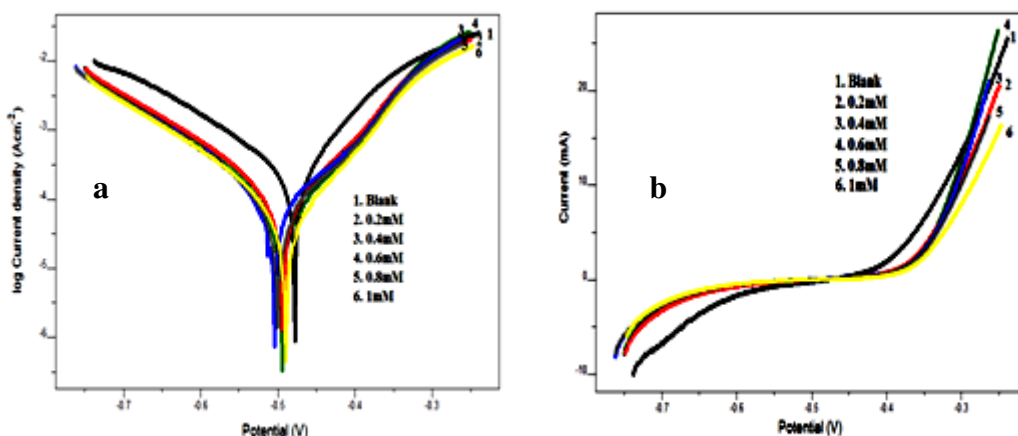


Figure 1.89: a) Tafel plots and b) linear polarization curves for MS corrosion in the presence and absence of R3FI3ABA in 1M HCl

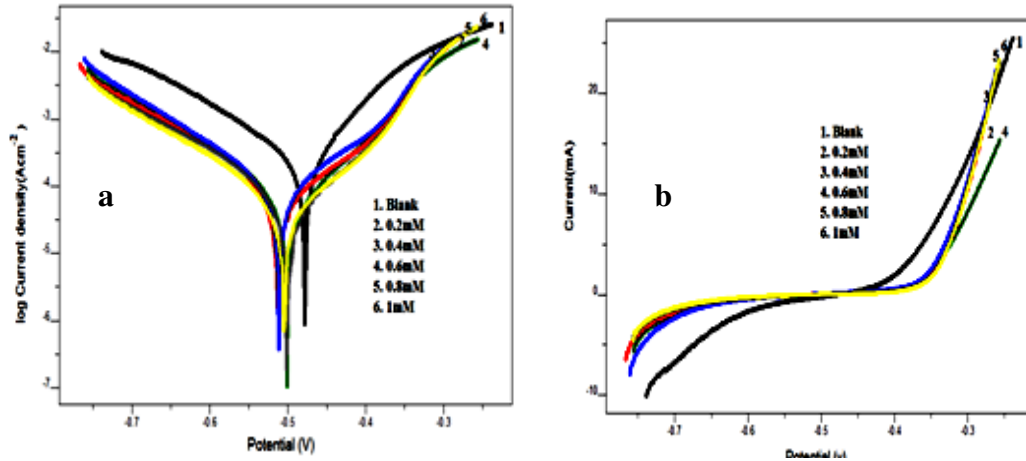


Figure 1.90: a) Tafel plots and b) linear polarization curves for MS corrosion in the presence and absence of R3FI4ABA in 1M HCl

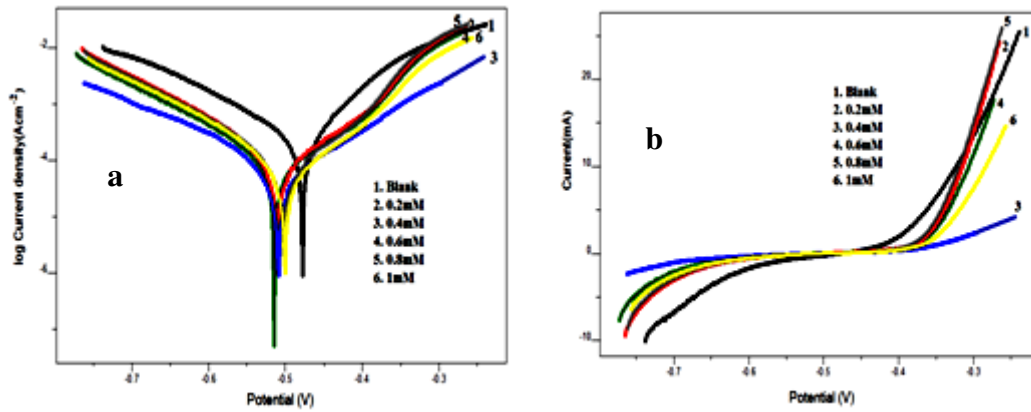


Figure 1.91: a) Tafel plots and b) linear polarization curves for MS corrosion in the presence and absence of RT2C3ABA in 1M HCl

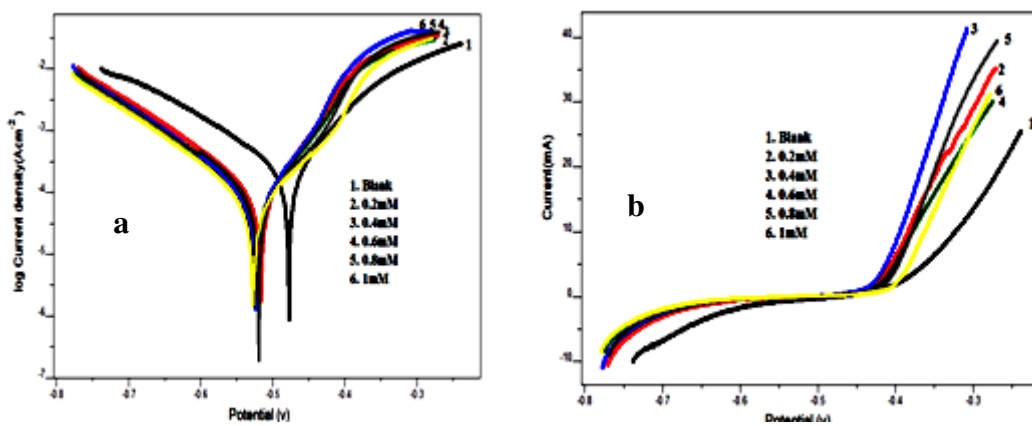


Figure 1.92: a) Tafel plots and b) linear polarization curves for MS corrosion in the presence and absence of R3APTSC in 1M HCl

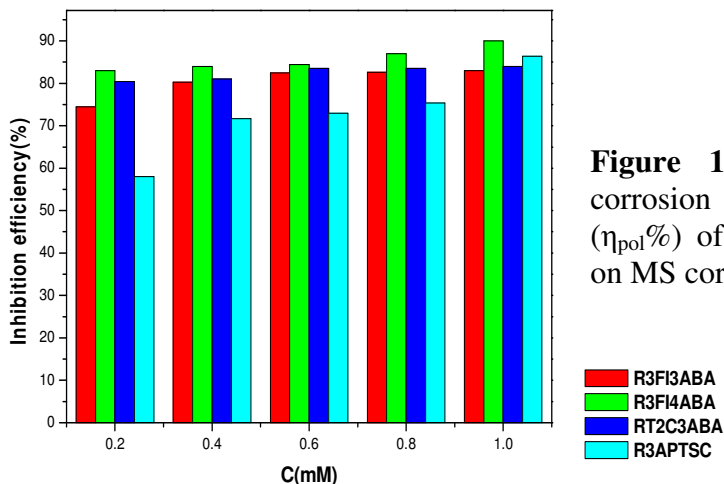


Figure 1.93: Comparison of corrosion inhibition efficiencies ($\eta_{pol}\%$) of reduced Schiff bases on MS corrosion in 1M HCl.

Tafel polarization curves and linear polarization curves obtained for the different concentrations of reduced Schiff bases are represented in the Figures 1.89 to 1.92. The corrosion parameters such as corrosion potential (E_{corr}), corrosion current density (i_{corr}), polarization resistance (R_p) and inhibition efficiency percentage ($\eta_{pol}\%$) are listed in the Table 1.22. From the Tafel data analysis it is indubitable that the corrosion current densities of MS specimen gradually reduce with the rise in concentration of reduced Schiff bases which is attributed to the fact that they can hinder the process of metal dissolution significantly by interceding either in the anodic or cathodic process of corrosion.

Investigations revealed that all the studied reduced Schiff bases displayed good inhibition efficiency in 1M HCl medium and their anodic as well as cathodic slopes (b_a and b_c) were not changed appreciably, indicated that the inhibitors are affecting equally on both anodic and cathodic sites. On comparing the results, it is clear that R3FI4ABA exhibit more efficiency than others at all concentrations. The maximum inhibition efficiency ($\eta_{pol}\%$) of 90% was achieved by R3FI4ABA at 1mM concentration. The inhibition efficiency follows the order R3FI4ABA > R3FI3ABA ~ RT2C3ABA > R3APTSC.

Table 1.22: Polarization data for MS corrosion in the presence and absence of reduced Schiff base inhibitors in 1M HCl

Reduced Schiff bases	Tafel Data					Polarization data		
	Conc (mM)	Ecorr (mV/SCE)	Icorr ($\mu\text{A}/\text{cm}^2$)	ba (mv/dec)	-bc (mV/dec)	η_{pol} %	Rp (ohm)	η_{Rp} %
R3FI3ABA	0	-498	360	122	150	-	83.23	-
	0.2	-471	91.8	79	146	74.5	241	65.4
	0.4	-504	70.7	74	143	80.3	300	72.2
	0.6	-464	62.9	79	146	82.5	317	73.7
	0.8	-499	62.7	72	141	82.6	331	75
	1	-467	61	75	142	83	349	76
R3FI4ABA	0.2	-469	60.9	8	157	83	376.8	78
	0.4	-478	57.8	79	138	84	377	78
	0.6	-468	56.1	74	150	84.4	385.4	78.4
	0.8	-457	47.2	66	161	87	431	80.6
	1	-462	36.4	66	152	90	548	85
RT2C3ABA	0.2	-471	70.4	74	139	80.4	296	71.8
	0.4	-475	68.4	110	190	81	442.5	81.2
	0.6	-475	59.4	76	144	83.5	364.9	77
	0.8	-465	59.4	64	139	83.5	320.4	74
	1	-464	56.0	74	141	84	377.9	78
R3APTSC	0.2	-532	150.8	86	128	58	147.9	44
	0.4	-527	101.7	71	123	71.7	192	57
	0.6	-524	97.2	76	129	73	213.9	61
	0.8	-507	88.5	65	131	75.4	240.5	65
	1	-497	48.8	59	126	86.4	359.1	77

Surface morphological analysis

To verify the inhibition mechanism of investigated Schiff base compounds on the MS surface, morphological studies were conducted by taking SEM images of steel surfaces. Figure 1.94 represents the SEM images of bare sample, metal immersed in 1M HCl and metal immersed in 1M HCl containing 1mM R3FI4ABA.

On close examination it was clear that the MS surface was highly corroded in blank HCl solution. But the surface damaging was appreciably decreased in the presence of R3FI4ABA, which indicates that the corrosion tendency was considerably suppressed due to the formation of a protective film of R3FI4ABA through adsorption.

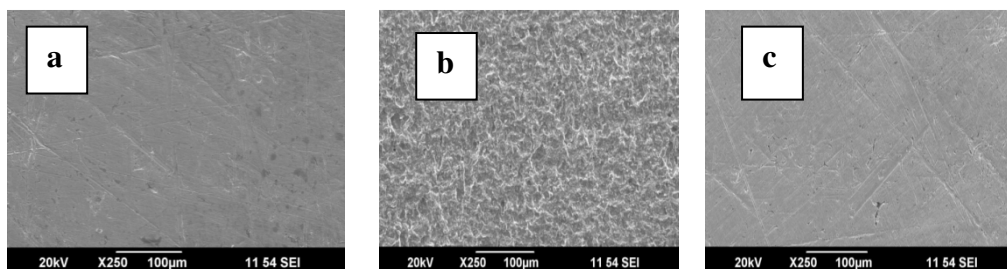


Figure 1.94: SEM images of a) bare sample b) metal immersed in 1M HCl c) metal immersed in 1M HCl containing 1mM R3FI4ABA

Quantum mechanical analysis

Quantum mechanical evaluations on the corrosion behaviour of reduced Schiff bases were carried out using DFT method by GAMMES software. Calculated quantum mechanical parameters like E_{HOMO} , E_{LUMO} , ΔE , electronegativity (χ), hardness (η) and number of transferred electrons (ΔN) for the investigated inhibitors are tabulated in the Table 1.23 and the HOMO and LUMO of the inhibitors are represented in the Figures 1.95 and 1.96 respectively.

Table 1.23: Quantum mechanical parameters of inhibitor compounds on MS

Molecule	$E_{\text{HOMO}}(\text{eV})$	$E_{\text{LUMO}}(\text{eV})$	ΔE (eV)	χ	η	ΔN
R3FI3ABA	-3.4286	1.6054	5.0340	0.9116	2.517	1.21
R3FI4ABA	-2.0136	0.1632	2.1768	0.9252	1.0884	2.79
R3APTSC	-2.6939	1.6871	4.3810	0.5034	2.1905	1.48
RT2C3ABA	-3.8912	1.2789	5.1701	1.3061	2.5850	1.10

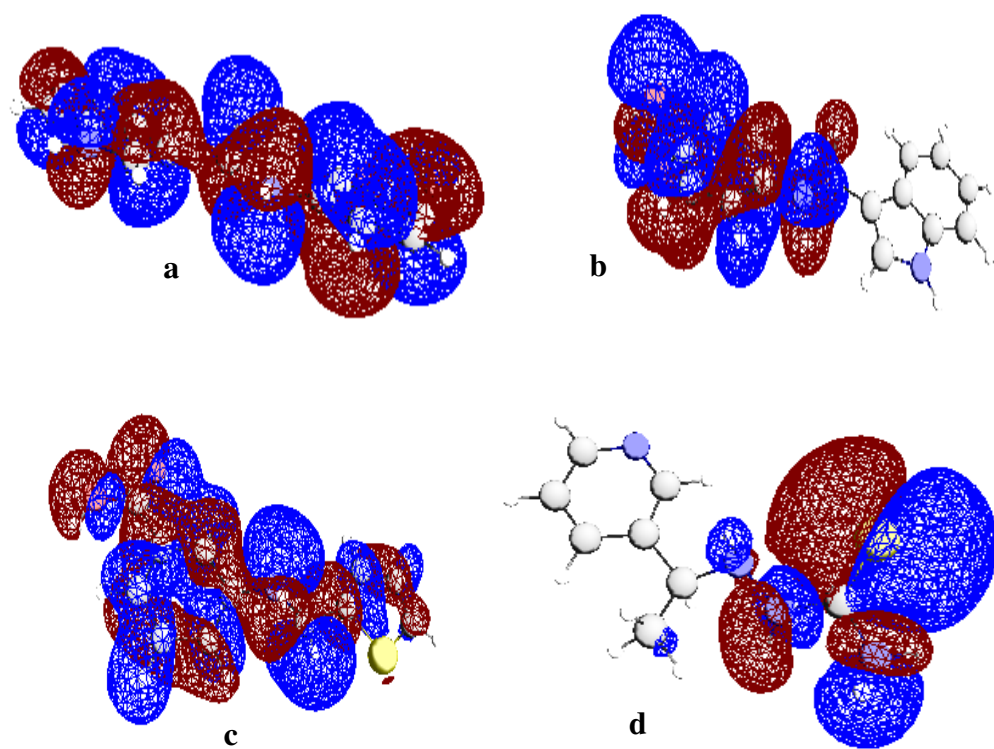


Figure 1.95: HOMO of a) R3FI3ABA b) R3FI4ABA
c) RT2C3ABA d) R3APTSC

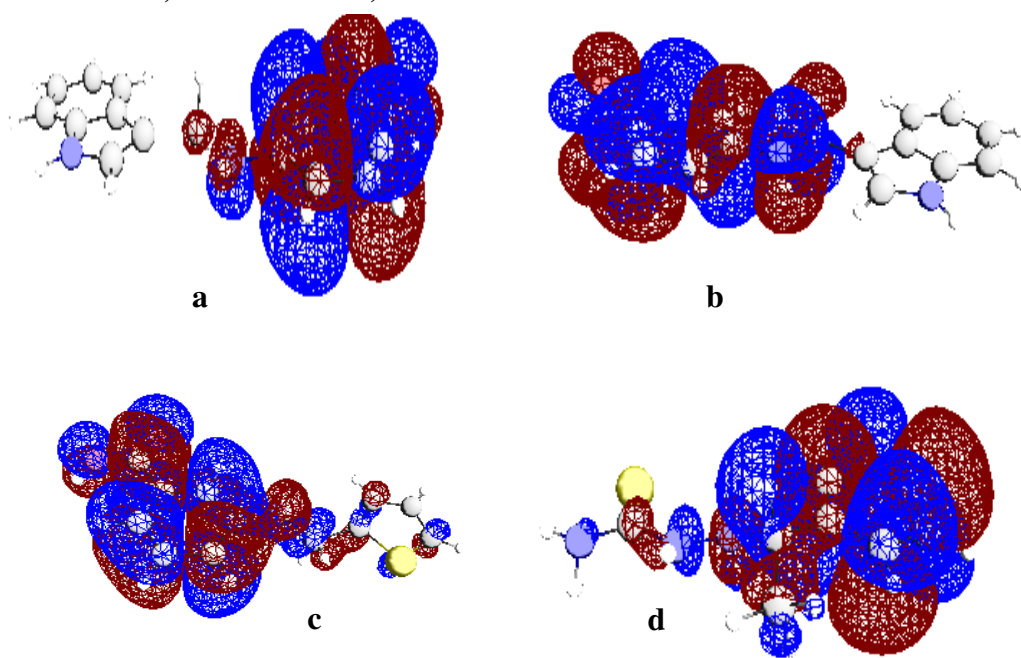


Figure 1.96: LUMO of of a) R3FI3ABA b) R3FI4ABA
c) RT2C3ABA d) R3APTSC

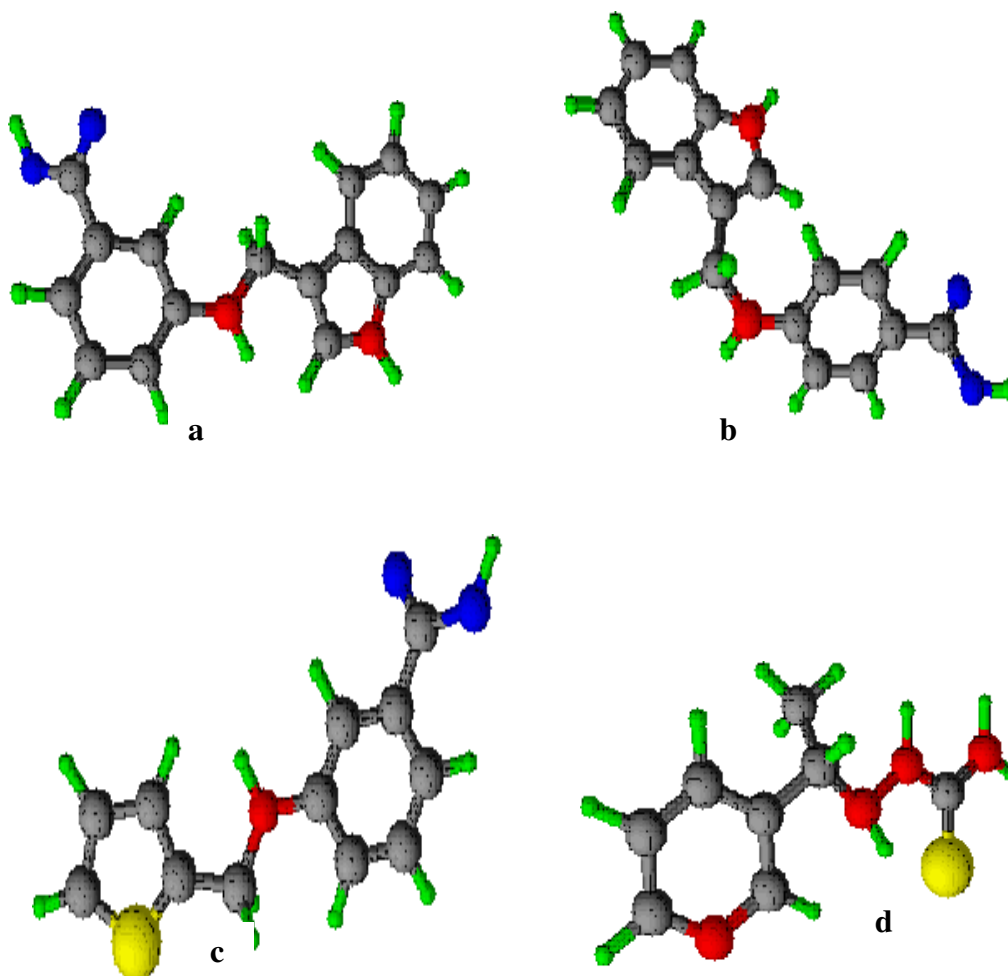


Figure 1.97: Optimized structures of a) R3FI3ABA b) R3FI4ABA c) RT2C3ABA d) R3APTSC

The ΔE between HOMO and LUMO is comparably lower for the compounds R3FI4ABA and R3APTSC than others, which imply that they have predominant corrosion inhibition efficiency. These data indicate that the energy required to move electrons from HOMO of these inhibitors to the vacant orbitals of Fe is very low. The ΔN from donor to acceptors are also evaluated from these quantum mechanical parameters which provide the information about interaction with the metal atoms. Optimized geometries of reduced Schiff bases are represented in the Figure 1.97.

SECTION 3

CORROSION BEHAVIOUR OF MILD STEEL IN THE PRESENCE OF REDUCED SCHIFF BASES IN 0.5M H₂SO₄

The corrosion inhibition behaviour of four reduced Schiff bases R3FI3ABA, R3FI4ABA, RT2C3ABA and R3APTSC were studied in 0.5M H₂SO₄ using the inhibitor solutions of the concentration range 0.2mM-1mM.

Gravimetric analysis

Weight loss analysis of mild steel was performed by immersing metal coupons of 1cm² area in 0.5M H₂SO₄ solution for 24 hour with and without the reduced Schiff bases at different concentrations and analysing them in order to study the effect of reduced Schiff bases on corrosion inhibition. The corrosion rate in mmy⁻¹ and percentage of inhibition efficiencies of reduced Schiff bases are represented in the Tables 1.24 and 1.25 respectively. The data was compared with the help of plots and are given in Figures 1.98 and 1.99 respectively.

Table 1.24: Corrosion rates of MS in the presence and absence of reduced Schiff bases in 0.5M H₂SO₄

Conc (mM)	Corrosion rate (mmy ⁻¹)			
	R3FI3ABA	R3FI4ABA	RT2C3ABA	R3APTSC
0	16.26	16.26	16.26	16.26
0.2	20.92	18.01	9.649	7.511
0.4	8.919	9.595	9.215	4.995
0.6	6.671	6.150	6.339	3.827
0.8	4.893	5.968	5.216	3.374
1	4.474	4.972	3.287	3.320

From the Figures 1.98 and 1.99, it is evident that the rate of corrosion of MS specimen in 0.5M H₂SO₄ medium in the presence and absence of reduced Schiff bases decreases significantly. In contrary to our expectation, the MS specimen immersed in H₂SO₄ with RT2C3ABA and R3APTSC showed higher inhibition efficiency than indole derivatives. This observation was not similar with the result obtained in HCl medium, where indole derivatives exhibited prominent inhibition efficiency in HCl medium as compared to others.

Table 1.25: Inhibition efficiency of MS in the presence and absence of reduced Schiff bases in 0.5M H₂SO₄

Conc (mM)	Inhibition efficiency (%)			
	R3FI3ABA	R3FI4ABA	RT2C3ABA	R3APTSC
0.2	-28.65	-10.75	40.65	53.80
0.4	45.15	40.99	43.32	69.27
0.6	58.97	62.17	61.01	76.46
0.8	69.90	63.29	67.92	79.24
1	72.48	69.42	79	79

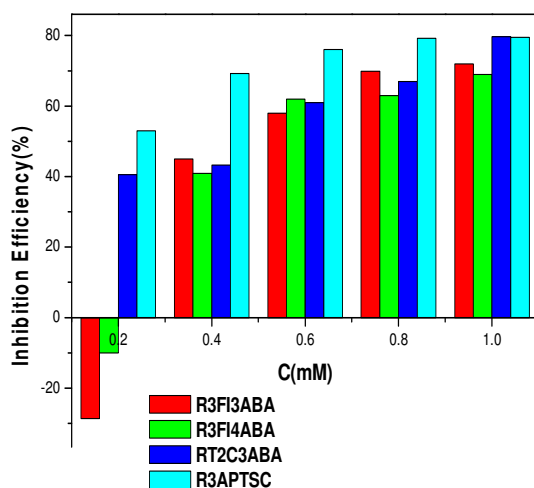


Figure 1.98: Comparison of corrosion inhibition efficiency of MS with different concentration of reduced Schiff bases in 0.5M H₂SO₄ for 24 hours

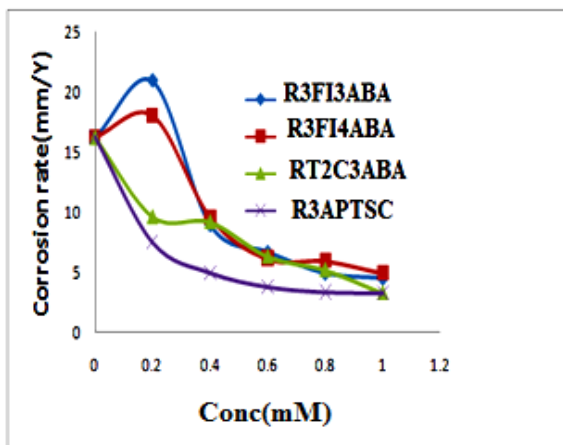


Figure 1.99: Change of corrosion rates of MS with different concentration of reduced Schiff bases in 0.5M H₂SO₄ for 24 hours

Following generalizations were derived on critical analysis of the results,

- All the reduced Schiff bases under examination are not acting as highly potential inhibitors and displayed only a moderate inhibition efficiency at all concentrations in 0.5M H₂SO₄.
- R3FI3ABA and R3FI4ABA have an antagonistic nature in 0.2mM concentration, and efficiency increased with increase in concentration.
- At all concentrations R3APTSC inhibited more effectively than others.
- R3FI4ABA exhibited relatively minimum efficiency and RT2C3ABA and R3APTSC displayed maximum efficiency of 79% at 1mM concentration.
- At 1mM concentration the inhibition efficiency of studied reduced Schiff bases followed the order R3FI4ABA < R3FI3ABA < RT2C3ABA ~ R3APTSC

Adsorption studies

The inhibition mechanism of reduced Schiff bases is mainly explained by the adsorption process and the mechanism can be easily described by suitable adsorption isotherms. The adsorption parameters can be evaluated by the selection of the best fit isotherm model with the assistance of correlation coefficient (R^2). Figures 1.100 to 1.103 represent the adsorption isotherms for R3FI3ABA,

R3FI4ABA, RT2C3ABA and R3APTSC respectively in 0.5M H₂SO₄. From the attempt of various isotherms, the adsorption behaviour of R3FI3ABA and R3FI4ABA can be described by Temkin isotherm while that of RT2C3ABA follows Freundlich isotherm. Langmuir adsorption isotherm is found best for R3APTSC.

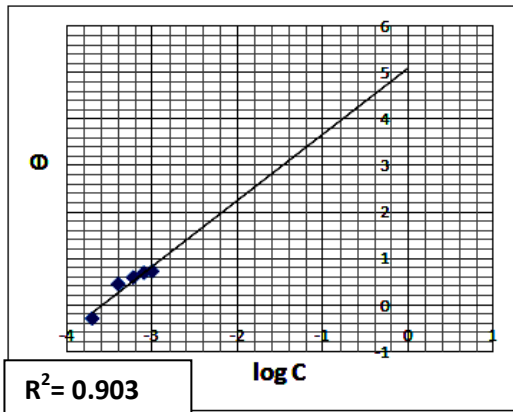


Figure 1.100: Temkin isotherm for R3FI3ABA on MS in 0.5M H₂SO₄

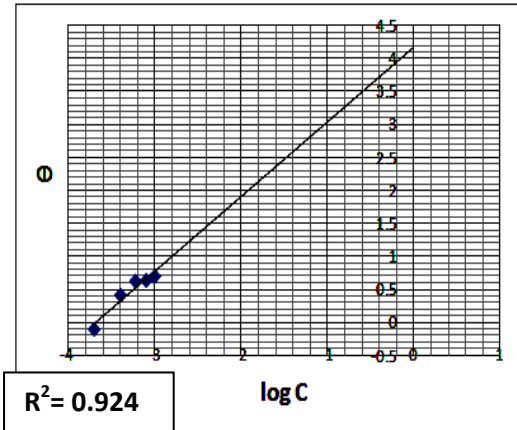


Figure 1.101: Temkin isotherm for R3FI4ABA on MS in 0.5M H₂SO₄

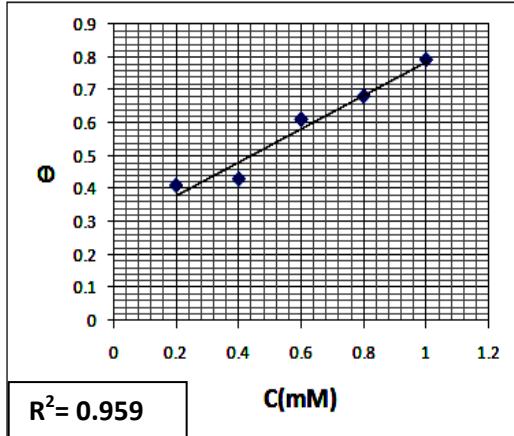


Figure 1.102: Freundlich isotherm for RT2C3ABA on MS in 0.5M H₂SO₄

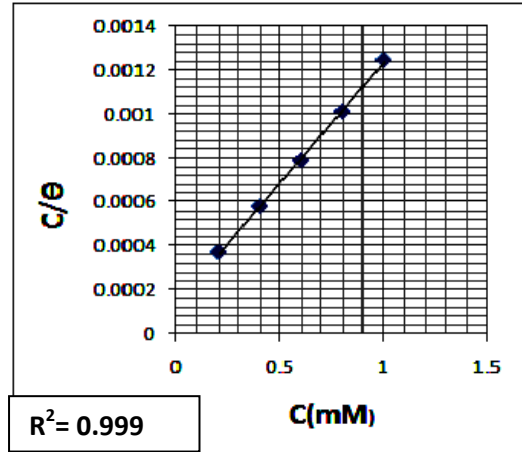


Figure 1.103: Langmuir isotherm for R3APTSC on MS in 0.5M H₂SO₄

The adsorption equilibrium constant K_{ads} is a measure of the amount of adsorption taking place on the metal surface. The Table 1.26 indicates that R3APTSC has comparatively high K_{ads} value than others suggesting that R3APTSC is adsorbed more efficiently on metal surface. ΔG^0_{ads} for all studied reduced Schiff bases have negative values showing the spontaneity of the process. In the present study, the compounds have ΔG^0_{ads} value between -39kJmol^{-1} and -33kJmol^{-1} revealing that the adsorption process involves both physisorption and chemisorption.

Table 1.26: Adsorption parameters of reduced Schiff bases for the adsorption on MS surface in 0.5M H_2SO_4

Adsorption parameter	R3FI3ABA	R3FI4ABA	RT2C3ABA	R3APTSC
K_{ads}	126473	14757	505	100000
$\Delta G^0_{ads}(\text{kJ/mol})$	-39.47	-34.09	-29.45	-33.12

Electrochemical corrosion investigations

Electrochemical investigations were carried out by using a three electrode system, which consists of saturated calomel electrode (SCE) as reference electrode, platinum electrode of 1cm^2 area as counter electrode and mild steel specimen with an area of 1cm^2 as working electrode. Electrochemical investigations include AC impedance analysis and potentiodynamic polarization studies which were performed by using Ivium Compactstat-e electrochemical system.

EIS analysis

The corrosion behaviour of MS in 0.5M H_2SO_4 in the presence and absence of inhibitor was studied using impedance spectroscopic analysis at 30°C . Figures 1.104 to 1.107 represent the Nyquist plots and Bode plots of reduced Schiff bases R3FI3ABA, R3FI4ABA, RT2C3ABA and R3APTSC respectively. The impedance parameters such as solution resistance (R_s), charge transfer resistance (R_{ct}), double

layer capacitance (C_{dl}) and inhibition efficiency percentage ($\eta_{EIS\%}$) were evaluated from the values of R_{ct} and are represented in the Table 1.27. The inhibition efficiency percentage was evaluated from R_{ct} values using the following equation.

$$\eta_{EIS\%} = \frac{R_{ct} - R'_{ct}}{R_{ct}} \times 100$$

where R_{ct} and R'_{ct} are the charge transfer resistances of working electrode in the presence and absence of inhibitor respectively.

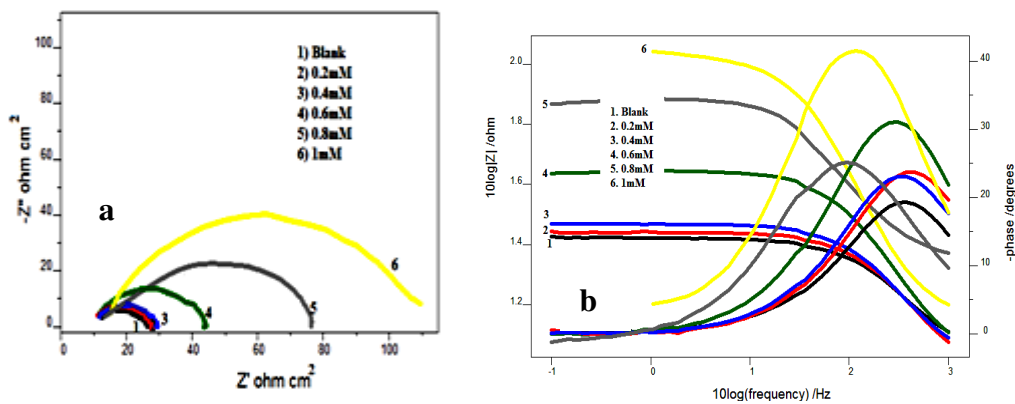


Figure 1.104: a) Nyquist plots and b) Bode plots of MS corrosion in the presence and absence of R3FI3ABA in 0.5M H₂SO₄

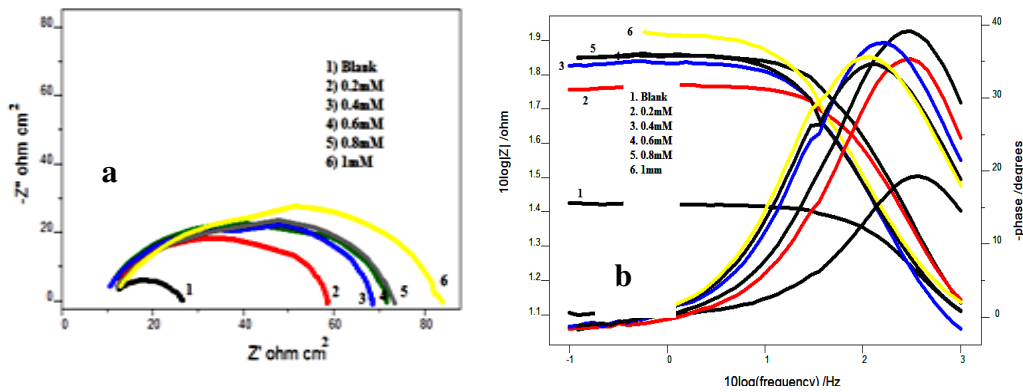


Figure 1.105: a) Nyquist plots and b) Bode plots of MS corrosion in the presence and absence of R3FI4ABA in 0.5 M H₂SO₄

From the above data, we can conclude the following points:

- 1) All studied reduced Schiff bases showed relatively lower inhibition efficiency.

- 2) Even if R3FI3ABA showed poor efficiency at lower concentrations, it displayed eminent efficiency at higher concentrations.
- 3) Among the reduced Schiff bases studied, R3APTSC showed comparatively good efficiency at all concentrations and displayed maximum efficiency of 92% at 1mM concentration.

These observations are in good agreement with the results obtained from gravimetric analysis for 24 h.

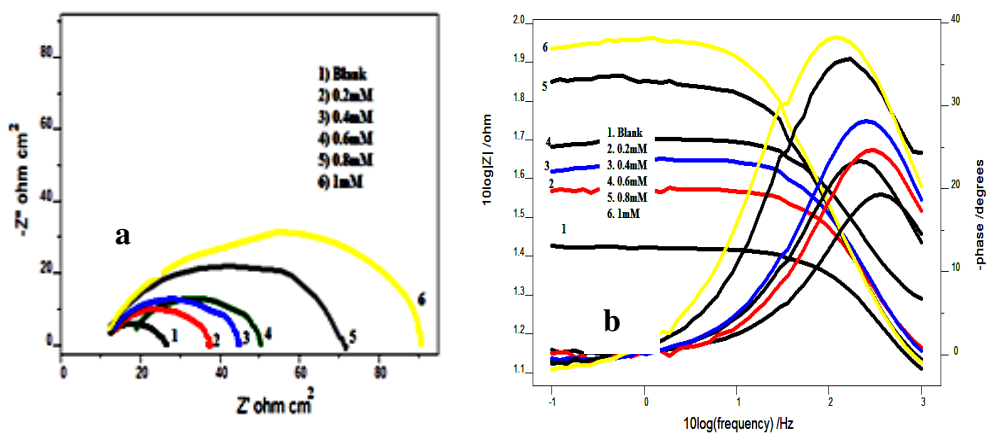


Figure 1.106: a) Nyquist plots and b) Bode plots of MS corrosion in the presence and absence of RT2C3ABA in 0.5M H₂SO₄

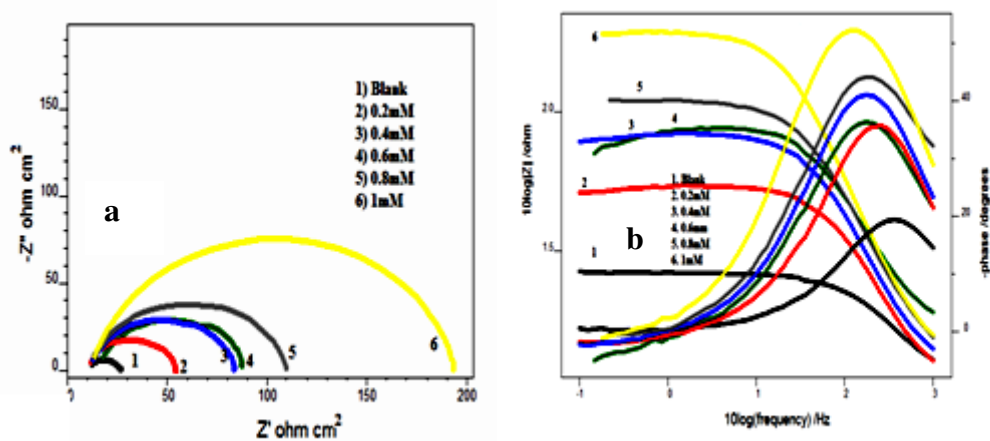


Figure 1.107: a) Nyquist plots and b) Bode plots of MS corrosion in the presence and absence of R3APTSC in 0.5M H₂SO₄

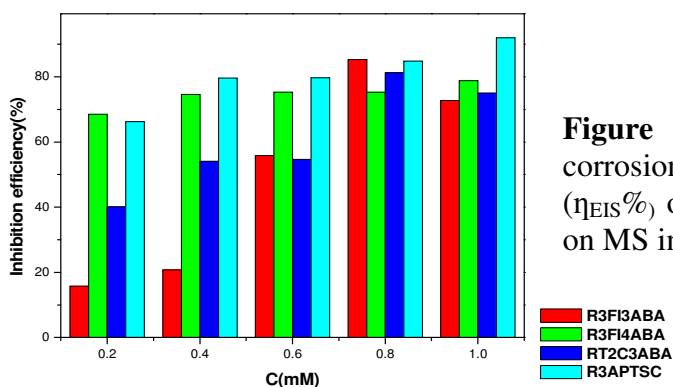


Figure 1.108: Comparison of corrosion inhibition efficiencies ($\eta_{EIS}\%$) of reduced Schiff bases on MS in 0.5M H_2SO_4

Table 1.27: Electrochemical impedance data of MS corrosion in the presence and absence of reduced Schiff bases in 0.5M H_2SO_4

Reduced Schiff base	Conc (mM)	R_{ct} (Ωcm^2)	C_{dl}	η_{EIS} %
	0	13.3	67.1	-
R3FI3ABA	0.2	15.8	53.9	15.8
	0.4	16.8	60.3	20.8
	0.6	30.1	49.5	55.8
	0.8	90.7	53	85.3
	1	48.8	77.7	72.7
R3FI4ABA	0.2	42.3	41.7	68.50
	0.4	52.4	71.3	74.6
	0.6	53.9	40.8	75.3
	0.8	54	82.1	75.3
	1	62.8	79.4	78.8
RT2C3ABA	0.2	22.2	52.6	40.1
	0.4	29	52.7	54.1
	0.6	29.4	53.3	54.7
	0.8	71.2	72.8	81.3
	1	53.3	66.4	75.0
R3APTSC	0.2	39.5	46.5	66.3
	0.4	65.4	38.7	79.6
	0.6	65.5	44.2	79.7
	0.8	87.7	38.7	84.8
	1	167	35.7	92.0

Potentiodynamic polarization analysis

Tafel extrapolation analysis and linear polarization studies were conducted to establish the impact of reduced Schiff base compounds towards the polarization of metal specimens by the determination of corrosion current density, polarization resistance and the percentage of inhibition efficiencies. The inhibition efficiency percentage was calculated from the polarization resistance using the equation

$$\eta_{R_p} \% = \frac{R'_p - R_p}{R'_p} \times 100$$

where R'_p and R_p are the polarization resistance with and without inhibitor respectively. From corrosion current densities, the percentage of inhibition efficiency can be calculated by the expression,

$$\eta_{pol} \% = \frac{i_{corr} - i'_{corr}}{i_{corr}} \times 100$$

where i_{corr} and i'_{corr} are uninhibited and inhibited corrosion current densities respectively. Tafel polarization curves and linear polarization curves obtained for the different concentrations of reduced Schiff bases are represented in the Figures 1.109 to 1.112 and the corrosion parameters such as corrosion current density (i_{corr}), corrosion potential (E_{corr}), polarization resistance (R_p) and inhibition efficiency percentage ($\eta_{pol} \%$) are listed in the Table 1.28

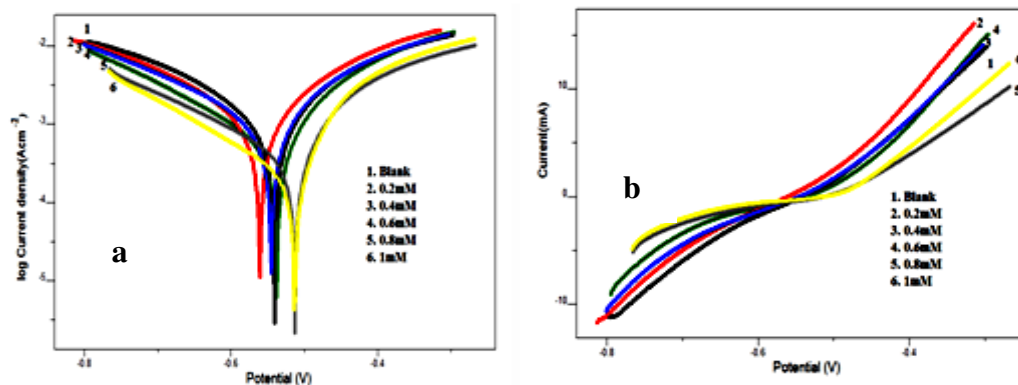


Figure 1.109: a) Tafel plots and b) linear polarization curves for MS corrosion in the presence and absence of R3FI3ABA in 0.5M H₂SO₄

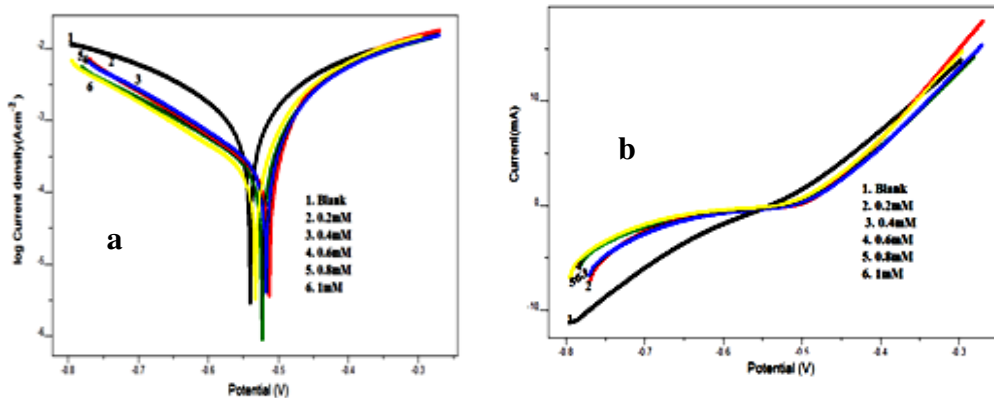


Figure 1.110: a) Tafel plots and b) linear polarization curves for MS corrosion in the presence and absence of R3FI4ABA in 0.5M H₂SO₄

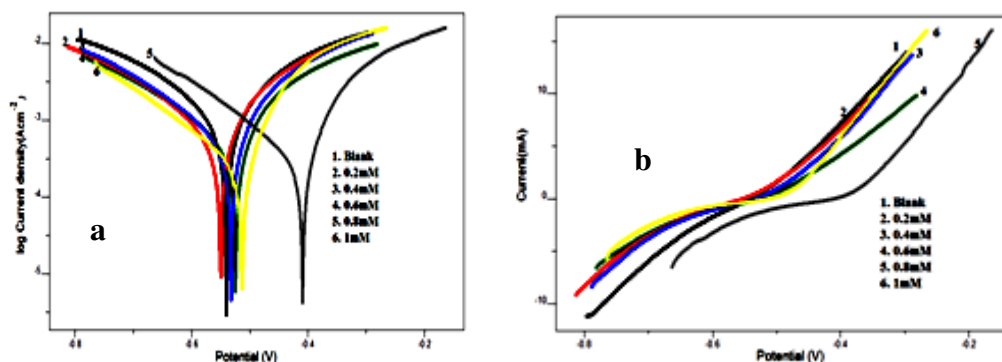


Figure 1.111: a) Tafel plots and b) linear polarization curves for MS corrosion in the presence and absence of RT2C3ABA in 0.5M H₂SO₄

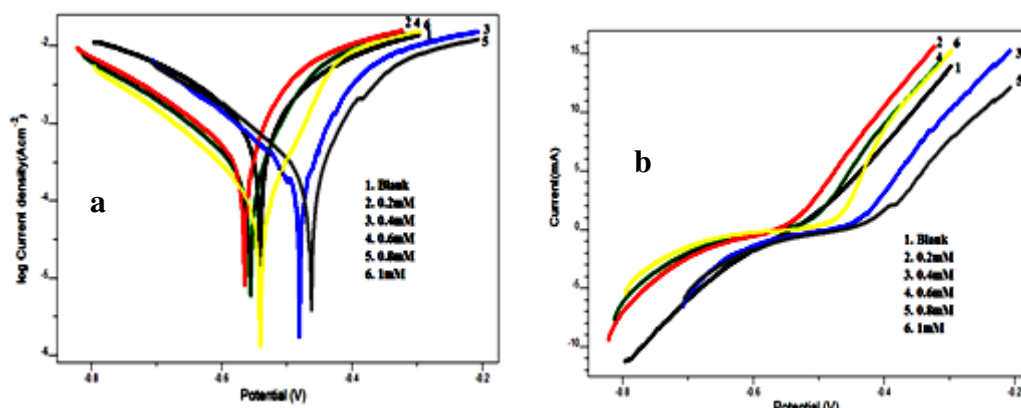


Figure 1.112: a) Tafel plots and b) linear polarization curves for MS corrosion in the presence and absence of R3APTSC in 0.5M H₂SO₄

The Tafel data represented in the Table 1.28 reveals that all studied reduced Schiff bases displayed moderate inhibition efficiency in 0.5M H₂SO₄ at all concentrations.

Table 1.28: Polarization data for MS corrosion in the presence and absence of reduced Schiff bases in 0.5M H₂SO₄

Reduced Schiff Bases	Tafel Data					Polarization data		
	Conc (mM)	E _{corr} (mV/SCE)	I _{corr} (μA/cm ²)	b _a (mv/dec)	-b _c (mV/dec)	η _{pol} %	R _p (ohm)	η _{RP} %
R3FI3ABA	0	-560	1468	236	232	-	34.62	-
	0.2	-571	1386	212	235	5	34.9	1
	0.4	-568.9	1242	224	238	15	40.35	14
	0.6	-575.2	817	195	202	44	52.81	34
	0.8	-573.1	681	233	223	54	72.59	52
	1	-594.7	558	217	185	62	77.82	56
R3FI4ABA	0.2	-605	688	215	164	53	58.5	41
	0.4	-592.9	648	209	172	56	63.29	45
	0.6	-599.1	591	206	187	60	71.96	52
	0.8	-599.1	533	189	167	64	72.21	52.1
	1	-602.9	487	184	168	67	78.43	56
RT2C3ABA	0.2	-580.5	963	216	176	34	48.67	29
	0.4	-572.6	871	213	200	41	51.38	33
	0.6	-566.9	800	235	215	46	58.57	41
	0.8	-479	717	208	180	51	61.02	43
	1	-589.8	667	205	183	55	62.87	45
R3APTSC	0.2	-639.7	1108	244	184	24	41.12	16
	0.4	-570.8	907	257	156	38	46.5	25
	0.6	-619	684	197	176	53	58.91	41x
	0.8	-514.7	563	192	177	62	71.02	51
	1	-594.2	308	140	154	79	103.7	67

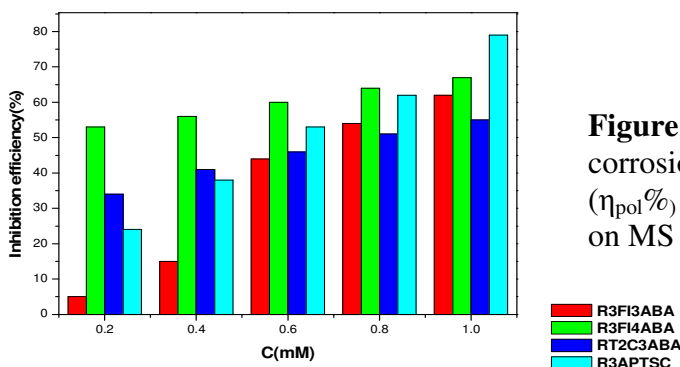


Figure 1.113: Comparison of corrosion inhibition efficiencies (η_{pol}%) of reduced Schiff bases on MS in 0.5M H₂SO₄

Among the reduced Schiff bases studied, R3APTSC showed comparatively good efficiency at all concentrations and displayed maximum efficiency of 79% at 1mM concentration. R3FI3ABA is almost inactive at lower concentrations and exhibited higher efficiency at higher concentration. The inhibition efficiency follows the order RT2C3ABA < R3FI3ABA < R3FI4ABA < R3APTSC.

For all reduced Schiff bases the anodic and cathodic slopes were not changed appreciably which established that the inhibitor molecules are equally affecting on both cathodic and anodic sites. Furthermore if the E_{corr} value didn't alter (>85) with respect to E_{corr} of blank experiment with the appreciable change in anodic or cathodic slopes, the inhibitor can be considered as cathodic or anodic type. In the present investigation the maximum shift of E_{corr} was not greater than 85 for all cases, suggesting that investigated reduced Schiff bases act as mixed type inhibitors for MS in 0.5M H_2SO_4 .

Electrochemical noise analysis

Electrochemical noise (ECN) measurements were performed using a three-electrode cell system, which consists of two carbon steel electrodes of 1 cm^2 area used as working electrode as well as counter electrode and SCE as reference electrode. All ECN analyses were performed for a period of 1200seconds using Ivium Compactstat-e electrochemical system controlled by Iviumsoft software.

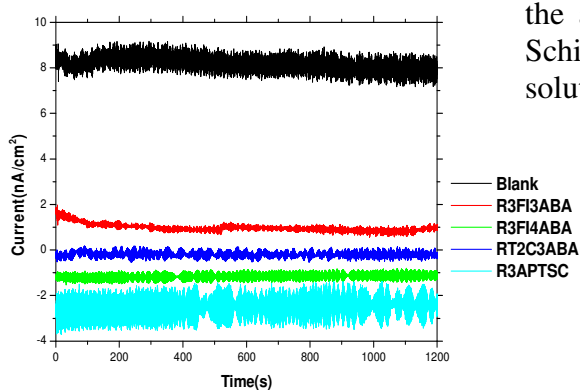


Figure 1.114: Noise current for MS in the absence and presence of reduced Schiff bases (1mM) in 0.5M H_2SO_4 solution.

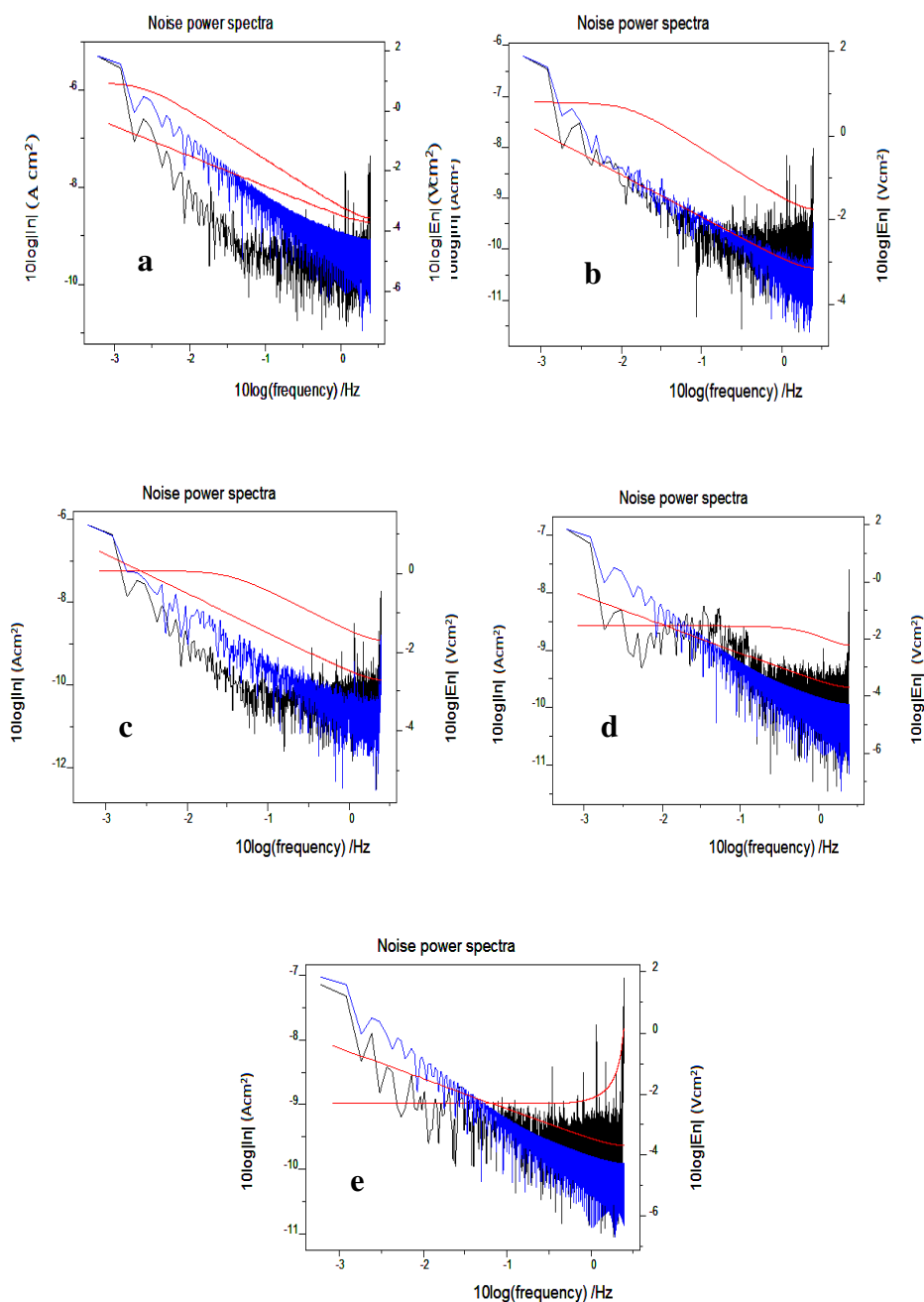


Figure 1.115: PSD curve of MS in **a)** blank **b)** R3FI3ABA **c)** R3FI4ABA **d)** RT2C3ABA **e)** R3APTSC

Figure 1.114 represents the noise current of metal specimen immersed in the acid solution with and without reduced Schiff base compounds. From this figure it is clear that the noise current in the presence of reduced Schiff base compounds have very low value than the blank metal specimen, which indicates corrosion protective power of reduced Schiff base compounds.

Pitting index or Pitting resistance equivalent number (PREN) is the measurement of resisting power to localized pitting corrosion. On analysing the pitting index curves represented in the Figure 1.116, it is quite evident that the amplitude of pitting index curves corresponding to the blank metal specimen is lower than the metal specimen treated with reduced Schiff base containing solution.

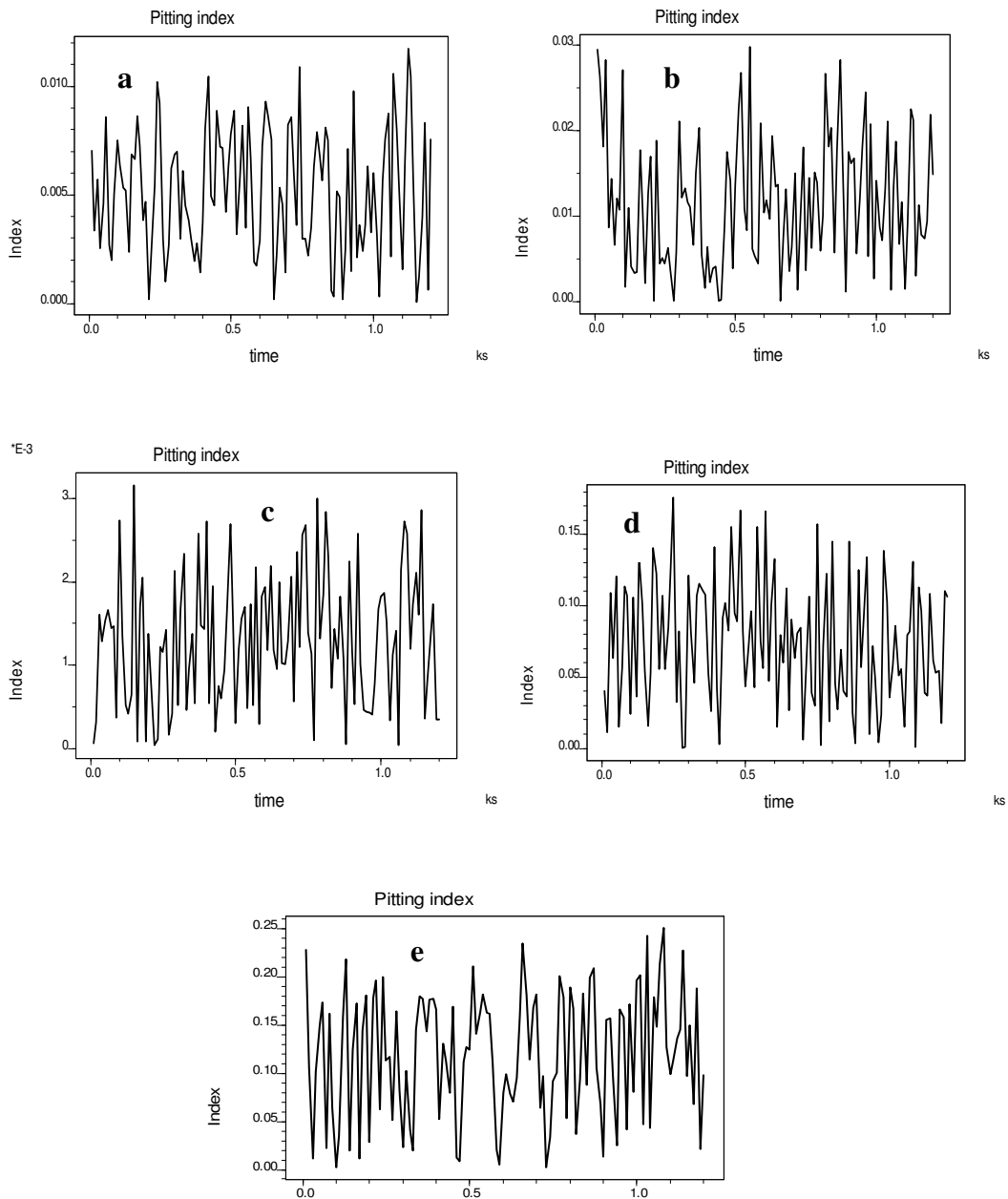


Figure 1.116: Pitting index curves of MS in a) blank b) R3FI3ABA c) R3FI4ABA d) RT2C3ABA e) R3APTSC

The frequency domain analysis of noise measurement gave the PSD (Power Spectral Density) of different systems, which is represented in the Figure 1.115. On close examination of PSD plots, it is understood that at all frequencies, the values of current noise are comparatively large for blank metal specimen than the metal dipped in the acid solution in the presence of R3FI3ABA, R3FI4ABA, RT2C3ABA and R3APTSC which is a clear implication of the occurrence of localized corrosion on MS surface in the absence of reduced Schiff base compounds.

SUMMARY

Heterocyclic Schiff bases such as 2APPH and 2APSC (derived from 2-acetylpyridine) and reduced Schiff bases R3FI3ABA, R3FI4ABA, R3APTSC and RT2C3ABA (derived from 3-formylindole, 3-acetylpyridine and thiophene-2-carbaldehyde) have been synthesized and characterized by spectral investigations and are well documented in this part.

Investigations on the efficiency of corrosion inhibition of the synthesized Schiff bases and reduced Schiff bases on mild steel in HCl medium and H₂SO₄ medium were performed by different corrosion monitoring methods such as gravimetric analysis, electrochemical investigations like polarization analysis, electrochemical impedance spectroscopic method and electrochemical noise measurement. All Schiff base derivatives under examination exhibited considerable corrosion inhibition efficiency on MS in acidic media. The corrosion inhibition mechanism of the compounds was confirmed by adsorption studies and surface morphological analysis. The effect of temperature and time on the corrosion inhibition efficiency of the compounds was also established. Quantum mechanical investigations using GAMMESS software was also performed.

All the studied Schiff bases and reduced Schiff bases displayed predominant corrosion inhibition efficiency on MS in 1M HCl medium. According to the gravimetric analysis, corrosion inhibition efficiency of the studied compounds followed the order 2APSC < 2APPH < R3APTSC < RT2C3ABA < R3FI3ABA < R3FI4ABA. For some compounds, the results obtained from gravimetric analysis slightly varied from electrochemical investigations. The higher efficiencies of 2APPH, R3FI3ABA, R3FI4ABA and RT2C3ABA were explained by the presence

of two aromatic ring systems in the molecule. The higher inhibition efficiency of RTC3ABA and R3APTSC were attributed to the presence of more polarisable sulphur atom and the resulting strong interaction on the metal surface. All studied compounds obeyed Langmuir adsorption isotherm on MS surface. Effect of time and temperature on inhibition efficiency was studied in 1M HCl in the presence of Schiff base derivatives. The inhibition efficiency of reduced Schiff bases didn't have appreciable change with respect to that of parent Schiff base compounds as the days progressed which was explained by the fact that the reduced form of Schiff bases were free from the azomethine moiety and were not susceptible to the hydrolysis process and showed eminent inhibition efficiency for days. These results derived to the conclusion that reduced Schiff base compounds have prolonged corrosion inhibition efficiency. All the studied Schiff base derivatives form a protective barrier on MS surface and resist the metallic disintegration appreciably, which was evident from surface morphological analysis.

In H_2SO_4 medium, these compounds have not exhibited prominent good inhibition efficiency and displayed only a moderate efficiency at all concentrations. In gravimetric analysis R3APTSC inhibits MS corrosion more effectively than other compounds. R3FI3ABA and R3FI4ABA possess an antagonistic nature in 0.2mM concentration, and efficiency increases with increase in concentration. In contrary to the behaviour in HCl medium, R3FI4ABA and 2APPH exhibit minimum efficiency and RT2C3ABA and R3APTSC displayed maximum efficiency at 1mM concentration. EIS and Tafel analysis were also performed to verify the response of inhibitors for 30 minutes and the results were not in good agreement with the data obtained from gravimetric analysis (24 hr). Langmuir isotherms were obtained for

2APPH, 2APSC and R3APTSC. R3FI3ABA and R3FI4ABA obeyed Temkin isotherm and Freundlich isotherm was followed by RT2C3ABA.

On comparison of the activities of the inhibitors in two aqueous acidic media say 1M HCl and 0.5M H₂SO₄, they exhibited different anticorrosion activities. All the reduced Schiff bases displayed moderate inhibition efficiency in H₂SO₄ whereas in HCl medium they acted as potential corrosion inhibitors. Moreover, in HCl medium, Schiff bases derived from indole derivatives exhibited remarkably higher corrosion inhibition efficiency, compared to other compounds. But this trend was not observed in H₂SO₄ medium. In contrary to the behaviour in 1M HCl medium, R3FI4ABA exhibited minimum efficiency whereas RT2C3ABA and R3APTSC displayed maximum efficiency in 0.5M H₂SO₄ medium.

Quantum mechanical parameters like E_{HOMO} , E_{LUMO} , ΔE , electronegativity (χ), hardness (η) and number of transferred electrons (ΔN) for the inhibitors are established using quantum mechanical software GAMMESS. The ΔE between HOMO and LUMO is comparably lower for the compounds, which imply that they have predominant corrosion inhibition efficiency.

The inhibition action of the molecules was further examined by electrochemical noise measurement and surface morphological analysis.

REFERENCES

1. L. Boulané Petermann, *The Journal of Bioadhesion and Biofilm Research*, 10 (1996) 275-300
2. J. F. Chen, W. F. Bogaerts, *Corrosion*, 52 (1996) 753-759.
3. H. Hoche, C. Rosenkranz, A. Delpa, M. Lohrengel, E. Broszeit, C. Bergera, *Surface and Coatings Technology*, (2005) 178-184.
4. Guangling Song, Birgir Johannesson, Sarath Hapugoda, David St John, *Corrosion Science*, 46, (2004) 955-977.
5. L. Rosenfeld, I. K. Marshakov, *Corrosion*, 64 (1964) 115-125.
6. Z. Szklarska-Smialowska, *Corrosion Science*, 41 (1999) 1743-1767.
7. L. Lapeire, E. M. Lombardia, K. Verbeken, I. De Graeve, *Corrosion Science*, 67 (2013) 179-183.
8. Pietro. Pedferri, *Construction and Building Materials*, 10 (1996) 391-402.
9. P. Singh, M. A. Quraishi, *Measurement*, 86 (2016) 114–124.
10. N. Birbilis, G. Williams, K. Gusieva, A. Samaniego, M. A. Gibson, H. N. Mc Murray, *Electrochemistry Communications*, 34 (2013) 295-298.
11. E. H. Cordes, W. P. Jencks, *Journal of American Chemical Society*, 84 (1962) 832–833
12. E. E. Elemike, D. C. Onwudiwe, H. U. Nwankwo, E. C. Hosten, *Journal of Molecular Structure*, 1136 (2017) 253–262.
13. A. Aouniti, H. Elmsellem, S. Tighadouini, *Journal of Taibah University for Science*, 10 (2016) 774–785.
14. H. Heydari, M. Talebian, Z. Salarvand, K. Raeissi, *Journal of Molecular Liquids*, 254 (2018) 177–187.

15. S. N. Pandeya, D. Sriram, G. Nath, E. De Clercq, *Pharmaceutica Acta Helvetica*, 74 (1999) 11-17.
16. M. S. Karthikeyan, D. J. Prasad, B. Poojary, K. S. Bhat, *Bioorganic & Medicinal Chemistry*, 14 (2006) 7482–7489.
17. R. Xing, S. Liu, Z. Guo, H. Yu, P. Wang, *Bioorganic and Medicinal Chemistry*, 13 (2005) 1573–1577.
18. C. M. Da Silva, L. V. Modolo, R. B. Alves, *Journal of Advanced Research*, 2 (2011) 1–8.
19. S. N. Pandeya, D. Sriram, G. Nath, E. De Clercq, *European Journal of Pharmaceutical Sciences*, 9 (1999) 25–31.
20. H. Ullah, A. Wadood, F. Khan, M. T. Javid, M. Taha, *Bioorganic Chemistry*, 78 (2018) 17–23.
21. M. Taha, M. Arbin, N. Ahmat, S. Imran, F. Rahim, *Bioorganic Chemistry*, 77 (2018) 47–55.
22. A. Fattah-alhosseini, M. Noori, *Measurement*, 94 (2016) 787–793.
23. D. K. Singh, E. E. Ebenso, M. K. Singh, D. Behera, *Journal of Molecular Liquids*, 250 (2018) 88–99.
24. M. Taha, N. H. Ismail, H. M. Zaki, A. Wadood, S. Imran, *Bioorganic Chemistry*, 75 (2017) 235–241.
25. M. Taha, H. Ullah, LMR Al Muqarrabun, M. N. Khan, *Bioorganic and Medicinal Chemistry*, 26 (2018) 152–160.
26. N. Ahmat, N.H. Ismail, I. Zakaria, N. Zawawi, *Research Journal of Medicinal Plant*, 6 (2012) 74–82.
27. Yuri N. Belokon, Natalia B. Beshpalova, Tatiana D. Churkina, Ivana Čísařová, G. Marina. *Journal of American Chemical Society*, 125 (2003) 12860–12871.

28. Mario D. Bachi, Jacob Vaya, *Journal of Organic Chemistry*, 44 (1949) 4393–4396.
29. Nataliya. E. Borisova, Marina. D. Reshetova, Yuri. A. Ustynyuk, *Chemical Reviews*, 107 (2007) 46–79.
30. Ronald Grigg, Theeravat Mongkolaussavaratanaa, C. Anthony Pounds, Sasikala Sivagnanama, *Tetrahedron Letters*, 31 (1990) 7215-7218.
31. B. Witkop, T. W. Beiler, *Journal of American Chemical Society*, 76 (1954) 5589–5597.
32. E. Hadjoudis, M. Vittorakis, I. Moustakali-Mavridis, *Tetrahedron* 43 (1987) 1345–1360.
33. E. J. Hadjoudis, *Journal of Photochemistry*, 17 (1981) 355–363.
34. Jisha Joseph, N. L. Mary, Raja Sidambaram, *Synthesis and Reactivity in Inorganic, Metal-Organic, and Nano-Metal Chemistry*, 40 (2010) 930-933.
35. M. Das, S. E. Livingstone, *Inorganica Chimica Acta*, 19 (1976) 5–10.
36. A. D. Garnovskii, A. L. Nivorozhkin, V. I. Minkin, *Coordination Chemistry Reviews*, 126 (1993) 1–69.
37. A. A. A. Aziz, S. H. Seda, S. F. Mohammed, *Sensors Actuators B Chemical*, 223 (2016) 566–575.
38. S. M. Sabry, *Journal of Pharmaceutical and Biomedical Analysis*, 40 (2006) 1057–1067.
39. A. K. Singh, V. K. Gupta, B. Gupta, *Analitica Chimica Acta*, 585 (2007) 171–178.
40. A. K. Sharma, B. Gupta, *Sensors Actuators B Chemical*, 182 (2013) 642–651.
41. L. P. Singh, J. M. Bhatnagar, *Talanta*, 64 (2004) 313–319.

42. V. K. Gupta, A. K. Singh, B. Gupta, *Analitica Chimica Acta*, 575 (2006) 198–204.
43. Y. M. Hijji, B. Barare, A. P. Kennedy, R. Butcher, *Sensors Actuators B Chemical*, 136 (2009) 297–302.
44. Z. Cimerman, N. Galic, N. Bosner, *Analitica Chimica Acta*, 343 (1997) 145–153.
45. N. Hirayama, J. Taga, S. Oshima, T. Honjo, *Analitica Chimica Acta*, 466 (2002) 295–301.
46. J. Aggett, R. A Richardson, *Analitica Chimica Acta*, 50 (1970) 269–275.
47. W. Al Zoubi, F. Kandil, M. K. Chebani, *Arabian Journal of Chemistry*, 9 (2016) 526–531.
48. N. Ôi, H. Kitahara, F. Aoki, *Journal of Chromatographic Science*, 631 (1993) 177–182.
49. A. Dumont, V. Jacques, J. F. Desreux, *Tetrahedron*, 56 (2000) 2043–2052.
50. L. L. Liao, S. Mo, H. Q. Luo, N. B. Li, *Journal of Colloid Interface Science*, 499 (2017) 110–119.
51. R. Kumar, R. Chopra, G. J. Singh, *Journal of Molecular Liquids*, 241 (2017) 9–19.
52. G. Bahlakeh, M. Ramezanzadeh, *Journal of Molecular Liquids*, 248 (2017) 854–870.
53. H. Shokry, M. Yuasa, I. Sekine, R. M Issa, H. Y. El-Baradie, *Corrosion Science*, 40 (1998) 2173–2186.
54. S. L. Li, Y. G. Wang, S. H. Chen, R. Yu, S. B. Lei, H. Y. Ma, *Corrosion Science*, 41 (1999) 1769–1782.

55. K. C. Emregül, O. Atakol, *Materials Chemistry and Physics*, 82 (2003) 188–193.
56. I. Ahamad, R. Prasad, R. Quraishi, *Corrosion Science*, 52 (2010) 933–942.
57. K. S. Shaju, Joby Thomas K, Vinod P. Raphael, Aby Paul, *ISRN Corrosion*, (2012) 1-8.
58. C. M. Goulart, A. Esteves-Souza, C. A. Martinez-Huitle, *Corrosion Science*, 67 (2013) 281–291.
59. A. Yurt, A. Balaban, S. U. Kandemir, G. Bereket, B. Erk, *Materials Chemistry and Physics*, 85 (2004) 420-426
60. K. C. Emregül, M. Hayvalı, *Corrosion Science*, 48 (2006) 797–812.
61. M. Behpour, S. M. Ghoreishi, N. Soltani, *Corrosion Science*, 50 (2008) 2172–2181.
62. Aby Paul, Joby Thomas K, Vinod P. Raphael, K. S. Shaju, *Oriental Journal of Chemistry*, 28 (2013) 1501-1507.
63. Vinod P. Raphael, Joby Thomas K, K. S. Shaju, Sini Varghese. C, *International Journal of Industrial Chemistry*, 8 (2017) 49-60.
64. U. J. Ekpe, U. J. Ibok, B. I. Ita, O. E. Offiong, E. E. Ebenso, *Materials Chemistry and Physics*, 40 (1995) 87–93.
65. S. L. A. Kumar, M. Gopiraman, M. S. Kumar, A. Sreekanth, *Industrial & Engineering Chemistry Research*, 50 (2011) 7824–7832.
66. A. Dandia, S. L. Gupta, P. Singh, M. A. Quraishi, *ACS Sustainable Chemistry & Engineering*, 1 (2013) 1303–1310.
67. Vinod P. Raphael, Joby Thomas K, K. S. Shaju, Aby Paul, *Research On Chemical Intermediates*, 40 (2014) 2689- 2701.

68. A. K. Singh, *Industrial & Engineering Chemistry Research*, 51 (2012) 3215–3223.
69. Aby Paul, Joby Thomas. K, Vinod P. Raphael, K. S. Shaju, *IOSR Journal of Applied Chemistry*, 1 (2012) 17-23.
70. D. Daoud, T. Douadi, S. Issaadi, S. Chafaa, *Corrosion Science*, 79 (2014) 50–58.
71. Nimmy Kuriakose, Joby Thomas K, Vinod P. Raphael, K. S. Shaju, *Indian Journal of Material Science*, 2014 (2014) 1-6.
72. A. B. da Silva, E. D. Elia, J. A. da Cunha Ponciano Gomes, *Corrosion Science*, 52 (2010) 788–793.
73. Vinod P. Raphael, K. S. Shaju, Joby Thomas, *International Journal of Corrosion*, 2016 (2016) 1-10.
74. S. Jeyaprabha, D. Muralidharan, G. Jayaperumal, N. S. Venkatachari, Rengaswamy, *Anticorrosion Methods & Materials*, 45 (1998) 148.
75. H. Hamani, T. Douadi, D. Daoud, M. Al-Noaimi, S. Chafaa, *Measurement*, 94 (2016) 837–846.
76. B. G. Ateya, B. E. El-Anadouli, F. M. El-Nizamy, *Corrosion Science*, 24, (1984) 509–515.
77. T. Zhao, G. Mu, *Corrosion Science*, 41 (1999) 1937–1944.
78. Sini Varghese. C, Joby. Thomas. K, Vinod. P. Raphael, K. S. Shaju, *Chemical Science Review and Letters*, 64 (2017) 2300-2308.
79. N. Soltani, H. Salavati, H. Rasouli, M. Paziresh, A. Moghadasi, *Chemical Engineering Communications*, 203 (2016) 840–854.
80. M. A. Bedair, M. M. B. El-Sabbah, A. S. Fouda, H. M. Elaryian, *Corrosion Science*, 128 (2017) 54–72.

81. M. Bouklah, N. Benchat, B. Hammouti, A. Aouniti, S. Kertit, *Material Letters*, 60 (2006) 1901.
82. H. Ashassi-Sorkhabi, B. Shaabani, D. Seifzadeh, *Applied Surface Science*, 239 (2005) 154–164.
83. M. Kuruvilla, S. John, A. Joseph, *Journal of Bio- Tribo-Corrosion*, 2 (2016) 19.
84. P. P. Kumari, S. A. Rao, P. Shetty, *Procedia Materials Science*, 5 (2014) 499–507.
85. K. C. Emregül, O. Atakol, *Materials Chemistry and Physics*, 83 (2004) 373–379.
86. F. Bentiss, M. Lagrenee, M. Traisnel, J. C. Hornez, *Corrosion*, 55 (1999) 968–976.
87. Xinming Xie, Jinlong Li, Minpeng Dong, *Surface Topography: Metrology and Properties*, 6 (2018) 1.
88. I. D Gopi, K. M. Govindaraju, K. Louis, *Journal of Applied Electrochemistry*, 40 (2010) 1349–1356.
89. K. C. Emregül, R. Kurtaran, O. Atakol, *Corrosion Science*, 45 (2003) 2803–2817.
90. N. D. Greene, M. G. Fontana, *Corrosion*, 15 (1959) 55-60.
91. S. Bilgic, N. Caliskan, *Journal of Applied Electrochemistry*, 31 (2001) 79-83.
92. A. Pandey, B. Singh, C. Verma, E. E. Ebenso, *RSC Advances*, 7 (2017) 47148–47163.
93. F. Mansfeld, *Corrosion*, 37 (1981) 301–307.
94. B. M. Mistry, S. K. Sahoo, D. H. Kim, S. Jauhari, *Surface and Interface Analysis*, 47 (2015) 706–718.

95. Y. K. Agrawal, J. D. Talati, M. D. Shah, M. N. Desai, N. K. Shah, *Corrosion Science*, 46 (2004) 633–651.
96. G. K. Gomma, M. H. Wahdan, *Materials Chemistry and Physics*, 39 (1995) 209–213.
97. H. Ashassi-Sorkhabi, B. Shaabani, D. Seifzadeh, *Electrochimica Acta*, 50 (2005) 3446–3452.
98. M. Hosseini, S. F. L. Mertens, M. Ghorbani, M. R. Arshadi, *Materials Chemistry & Physics*, 78 (2003) 800–808.
99. M. Behpour, S. M. Ghoreishi, N. Soltani, M. Salavati-Niasari, *Corrosion Science*, 51 (2009) 1073–1082.
100. J. Smulko, K. Darowicki, A. Zieliński, *Electrochemistry Communications*, 4 (2002) 388–391.
101. S. Abd El Wanees, A. Abd, M. Abdel Azzem, *International Journal of Electrochemical Science*, 3 (2008) 21–25.
102. J. F. Chen, W. F. Bogaerts, *Corrosion Science*, 37 (1995) 1839–1842.
103. Y. J. Tan, S. Bailey, B. Kinsella, *Corrosion Science*, 38 (1996) 1681–1695.
104. F. Mansfeld, Z. Sun, C. H. Hsu, A. Nagiub, *Corrosion Science*, 43 (2001) 341–352.
105. H. Ashassi-Sorkhabi, D. Seifzadeh, M. Raghbi-Boroujeni, *Arabian Journal of Chemistry*, 9 (2016) 1320–1327.
106. A. M. Homborg, R. A. Cottis, J. M. Mol, *Electrochimica Acta*, 222 (2016) 627–640.
107. A. M. Homborg, EPM Van Westing, T. Tinga, X. Zhang, *Corrosion Science*, 66 (2013) 97–110.

108. S. F. Burch, S. F. Gull, J. Skilling, *Computer Vision Graphics and Image Processing*, 23 (1983) 113–128.
109. D. K. Yadav, M. A. Quraishi, B. Maiti, *Corrosion Science*, 55 (2012) 254–266.
110. S. Benabid, T. Douadi, S. Issaadi, C. Penverne, S. Chafaa, *Measurement*, 99 (2017) 53–63.
111. D. Daoud, T. Douadi, H. Hamani, S. Chafaa, M. Al-Noaimi, *Corrosion Science*, 88 (2014) 234–245.
112. V. S. Sastri, J. R. Perumareddi, *Corrosion*, 53 (1997) 617–622.
113. M. Shahraki, M. Dehdab, S. Elmi, *Journal of the Taiwan Institute of Chemical Engineers*, 62 (2016) 313–321.
114. A. S. Fouda, M. A. Ismail, G. Y. EL-ewady, A. S. Abousalem, *Journal of Molecular Liquids*, 240 (2017) 372–388.
115. E. Cano, J. L. Polo, A. La Iglesia, J. M. Bastidas, *Adsorption*, 10 (2004) 219.
116. P. Bommersbach, C. Alemany-Dumont, J. P. Millet, B. Normand, *Electrochimica Acta*, 51 (2005) 1076.
117. M. El Azhar, B. Mernari, M. Traisnel, F. Bentiss, M. Lagrenee, *Corrosion Science*, 43 (2001) 2229.
118. F. El-Taib, A. S. Fouda, M. S. Radwan, *Materials Chemistry and Physics*, 125 (2011) 26.
119. S. John, A. Joseph, *Materials Chemistry and Physics*, 133 (2012) 1083.

PART - II

CONCRETE CORROSION



CONCRETE CORROSION – AN INTRODUCTION

Reinforced concrete structures are versatile, inexpensive and successful materials for construction purposes. It can be constructed to various shapes and structures. They are introduced to reassure the existence and strength during their service life period. But in some cases, it can't perform sufficiently. The disintegration of reinforced concrete structure is a main problem for the civil engineers and the durability of these structures become an important discussion for the global development. The concrete corrosion makes extensive damage to bridges, sewage pipelines and other assets made with concrete. Even if many reasons are established for the concrete disintegration, it is mainly occurs due to the reinforced steel corrosion. Generally steel in concrete structures has a passive film generated by the concrete alkalinity for the protection from corrosion. This protective film can be destructed by sea water effects, aggregate expansion, fire, bacterial corrosion, calcium leaching and chemical damage by chlorides, sulphates and carbonation, etc.

Sea water effects

Concrete structures, in contact with sea water are highly liable for corrosion. The effects of corrosion are highly conspicuous above the intertidal zone area, where the concrete structure is immersed permanently [1-3]. In the immersed area, magnesium ions and hydrogen carbonate form a brucite layer of about 30 micrometers thickness and calcium carbonate will deposit on it. These layers are capable for the protection of the concrete structures from processes such as attack of sulfate and chloride ions and carbonation. The erosion of waves or gravel and sand carried by waves, and the crystallization of salt components in the water soaked into the concrete pores leads to mechanical damage.

Aggregate expansion

Different types of aggregates subjected to chemical reactions in concrete, resulting to damage the expansive phenomena. For example, the most common aggregate containing reactive silica, undergo reaction with the alkaline compounds in concrete which leads to the formation of an expansive gel and it forms cracks and damage the structures. When dolomite containing aggregates are used, a dedolomitization reaction will occurs where the reaction between hydroxyl ions and magnesium carbonate takes place and forms a carbonate ion and magnesium hydroxide. The resulting expansion process may destroy the concrete material.

Leaching

The flow of water through the cracks in concrete structures may dissolve different minerals in the hardened cement paste. Thus dissolved ions, like calcium (Ca^{2+}), will leach out and transport in solution, thereby supersaturating water with the minerals. It will lead to further precipitation, forms deposition of calthemite inside the cracks and in particular conditions it will cause self-healing of fractures.

Bacterial corrosion

Bacteria have not considerable effect on concrete itself. But the sulfate-reducing bacteria in sewage may produce H_2S and it undergoes oxidation by aerobic bacteria to H_2SO_4 . The formed H_2SO_4 dissolves the carbonates in the cement and may cause strength loss and it produces harmful sulfates also [4-8].

Physical damage

Physical damage may occur at the casting and de-shuttering period. Sometimes, the beam corners may be damaged at the de-shuttering time and other physical damage may occur during the shuttering of steel without base plates.

Concrete slabs, pipelines and block walls are susceptible to damage during ground settlement or other sources of vibration and also by the contraction and expansion during temperature changes adversely.

Thermal damage

Concrete layers are commonly used for the fire proofing process of steel structures due to its low thermal conductivity. But the fire itself can damage the concrete structures [9, 10]. The concrete structures normally have thermal expansion up to the temperature 300°C. Above that temperature, water loss leads to shrinkage and leads to internal stresses. The major structural changes like coarsening of pores and carbonation occurs at about 500°C. The cement hydrate decomposes and forms calcium oxide at 450-550°C temperature. Calcium carbonate will decompose at about 600°C. On cooling rehydration process of the calcium oxide makes expansion and destroys the material. Concrete is considered as healthy up to 100°C. Above 300°C, the concrete parts exposed to temperatures will get a pink colour and it turn grey in colour above 600°C and above 1000°C it becomes yellow-brown. Fire will also produce liquids and gases which are harmful to the concrete. At very high temperatures the water inside the concrete will boil and the steam makes pressure on the concrete and leads to crack.

Chemical damages

Sulfates

Sulfates can make significant microstructural effects in concrete resulting to the decrease in the cement binder strength. Sulfate solutions leads to the damage of the porous materials in the cement by the crystallization and recrystallization process. Sulfates and sulfites are found in many sources, like gypsum which is used as an additive in cements.

Chlorides

Chlorides, especially calcium chloride, are used to reduce the setting time of concrete. But these chlorides may leach calcium hydroxide and make chemical changes in concrete structures, resulting to strength loss.

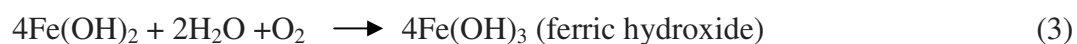
Carbonation

The formation of calcium carbonate occurs by the reaction of CO₂ from air with the calcium hydroxide in concrete structures called carbonation. Carbonation process decreases the alkalinity which is essential for the prevention of reinforcement corrosion. Reinforcement corrosion in concrete structures can be considered as an electrochemical process and the potential resulting to the corrosion cells can be occurred as follows:

- (a) Composition cells can be generated by the insertion of two dissimilar metals such as steel rebar and aluminium pipes in concrete.
- (b) Concentration cells can be generated by the presence of alkalies, oxygen and chlorides in different concentrations near the steel surface.

Thus, significant chemical changes take place at the cathodic and anodic areas, connected by the electrolyte of pore water in the cement paste are given as follows.

Anodic reactions:



Cathodic reaction



The different stages of concrete corrosion are given as follows:

Stage 1: White patches formation

The reaction of water and carbon dioxide leads to the process of carbonation. The formation of calcium carbonate occurs by the reaction of CO₂ from air with the calcium hydroxide in concrete structures. The free water movement take the calcium carbonate to the concrete surface and develops white patches.

Stage 2: Formation of brown patches

When reinforcement corrosion occurs, a layer of ferric oxide develops on the surface of reinforcement. This brown product formed may pervade with moisture towards the concrete surface accompany with cracking.

Stage 3: Formation of cracks

The corrosion of metal normally increases the volume 6 to 10 times than the volume of parent metal which produces considerable pressure on the surface of concrete and makes cracking.

Stage 4: Formation of multiple cracking

The progress of corrosion will leads to the development of multiple ferric oxide layers which exerts pressure on the concrete and make multiple cracking. In addition the bond between reinforcement and concrete is reduced and make a hollow sound when bit at the concrete surface.

Stage 5: Snapping of bars

The reduction of size of bars causes to the snapping or sudden break of concrete bars.

Stage 6: Concrete cover spalling

Due to the weakening of bond between reinforcement and steel and multiple cracking formations, the concrete cover spalling occurs and reduces the size of the bars.

Stage 7: Bulging of concrete

The spalling of concrete cover and snapping of bars leads to the bulging of concrete in the particular region and resulting to the collapse of the structure.

The concrete corrosion can be handled by many ways. 1) seal the concrete surface to reduce the ingress of carbon dioxides, chloride ion, and water (2) modification of concrete to minimize its permeability and (3) addition of suitable substances during the casting of concrete. The reinforcement corrosion prevention is mainly achieved by using good quality concrete of low W/C ratio in the design stage as given in the European standard EN 206. Literature survey indicated that many researchers are interested in this field of concrete corrosion and conducted different studies to introduce different methods to improve the service life of concrete. In order to conduct studies of concrete reinforcement corrosion researchers mainly depend on either concrete block materials or simulated concrete pore solution.

In 2002, Luca Bertolini *et.al.*, investigated the efficiency of submerged sacrificial anodes in the pitting corrosion prevention in the emerged areas of marine piles [11]. Experimental study was conducted on reinforced concrete with steel embedded in concrete with and without the contamination of chloride. The obtained result indicated that sacrificial anodes are more effective in preventing initiation of corrosion than in controlling pitting corrosion.

In 2003, H Castro *et.al.*, studied the mechanical properties of two different stainless steels like 304LN and 316LN grades [12]. The J–R curves analysis helps to find out their mechanical properties. This experimental work was conducted to determine the corrosion behaviour of bars in the saline environment and the results justified the fabrication method conducted in each case.

In 2012, Fujian Tang *et.al.*, investigated the electrochemical behaviour of carbon steel with enamel coating in concrete pore solution with different concentrations of chloride ions, using open circuit potential, linear polarization resistance and electrochemical impedance spectroscopy [13]. The phase composition, tensile strength and microstructure were analyzed by scanning electron microscopy and X-ray diffraction. Three different types of coatings with pure, double and mixed enamels were investigated for their corrosion response. The results revealed that all three types of coatings effectively reduce the corrosion of carbon steel exposed with chloride and the pure as well as double coatings are more resistant than the mixed enamel coating.

In 2013, Marijana Serdar *et.al.*, investigated long time corrosion response of six reinforced steels embedded in mortar in the presence of chloride by making use of impedance spectroscopy for 2 years [14]. The corrosion response of investigated steels was divided into 2 phases, passive phase and pitting propagation phase. Data revealed that duplex steel exhibited good corrosion response even after 2 years. The steels having high Mn and N content and low Ni content exhibited low corrosion prevention compared to austenitic steel.

In 2015, Tingting Zhu *et.al.*, introduced microbial carbonate precipitation (MCP) method for removing cracks in the concrete using heterotrophic nitrogen containing bacteria [15]. A modern technology by autophototrophs was invented to

control the pollution by MCP (urea-based). They analysed biomineralization process of *Synechococcus* (cyanobacteria) in the simulated concrete pore solution, and checked its effect on the concrete properties. The experimental study conducted on concrete cubes established that a thick layer of calcite-cell aggregate is adhering on the concrete structure resulting the reduction of water absorption process and thereby blocking the thorough setting of the concrete. But *Synechococcus* shows a predominant potential for concrete restoring.

In 2015, Ming Liu *et.al.*, investigated the corrosion resistance of Cr modified steels in saturated $\text{Ca}(\text{OH})_2$ solution by open circuit potential, impedance spectroscopy and X-ray photoelectron spectroscopy [16]. The result indicated that the modified steels exhibit eminent corrosion resistance power with a high chloride threshold values, low corrosion current density and high impedance. The immersion test revealed that the new steels have low corrosion rates and long durability.

In 2016, Jinjie Shi *et.al.*, studied the effect of concentration of chloride ions and effect on prevention of pitting corrosion of low-carbon steel and low-alloy steel in concrete pore solution by electrochemical, physicochemical and surface morphological methods [17]. From the results, it is established that the generated passive film have the capacity to resist the pitting corrosion on steels. Compared to low-carbon steel, lower pitting corrosion resistance was reported for low-alloy steel at low chloride concentration and exhibits eminent pitting corrosion resistance at higher chloride concentration.

The detailed investigations conducted on the concrete corrosion using the inhibitors are represented in this part as two subdivisions.

Part II A: Corrosion of steel in concrete pore solution.

Part II B: Steel reinforced concrete corrosion.

PART - II A
CORROSION OF STEEL IN
CONCRETE PORE SOLUTION



CHAPTER 1

INTRODUCTION AND REVIEW

The concrete reinforcement corrosion is a major problem that affects not only the civil engineering industry but also all other areas even nuclear industry. Premature disintegration of concrete structures mostly occurs by the ingress of carbon dioxide and chloride ions [18]. Pitting corrosion is occurring due to the local depassivation on the reinforcement steel by chloride ions. The reaction of alkaline compounds with carbon dioxide in the concrete structures decreases the pH value and makes depassivation on the reinforcement steel [19-22]. Among numerous methods to resist the concrete reinforcement corrosion, the use of corrosion inhibitors offers simplest and economic prevention technique [23-28]. Inhibitors can influence the kinetics of the electrochemical reactions occurring in the corrosion process of steel [29-32]. A corrosion inhibitor can be defined as a chemical compound which may be added to concrete to prevent the corrosion without causing any unfavourable changes for the mechanical properties of the concrete.

The corrosion inhibitors are capable to resist the concrete reinforcement corrosion by the following mechanisms, i) diffusion rate of the ingress of chloride reduces ii) the chloride concentration trapped inside the concrete increases iii) threshold energy of chloride ion increases or iv) prevent the cathodic, anodic or both reactions [33-37]. Many controversies are known about the corrosion inhibition efficiency as well as its mechanism. Some argued that in the presence of chlorides, inhibitors are not effectively resist the concrete reinforcement corrosion, whereas some others reported that there are some compounds which have predominant

efficiency to resist the reinforcement corrosion even in the presence of chloride ions [38, 39].

The inhibitors commonly used for the prevention of the reinforcement corrosion are mainly classified as two: (i) corrosion inhibitors added to concrete mixture at the casting time (admixture) and (ii) corrosion inhibitors which applied on the concrete surface during the maintenance period and they can migrate into the concrete structure [40-42]. Nowadays many inorganic or organic compounds based admixtures are commercially available in the market. Inorganic inhibitors include mainly nitrites or sodium mono fluoro-phosphate [43-45]. High corrosion inhibition efficiency of nitrites has already been established by many researchers [46-48]. Even if several organic compounds like aminoethanols and alkanolamines have been studied as corrosion inhibitors eventhough they are not considered as potential inhibitors as nitrites [49-51]. New generation researchers are also very much interested in this field of concrete corrosion and try to establish different kinds of corrosion inhibitors with eminent efficiency [52-54]. Silver nanoparticle doped palm oil leaf extracts, ethylenediamine tetra acetic acid disodium salt, and naturally occurring Neem gum and Welan gum are concrete corrosion inhibitors invented recently with predominant efficiency [55, 56].

The investigations on concrete reinforcement corrosion are conducted by the researchers either by concrete pore solution or concrete specimens. Since the method, using concrete specimen, is a time consuming process, many researchers are adopting the method using concrete pore solution as a quick procedure. It helps to get a peripheral idea about the corrosion response of steel rebar within a short period. Thus investigations employed using the pore solution is considered as a jet study of concrete corrosion.

Effective inhibitors for steel corrosion in concrete pore solution - A Review

In 2008, L. Benzina Mechmeche *et.al.*, conducted a study to determine the corrosion inhibition efficiency of an amino-alcohol based inhibitor [57]. The experiment was performed in concrete pore solutions. Effectiveness of the inhibitor was studied by corrosion potential analysis, polarisation method and microscopic observations. The result showed that when the inhibitor was added in the pore solution, predominant inhibition efficiency was exhibited before it was contaminated with chlorides

In 2009, M. M. Mennucci *et.al.*, investigated benzotriazole (BTAH) as a potential inhibitor for CS (carbon steel) corrosion in concrete structures [58]. The experimental study was conducted using concrete pore solution with the addition of BTAH in the presence of 3.5% NaCl for mimicking marine conditions. The efficiency of BTAH was studied using electrochemical impedance spectroscopic analysis and potentiodynamic polarization method. The efficiency of BTAH was superior to that of nitrite, which revealed that, for the inhibition of concrete reinforcement corrosion BTAH is a best substitute to nitrites.

In 2011, P. Garcés *et.al.*, investigated the corrosion response of steel reinforcement in CPS (concrete pore solution) in the presence of chloride with sodium nitrite [59]. Significant inhibition efficiency was obtained at low chloride concentrations due to the presence of sodium nitrite, but its efficiency significantly reduced when the pH is decreased and the corrosion intensity has a dependence on the $[Cl^-]/[OH^-]$ ratio.

In 2011, Xin Zhou *et.al.*, synthesized pentaerythritol glycoside (PG) and studied its corrosion inhibition efficiency on carbon steel(CS) immersed in 3.5% NaCl containing saturated $Ca(OH)_2$ solution [60]. The investigations carried out by

potentiodynamic polarization method, electrochemical impedance spectroscopy, atomic force microscopy and X-ray photoelectron spectroscopy showed that the PG compound acted as a potential inhibitor by the strong interaction with the carbon steel surface.

In 2011, Lijuan Feng *et.al.*, synthesized an imidazoline derivative, 1-[N,N'-bis(hydroxyethylether)-aminoethyl]-2-stearicimidazoline (HASI) and investigated the inhibition efficiency on CS corrosion in saturated $\text{Ca}(\text{OH})_2$ solution contaminated with 5% NaCl solution using electrochemical methods and spectroscopy techniques [61]. Quantum chemical evaluations were applied to explain the inhibition mechanism and adsorption behaviour of inhibitor. The results established that HASI is a potential inhibitor to resist CS corrosion in chloride solution.

In 2014, Fei-long *et.al.*, studied the corrosion response of reinforced steel in CPS containing 3.5% NaCl in the presence of imidazoline quaternary ammonium salt (IQS) [62]. The experimental study was carried out using electrochemical method and surface morphological analysis. The derived results revealed that the IQS can appreciably increase the polarization resistance and pitting potential which leads to reduce the corrosion current density.

Scope and objectives of the present investigation

Since 1970s, several research works have been reported by different methods to prevent reinforced concrete corrosion. The methods mainly include replacement of reinforcement and slab design, electrochemical methods, barrier methods and applying corrosion inhibitors. Generally good quality concrete is obtained by the effective methods used during the casting period of concrete, but in many situations, it doesn't give appreciable result. Researchers were introduced a number of effective

corrosion protection techniques to ensure the adequate durability of concrete. But, so far none of this corrosion protection methods invented is completely effective in all situations. However, among numerous invented methods, mixing of corrosion inhibitors (admixture) is most simple and economic prevention method. These are added to concrete mixture during its preparation time. Corrosion inhibitors are added in small quantities and they can appreciably increase the concrete life time and reduce maintenance costs of reinforced concrete for 30 to 40 years. Majority of the corrosion inhibitors are toxic or hazardous in their use. Thus the invention of economic and environment friendly corrosion inhibitors would be very advantageous to the society.

The investigations on concrete reinforcement corrosion are conducted either by employing concrete pore solution or concrete specimens. Since the method using concrete specimen is a time consuming process, many researchers are adopting the method of concrete pore solution as a quick procedure.

The present investigation focuses to study the inhibition efficiency of different sodium salts, natural products and water soluble Schiff bases to inhibit the reinforcement corrosion in simulated concrete pore solution. The various techniques like electrochemical studies such as impedance spectroscopy and Tafel polarization study and half cell potential measurements are proposed to find out the corrosion inhibition efficiency of compounds. The different spectroscopic methods such as UV- visible and FTIR spectroscopy are proposed to explain the interaction mechanism of the added compounds. Microscopic studies are also planned to conduct so as to investigate the changes observed in the surface of the steel rebar.

CHAPTER 2

MATERIALS AND METHODS

This chapter includes all the details about the common reagents, materials and the procedure used for the synthesis and corrosion study of the investigated compounds such as sodium salts, natural products and water soluble Schiff bases in concrete pore solution (CPS) contaminated with NaCl.

Reagents and materials

Portland cement (Malabar Cements Ltd, Kerala), used for the preparation of CPS, is purchased from the market. 10cm of steel rebar with approximate composition 0.62% Mn, 0.1% P, 0.04% S, 0.021% Si, and rest Fe (estimated by EDAX technique- SEM, Hitachi SU6600 model) was cut and cleaned by pickling process of 20 minutes with 2M HCl, washed with distilled water, degreased with acetone and dried. The CPS was prepared by mixing water and cement with a water/cement ratio of 0.5 [63]. The exothermic hydration of cement leads to the temperature rise of the mixture. The continuous stirring of mixture for 15-20 minutes using a mechanical stirrer helps to maintain the temperature stabilisation and homogeneity. A clear CPS was obtained by filtering the mixture using a vacuum pump and the pH of the solution maintained at a range of 12.5-13 and 3.5% NaCl contamination was introduced by adding 3.5g of NaCl to 100ml of CPS. Approximate chemical composition of the CPS was established by volumetric and photometric methods and is represented in the Table 2.1

Table 2.1: Composition of CPS

Species	Ca ²⁺	SO ₄ ²⁻	Fe ³⁺	PO ₄ ³⁻	Cl ⁻	F ⁻	Mg ²⁺
Conc (ppm)	854	6642	1700	7.54	214	4.89	< 2

Chemicals such as sodium chloride (>99.9 %), trisodium citrate (98%), zinc acetate (>99%), NaNO₂ (EMSURE®), monosodium phosphate, sodium phosphate, pentasodium triphosphate and sodium lauryl sulphate were procured from Merck millipore. The preparation of imines was carried out in ethanol medium using analar grade samples of 2-acetylpyridine procured from Fluka and other reagents such as phenylhydrazine hydrochloride and semicarbazide were purchased from E-Merck. Extract of five natural products such as garlic, ginger, beetroot, stonebreaker (keezharnelli) and Christmas bush (communist pacha) were also prepared for the investigation using common methods.

Electrochemical Corrosion Investigations

Potentiodynamic Polarization Analysis

The polarization studies were carried out using mild steel specimens immersed in CPS with and without of inhibitor compounds for 3 days. Potentiodynamic polarization studies were performed using a three electrode cell system consisting of saturated calomel electrode (SCE) as reference electrode, steel rod as working electrode (exposed area 4cm²) and platinum electrode as counter electrode (1cm²) at 30°C. The study was conducted at a potential range of +250 to -250 mV [64-66]. Corrosion current densities and the inhibition efficiencies were evaluated by the analysis of Tafel slopes using the following equation 6.

$$\eta_{\text{pol}} \% = \frac{i_{\text{corr}} - i'_{\text{corr}}}{i_{\text{corr}}} \times 100 \quad (6)$$

where i'_{corr} and i_{corr} are corrosion current densities of steel rebar with and without inhibitor respectively.

EIS analysis

EIS studies were conducted in the frequency range of 1 KHz to 100 mHz at constant potential with an excitation signal of 10mV amplitude. The charge transfer resistance (R_{ct}) was evaluated by the examination of the Nyquist and Bode plots using suitable equivalent circuit and inhibition efficacy was determined by the equation 7.

$$\eta_{\text{EIS}} \% = \frac{R'_{ct} - R_{ct}}{R_{ct}} \times 100 \quad (7)$$

where R'_{ct} and R_{ct} are the charge transfer resistance of working electrode in the presence and absence of inhibitor respectively. EIS measurements were carried out using Iviumsoft software (Ivium compactstat-e electrochemical work station). The most suitable equivalent circuit corresponding to the EIS measurements (Figure 2.1) consists of double layer capacitance (C_{dl}) which is connected in series to solution resistance (R_s) and this combination is connected in parallel to a series combination of charge transfer resistance (R_{ct}) and Warburg resistance (W).

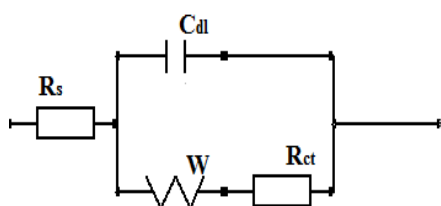


Figure 2.1 Equivalent circuit fitted for EIS measurements of steel specimen in contaminated CPS

Half cell Potential Analysis

The corrosion response of steel specimen dipped in different medium immediately investigated by half cell potential measurements using a high impedance voltmeter (HP E2378A) and SCE (saturated calomel electrode). In this electrochemical cell assembly, SCE and steel specimen were acted as cathode and

anode respectively. Half cell potential values of steel specimen were calculated by subtracting the EMF from standard electrode potential of SCE at 30⁰C.

Spectroscopic studies

The interaction mechanism of the inhibitors on steel rebar immersed in simulated CPS was studied by UV- visible (Schimadzu UV-visible-1800 spectrophotometer) and FTIR spectroscopic studies after 3 days. The deposited oxide film on the steel specimen surface was scratched carefully using a stainless steel blade and FT-IR spectral pattern of the scratched powder was recorded by KBr pellet method in the frequency range of 4000-400cm⁻¹ using Shimadzu IR Affinity-1 model FT-IR spectrophotometer.

Microscopic surface analysis

The changes produced on the surface morphology of the steel specimen immersed in simulated CPS were investigated by the microscopic surface analysis using Leica Stereo Microscope -S8ACO [67, 68].

CHAPTER 3

CORROSION INHIBITION BEHAVIOUR OF SYNTHETIC AND NATURAL PRODUCTS IN CONCRETE PORE SOLUTION

Investigations were carried out to establish the effectiveness of different synthetic and natural products to inhibit the corrosion of steel rebar in concrete pore solution contaminated with chloride. Inhibition efficiency of these systems was studied by potentiodynamic polarization and half cell potential measurements. Electronic spectral studies of simulated pore solution and FT-IR spectral investigations of the film deposited on steel surface were carried out for understanding the corrosion inhibition mechanism. Microscopic surface analysis was conducted to obtain the surface morphological behaviour of steel rebar. The four sections in this chapter comprise the detailed explanation of the corrosion studies on different sodium salts, natural products, and Schiff bases.

SECTION 1: Effect of sodium salts of nitrites, citrates and citrate – acetate mixture on corrosion of steel in concrete pore solution.

SECTION 2: Effect of sodium salts of phosphates and sulphates on corrosion of steel in concrete pore solution.

SECTION 3: Effect of plant extracts on corrosion of steel in concrete pore solution.

SECTION 4: Effect of Schiff bases on corrosion of steel in concrete pore solution.

SECTION 1

CORROSION BEHAVIOUR OF STEEL IN THE PRESENCE OF SODIUM SALTS OF NITRITE, CITRATE AND CITRATE-ACETATE MIXTURE IN CONCRETE PORE SOLUTION

Many researchers were introduced and studied a number of effective corrosion inhibitors (admixture) to prevent the steel rebar corrosion in concrete. But majority of the corrosion inhibitors are toxic and hazardous to human being. Thus the invention of environment friendly corrosion inhibitors would be very advantageous to society.

Preparation of inhibitor solutions

The inhibitor solutions were prepared by the addition of trisodium citrate (TSC) and NaNO_2 to the working solution (CPS) to attain the concentrations 50, 100, 150, 200 and 1500ppm. Another set of sodium citrate solutions were also prepared in CPS (50-200ppm) with 50ppm zinc acetate (ZnAc). Iron rebar having 10 cm of length was cleaned by pickling in 2M HCl solution for 20 minutes, washed, dried and dipped into these test solutions.

Potentiodynamic polarization analysis

Potentiodynamic polarization studies were carried out using a three electrode system, which consists of saturated calomel electrode (SCE) as reference electrode, platinum electrode as counter electrode and steel immersed in CPS as working electrode using Ivium Compactstat-e electrochemical system.

Interaction of sodium nitrite with steel rebar

The effect of concentration of sodium nitrite on the corrosion of steel rebar in the CPS was investigated using polarization studies. Data obtained from polarization studies is given in the Table 2.2. Sodium nitrite solutions of concentrations 50-1500 ppm were considered for the study. From the polarization data it is revealed that at very low concentration (50 ppm), the corrosion rate of steel rebar treated with sodium nitrite was higher than that of the steel rebar immersed in CPS without nitrite (blank), ie; sodium nitrite acted as a corrosion antagonist. This result indicates that one must be very careful regarding the concentration of the nitrite when it is employed as an admixture in concrete. However the corrosion inhibition efficiency increased as the concentration of sodium nitrite exceed 50ppm in CPS. Sodium nitrite exhibited only 54.84% inhibition efficiency at a concentration of 1500 ppm in the CPS.

From the Tafel plots (Figure 2.2) it is clear that, at lower concentrations of nitrite, the cathodic slopes of Tafel curves undergo significant change, compared with blank steel rebar. But the anodic slopes of Tafel plots changed drastically with increase of concentration. Thus it can be concluded that at higher concentrations, nitrites mainly influence on the anodic process of corrosion. It has already established by the researchers that sodium nitrite, an anodic inhibitor, can modify the oxide film on the rebar surface which is more protective than naturally occurring film in concrete. The inhibitive power of NaNO_2 is explained by the reaction of nitrite ions with Fe^{2+} ions as shown in the following equation.



Sodium nitrite always competes with the Cl^- ions for Fe^{2+} ions produced in concrete and incorporates them into a passive layer on the steel surface and hence resisting further corrosion.

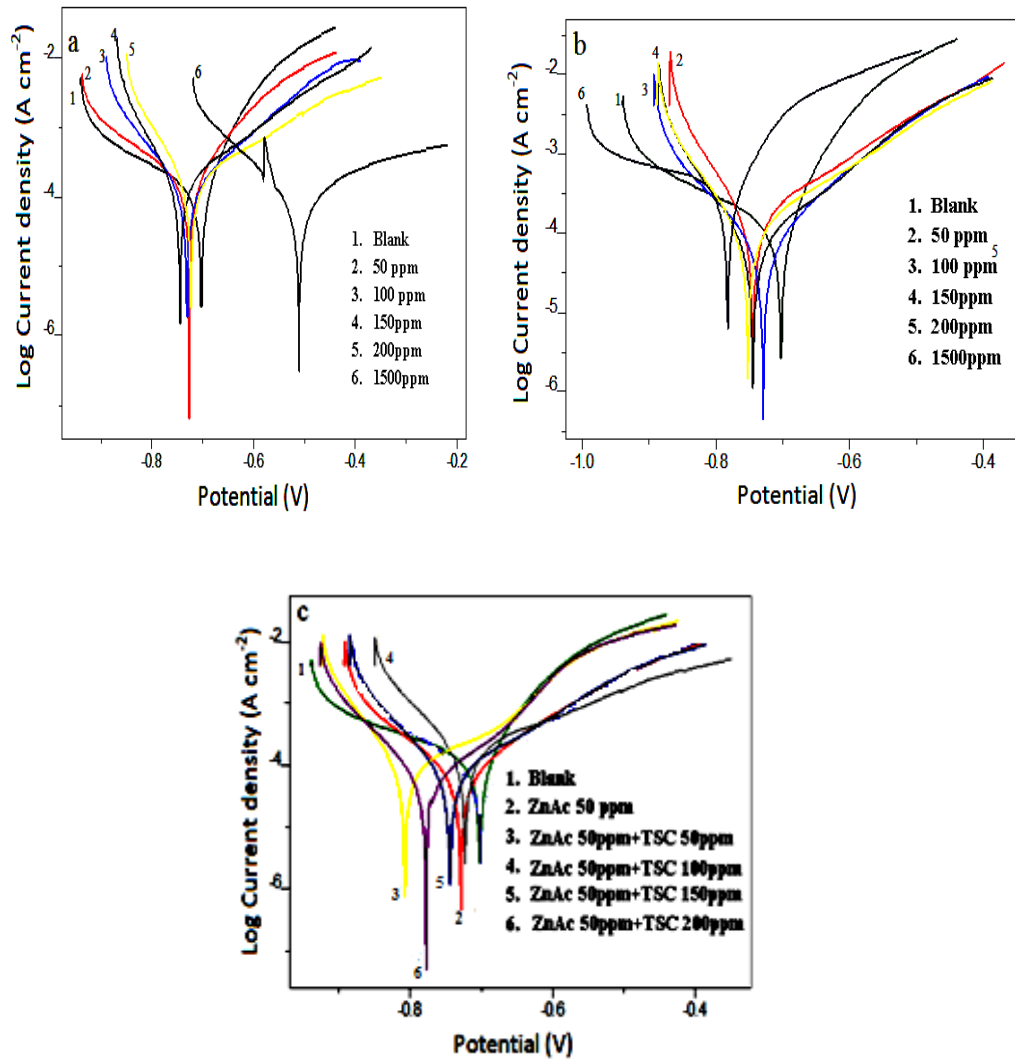


Figure 2.2: Tafel plots of steel rebar in CPS containing a) sodium nitrite b) TSC and c) ZnAc+TSC at different concentrations

Interaction of trisodium citrate with steel rebar

Polarization experiments were conducted on steel rebar after an immersion period of 3 days in concrete pore solution containing TSC and 3.5% NaCl (Figure 2.2). The corrosion protection capacity of TSC on steel rebar was 25% at 50 ppm concentration (Table 2.2). The inhibition efficiency ($\eta_{\text{pol}}\%$) increased with the

concentration and a maximum of 66% was reached at 150ppm of TSC. After this concentration, $\eta_{\text{pol}}\%$ started to decrease. At a concentration of 1500ppm, TSC showed corrosion antagonistic behaviour on steel rebar in CPS. This change in the behaviour of TSC on the steel rebar can be illustrated with the help of two competitive reactions. Citrate ions have a substantial capacity to adsorb on the steel surface from CPS and hence at lower concentrations they can decrease the rate of corrosion. Simultaneously, citrate ions have a strong tendency to make co-ordinate bonds with Fe^{2+} ions. The strong complexation between Fe(II) with citrate ions has been well established by Krishnamurthy and Huang [69]. In other words, tendency of TSC to adsorb on steel surface leads to the corrosion inhibition behaviour of the molecule and the affinity of TSC towards ferrous ions favours corrosion antagonistic behaviour. As the concentration of TSC increases, the second process will predominate in the solution over first. This causes to dissolve more and more Fe atoms from the rebar surface to the solution. The mechanism of the interaction of citrate ions on steel rebar surface in CPS can be represented as shown in the Figure 2.3. Some of the TSC molecules adsorb on steel surface through oxygen atoms. The species present in the bulk of the solution is Fe(II)-citrate complex. From the figure it can be realized that enhanced dissolution of Fe takes place due to the strong coordinating tendency of citrate ion with ferrous ions.

The behaviour of sodium citrate on steel rebar in concrete pore solution was further verified by electronic spectroscopy. Two significant peaks appeared in the electronic spectrum of TSC in the simulated concrete pore solution at 340nm and 217nm can be explained due to $n \rightarrow \pi^*$ and $\pi \rightarrow \pi^*$ electronic transitions respectively. CPS containing TSC (1500ppm) when treated with steel rebar for three days, showed three peaks in addition to the above mentioned peaks in UV-visible

spectrum. Additional peaks displayed at 682, 757 and 788nm can be assigned to the electronic transitions of Fe(II)-citrate complex. Furthermore, it is noticed that the colour of the concrete pore solution containing TSC (1500ppm) gradually changed into pale green when it was treated with steel rebar. This colour was persisted for ~10 days. This indicates the stability of Fe(II)-citrate complex in the alkaline CPS. All other concrete pore test solutions (including nitrite added CPS) were changed into brown colour during 2-3 days. This implies that the Fe(II) ions produced due to corrosion is converted into Fe(III) ions quickly. Hence it can be concluded that the reluctance of Fe(II) to convert into Fe(III) in CPS containing NaCl and TSC is definitely due to the strong complex formation between Fe(II) and citrate ions.

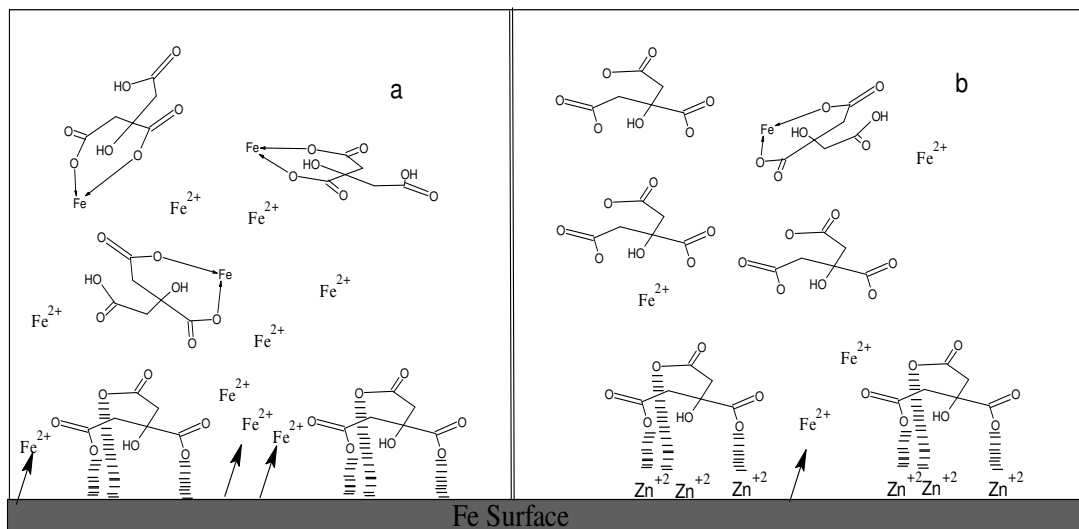


Figure 2.3: Interaction of citrate ions on steel surface CPS **a)** in the absence of zinc acetate and **b)** in the presence of zinc acetate.

To improve the corrosion inhibition efficiency of TSC on steel rebar, zinc acetate (ZnAc) was added to the concrete pore solution. Table 2 describes the corrosion inhibition efficacy of TSC-ZnAc system and the potentiodynamic polarization parameters of steel rebar. Tafel plots are depicted in the Figure 2.2. Data show that $\eta_{pol}\%$ of TSC is enhanced appreciably in the presence of zinc acetate. Highest value of $\eta_{pol}\%$ (80.23%) was shown by TSC at 100ppm in the presence of

50ppm ZnAc, while it was only 56.11% in absence of ZnAc. Thus a drastic depletion in the rate of corrosion of steel rebar was noticed in the presence of TSC-ZnAc mixture in concrete pore solution. This is definitely due to the involvement of zinc ions which favours the strong adsorption of citrate ions on the steel rebar surface. TSC alone does not satisfactorily obey any adsorption isotherm on steel surface [70, 71]. But on the addition of ZnAc, it followed Langmuir adsorption isotherm for a concentration range of 100-200ppm (Figure 2.4).

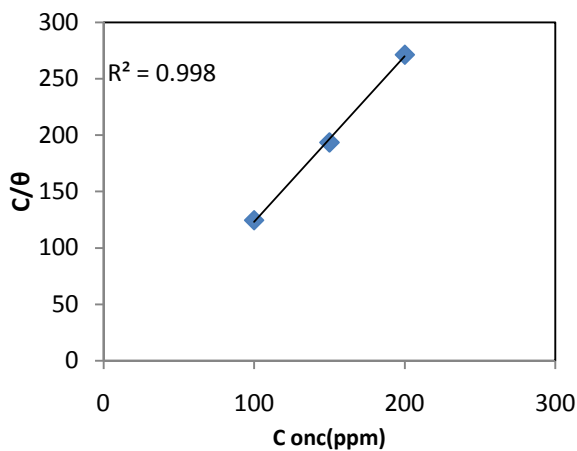


Figure 2.4: Langmuir adsorption isotherm for TSC+ZnAc system on steel surface in CPS contaminated with 3.5% NaCl (TSC 100-200ppm and ZnAc 50ppm)

It can be assumed that affinity of Fe(II) ions to coordinate with citrate ions is minimized considerably in the presence of zinc acetate. This can be easily visualized with the help of the Figure 2.3. Zinc ions attach on the steel surface first followed by the adsorption of citrate ions through zinc ions. But as the concentration of TSC was increased, the corrosion inhibition efficiency began to decrease slowly. This can be illustrated by the same mechanism proposed for Fe-citrate interaction without ZnAc.

On examination of the polarization data it is quite evident that the citrate ion mainly acts on cathodic sites of corrosion. The cathodic slopes of polarization curves of steel rebar in TSC +solution were considerably changed than that of blank experiment. Similar trend was observed for the polarization curves of steel rebar in TSC-ZnAc solution (Figure 2.2).

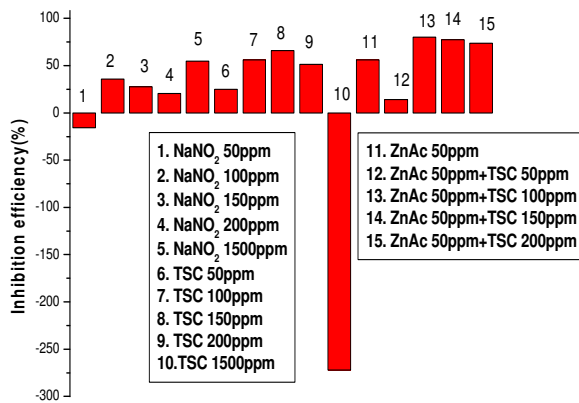


Figure 2.5: Comparison of $\eta_{pol}\%$ of various systems on steel rebar in CPS contaminated with 3.5% NaCl at 30⁰C

Table 2.2: Polarization data of steel rebar immersed in CPS in the presence and absence of sodium salts of nitite, citrate and citrate-acetate mixture at 30⁰C

System Conc(ppm)	I_{corr} (μAcm^{-2})	b_a (mVdec ⁻¹)	$-b_c$ (mVdec ⁻¹)	$-E_{corr}$ (mV)	η_{pol} %
Blank	45.6	136	222	777.7	-
NaNO ₂ (50)	52.79	156	192	752.5	- 15.76
NaNO ₂ (100)	29.26	155	106	735.2	35.83
NaNO ₂ (150)	33.09	182	74	751.6	27.56
NaNO ₂ (200)	36.20	215	83	727.8	20.61
NaNO ₂ (1500)	20.59	407	176	472.7	54.84
TSC (50)	34.24	142	97	746.1	24.91
TSC(100)	20.01	156	112	742.9	56.11
TSC(150)	15.50	146	81	746.9	66.01
TSC(200)	22.17	177	82	756.2	51.38
TSC(1500)	170.20	254	451	889.1	- 272.0
ZnAc(50)	20.09	167	71	714.9	55.94
TSC(50)+ZnAc(50)	39.13	160	145	709.0	14.18
TSC(100)+ZnAc(50)	9.021	105	63	789.9	80.23
TSC(150)+ZnAc(50)	10.27	101	95	782.8	77.47
TSC(200)+ZnAc(50)	11.99	104	87	774.8	73.70

The steel rebar treated with concrete pore solution containing 100ppm of citrate and 50 ppm of zinc acetate displayed least value for cathodic slope in Tafel

plot, suggesting that this particular combination has a great influence on the cathodic process of corrosion than any other combination. In alkaline medium, the main half cell reactions responsible for the corrosion are the oxidation of Fe into Fe^{2+} (anodic) and reduction of O_2 into OH^- (cathodic). Citrates and citric acid are well known for its anti-oxidant property. The anti-oxidant property of citrate ion arises due to the scavenging of oxygen molecules [72]. Since citrate ions mainly affect the cathodic sites of corrosion, it can be robustly believe that the oxygen molecules available for the reduction process are considerably reduced in the presence of citrate ions. Thus, it can be concluded that the ability of TSC and TSC-ZnAc systems to decrease the rate of corrosion of steel rebar in concrete pore solution is due to the combined action of adsorption and scavenging of oxygen molecules. Comparison of $\eta_{\text{pol}}\%$ of various systems on steel rebar in CPS contaminated with 3.5% NaCl at 30°C is shown in the Figure 2.5

EIS analysis

The corrosion response of steel rebar in CPS in the presence and absence of inhibitors was monitored using electrochemical impedance spectroscopy and the corresponding Nyquist plots are represented in the Figure 2.6. The corrosion behaviour of steel rebar was considerably differed in the presence and absence of inhibitors. The EIS parameters of the test solutions are represented in the Table 2.3. Generally, addition of inhibitors leads to the decrease of double layer capacitance and increase of charge transfer resistance. From the impedance data it is revealed that at very low concentration (50 ppm), the corrosion rate of steel rebar treated with sodium nitrite was higher than that of the steel rebar immersed in CPS without nitrite (blank), ie; sodium nitrite acted as a corrosion antagonist. However the corrosion inhibition efficiency was increased as the concentration of sodium nitrite

exceed 50ppm in CPS. Sodium nitrite exhibited only 51% inhibition efficiency at a concentration of 1500 ppm in the CPS.

Table 2.3: Electrochemical impedance data of steel rebar immersed in CPS in the presence and absence of sodium salts of nitrite, citrate and citrate-acetate mixture at 30°C

System Conc (ppm)	W (Ωcm^2)	R _s (Ωcm^2)	C _{dl} (μFcm^{-2})	R _{ct} (Ωcm^2)	η_{EIS} %
Blank	22.8	247	866	3.2	
NaNO ₂ (50)	13.1	36.7	692	2.34	-36
NaNO ₂ (100)	12.2	577	458	4.46	28
NaNO ₂ (150)	6.25	235	436	4.48	29
NaNO ₂ (200)	6.25	248	380	4.65	31
NaNO ₂ (1500)	7.3	390	229	6.6	51
TSC(50)	6.3	228	426	4.5	28
TSC(100)	7.6	530	395	6.4	50
TSC(150)	6.27	430	432	6.8	53
TSC(200)	6.96	300	254	6.56	51
TSC(1500)	79.5	347	151	2.1	-60
ZnAc(50)	6	231	263	4.99	36
TSC(50)+ZnAc(50)	7.89	210	532	3.84	16
TSC(100)+ZnAc(50)	8.74	3.68	134	28.2	89
TSC(150)+ZnAc(50)	10.7	76	216	12.9	75
TSC(200)+ZnAc(50)	6.74	422	155	13.9	77

From the corrosion response of TSC, it was clear that at very low and higher concentrations, TSC showed corrosion antagonistic behaviour and exhibited maximum efficiency of 51% at 200ppm concentration. To improve the corrosion inhibition efficiency of TSC on steel rebar, zinc acetate (ZnAc) was added to the concrete pore solution. Table 2.3 represents the corrosion inhibition efficacy of TSC-ZnAc system and the EIS parameters of steel rebar. Data show that inhibition efficiency of TSC enhanced appreciably in the presence of zinc acetate. Highest

value of efficiency 89% was shown by TSC at 100ppm in the presence of 50ppm ZnAc, while it was very poor in the absence of ZnAc. Thus a drastic depletion in the rate of corrosion of steel rebar was noticed in the presence of TSC-ZnAc mixture in concrete pore solution. These results are in good agreement with Tafel data.

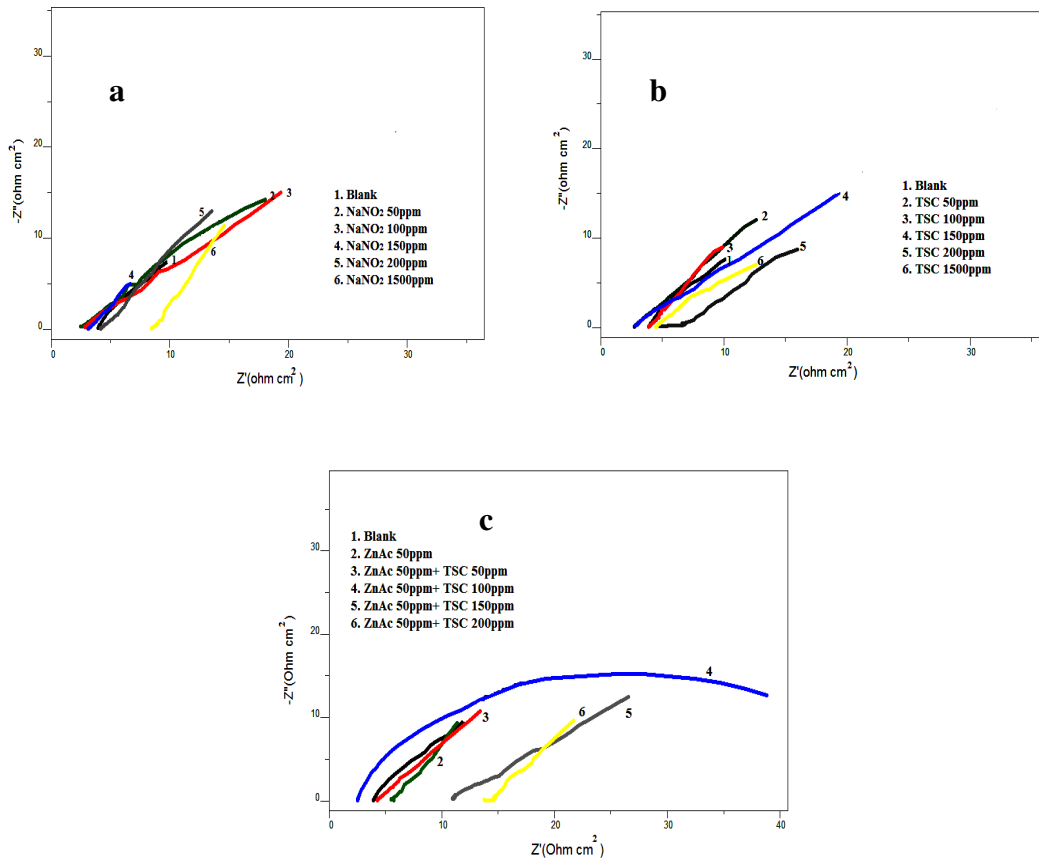


Figure 2.6: EIS plots of steel rebar in CPS containing a) sodium nitrite b) TSC and c) ZnAc+TSC at different concentrations

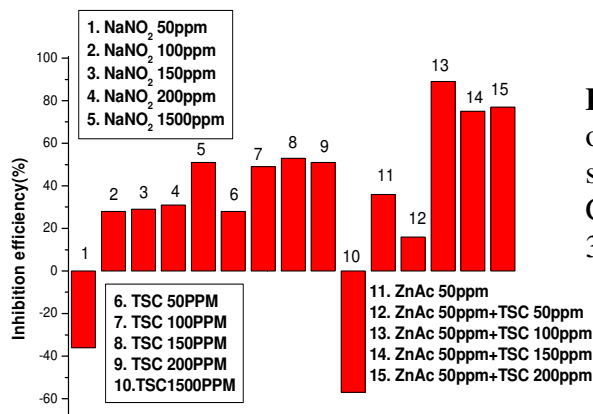


Figure 2.7: Comparison of $\eta_{EIS}\%$ of various systems on steel rebar in CPS contaminated with 3.5% NaCl at 30⁰C

Half cell potential analysis

Measurement of half cell potential of steel rebar gave a rough idea about the probability of corrosion. It has been generally accepted by the scientists that more negative the half cell potential, greater will be the possibility of corrosion. Half cell potentials of steel rebar immersed in concrete pore solution for a period of 24 hour in the presence and absence of various compounds are given in the Table 2.4 and compared with the help of a bar diagram (Figure 2.8). According to the data, the steel rebar immersed in concrete pore solution (blank) showed a potential of -460 mV against SCE. This is a clear indication of high corrosion rate of steel rebar. A regular increase of electrode potential (towards cathodic) was noted with the addition of TSC. But as the concentration reaches 200ppm, electrode potential is shifted to more anodic side. At 1500ppm of TSC concentration, the electrode potential of the steel rebar was -518mV, indicating that the corrosion rate of steel rebar increased tremendously. Both half cell potential measurements and polarization studies revealed the similar corrosion behaviour of steel rebar in CPS solution. On comparing the potentials of steel rebars in CPS-NaNO₂ solution with those rebars treated with CPS-TSC solution, it can be concluded that TSC is acting as a better corrosion inhibiting agent than nitrite at lower concentrations. The steel rebar treated with concrete pore solution containing 100ppm TSC and 50ppm ZnAc displayed very low anodic potential (-283mV), suggesting that this particular combination works well on the steel surface to reduce the corrosion. Similar result was obtained by potentiodynamic polarization studies.

Table 2.4: Half cell potential(mV) measured on steel rebar immersed in contaminated CPS containing NaNO₂, TSC and TSC-ZnAc(50) svstems at 24 hour

Conc (ppm)	NaNO ₂	TSC	TSC+ ZnAc
0	-460	-460	-460
50	-358	-333	-349
100	-338	-314	-283
150	-328	-307	-304
200	-346	-316	-307
1500	-293	-518	-508

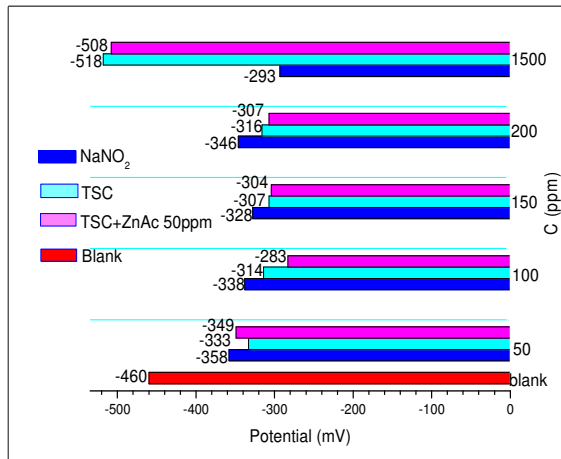


Figure 2.8: Comparison of half cell potentials of steel rebar in contaminated CPS containing NaNO₂, TSC and TSC-ZnAc systems

Infrared spectral analysis

To investigate mechanism of molecular interaction on steel surface in simulated CPS, IR spectral studies were performed. Due to the presence of many species in the simulated concrete pore solution, it is rather difficult to interpret the spectrum of deposited products on steel rebar surface precisely. However, on close inspection of the spectra it is obvious that considerable shift in the frequencies occurred for the samples treated with and without ZnAc. Surface deposition of steel rebar mainly consists of mixtures of compounds such as hydrated ferric oxide, ferrous and ferric hydroxides, ferrous chloride etc. In the IR spectrum of products on steel rebar surface (blank), a broad band appeared at 3375 cm⁻¹ may be due to -OH

stretching frequency of $\text{Fe}(\text{OH})_2$ or amorphous hydrated ferric oxide (or both) [73]. The broadness of this peak is considerably reduced in the IR spectra of steel samples treated with TSC and TSC-ZnAc. This is due to the interaction of these species with $\text{Fe}(\text{OH})_2$. The bending frequency of $-\text{OH}$ appeared in the spectrum of blank (1619 cm^{-1}) was also shifted to lower frequency side in other two samples. Signals observed at $\sim 440\text{ cm}^{-1}$ in the IR spectrum of blank and citrate treated steel rebar are lowered to 401 cm^{-1} in TSC-ZnAc treated steel rebar. This can be attributed to the change of lattice vibration of free OH^- ions due to the interaction of O-H-Zn-Citrate . Peaks displayed at 1392 and 1383 cm^{-1} in the IR spectra are due to the deformation of $-\text{CH}_2$ group present in sodium citrate. A weak peak appeared at 1471 cm^{-1} in the IR spectrum of surface products of blank specimen is due to the existence of ferroxihite phase associated with the amorphous ferric oxide on the steel surface. Figure 2.9 represents the IR spectrum of products deposited on steel rebar surface.

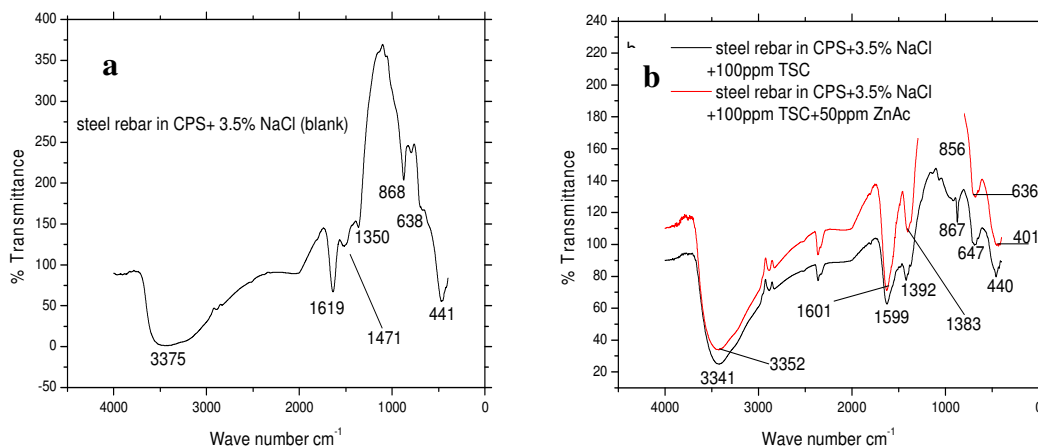


Figure 2.9: IR spectrum of corrosion products on steel rebar in CPS **a)** contaminated with 3.5% NaCl **b)** containing 3.5% NaCl+ TSC (100ppm) and 3.5% NaCl+ TSC (100ppm)+ ZnAc (50 ppm)

Microscopic surface analysis

Visual examination of the micrographs showed that the ferric oxide layer formed on the steel rod immersed in the sample solutions was uneven, brittle, blistered and black in colour, quite different from the bare, where it was dark brown in colour. Removal of oxide film from the immersed steel rebars was easier due to the non-uniform distribution over the surface as compared to the bare where it was tightly adherent. The textures of immersed steel rods in CPS were different from each other and they also differed from the bare sample. The surface morphology of the steel sample treated with concrete pore solution containing TSC (1500ppm) showed a unique appearance as its surface do not contains little or no oxide deposit. The complexing nature of citrate ions with Fe^{2+} enhanced the removal of more and more Fe atoms from the surface of rebar into the solution (Figure 2.10).

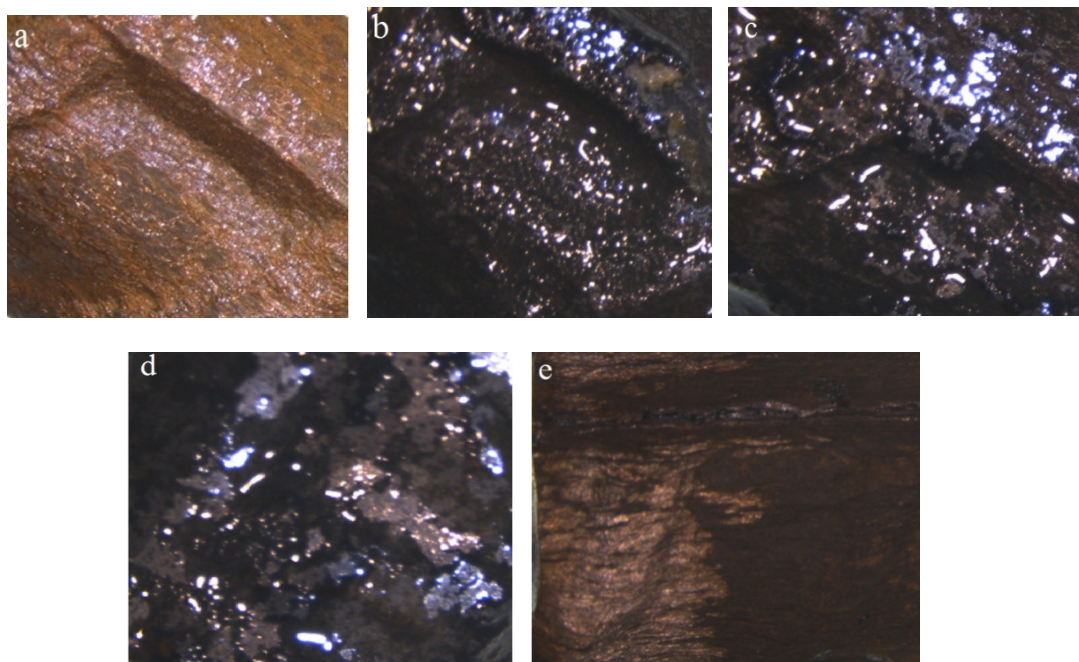


Figure 2.10: Optical micrographs of Fe rebar immersed in CPS **a)** bare **b)** with NaCl (3.5%) **c)** with NaCl (3.5%) + TSC (100ppm) **d)** with NaCl (3.5%) + TSC (100ppm) + ZnAc (50ppm) **e)** with NaCl (3.5%) + TSC (1500ppm) at 30°C.

SECTION 2

CORROSION BEHAVIOUR OF STEEL IN THE PRESENCE OF SODIUM SALTS OF PHOSPHATES AND SULPHATES IN CONCRETE PORE SOLUTION

Different sodium salts are employed as more convenient agent in many reactions. Generally sodium salts are considered as less toxic synthetic product. Since different sodium salts are easily available in our market, they can chiefly use for the corrosion inhibition study.

Preparation of inhibitor solutions

The inhibitor solutions were prepared by the addition of sodium phosphate (SP, Na_2HPO_4), monosodium phosphate (MSP, NaH_2PO_4), sodium lauryl sulphate (SLS) and pentasodium triphosphate (PST) to the working solution (CPS) to attain the concentrations 50, 150 and 1500ppm. Iron rebar having 10 cm of length was cleaned by pickling in 2M HCl solution for 20 minutes, washed, dried and dipped into these test solutions.

Potentiodynamic polarization analysis

Polarization studies were conducted on steel rebar immersed in CPS containing different concentrations of various sodium salts after a period of 3 days and the derived plots are represented in the Figure 2.15. Data obtained from polarization studies are given in the Table 2.5. From the polarization data it is revealed that the corrosion rate of steel rebar treated with monosodium phosphate (MSP) was very lower than that of the steel rebar immersed in CPS without MSP (blank), ie; MSP acted as a very potential corrosion inhibitor with above 90%

efficiency at every concentrations. SLS and PST showed remarkable inhibition efficiency at 50 and 1500ppm concentrations, but both were acted as poor corrosion inhibitor at 150ppm concentration. The response of steel rebar immersed in CPS solution containing SP is quite different from others. Even if they exhibited appreciable inhibition efficiency in 150ppm concentration, they have very low efficiency in 1500ppm and showed antagonistic nature in 50ppm concentration.

From the Tafel plots (Figure 2.15) it is clear that, at all concentrations of SP, SLS and PST the anodic slopes of Tafel curves significantly changed as compared with steel rebar immersed in blank CPS solution. Thus it can be concluded that these inhibitors mainly influence on the anodic process of corrosion and acted as anodic inhibitor. But for MSP both anodic and cathodic slopes were not changed considerably. This established that MSP molecules are equally affecting on cathodic and anodic sites, suggesting that it acts as a mixed type inhibitor.

The gradation in the corrosion inhibition efficiency of SLS can be explained by the following hypothesis. At lower concentration, SLS molecules adjacent to the steel rod can bind with ferrous ions and prevent diffusion of water molecules and chloride ions towards the surface of steel considerably (Figure 2.11). Thus they protect well the steel corrosion. When concentration increases it is noticed that the corrosion rate also increased significantly. It can be explained by the process of miscelle formation, which is the characteristic property of surfactants like SLS (Figure 2.12). Generally micelles are generated from the compounds which have geometrically separated hydrophilic and hydrophobic moieties. When more number of SLS molecules comes closer, there is a chance for the miscelle formation and they become unavailable for binding with iron. Thus rate of corrosion increases. At higher concentration, the corrosion rate was appeared to decrease appreciably

because when concentration increases, more SLS molecules, which do not participate in the miscelle formation, may be migrated towards the steel surface making coordinate bonds with ferrous ions and protect the steel surface.

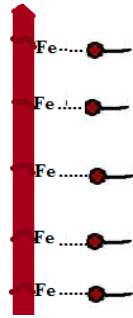


Figure 2.11: Bond formation of SLS with Fe atoms

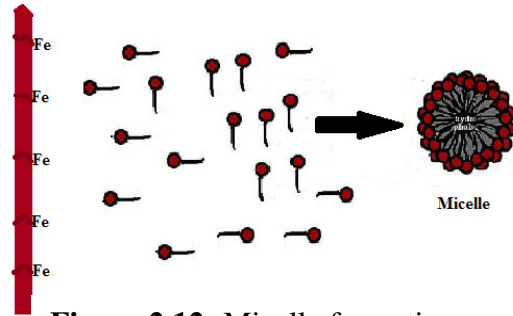
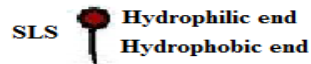


Figure 2.12: Micelle formation of SLS



The trend visible in the inhibition efficiency of PST can be explained as follows. Generally in the presence of iron atoms, PST molecules can undergo two different processes, ie; adsorption and complexation. At lower concentration, the adsorption tendency of PST molecules on iron atoms will predominate and they protect well the steel corrosion (Figure 2.13) (equation 1). When concentration increases the PST adsorption will takes place in large scale, naturally, there is a chance to change the adsorption process to complexation and form more stable Fe^{2+} -PST complex (Figure 2.14) (equation 2). It leads to increase the rate of iron dissolution and increase the corrosion rate. At higher concentration, more and more PST molecules migrated towards the steel surface make coordinate bonds with ferrous ions and protect steel surface with predominant inhibition efficiency.





Figure 2.13: Adsorption of PST on iron atoms

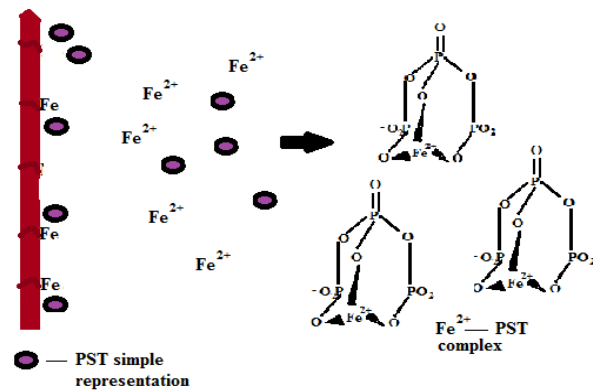


Figure 2.14: Formation of $[\text{Fe}^{2+} - \text{PST}]$ complex

The significant variation in the corrosion inhibition efficiency of sodium phosphate (SP) can be explained by the following hypothesis. The phosphates have prominent tendency to form complex with Ca^{2+} and Mg^{2+} ions and it is commonly employed for the treatment of hard water. Since at lower concentration (50ppm) all SP molecules are going to make complex with Ca^{2+} ions, they will not be available for the protection of steel surface and SP didn't exhibit inhibition efficiency. But when concentration increases, more SP molecules will be attainable and may migrated towards the steel surface from the bulk to make coordinate bonds with ferrous ions. It prevents the diffusion of chloride ions and water molecules towards the steel surface considerably and protects from the corrosion. At high concentration more SP will form Ca-phosphate complex and they have a tendency for aggregation, which is the characteristic property of calcium phosphates. Thus SP will not be available for the protection of steel surface.

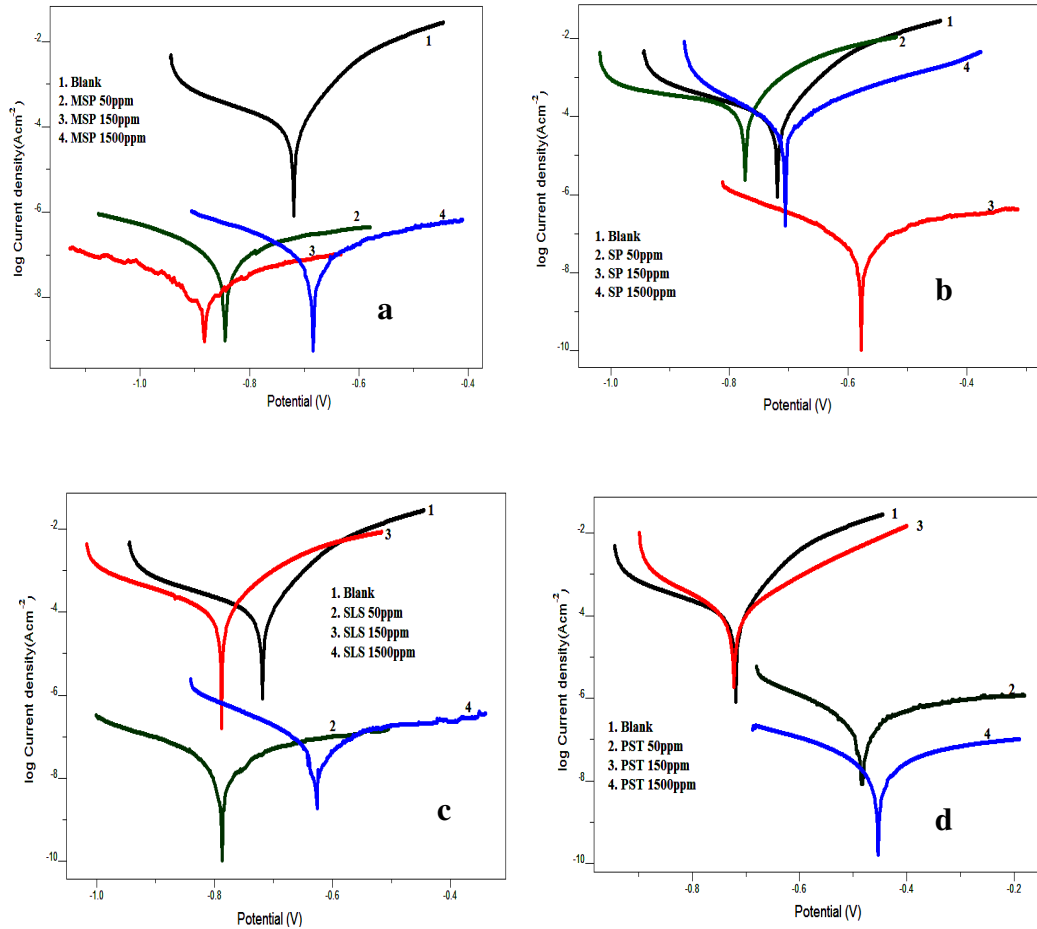


Figure 2.15: Tafel curves of steel rebar in contaminated CPS containing sodium salts a) MSP b) SP c) SLS d) PST

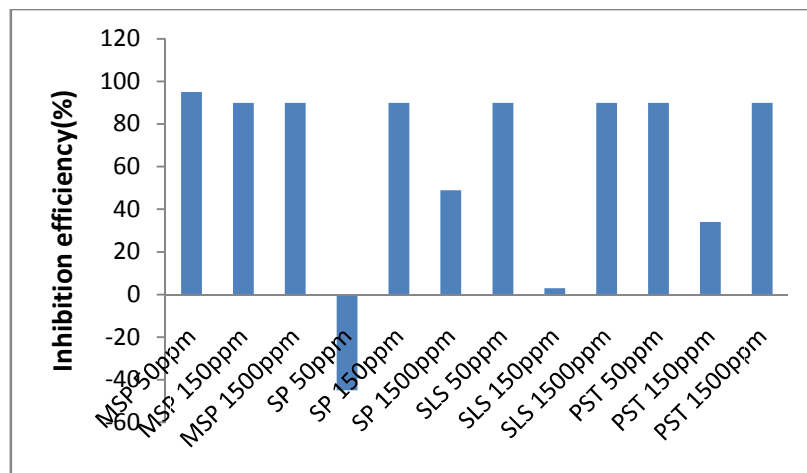


Figure 2.16: Comparison of η_{pol} % of different sodium salts on steel rebar in CPS contaminated with 3.5% NaCl.

Table 2.5: Polarization data of steel rebar immersed in contaminated CPS in the presence and absence various sodium salts at at 30⁰C

System Conc(ppm)	I _{corr} (μAcm^{-2})	b _a (mVdec ⁻¹)	-b _c (mVdec ⁻¹)	-E _{corr} (mV)	η_{pol} %
Blank	45.6	136	22	777.7	
MSP (50)	1.5	408	228	851	96
MSP (150)	4.05	318	258	883	91
MSP (1500)	2.79	329	218	691	94
SP (50)	66	178	440	841	-45
SP (150)	2.54	429	176	608	94
SP (1500)	23.0	218	123	736	49
SLS (50)	4.15	403	222	797	91
SLS (150)	44.2	166	212	836	3
SLS (1500)	2.62	667	165	656	94
PST (50)	3.62	507	170	508	92
PST (150)	30.2	155	148	735	34
PST (1500)	4.66	391	228	458	90

EIS analysis

The corrosion response of steel rebar in CPS in the presence and absence of different concentrations of sodium salts was monitored using electrochemical impedance spectroscopy and the corresponding Nyquist plots are represented in the Figure 2.17. The corrosion behaviour of steel rebar was considerably differed in the presence and absence of inhibitors. The EIS parameters of the test solutions are represented in the Table 2.6. Generally, addition of inhibitors leads to the decrease in double layer capacitance and increase of charge transfer resistance.

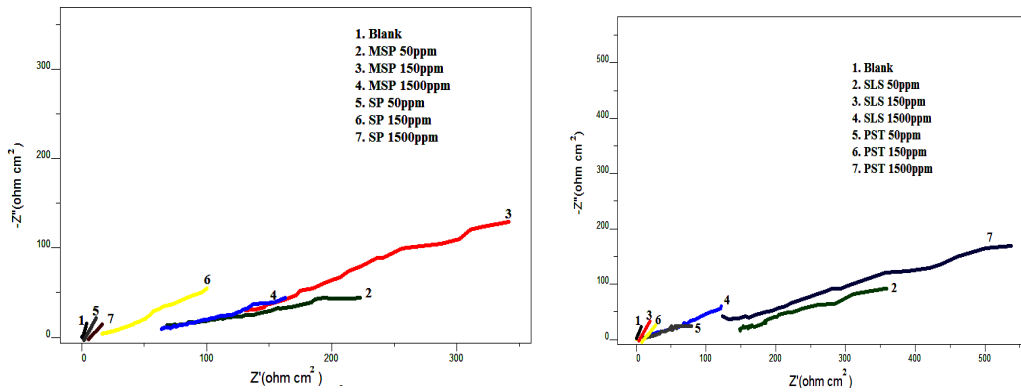


Figure 2.17: Nyquist plots of steel rebar in contaminated CPS in the presence and absence of sodium salts.

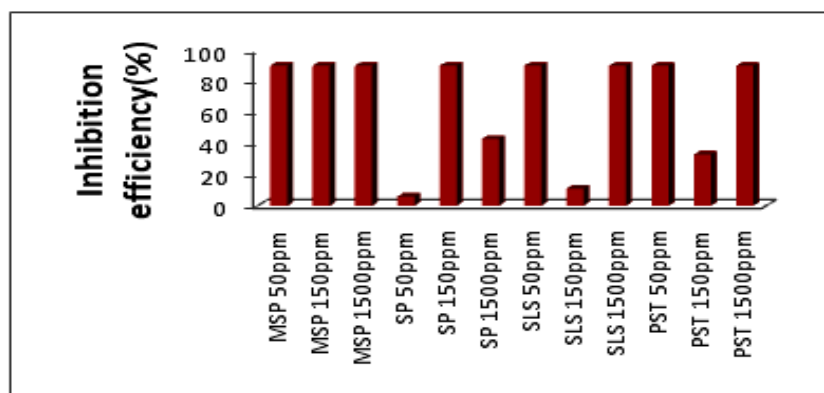


Figure 2.18: Comparison of $\eta_{EIS}\%$ of different sodium salts on steel rebar in CPS contaminated with 3.5% NaCl

The impedance data established that MSP has predominant efficiency (>90%) at all concentrations and all other sodium salts exhibited appreciable efficiency at certain concentrations only. SLS and PST showed remarkable inhibition efficiency at 50 and 1500ppm concentrations, but both were acted as poor corrosion inhibitor at 150ppm concentration. From the corrosion response data of SP, it was clear that at very low and higher concentrations SP showed poor corrosion inhibition behaviour and exhibited maximum efficiency of >90% at 150ppm concentration. These results are in good agreement with Tafel data.

Table 2.6: Electrochemical impedance data of steel rebar immersed in contaminated CPS in the presence and absence of sodium salts at 30⁰C

System Conc(ppm)	W (Ωcm^2)	R _s (Ωcm^2)	C _{dl} (μFcm^{-2})	R _{ct} (Ωcm^2)	η_{EIS} %
Blank	22.8	247	866	3.2	-
MSP (50)	6.62	262	193	108	97
MSP (150)	1.33	124	132	166	98
MSP (1500)	5.10	219	163	137	97
SP (50)	2.7	249	711	3.4	6
SP (150)	8.92	334	181	231	98
SP (1500)	7.04	482	688	5.68	43
SLS (50)	5.85	578	164	204	98
SLS (150)	2.26	180	686	3.6	11
SLS (1500)	2.47	177	140	222	99
PST (50)	1.05	788	178	155	98
PST (150)	6.85	113	613	4.8	33
PST (1500)	1.40	100	173	171	98

Half cell potential analysis

Half cell potential measurements of steel rebar gave a rough idea about the probability of corrosion. It has been generally established that more negative the half cell potential, greater will be the possibility of corrosion. Half cell potentials of steel rebar in CPS for a period of 24h in the presence and absence of investigated sodium salts are depicted in the Table 2.7 and compared with the help of a bar diagram (Figure 2.19). According to the data, the steel rebar immersed in CPS (blank) showed a potential of -460mV against SCE. This is a clear indication of high corrosion rate of steel rebar. But the electrode potential values were increased in the presence of various sodium salts indicating that the corrosion rate of steel rebar decreased considerably. Both half cell potential measurements and electrochemical

investigations revealed the similar corrosion behaviour of steel rebar in CPS solution.

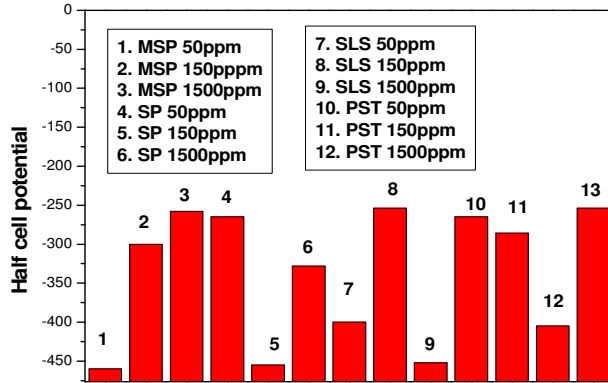


Figure 2.19: Comparison of half cell potentials (mV) of steel rebar in the presence and absence of sodium salts in contaminated CPS

Table 2.7 Half cell potential measurements of different sodium salts on steel rebar in CPS contaminated with 3.5% NaCl

System	Half cell potential(mV)	System	Half cell potential(mV)
MSP(50)	-300	SLS(50)	-254
MSP(150)	-258	SLS(150)	-452
MSP(1500)	-265	SLS(1500)	-265
SP(50)	-455	PST(50)	-286
SP(150)	-328	PST(150)	-405
SP(1500)	-400	PST(1500)	-254

Half cell potential of blank = -460

Microscopic surface analysis

Micrographs of bare steel rebar, steel rebars immersed in test solutions after the investigation period are given in the Figure 2.20. Surface of steel rebar in CPS without sodium salts contained have large amount of hydrated ferric oxide. It is evident that enhanced corrosion of the steel rebar was occurred due to the continuous contact of the contaminated concrete pore solution. It was noticed that

the surface of steel reinforcement, in CPS containing sodium salts, has a little or no oxide which proves their inhibition efficiency.



Figure 2.20: Optical micrographs of steel rebars in CPS **a)** bare **b)** in the absence of MSP **c)** in the presence of MSP

SECTION 3

CORROSION BEHAVIOUR OF STEEL IN THE PRESENCE OF PLANT EXTRACTS IN CONCRETE PORE SOLUTION

Corrosion control of steel rebar in concrete has technical and environmental importance. The use of plant extract inhibitors is a best option for protecting concrete as it is readily available and environmentally acceptable.

Preparation of inhibitor solutions

Five test solutions for the investigation were prepared by the addition of 5ml of different plant extracts to working solution (CPS). The illustration of the employed extracts and their abbreviations are represented in the Table 2.8. Iron rebar having 10 cm of length was cleaned by pickling in 2M HCl solution for 20 minutes, washed, dried and were dipped into these test solutions.

Table 2.8: Common name, scientific name and abbreviation for plant extracts

Common name	Scientific name	Abbreviation
Ginger	Zingiber officinale	ZO
Garlic	Allium sativum	AS
Christmas bush (communist pacha)	Chromolaena odorata	CO
Stonebreaker (keezharnelli)	Phyllanthus niruri	PN
Beetroot	Beta vulgaris	BV

Potentiodynamic polarization analysis

The corrosion inhibition efficacy of different plant extracts on steel rebar in the contaminated CPS was monitored using potentiodynamic polarization studies.

Polarization curve analysis helps to determine Tafel slopes, current densities and percentage of inhibition efficiency which are depicted in the Table 2.9. From the data it is evident that the steel rebar in the CPS containing plant extracts was less corroded than blank solution. Experimental study was conducted for one week and polarization measurements were taken on the third day of experiment.

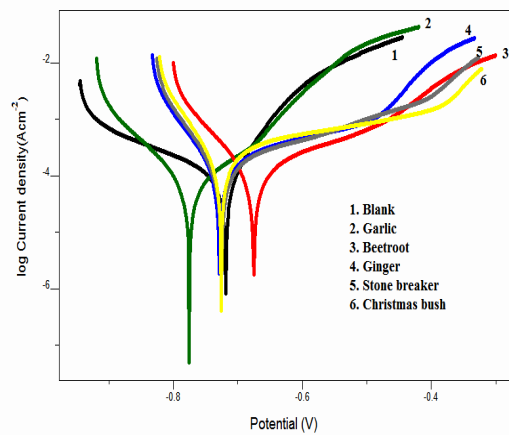


Figure 2.21: Tafel plots of steel rebar in CPS containing various plant extracts.

Table 2.9: Polarization data of steel rebar immersed in contaminated CPS in the presence and absence of various plant extract at 30⁰C

System	I_{corr} (μAcm^{-2})	b_a ($mVdec^{-1}$)	$-b_c$ ($mVdec^{-1}$)	$-E_{corr}$ (mV)	η_{pol} %
Blank	45.6	136	222	777.7	-
ZO	13.5	194	64	723	71
AS	8.72	96	93	764	81
CO	45.5	498	59	745	3
PN	21.5	264	60	733	53
BV	10.7	159	80	663	77

Figure 2.21 represents the Tafel plots obtained by the potentiodynamic polarization for the corroding steel rebar with and without the addition of various plant extracts. From the data, it was noticed that the i_{corr} have low values in the

presence of plant extracts leading to exhibit significant corrosion inhibition efficiency. Extracts AS, PN, ZO and BV inhibited the corrosion of steel rebar appreciably. However, on comparing with others, AS (Garlic) extract acted as a potential corrosion inhibitor with maximum efficiency of 81% and CO (Christmas bush) extract acted as a poor inhibitor with minimum efficiency of 3%. The Tafel parameters indicated that the inhibition efficiency follows the order, CO < PN < ZO < BV < AS. As described in earlier cases, there was a considerable shift occurred in anodic curves implies that all investigated plant extracts have acted as the anodic inhibitors for steel rebar in contaminated CPS.

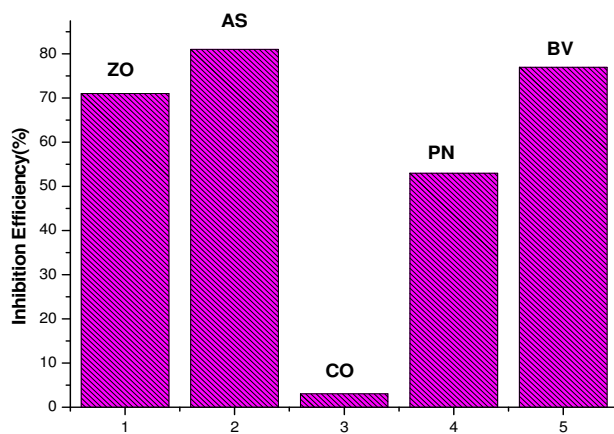


Figure 2.22: Comparison of $\eta_{pol}\%$ of various plant extracts on steel rebar in CPS contaminated with 3.5% NaCl at 30⁰C

EIS analysis

The corrosion response of steel rebar in CPS in the presence and absence of various plant extracts was monitored using electrochemical impedance spectroscopy and the corresponding Nyquist plots are represented in Figure 2.23. The corrosion behaviour of steel rebar was considerably differed in the presence and absence of plant extracts. The EIS parameters of the test solutions are represented in table 2.10. Generally, addition of plant extracts leads to the decrease in double layer capacitance and increase of charge transfer resistance. From the impedance data it is quite evident that the steel rebar in the CPS containing plant extracts was less

corroded than blank solution except CO (Christmas bush). The corrosion rate of steel rebar treated with CO extract was higher than that of the steel rebar immersed in CPS without extract (blank), ie; CO acted as a corrosion antagonist. Extracts AS, PN, ZO and BV inhibited the corrosion of steel rebar appreciably. However, on comparing with others, AS (Garlic) extract acted as a potential corrosion inhibitor with maximum efficiency of 81% and CO (Christmas bush) extract acted as a corrosion antagonist with negative inhibition efficiency. From EIS parameters, it is concluded that the inhibition efficiency follows the order, CO < PN < ZO < BV < AS. These results are in good agreement with Tafel data.

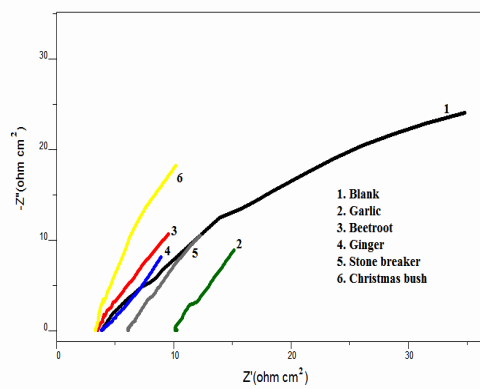


Figure 2.23: Nyquist plots of steel rebar in contaminated CPS in the presence and absence of plant extracts

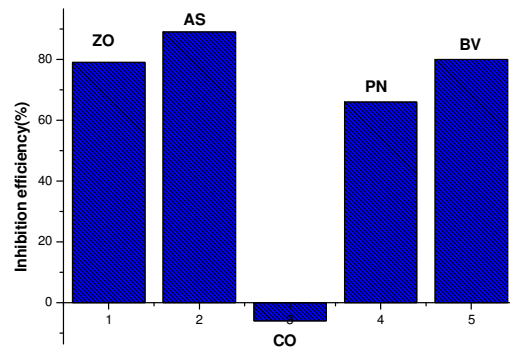


Figure 2.24: Comparison of η_{EIS} % of various plant extracts on steel rebar in CPS contaminated with 3.5% NaCl at 30°C

Table 2.10 : Electrochemical impedance parameters of steel rebar in CPS in the presence and absence of plant

System	W (Ωcm^2)	R_s (Ωcm^2)	C_{dl} (μFcm^{-2})	R_{ct} (Ωcm^2)	η_{EIS} %
Blank	22.8	247	866	3.2	-
ZO	10.2	14.5	385	15.5	79
AS	8.17	21.8	220	31.2	89
CO	17.3	72.7	800	3	-6
PN	13.1	19.8	458	9.39	66
BV	17.9	22.7	352	16.2	80

Half cell potential analysis

Half cell potential measurements of steel rebar gave a rough idea about the probability of corrosion. It has been generally established that more negative the half cell potential, greater will be the possibility of corrosion. Half cell potentials of steel rebar in CPS for a period of 24h in the presence and absence of various plant extracts are depicted in the Table 2.11 and compared with the help of a bar diagram (Figure 2.25). According to the data, the steel rebar immersed in CPS (blank) showed a potential of -460 mV against SCE. This is a clear indication of high corrosion rate of steel rebar. A significant increase of electrode potential (towards cathodic) was noted in the presence of plant extracts indicates their corrosion inhibition efficiency. But in the presence of CO, the electrode potential of the steel rebar was -605 mV, indicating that the corrosion rate of steel rebar increased tremendously. On comparing the potentials of steel rebars in CPS with various plant extracts, it can be concluded that AS is acting as a potential corrosion inhibiting agent in CPS with an electrode potential of -225 mV. Both half cell potential measurements and electrochemical investigations revealed the similar corrosion behaviour of steel rebar in CPS solution.

Table 2.11: Half cell potential (mV) measured on steel rebar immersed in contaminated CPS containing plant extracts at 24 hour

System	Blank	ZO	AS	CO	PN	BV
Half cell potential(mV)	-460	-410	-225	-605	-390	-400

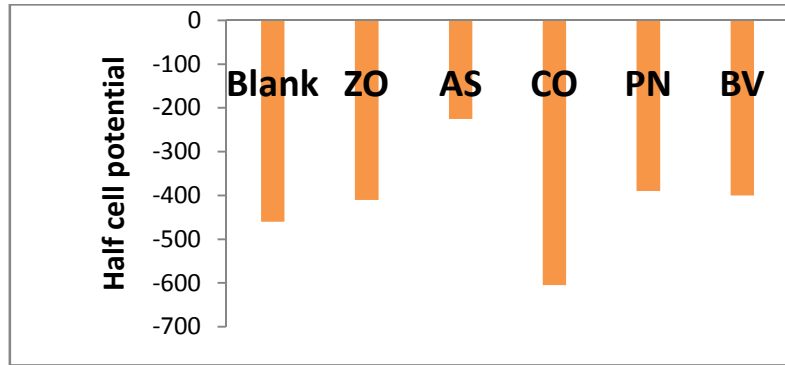


Figure 2.25: Comparison of half cell potentials of steel rebar in contaminated CPS containing various plant extracts

Mechanism of inhibition

Generally the plant extracts contains different types of compounds such as saponins, flavonoids and steroidal sapogenins and other phenolic compounds. Among these compounds flavanoids and phenolic compounds are assumed as the species which are mainly responsible for the inhibition efficiency of the compounds, since they contain aromatic rings. The corrosion inhibition mechanism of the compounds can be explained by the adsorption process of compounds on the steel rebar surface and the overall mechanism is depicted in the Figure 2.26.

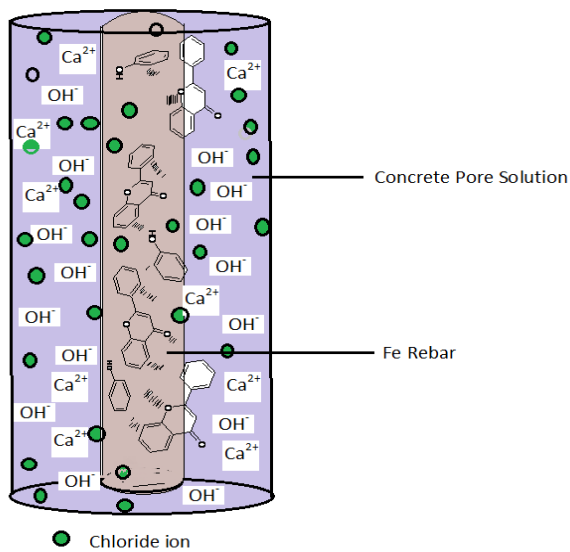


Fig 2.26: Mechanism of interaction of flavanoids and phenolic compounds on steel rebar in CPS

Microscopic surface analysis

Micrographs of bare steel rebar, steel rebars immersed in test solutions after the investigation period are given in Figure 2.27. Surface of steel rebar in CPS without plant extract have contained large amount of hydrated ferric oxide. It is evident that enhanced corrosion of the steel rebar was occurred due to the continuous contact with the contaminated concrete pore solution. It was noticed that the surface of steel reinforcement in CPS containing plant extract has a little or no oxide which proves their inhibition efficiency.

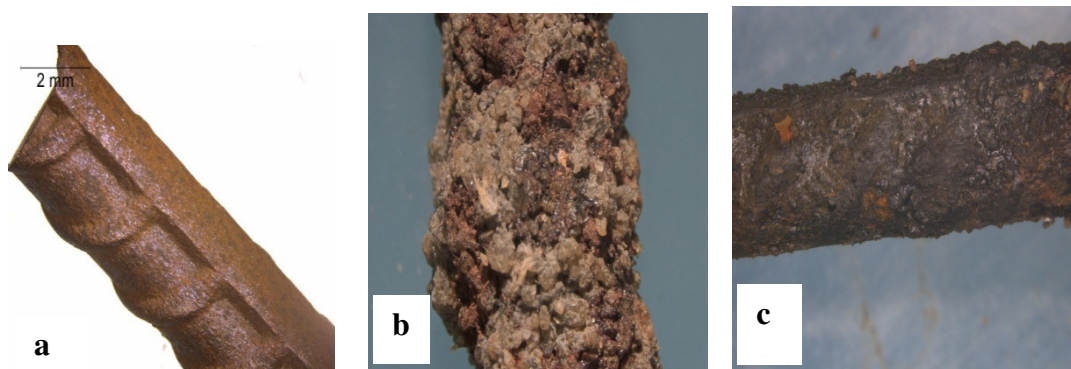


Figure 2.27: Optical micrographs of steel rebars in CPS a) bare b) in the absence of plant extract c) in the presence of plant extract of AS

SECTION 4

CORROSION BEHAVIOUR OF STEEL IN THE PRESENCE OF SCHIFF BASES IN CONCRETE PORE SOLUTION

Generally water soluble inhibitors can use for the corrosion study in concrete pore solution. Since the newly synthesized Schiff bases are highly water soluble, they can consider for the present study.

Preparation of inhibitor solutions

The inhibitor solutions were prepared by the addition of previously synthesized water soluble imines namely 2APPH and 2APSC to the working solution (CPS) to attain the concentration of 100ppm. Steel rebar having 10 cm of length was cleaned by pickling in 2M HCl solution for 20 minutes, washed, dried and were dipped into these test solutions.

Potentiodynamic polarization analysis

The corrosion inhibition efficacy of synthesized imines on steel rebar in the contaminated CPS was monitored using potentiodynamic polarization studies. Polarization curve analysis helps to determine Tafel slopes, current densities and percentage of inhibition efficiency which are depicted in the Table 2.12. From the data it is quite evident that the steel rebar in the CPS containing imines was less corroded than blank solution. Experimental study was conducted for one week and polarization measurements were taken on the third day of experiment. Figure 2.28 represents the Tafel plots obtained by the potentiodynamic polarization studies on the corroding steel rebar with and without the addition of imines.

Table 2.12: Polarization data of steel rebar immersed in contaminated CPS in the presence and absence of imines.

System	I_{corr} (μAcm^{-2})	b_a (mVdec^{-1})	$-b_c$ (mVdec^{-1})	$-E_{\text{corr}}$ (mV)	η_{pol} %
Blank	45.6	136	222	777.7	-
2APPH	32	273	180	688	30
2APSC	20	168	132	724	57

From the observation of the Table 2.12, it was noticed that the i_{corr} have low values in the presence of imines leading to exhibit corrosion inhibition property. The Tafel analysis results indicated that the investigated imines have low inhibition efficiency in contaminated CPS contrary to the observation in acidic media and comparably little more efficiency was exhibited by 2APSC than 2APPH. As described previously, there was a considerable shift occurred in anodic curves implies that both imines acted as the anodic inhibitors for steel rebar in contaminated CPS.

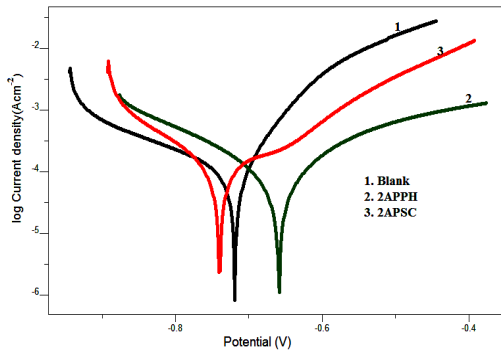


Figure 2.28: Tafel plots of steel rebar in contaminated CPS containing imines.

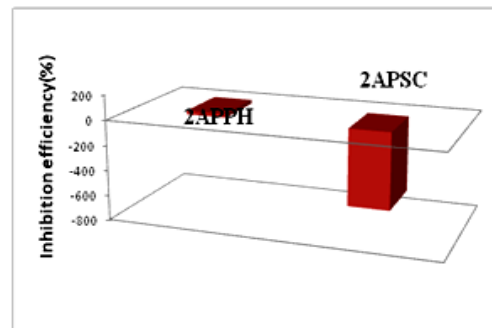


Fig 2.29: Comparison of $\eta_{\text{pol}}\%$ of imines on steel rebar in CPS contaminated with 3.5% NaCl at 30°C

EIS analysis

The corrosion response of steel rebar in CPS in the presence and absence of both imines were monitored using electrochemical impedance spectroscopy and the corresponding Nyquist plots are represented in the Figure 2.30. The corrosion behaviour of steel rebar was considerably differed in the presence and absence of

Schiff bases. The EIS parameters of the test solutions are represented in the Table 2.13. Generally, addition of Schiff bases leads to the decrease in double layer capacitance and increase of charge transfer resistance.

Table 2.13: Electrochemical impedance parameters of steel rebar in CPS in the presence and absence of imines

System	W (Ωcm^2)	R_s (Ωcm^2)	C_{dl} (μFcm^{-2})	R_{ct} (Ωcm^2)	η_{EIS} %
Blank	22.8	247	866	3.2	
2APPH	14.7	154	351	5.11	37
2APSC	20.5	148	312	8.40	62

From the impedance data it is revealed that the steel rebar in the CPS containing imines was less corroded than blank solution which implies the marked corrosion inhibition capacity on steel rebar. However, they exhibited low inhibition efficiency in contaminated CPS contrary to the observation in acidic media. The imine 2APSC possess little bit more efficiency than 2APPH and the results are in good agreement with Tafel analysis.

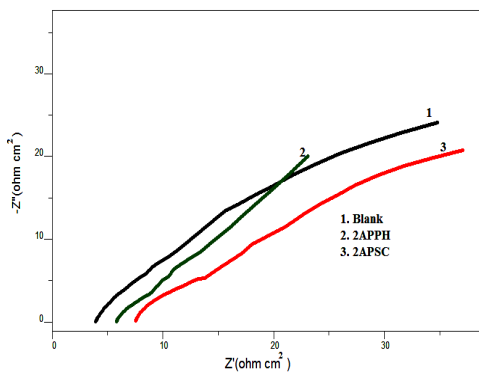


Figure 2.30: Nyquist plots of steel rebar in contaminated CPS in the presence and absence of imines

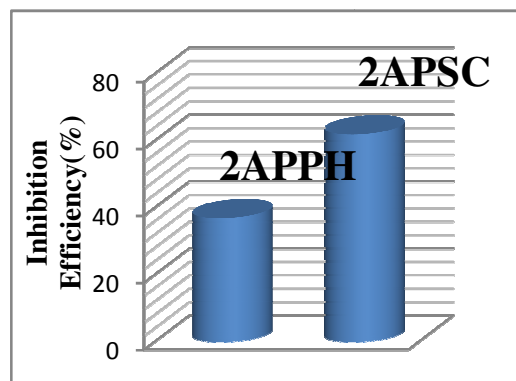


Figure 2.31: Comparison of $\eta_{\text{EIS}}\%$ of imines on steel rebar in CPS contaminated with 3.5% NaCl at 30°C

Half cell potential analysis

Half cell potential measurements of steel rebar gave a rough idea about the probability of corrosion. It has been generally established that more negative the half

cell potential, greater will be the possibility of corrosion. Half cell potentials of steel rebar in CPS for a period of 24 hour in the presence and absence of investigated imines are depicted in the Table 2.14 and compared with the help of a bar diagram (Figure 2.32). According to the data, the steel rebar immersed in CPS (blank) showed a potential of -460 mV against SCE. This is a clear indication of high corrosion rate of steel rebar.

Table 2.14: Half cell potential (mV) measured on steel rebar immersed in contaminated CPS containing imines at 24 hour

System	Blank	2APPH	2APSC
Half cell potential(mV)	-460	-400	-352

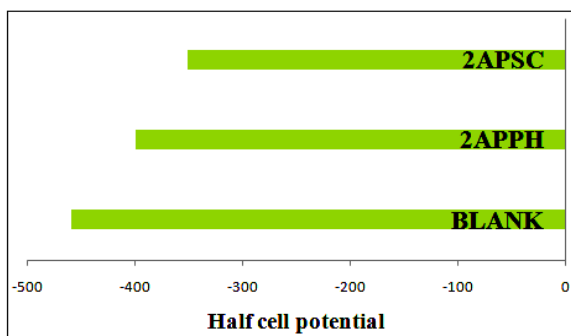


Figure 2.32: Comparison of half cell potentials of steel rebar in contaminated CPS containing imines.

A significant increase of electrode potential (towards cathodic) was noted in the presence of imines indicates their corrosion inhibition efficiency. In the presence of 2APPH and 2APSC, the electrode potentials of the steel rebar were -400mV and -352mV respectively, indicating that the corrosion rate of steel rebar decreased considerably. Both half cell potential measurements and electrochemical investigations revealed the similar corrosion behaviour of steel rebar in CPS solution.

Mechanism of inhibition

The corrosion inhibition efficacy of the both imines can be attributed to various factors including the functional group attached to the compound under study, structural backbone of the compound, presence of hetero atom in the compound contributing to the high electron density and therefore high basicity, the geometry or the three dimensional orientation of the molecule contributing to the adsorption of inhibitor on steel surface and the stability of the chelated state formed.

Fig 2.33 represents the adsorption mechanism of inhibitors.

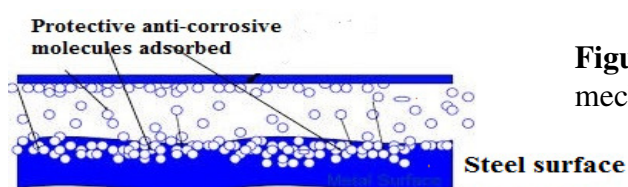


Figure 2.33: Adsorption mechanism of inhibitors

Microscopic surface analysis

Micrographs of bare steel rebar, steel rebars immersed in test solutions after the investigation period are given in the Figure 2.34. Surface of steel rebar in CPS in the presence of imines has large amount of hydrated ferric oxide. It is evident that enhanced corrosion of the steel rebar was occurred due to the continuous contact with the contaminated concrete pore solution. It was noticed that the surface of steel reinforcement in CPS containing imines contains has a little or no oxide which proves their inhibition efficiency.



Figure 2.34: Optical micrographs of steel rebars in CPS **a)** bare **b)** in the absence of 2APSC **c)** in the presence of 2APSC

PART - II B
STEEL REINFORCED CONCRETE
CORROSION



CHAPTER 1

INTRODUCTION AND REVIEW

Reinforced concrete specimens are introduced to ensure the existence and the mechanical strength throughout their service life period. Reinforced concrete structures are economically successful materials using for construction. It can be casted to various shapes and designs. Generally it is strong and performing well during its life time. However in some cases, it cannot perform satisfactorily due to the disintegration of steel rebar in concrete structures called concrete corrosion. Concrete corrosion may lead to the damage of pipelines, bridges and other important assets of concrete. When the concentration of chlorides exceeds a threshold value about 0.4 – 1 % by weight of cement, corrosion is initiated and resulting to pitting corrosion. Corrosion of steel results in the formation of rust or hydrated iron oxide, which expands in the concrete and makes internal pressure in concrete leading to concrete deterioration. But the disintegration and collapse of concrete reinforcement structures is a major problem in the field of construction [74-79]. CO₂ from the surroundings and chloride ions present in the sea water have tendency to enter into the concrete structures and the concrete interstitial solution become aggressive more than before. Disintegration of the steel reinforcement by the chloride ions occurs locally and resulting to pitting corrosion [80-85]. Alkaline compounds in the concrete structures leads to the passivation of the reinforcement [86-90]. Replacing of damaged concrete specimens have large cost and may adversely affect the Gross Domestic Product (GDP) of the country. Researchers, for the last two decades, have been attracted to discover an effective and more economic method to prevent the concrete reinforcement corrosion [91-94].

Mixing of the corrosion inhibitors with the concrete mixture during casting period is the most practical solution to control the steel reinforcement corrosion [95-100]. An ideal corrosion inhibitor has the ability to protect concrete without affecting its mechanical properties. The corrosion inhibition mechanism of the inhibitors can be explained by increasing the threshold value of chloride ion, lowering of the diffusion rate of chlorides, and reducing the rate of cathodic and anodic process of corrosion.

Economically available corrosion inhibitors contain either inorganic or organic compounds such as sodium nitrite, amino ethanols, sodium monofluorophosphate etc [101, 102]. Because of the toxicity, the use of nitrites is not recommended and at elevated chloride concentrations the efficiency of organic inhibitors are questionable. Thus many researchers and scientists are always trying to find out more efficient, simple and economic admixtures to resist the steel reinforced concrete corrosion [103-105].

Effective inhibitors for steel reinforced concrete corrosion - A Review

In 2004, Neal S. Berke *et.al.*, studied the prolonged efficiency of steel reinforced concrete in the presence of calcium nitrite corrosion inhibitor [106]. Calcium nitrite is widely used as a corrosion inhibitor, due to its eminent inhibitor properties. They established the chloride levels at which the protecting capacity of the calcium nitrite will effectively occur. Furthermore, they demonstrated that how the obtained results can apply to make use of reinforced concrete structures with prolonged efficiency of 50–100 years.

In 2006, M. Ormellese *et.al.*, investigated the efficiency of three organic inhibitors of amine-esters, aminoalcohols and alkanolamines in resisting carbon steel corrosion in concrete structures contaminated with a 3.5% sodium chloride solution

[107]. Inhibitors were mixed with the concrete in dosage recommended by the manufacturers. The efficiency of the inhibitors has been measured by rebar corrosion evaluation in reinforced concrete structures and by visual inspection of rebar after the tests of 3 years.

D. M. Bastidas *et.al.*, in 2013, performed a comparative study on the corrosion inhibition efficiency of three phosphates such as sodium monofluorophosphate ($\text{Na}_2\text{PO}_3\text{F}$), disodium hydrogen phosphate (Na_2HPO_4) and trisodium phosphate (Na_3PO_4). Investigations were conducted by OPC (ordinary Portland cement) [108]. The inhibitors were applied by two ways, (1) OPC specimens immersed in phosphate solutions (migrating corrosion inhibitor) (2) phosphate powders mixed with a fresh OPC. The efficiency was measured using wavelength-dispersive electron microprobe analysis, X-ray diffraction, linear polarisation resistance and electrochemical corrosion potential.

The effectiveness of maize gluten meal extract (MGME) for concrete reinforcement corrosion was established by Zhaocai Zhang *et.al.*, in 2018 [109]. The results indicated that the MGME has an eminent inhibition efficiency including Glu and Leu, with efficiency of 83.15% and 79.27%, respectively. The antagonistic behaviour between Glu and Leu in MGME and the efficiency of MGME is monitored by the electrochemical measurements and XPS analysis.

Scope and objectives of the present investigation

Corrosion process is responsible for many losses in different fields, mainly in the industrial areas. Among the numerous methods to prevent destruction of the steel surface, the mixing of corrosion inhibitor is considered as one of the best method for corrosion protection. Historically, the usage of corrosion inhibitors had great acceptance in the industrial field due to their eminent anti-corrosive characters.

However, many inhibitors have a secondary effect, they lead to environmental damage. Thus the invention of eco - friendly inhibitors have important relevance in modern research field.

The present investigation focuses to study the inhibition efficiency of different sodium salts such as monosodium phosphate, sodium phosphate, sodium lauryl sulphate, sodium nitrite and pentasodium triphosphate for 480 days to inhibit the steel reinforced concrete corrosion in concrete specimen contaminated with NaCl. The various techniques like half cell potential measurements, gravimetric studies and electrochemical studies such as impedance spectroscopy and Tafel polarization study are proposed to find out the corrosion inhibition efficiency of compounds. The FTIR spectroscopic method and microscopic studies using Leica Stereo Microscope were also planned to explain the interaction mechanism of the added compounds. Concrete strength measurements were taken to find out the effect of added inhibitors on the mechanical properties of the concrete structures.

CHAPTER 2

MATERIALS AND METHODS

This chapter includes the details about the common reagents, materials and the procedure used for the synthesis and corrosion study of the investigated sodium salts mixed with concrete specimen contaminated with NaCl.

Reagents and Materials

Portland cement (Malabar Cements Ltd, Kerala), employed for the preparation of concrete specimen, was procured from the market. Each rectangular block of concrete specimen having dimension 200x80x80mm was prepared by mixing water and cement in the ratio 0.5. The ratio between cement, fine aggregate and coarse aggregate was 1:1.5:3 which will exactly mimic M-20 grade concrete. The approximate composition of steel rod was estimated by EDAX method: 0.1 % P, 0.62 % Mn, 0.021 % Si, 0.04 % S and rest Fe. Steel rebars were cut (22 cm) and immersed in 2M HCl for 10 minutes for removing the rust, washed with distilled water, degreased with acetone, dried, weighed and used as the reinforcement in concrete. After a period of 24 hour, the test specimens were removed from the mould and cured for 30 days for the proper hydration and setting of the cement. After the curing period, five sides of the test specimens were coated with epoxy resin and one open reservoir (100x40x20mm) was built on the remaining side with polypropylene and silicon adhesive. 25mL 3.5% NaCl was added to the reservoir of the specimens and kept for 2 days. This will ensure the complete diffusion of NaCl throughout the specimen. This process was repeated three times during 30-60 days. Chemicals such as Trisodium citrate (98%), sodium chloride (>99.9 %), NaNO₂ (EMSURE®), zinc acetate (>99%), monosodium phosphate, sodium phosphate,

pentasodium triphosphate and sodium lauryl sulphate were procured from Merck millipore.

Electrochemical corrosion investigations

Three electrode cell assembly consisting of steel reinforcement present in concrete as working electrode, concrete specimen covered with a stainless steel mesh as counter electrode and saturated calomel electrode (SCE) as reference electrode were used for the electrochemical studies. For good electrical contact a wet sponge was used on the concrete surface between SCE and concrete surface.

Potentiodynamic polarization analysis

A potential range of +250 to -250 mV with a sweep rate of 1mV/s was employed for the potentiodynamic study. Corrosion current densities and the inhibition efficiency were calculated by the slope analysis of Tafel curves using the following equation.

$$\eta_{\text{pol}} \% = \frac{i_{\text{corr}} - i'_{\text{corr}}}{i_{\text{corr}}} \times 100$$

where i_{corr} and i'_{corr} are corrosion current densities of steel rebar in the absence and presence of inhibitor respectively.

EIS analysis

EIS studies were conducted at constant potential in the frequency range 1 KHz to 100 mHz with 10mV amplitude excitation signal. The charge transfer resistance (R_{ct}) was evaluated by the analysis of the Nyquist curves and Bode plots using suitable equivalent circuit and inhibition efficacy was determined by the equation.

$$\eta_{\text{EIS}} \% = \frac{R'_{\text{ct}} - R_{\text{ct}}}{R_{\text{ct}}} \times 100$$

where R'_{ct} and R_{ct} are the charge transfer resistance of working electrode with and without inhibitor respectively. Polarization and EIS measurements were conducted using Ivium compactstat-e electrochemical work station (iviumsoft).

The equivalent circuit fitted for EIS measurements (Figure 2.35) consists of solution resistance (R_s) which is connected in series to double layer capacitance (C_{dl}) and this combination is connected in parallel to a series combination of Warburg resistance (W) and charge transfer resistance (R_{ct}).

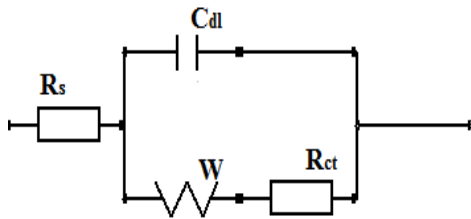


Figure 2.35: Equivalent circuit fitted for EIS measurements of steel reinforcement in concrete

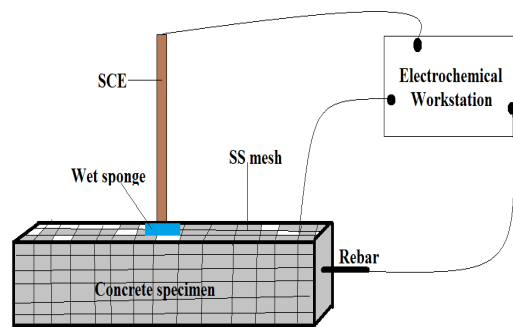


Figure 2.36: Three electrode circuit for electrochemical studies

Half cell potential analysis

For a quick determination of the corrosion behaviour of steel specimen in different medium, half cell potential measurements were conducted using saturated calomel electrode (SCE) and high impedance voltmeter (HP E2378A). In this electrochemical cell assembly, steel specimen and SCE were acted as anode and cathode respectively. Half cell potential of steel specimen was evaluated by deducting the EMF from standard electrode potential of SCE at 30⁰C. Sixteen readings of half cell potential values were measured monthly once during 480 days.

Gravimetric analysis

Before casting the concrete blocks, each steel rebars were pickled with 2M HCl for 10 minutes, washed with water, degreased with acetone, dried and weighed.

The surface area of all reinforcements was same (10.5cm²). After 480 days, concrete blocks were broken and the steel reinforcements were taken outside, pickled using 2M HCl for 15 minutes to remove the adhered rust, washed with water, dried and weighed. From the weight loss of the steel specimens, approximate corrosion inhibition efficiency of inhibitors was calculated by equation,

$$\eta\% = \frac{w_0 - w}{w_0} \times 100$$

where w and w₀ are the weight loss of steel rebar with and without inhibitor

Infrared spectral analysis

After 480 days of electrochemical investigation the steel specimens were taken outside from the concrete and Fourier Transform Infra-Red spectroscopic study (FTIR) of the scratched products on the steel reinforcement was conducted using KBr pellet method. The spectrum was recorded in the range 400-4000cm⁻¹ using Shimadzu IR Affinity-1 model FT-IR spectrophotometer.

Microscopic surface analysis

After 480 days of electrochemical investigation the steel specimens were taken outside from the concrete and analysed using a high resolution optical microscope (Leica Stereo Microscope-No. S8ACO). This study mainly aims to understand the surface modifications occurred for steel specimen during the period of investigation.

Compressive strength analysis

The effect of inhibitors on the strength of concrete was determined by compressive strength analysis of concrete by means of a standard vibration machine (Make AIMIL) after 28 days. As described in experimental procedure M-20 concrete blocks of size 15cm×15cm×15cm were casted with and without inhibitors and the compressive strength were determined.

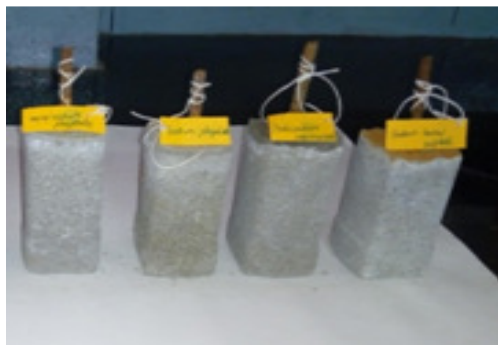
CHAPTER 3

CORROSION INHIBITION BEHAVIOUR OF SYNTHETIC PRODUCTS ON STEEL REINFORCED CONCRETE CORROSION

Investigations were carried out to establish the effectiveness of different sodium salts to inhibit the corrosion of steel rebar in concrete specimen contaminated with chloride. Inhibition efficiency of these systems was studied by gravimetric method, electrochemical techniques such as potentiodynamic polarization and half cell potential measurements. FT-IR spectral investigations of the film deposited on steel surface were carried out for understanding the corrosion inhibition mechanism. Microscopic surface analysis was conducted to obtain the surface morphological behaviour of steel rebar. Detailed investigations of the corrosion inhibition properties of various sodium salts on steel reinforced concrete corrosion are well documented in this chapter as two sections.

SECTION 1: Effect of sodium salts of citrate and citrate – acetate mixture on steel reinforced concrete corrosion.

SECTION 2: Effect of sodium salts of nitrite, phosphate and sulphate on steel reinforced concrete corrosion.



SECTION 1

CORROSION INHIBITION BEHAVIOUR OF SODIUM SALTS OF CITRATE AND CITRATE- ACETATE MIXTURE ON STEEL REINFORCED CONCRETE CORROSION

The main purpose of the present investigation is to establish the durability of concrete steel reinforcement in the presence of some commercially available compounds.

Preparation of concrete specimens

Four sets of concrete specimens were casted as follows with and without the addition of inhibitor.

Sample 1; Cement: sand: gravel (1: 1.5: 3) + 3.5% NaCl

Sample 2: Cement: sand: gravel (1: 1.5: 3) + 3.5% NaCl + TSC (100ppm)

Sample 3: Cement: sand: gravel (1: 1.5: 3) + 3.5% NaCl + TSC (250ppm)

Sample 4: Cement: sand: gravel (1: 1.5: 3) + 3.5% NaCl + TSC (250ppm) +
Zinc acetate (50ppm)

The steel rebar was cut in 22 cm and made rust free by immersing for 10 minutes in 2M HCl, washed, degreased with acetone, dried, weighed and embedded in the concrete specimen while casting. For electrical connections, 5 cm of steel rod left outside during the process of specimen making.

Potentiodynamic polarization analysis

The inhibition efficiency of added inhibitors on steel reinforcement corrosion was investigated by polarization experiments. Three set of measurements were taken during 480 days in 160 days interval. Data obtained by the analysis of Tafel curves are given in the Table 2.15. The results indicated that the steel reinforcement in samples 2, 3 and 4 has comparatively less corroded than sample 1. Up to 320th day of investigation samples casted with TSC alone showed prominent inhibition efficiency. But it is decreased with time and displayed only around 54% on 480th day of investigation

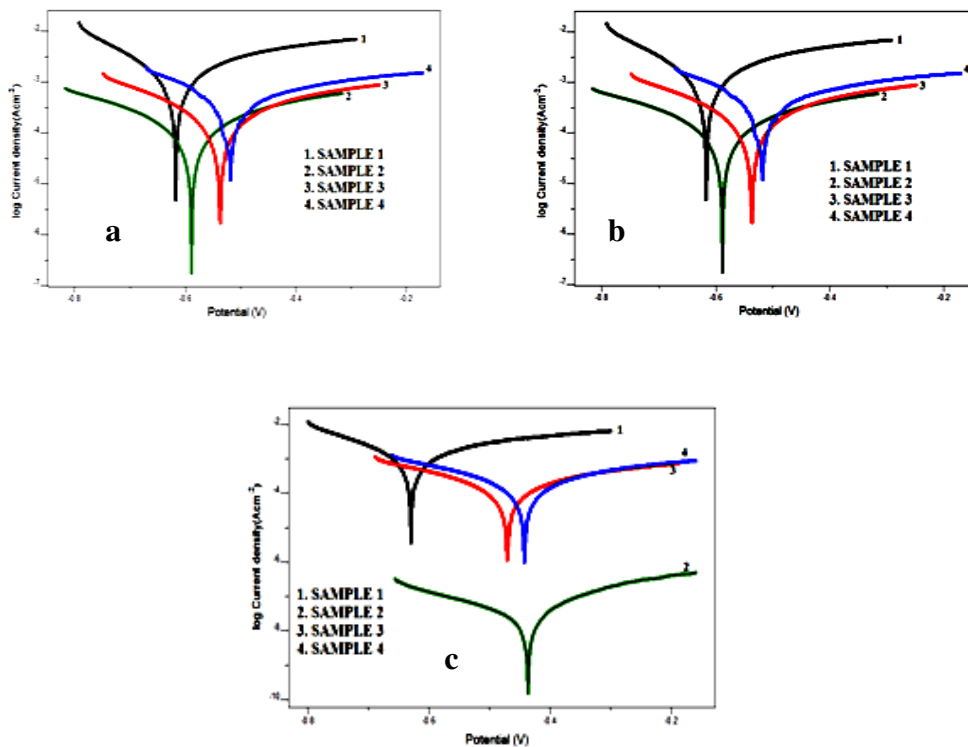


Figure 2.37: Tafel plots of reinforced steel rebar in concrete containing TSC and TSC-Zn acetate mixture **a)** 160 days **b)** 320 days and **c)** 480 days.

But samples casted with TSC and zinc acetate mixture showed above 90% efficiency throughout the experiment and their inhibition efficiency increased with time. Thus it can be concluded that TSC-Zn mixture is behaving as a good corrosion

inhibiting agent for the embedded steel in concrete structure for a long period. From the Tafel plot (Figure 2.37) it is evident that added inhibitors affected mainly on anodic process of corrosion, indicating that they act as anodic type corrosion inhibitor throughout the experiment.

Table 2.15: Polarization data of steel rebar embedded in contaminated concrete specimen in the presence and absence of added inhibitors

Time	System	I_{corr} (μAcm^{-2})	b_a (mVdec^{-1})	$-b_c$ (mVdec^{-1})	$-E_{\text{corr}}$ (mV)	η_{pol} %
160 Days	Sample 1	161.3	496	159	651	-
	Sample 2	11.59	348	251	600	99
	Sample 3	18.65	399	213	557	91
	Sample 4	40.83	565	172	544	74
320 Days	Sample 1	138.7	489	156	661	-
	Sample 2	3.59	244	217	474	92
	Sample 3	13.1	354	224	486	88
	Sample 4	16.2	358	227	460	89
480 Days	Sample 1	107	373	215	550	-
	Sample 2	49.1	323	173	651	54
	Sample 3	49.9	187	187	555	53
	Sample 4	6.81	228	226	551	99

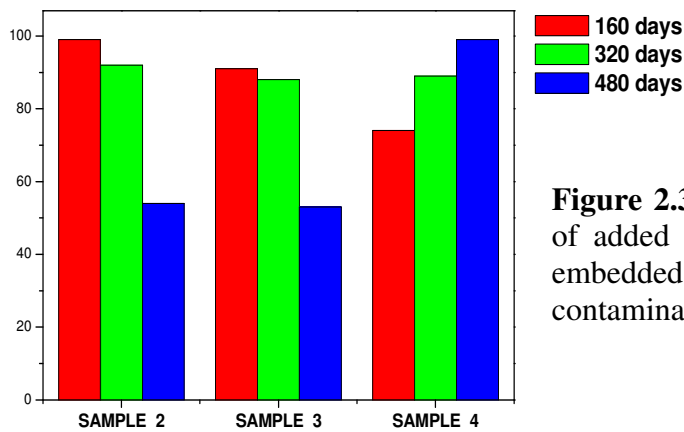


Figure 2.38: Comparison of $\eta_{\text{pol}}\%$ of added inhibitors on steel rebar embedded in concrete specimen contaminated with 3.5% NaCl.

EIS analysis

The corrosion response of reinforced steel in concrete specimen in the presence and absence of added inhibitors was measured using electrochemical impedance spectroscopy and the resulted Nyquist plots are represented in the Figure 2.40. Three set of measurements were taken during 480 days in 160 days interval. Data obtained by the curves are given in the Table 2.16. The results are in good agreement with the Tafel data.

Table 2.16: Electrochemical impedance data of steel rebar embedded in contaminated concrete specimen in the presence and absence of added inhibitors

Time	System	W (Ωcm^2)	R _s (Ωcm^2)	C _{dl} (μFcm^{-2})	R _{ct} (Ωcm^2)	η_{EIS} %
160 Days	Sample 1	2.74	78.5	756	11.9	-
	Sample 2	26.5	791	320	299	96
	Sample 3	31.8	299	370	270	95
	Sample 4	15.3	1160	473	108	89
320 Days	Sample 1	3.78	75.6	710	14.7	-
	Sample 2	32.9	654	252	398	96
	Sample 3	45.4	358	298	320	95
	Sample 4	58.6	985	357	258	94
480 Days	Sample 1	3.23	223	700	24.3	-
	Sample 2	8.34	97.9	699	27.1	11
	Sample 3	10.2	91.8	655	33.7	28
	Sample 4	165	953	363	171	98

Up to 320th day of investigation samples casted with TSC alone acted effectively with 96% efficiency. But it is decreased with time and displayed low efficiency on 480th day of investigation. But samples casted with TSC and zinc acetate mixture exhibited around 90% efficiency throughout the experiment and

their inhibition efficiency increased with time. Thus it can be concluded that TSC-Zn mixture is behaving as a good corrosion inhibiting agent for the embedded steel in concrete structure with prolonged efficiency.

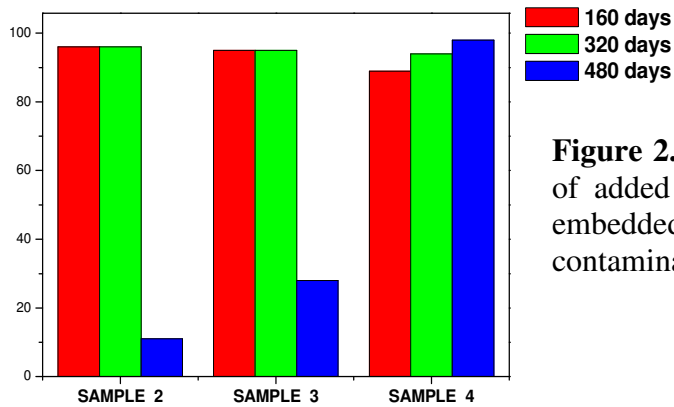


Figure 2.39: Comparison of $\eta_{EIS}\%$ of added inhibitors on steel rebar embedded in concrete specimen contaminated with 3.5% NaCl.

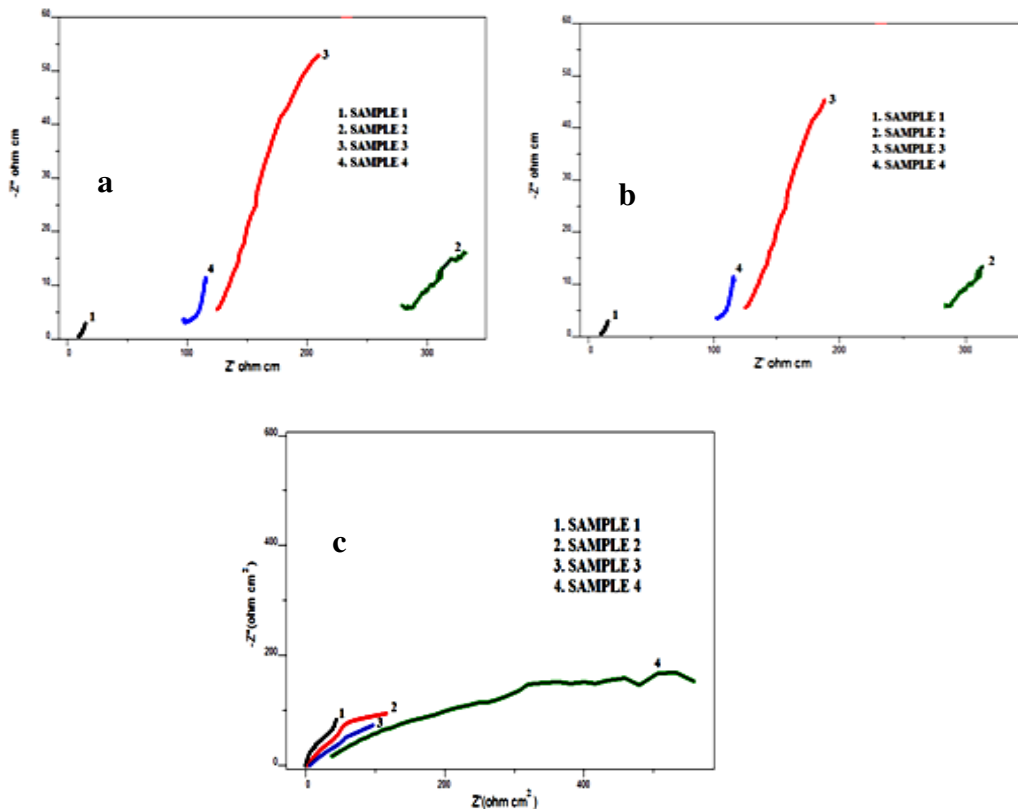


Figure 2.40: Nyquist plots of reinforced steel rebar embedded in concrete containing TSC and TSC-Zn acetate mixture a) 160 days b) 320 days and c) 480 days.

Half cell potential analysis

The corrosion response of steel reinforcement in concrete structures was immediately visualized by means of half cell potential measurements. Previously it was established by many researchers that corrosion tendency increases as the steel reinforcement potential become anodic. Half cell potentials measurements during 480 days were taken at 30 days time interval and are depicted in the Table 2.17 and compared graphically given in the Figure 2.41. Data clearly indicated that the steel reinforcement potential in sample 1 displayed high anodic values which reflects highly it's corrosive nature. Half cell potentials of samples 2 and 3 were less negative than sample 1 at the initial period of experiment and become more negative as sample 1 at the end of investigation. But the half cell potential values of sample 4 were comparably very less negative than sample 1 throughout the experiment, which indicate TSC-Zn acetate mixture is behaving as a good corrosion inhibiting agent for the embedded steel in concrete structure with prolonged efficiency.

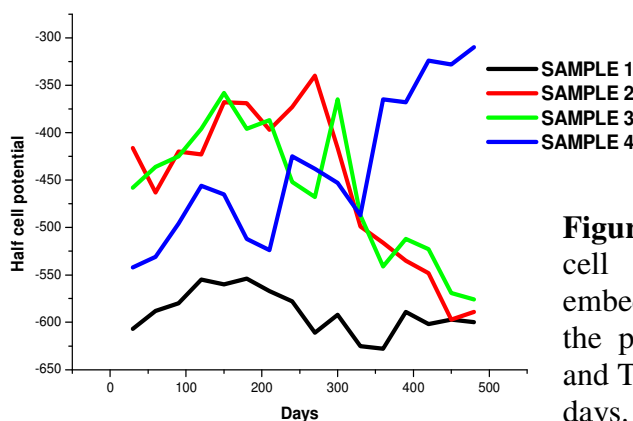


Figure 2.41: Comparison of half cell potentials of steel rebar embedded in concrete specimen in the presence and absence of TSC and TSC-Zn acetate mixture for 480 days.

Gravimetric analysis

Gravimetric studies on reinforced steel in various concrete samples were conducted for determining the weight loss percentage and to estimate corrosion inhibition efficacy. After 480 days of experiment, steel rebar were taken from the

concrete specimen, pickled with HCl, dried and recorded the weight. Steel reinforcements of samples 1, 2 and 3 displayed weight losses of 24%, 20% and 21% respectively. But the reinforcement steel taken from sample 4 displayed only 4% weight loss and exhibit predominant corrosion inhibition efficiency of 83%.

Table 2.17: Half cell potential (mV) measured on reinforced steel rebar in concrete containing TSC and TSC-Zn mixture for 480 days

Day	Blank	TSC (100)	TSC (250)	TSC(100) + Zn(50)
30	-607	-416	-458	-542
60	-588	-463	-436	-531
90	-580	-420	-425	-496
120	-555	-423	-396	-456
150	-560	-368	-358	-465
180	-554	-369	-396	-512
210	-567	-397	-387	-524
240	-578	-373	-452	-425
270	-611	-340	-468	-438
300	-592	-416	-365	-453
330	-625	-499	-487	-487
360	-628	-516	-541	-365
390	-589	-535	-512	-368
420	-602	-548	-523	-324
450	-597	-597	-569	-328
480	-600	-589	-576	-310

Microscopic surface analysis

Optical microscopic image of bare steel rebar, reinforced steel rebar of sample 1 and 4 after 480 days are represented in the Figure 2.42. A significant quantity of hydrated ferric oxide was present on the steel rebar surface of sample 1. It is clearly established that sample 1 has enhanced corrosion due to the contamination of 3.5% NaCl whereas the steel rebar surface of sample 4 has only little oxide content. Thus

the capacity of TSC- Zn acetate mixture to prevent the reinforced steel corrosion in concrete contaminated with 3.5% NaCl was again verified and successfully proved by this method.



Figure 2.42: Optical micrographs of steel reinforcements **a)** bare **b)** in sample 1 **c)** in sample 4

Compressive strength analysis

Compressive strength of concrete specimens was measured to check the effect of sodium citrate-zinc acetate mixture on the strength of concrete. As described in experimental procedure M-20 concrete blocks were casted with and without inhibitor and allowed to setting. The inhibitor mixed specimen displayed only half of the compressive strength of sample 1. M-20 concrete specimen corresponding to samples 1 and 4 showed compressive strengths of 21.3 and 10.5 N/m^2 respectively, suggesting that sodium citrate – zinc acetate mixture has some adverse effect on the strength of concrete.

SECTION 2

CORROSION INHIBITION BEHAVIOUR OF SODIUM SALTS OF PHOSPHATES, SULPHATES AND NITRITES ON STEEL REINFORCED CONCRETE CORROSION

Inhibitors are mixed to concrete to enhance its quality and durability. Among numerous available inhibitors, most of the compounds are cause difficulties to the environment and society. Thus the objective of the present study is to introduce a novel, effective and environment- friendly inhibitor to prevent steel reinforced concrete corrosion.

Preparation of concrete specimens

Preparation of concrete specimens was initiated by conducting preliminary tests to decide the concentration of inhibitor which have to be added in the concrete mixture. After measuring the SCE potentials of steel reinforcements immersed in CPS containing different concentrations of various sodium salts, contaminated with 3.5% NaCl, added 2.5% salts by weight of cement. Six sets of concrete specimens were casted as follows with and without the addition of inhibitor.

Sample 1: Cement: sand: gravel (1: 1.5: 3) + 3.5% NaCl

Sample 2: Cement: sand: gravel (1: 1.5: 3) + 3.5% NaCl + pentasodium triphosphate (2.5% by weight of cement)

Sample 3: Cement: sand: gravel (1: 1.5: 3) + 3.5% NaCl + monosodium phosphate (2.5% by weight of cement)

Sample 4: Cement: sand: gravel (1: 1.5: 3) + 3.5% NaCl + sodium phosphate (2.5% by weight of cement)

Sample 5: Cement: sand: gravel (1: 1.5: 3) + 3.5% NaCl + sodium lauryl sulphate (2.5% by weight of cement)

Sample 6: Cement: sand: gravel (1: 1.5: 3) + 3.5% NaCl + sodium nitrite (2.5% by weight of cement)

The steel reinforcement was cut in 22 cm and made rust free by immersing for 10 minutes in 2 M HCl, washed, degreased with acetone, dried, weighed and embedded in the concrete specimen while casting. For electrical connections, 5 cm of steel rod left outside during the process of specimen making.

Potentiodynamic polarization analysis

The inhibition efficiency of added inhibitors on steel reinforcement corrosion was investigated by polarization experiments. Three set of measurements were taken during 480 days in 160 days interval. Data obtained by the analysis of Tafel curves (Figure 2.44) are given in the Table 2.18. The results indicated that the steel reinforcement in samples 2, 3, 4, 5 and 6 are comparatively less corroded than sample 1. Up to 160th day of investigation samples casted with sodium salts showed prominent inhibition efficiency. But efficiency of samples 3, 4 and 6 decreased with time and displayed only moderate efficiency on 480th day of investigation and samples 2 and 5 were showed appreciable efficiency throughout the experiment. Thus it is a clear indication of the fact that sodium lauryl sulphate and pentasodium triphosphate are behaving as good corrosion inhibiting agents for the embedded steel in concrete structure for a long period.

Table 2.18: Polarization data of steel rebar embedded in contaminated concrete specimen in the presence and absence of added inhibitors

Time	System	I_{corr} (μAcm^{-2})	b_a (mVdec^{-1})	$-b_c$ (mVdec^{-1})	$-E_{\text{corr}}$ (mV)	η_{pol} %
160 Days	Sample 1	161.3	496	159	651	-
	Sample 2	63	535	176	628	61
	Sample 3	44	421	209	554	73
	Sample 4	23.9	385	230	533	85
	Sample 5	18.4	430	232	573	89
	Sample 6	13.7	651	136	600	91
320 Days	Sample 1	138.7	489	156	661	-
	Sample 2	44.5	411	207	614	68
	Sample 3	34.5	355	268	618	75
	Sample 4	49.5	373	204	642	64
	Sample 5	41	469	229	520	71
	Sample 6	35.1	744	131	706	75
480 Days	Sample 1	107	373	215	550	-
	Sample 2	23.6	375	218	493	71
	Sample 3	44.7	857	254	445	58
	Sample 4	56.4	423	200	482	47
	Sample 5	21	341	230	560	81
	Sample 6	52.5	395	182	602	51

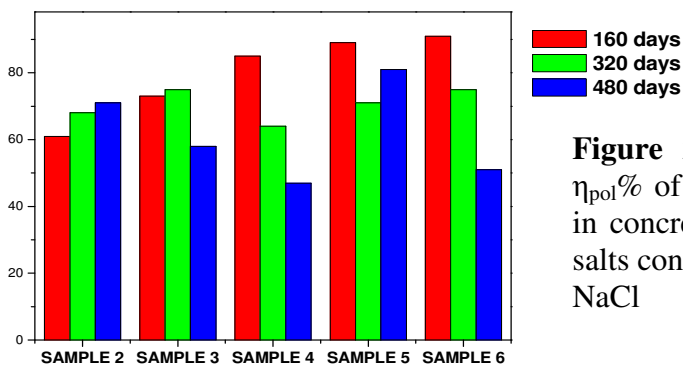


Figure 2.43: Comparison of $\eta_{\text{pol}}\%$ of steel rebar embedded in concrete containing sodium salts contaminated with 3.5% NaCl

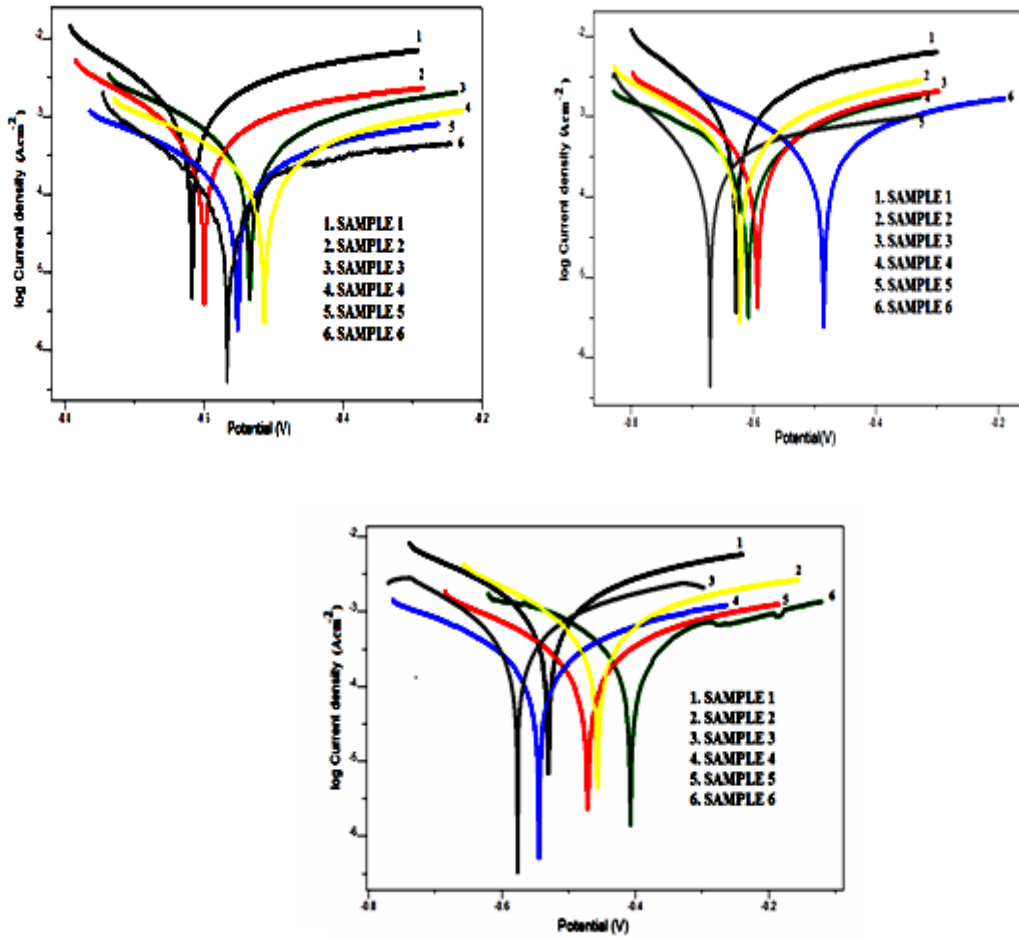


Figure 2.44: Tafel plots of reinforced steel rebar in concrete containing sodium salts **a)** 160 days **b)** 320 days and **c)** 480 days.

EIS analysis

The corrosion response of reinforcement steel in concrete specimen in the presence and absence of added sodium salts was measured using electrochemical impedance spectroscopy and the Nyquist plots recorded are represented in the Figure 2.45. Three set of measurements were taken during 480 days at an interval of 160 days. Data derived by the curves are represented in the Table 2.19.

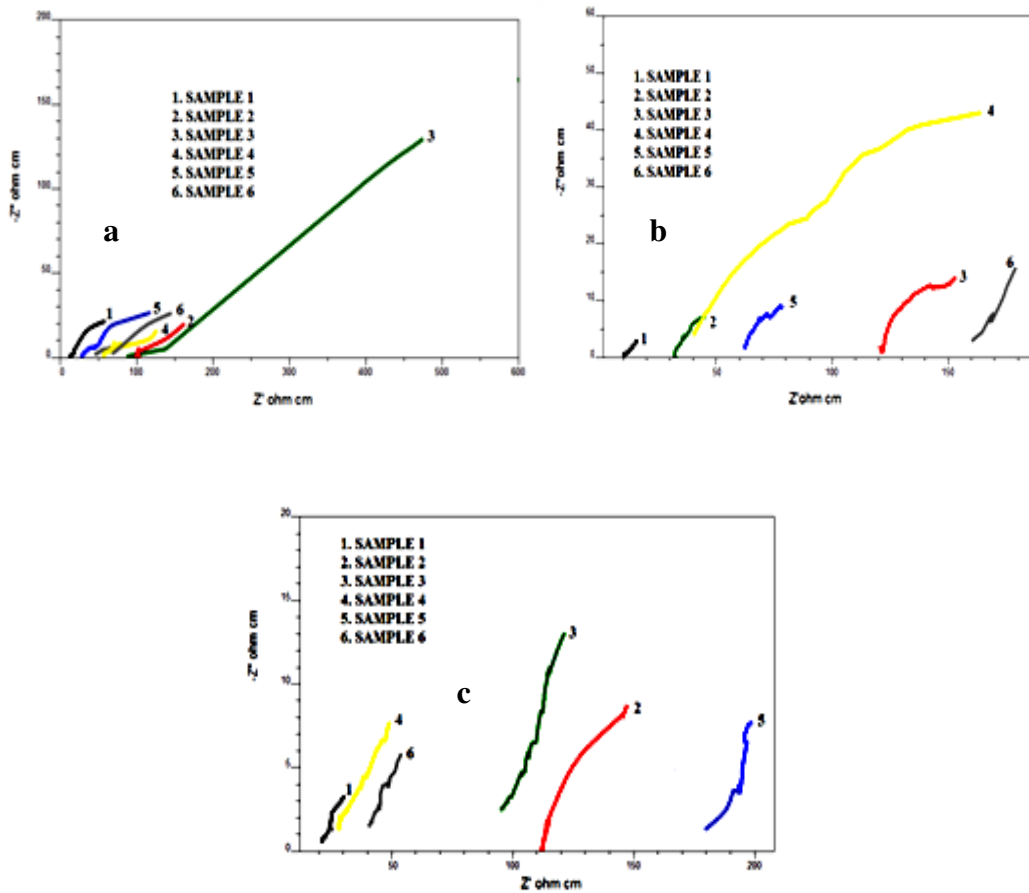


Figure 2.45: Nyquist plots of reinforced steel rebar embedded in concrete containing sodium salts **a)** 160 days **b)** 320 days and **c)** 480 days.

Up to 160th day of investigation, samples casted with sodium salts showed prominent inhibition efficiency. But efficiency of samples 3, 4 and 6 decreased with time and displayed only moderate efficiency on 480th day of investigation and samples 2 and 5 were showed appreciable efficiency throughout the experiment. The results are in good agreement with the Tafel data and can be concluded that sodium lauryl sulphate and penta sodium triphosphate are behaving as good corrosion inhibiting agents for the embedded steel in concrete structure with prolonged efficiency.

Table 2.19: Electrochemical impedance data of steel rebar embedded in contaminated concrete specimen in the presence and absence of added inhibitors

Time	System	W (Ωcm^2)	Rs (Ωcm^2)	C _{dl} (μFcm^{-2})	R _{ct} (Ωcm^2)	η_{EIS} %
160 Days	Sample 1	2.74	78.5	886	11.9	-
	Sample 2	8.69	162	512	32.45	63
	Sample 3	56.8	836	386	106	98
	Sample 4	21.5	609	432	108	89
	Sample 5	15.8	574	467	93.1	87.2
	Sample 6	50.2	575	470	93.1	87
320 Days	Sample 1	3.78	75.6	839	14.7	-
	Sample 2	12.8	128	506	61	76
	Sample 3	7.78	523	435	85	82
	Sample 4	5.55	163	512	61	74
	Sample 5	8.29	162	498	66.5	78
	Sample 6	12.7	125	581	40.9	61
480 Days	Sample 1	3.23	223	801	24.3	-
	Sample 2	9.27	459	242	117	79.2
	Sample 3	17.6	112	444	74	67
	Sample 4	6.1	373	470	44.9	45
	Sample 5	4.2	559	216	173	86
	Sample 6	7.78	148	501	37.9	36

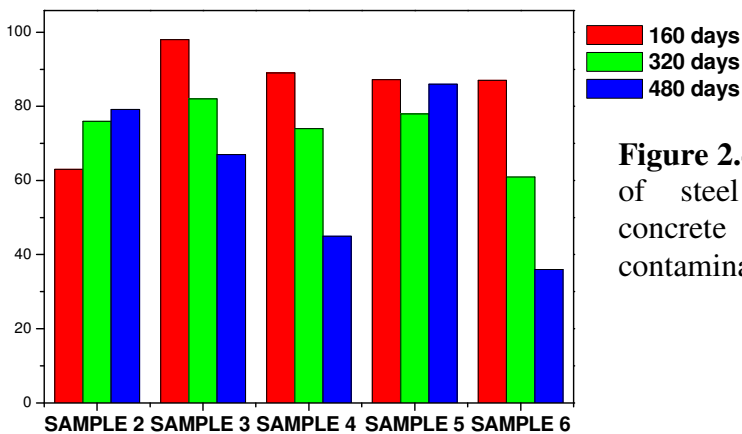


Figure 2.46: Comparison of $\eta_{\text{EIS}}\%$ of steel rebar embedded in concrete containing sodium salts contaminated with 3.5% NaCl

Half cell potential analysis

The corrosion response of steel reinforcement in concrete structures was immediately visualized by means of half cell potential measurements. Previously it was established by many researchers that corrosion tendency increases as the steel reinforcement potential become anodic. Half cell potentials measurements during 480 days were taken at 30 days time interval and are depicted in the Table 2.20 and compared by a line graph are given in the figure 2.47. Data clearly indicated that the steel reinforcement potential in sample 1 displayed high anodic values which reflect it's highly corrosive nature. Half cell potentials of samples containing sodium salts were very less negative than sample 1 at the initial period of experiment but becomes more anodic towards the end of the experiment except in the case of samples 2 and 5. They exhibited comparably very less negative values at the end of the experiment, which give a further evidence for the prolonged anticorrosive nature of sodium lauryl sulphate and pentasodium triphosphate for the embedded steel in concrete structure.

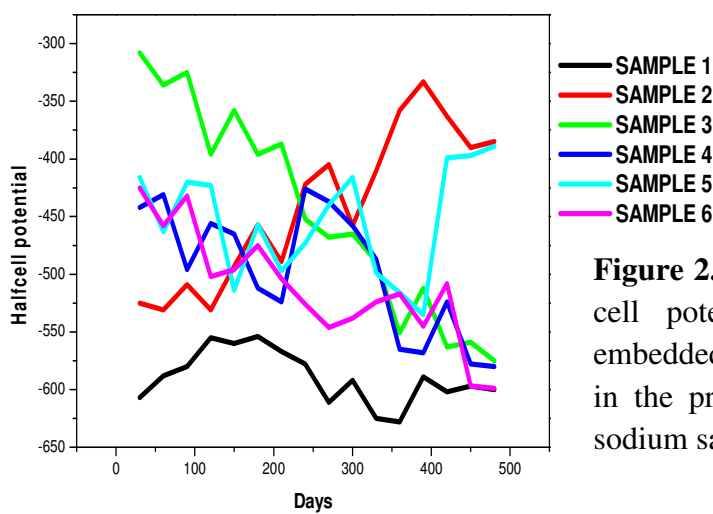


Figure 2.47: Comparison of half cell potentials of steel rebar embedded in concrete specimen in the presence and absence of sodium salts for 480 days.

Table 2.20: Half cell potential (mV) measured on reinforced steel rebar in concrete containing sodium salts for 480 days.

Day	Sample 1	Sample 2	Sample 3	Sample 4	Sample 5	Sample 6
30	-607	-525	-308	-442	-416	-425
60	-588	-531	-336	-431	-463	-458
90	-580	-509	-325	-496	-420	-432
120	-555	-531	-396	-456	-423	-502
150	-560	-493	-358	-465	-514	-496
180	-554	-457	-396	-512	-457	-475
210	-567	-489	-387	-524	-497	-504
240	-578	-422	-452	-426	-473	-526
270	-611	-405	-468	-437	-440	-546
300	-592	-458	-465	-458	-416	-538
330	-625	-410	-489	-487	-499	-524
360	-628	-358	-551	-565	-516	-517
390	-589	-333	-512	-568	-535	-545
420	-602	-363	-563	-524	-399	-508
450	-597	-390	-559	-578	-397	-597
480	-600	-385	-575	-580	-389	-599

Gravimetric analysis

Gravimetric study of steel reinforcement embedded in concrete specimens was done for evaluating the weight loss percentage and corrosion inhibition efficiency of investigated sodium salts. After the period of investigation, steel rebar were taken from the concrete specimen, pickled with HCl, dried and determined its weight. The values are depicted in the Table 2.21. Steel reinforcements of samples 2 and 5 displayed comparatively low weight losses of 3.9% and 3.6% respectively. Thus the inhibition efficacy of penta sodium triphosphate and sodium lauryl sulphate on the steel reinforcement in concrete specimen contaminated with NaCl was established well. The corrosion inhibition efficiency of penta sodium

triphosphate and sodium lauryl sulphate determined by gravimetric analysis was 84% and 86% respectively.

Table 2.21: Weight loss percentage and inhibition efficiency of steel reinforcement of investigated samples.

Samples	1	2	3	4	5	6
Weight loss(%)	24.6	3.9	8.9	12.6	3.6	16.4
Inhibition efficiency (%)	-	84	64	48	86	33

Infrared spectral analysis

IR spectral studies of the corroded product gave an idea about the nature of interaction of sodium salts on steel reinforcement. The interpretation of the spectrum of the corrosion product on the steel surface was very difficult due to the presence of various compounds in concrete. Surface deposits were removed from steel reinforcement embedded in concrete specimens containing effective inhibitors, pentasodium triphosphate (PST) and sodium lauryl sulphate (SLS) and subjected to spectral analysis. A broad peak observed at 3375cm^{-1} in the spectrum of products from sample 1 is due to the $-\text{OH}$ stretching vibration of both ferrous hydroxide and hydrated ferric oxide deposited on steel rebar surface. This peak was shifted to 3016cm^{-1} in the spectrum of corrosion product collected from sample 2. The FTIR spectrum of PST displayed two asymmetric stretching peaks of phosphate at 1065cm^{-1} and 1415cm^{-1} and bending peaks at 479cm^{-1} and 606cm^{-1} . The stretching frequencies were shifted to 1382cm^{-1} and 922cm^{-1} and bending peaks were shifted to 447cm^{-1} and 557cm^{-1} in IR spectrum of products of sample 2. Some of the intense peaks observed in IR spectrum of PST was absent in spectrum of corrosion products of sample 2. These significant changes in the IR spectra are clear indication of the interactions of PST with the steel surface.

A broad signal observed at 3375 cm^{-1} in the spectrum of corroded product of sample 1 was due to -OH stretching frequency of ferrous hydroxide or hydrated ferric oxide (or both). In the IR spectrum of corroded product of sample 5, it was noticed that the peak due to -OH frequency shifted to 3349 cm^{-1} . This may be due to the interaction of SLS with the ferrous or ferric hydroxide. The IR spectrum of SLS contains peaks at 2922 and 2821 cm^{-1} which can be assigned to the stretching frequencies of various C-H bonds. This peak was visible at 2895 cm^{-1} in the spectrum of surface product of sample 5 steel specimens. In the IR spectrum of SLS, two IR regions corresponding to symmetric and asymmetric stretching frequency of sulphate group were appeared at $826\text{-}1240\text{ cm}^{-1}$ and $1240\text{-}1466\text{ cm}^{-1}$ respectively. These peaks were shifted to $789\text{-}1104\text{ cm}^{-1}$ and $1104\text{-}1420\text{ cm}^{-1}$ in the spectrum of corroded product of sample 5. This is clear indication of the interaction of SLS through the sulphate end. A weak peak corresponding to the C-C stretching frequency of carbon skelton displayed at 964 cm^{-1} in the IR spectrum of SLS was also shifted to 955 cm^{-1} . Two intense peaks at 2821 cm^{-1} and 2922 cm^{-1} corresponding to symmetric and asymmetric stretching frequencies of CH_2 groups of SLS also shifted to 2802 cm^{-1} and 2895 cm^{-1} respectively in the FTIR spectrum of surface deposits of steel in sample 5. The IR spectra are given in the Figure 2.48.

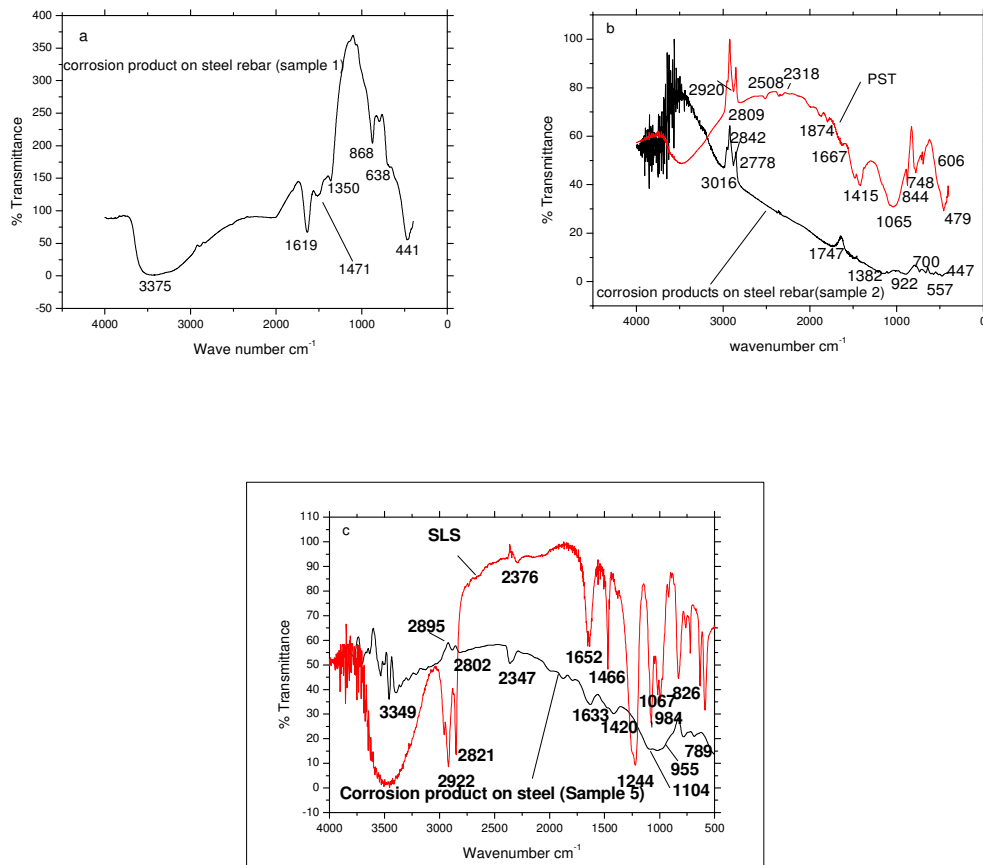


Figure 2.48: IR spectra of corrosion products deposited on the steel rebar in **a)** sample 1 **b)** sample 2 and PST **c)** sample 5 and SLS

Microscopic surface analysis

Examination of the optical micrographs indicated that the surface morphology of steel rebars embedded in the concrete specimens was changed appreciably, compared to that of bare rebar. This may be due to deposition of hydrated ferric oxide (rust) on the steel surface. The texture of steel rebar corresponding to samples 2 and 5 was significantly differed from that of sample 1. The surface of steel reinforcement corresponding to samples 2 and 5 seemed to be less corroded as its surface contains little oxide film (Figure 2.49), compared to the steel rebar in sample 1. This suggests that PST and SLS possess marked

anticorrosive ability to prevent reinforced steel corrosion in concrete contaminated with NaCl.)

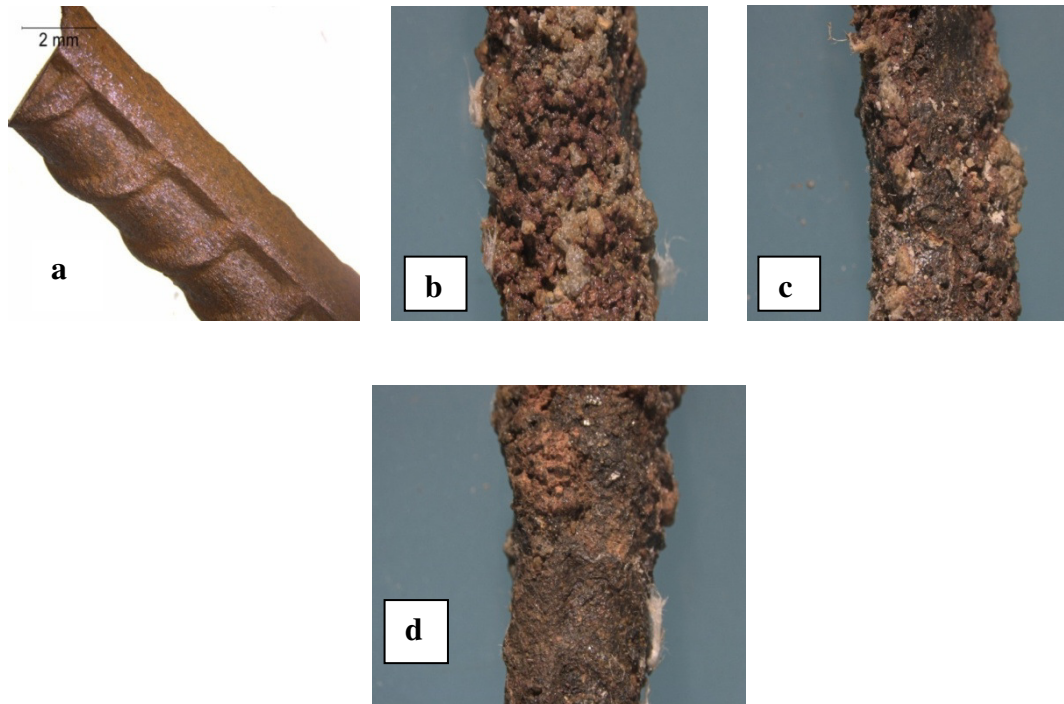


Figure 2.49: Optical micrographs of steel reinforcements
a) bare b) in sample 1 c) in sample 2 d) in sample 5

Mechanism of inhibition of SLS

Sodium lauryl sulphate is a surfactant molecule and can perform well on the steel surface to decrease the rate of anodic and cathodic processes of corrosion [110,111]. It can be assumed that SLS molecules present in concrete pore solution slowly migrate towards the steel surface and make coordinate bonds with the ferrous ions on the surface through the polar end. Since SLS has a long hydrophobic chain, pointing away from the steel surface, it can repel water molecules and chloride ions diffusing towards the surface. This process is really beneficial to control the electrochemical process of corrosion. In other words, SLS efficiently resists the conversion of ferrous ions into hydrated ferric oxide (rust). The overall mechanism of the inhibition and the structure of SLS are represented in the Figure 2.50

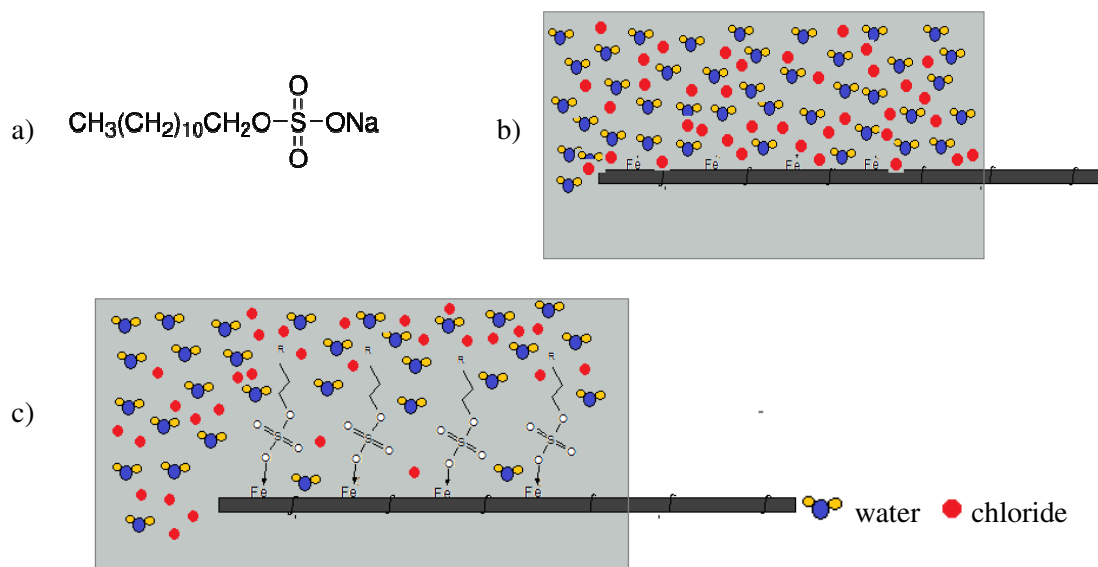


Figure 2.50: a) structure of SLS b) sample 1: water molecules and chloride ions are attached on steel surface c) sample 5: coordinated SLS prevent the migration of water molecules and chloride ions towards steel surface

Mechanism of inhibition of PST

PST is an inorganic compound with chemical formula $\text{Na}_5\text{P}_3\text{O}_{10}$. Literature survey reveals that not much data are available about the behaviour of PST as corrosion inhibitor [113-116]. Generally the corrosion inhibition efficacy of inhibitors depends on various factors including their molecular size, way of interaction and complex formation with metals.

The adsorption of PST on the steel rebar surface can be described by the presence of pi- electrons containing phosphate group, which effectively reduce the anodic dissolution of steel surface. On the other hand, chemical structure of PST established that, they have the capability to bind with metals as a bidentate and tridentate chelating agent and it facilitates the complex formation with dissolved Fe ions. The overall inhibition mechanism and the structure of PST are represented in the Figure 2.51.

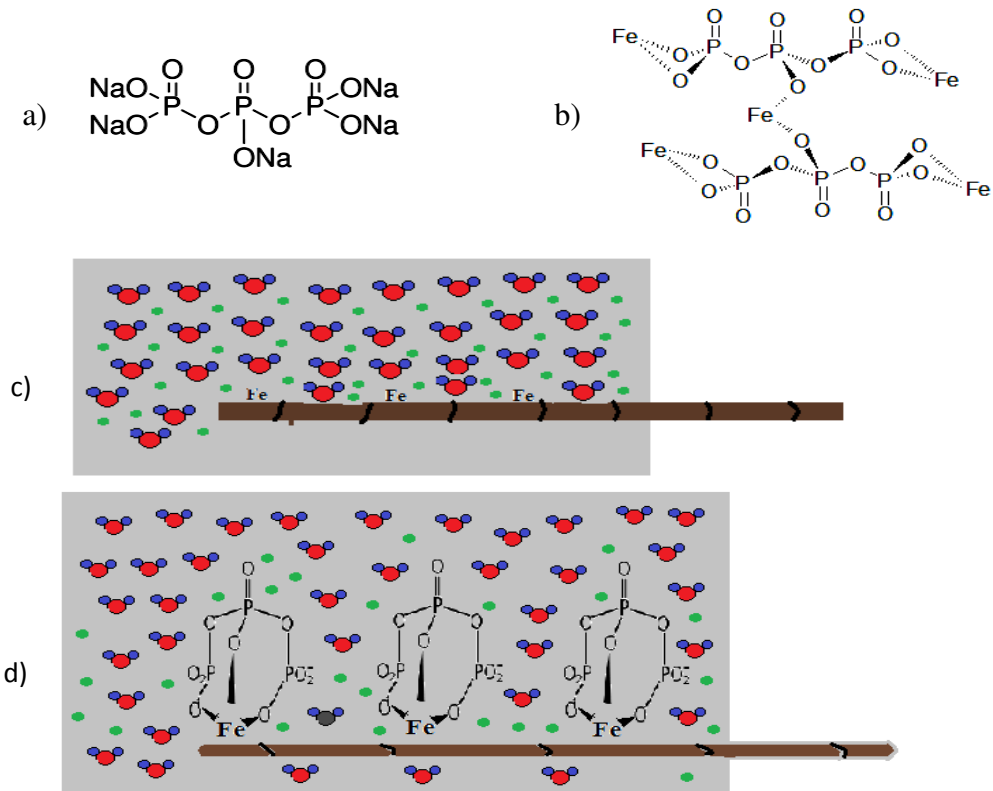


Figure 2.51: a) Structure of PST b) chelated structure formula of PST with iron c) sample 1: Chloride ions and water molecules are attached on steel rebar surface d) sample 2: coordinated PST molecules inhibit the migration of chloride ions and water molecules towards steel rebar surface.

Compressive strength analysis

Compressive strength of concrete specimens was measured to check the effect of PST and SLS on the strength of concrete. As described in experimental procedure M-20 concrete blocks were casted with and without PST and SLS and allowed to setting. Samples 1 and 2 were taken normal 28 days for complete setting, whereas concrete specimen casted with SLS (sample 5) was taken approximately 4 months. All the test specimens displayed almost equal values of compressive strength. M-20 concrete specimen corresponding to samples 1, 2 and 5 showed compressive strengths of 21.3, 21.30 and 21 N/m² respectively, suggesting that PST and SLS molecules have no influence on the strength of concrete.

SUMMARY

The concrete corrosion is a major problem that affects not only the civil engineering industry but also all other areas even nuclear industry. Part II deals with the study of concrete corrosion. The investigations on steel reinforced concrete corrosion are conducted by the researchers either by concrete pore solution or concrete specimens.

In Part II A, the investigations on concrete reinforcement corrosion are conducted in concrete pore solution. The present investigation included the study of the inhibition efficiency of different sodium salts, natural products and water soluble Schiff bases to inhibit the reinforced steel corrosion in simulated concrete pore solution. The experimental study was performed by different corrosion monitoring methods like electrochemical studies such as impedance spectroscopy and Tafel polarization study and half cell potential measurements. The corrosion inhibition mechanism of the compounds was confirmed by different spectroscopic methods such as UV- visible spectroscopy and FTIR. Microscopic studies were conducted to investigate the changes observed in the surface of the steel rebar.

All studied compounds displayed considerable corrosion inhibition efficiency on steel rebar in simulated concrete interstitial. At low concentrations, NaNO_2 acted as a corrosion accelerator. As the concentration of NaNO_2 increased protection efficiency increased. Generally, trisodium citrate exhibited better protection capacity than NaNO_2 . But, in the presence of TSC-zinc acetate system very appreciable lowering of the corrosion rate was noticed. According to Tafel polarization studies, steel rebar is well protected in concrete pore solution contaminated with 3.5% NaCl with TSC 100ppm-ZnAc 50ppm system.

. From the inhibition data of investigated sodium salts, it is revealed that MSP acted as a very potential corrosion inhibitor with above 90% efficiency at every concentration. SLS and PST showed remarkable inhibition efficiency at 50 and 1500ppm concentrations, but both were acted as poor corrosion inhibitor at 150ppm concentration. The response of steel rebar immersed in CPS solution containing SP is quite different from others. Even if they exhibited appreciable inhibition efficiency in 150ppm concentration, they have very low efficiency in 1500ppm and showed antagonistic nature in 50ppm concentration.

According to the data on the inhibition efficiency of plant extracts, it was noticed that the I_{corr} have low values in the presence of plant extracts leading to exhibit significant corrosion inhibition efficiency. Extracts AS, PN, ZO and BV inhibited the corrosion of steel rebar appreciably. AS acted as a potential corrosion inhibitor with maximum efficiency of 81% and CO acted as a poor inhibitor with minimum efficiency of 3%. The Tafel analysis results indicated that the investigated imines have low inhibition efficiency in contaminated CPS contrary to the observation in acidic media and comparably slightly excess efficiency was exhibited by 2APSC than 2APPH.

In part II B, the investigations on concrete reinforcement corrosion were conducted by concrete specimens. The present investigation included the study of the inhibition efficiency of different sodium salts to inhibit the concrete reinforcement corrosion. The experimental study was performed by different corrosion monitoring methods like gravimetric studies, electrochemical studies such as impedance spectroscopy and Tafel polarization study and half cell potential measurements. The corrosion inhibition mechanism of the compounds was confirmed by FTIR and microscopic studies.

All studied compounds displayed considerable corrosion inhibition efficiency on concrete reinforced steel. At the initial period of investigation samples casted with TSC alone showed prominent inhibition efficiency. But it is decreased with time and displayed only around 54% at the end of investigation. But, in the presence of TSC-zinc acetate system very appreciable lowering of the corrosion rate was noticed throughout the experiment.

. From the inhibition data of investigated sodium salts, it was revealed that SLS and PST are potent corrosion inhibitors for the steel reinforcement in contaminated concrete for a long time. Electrochemical studies proved that as time proceed, the corrosion inhibition efficacy of SLS didn't alter appreciably while PST shows appreciable increase in inhibition efficiency. FTIR and microscopic surface analysis proved the interaction of SLS and PST on steel reinforcement. Compressive strength measurement of concrete was proved that addition of these sodium salts have not any adverse effect on the strength of concrete.

On comparing the results of parts II A and II B, it was revealed that most of the sodium salts especially sodium citrate –zinc acetate mixture, PST and SLS were displayed effective corrosion inhibition efficiency in both experimental conditions, ie; in concrete pore solution and in concrete specimens. However, on considering the compressive strength measurements, it is established that SLS and PST exhibited predominant corrosion inhibition efficiency without making any adverse effect on the mechanical strength of concrete.

REFERENCES

1. A. Mance, D. Cerović, A. Mihajlović, *Journal of Applied Electrochemistry*, 14 (1984) 459-466.
2. T. R. Beck, *Electrochimica Acta*, 29 (1984) 485-491.
3. P. Kritzer, *The Journal of Super Critical Fluids*, 29 (2004) 1-29.
4. Hendrik Venzlaff, Dennis Enning, Jayendran Srinivasan, Karl. J.J. Mayrhofer, *Corrosion Science*, 66 (2013) 88-96.
5. T. S. Rao, *Corrosion Science*, 42 (2000) 1417-1431.
6. Dake Xu, Yingchao Li, Fengmei Song, Tingyue Gu, *Corrosion Science*, 77 (2013) 385-390.
7. M. Diercks, W. Sand, E. Bock, *Experientia*, 47 (1991) 514-516.
8. Ji-Dong Gu, Tim. E. Ford, Neal. S. Berke, Ralph Mitchell, *International Bio deterioration and Biodegradation*, 41 (1998) 101-109.
9. W. Nechnech, F. Meftah, J. M. Reynouard, *Engineering Structures*, 24 (2002) 597-611.
10. D. Gawin, *Computer Methods in Applied Mechanics and Engineering*, 192 (2002) 1731-1771.
11. Luca Bertolini, Matteo Gastaldi, Maria Pia Pedferri, Elena Redaelli, *Corrosion Science*, 44 (2002) 1497-1513.
12. H Castro, *Journal of Materials Processing Technology*, 143 (2003) 134-137.
13. Fujian Tang, Genda Chen, Richard. K. Brow, Jeffery. S. Volz, Michael. L. Koenigstein, *Corrosion Science*, 59 (2012) 157-168.
14. Marijana Serdar, Lidija Valek Žulj, Dubravka Bjegović, *Corrosion Science*, 69 (2013) 149-157.

15. Tingting Zhu, Maria Dittrich, *Frontiers in Bioengineering and Biotechnology*, 4 (2016) 1-21.
16. Ming Liu, Xuequn Cheng, Xiaogang Li, Zhu Jin, Haixia Liu, *Construction and Building Materials*, 93 (2015) 884-890.
17. Jinjie Shi, Wei Sun, Jinyang Jiang, Yamei Zhang, *Construction and Building Materials*, 111 (2016) 805-813.
18. M. Moreno, W. Morris, M. G. Alvarez, Duffó, *Corrosion Science*, 46 (2004) 2681–2699.
19. M. B. Valcarce, M. Vázquez, *Electrochimica Acta*, 53 (2008) 5007–5015.
20. M. F. Montemor, A. M. P. Simoes, M. G. S. Ferreira, *Cement and Concrete Composites*, 25 (2003) 491–502.
21. M. Ormellese, Luciano Lazzari, Sara Goidanich, Gabriele Fumagalli, Andrea Brenna, *Corrosion Science*, 51 (2009) 2959–2968.
22. M. Pandiarajan, *Chemical Science*, 2 (2013) 605-613.
23. B. Elsener, M. Büchler, F. Stalder, H. Böhni, *Corrosion*, 56 (2000) 727–732.
24. L. Dhouibi, E. Triki, A. Raharinaivo, *Cement and Concrete Composites*, 24 (2002) 35–43.
25. O T. Rincón, O. Pérez , O. Paredes, Y. Caldera, Y. Urdaneta, I. Sandoval *Cement and Concrete Composites*, 24 (2002) 79–87.
26. H. Liang, *Cement & Concrete Research*, 33 (2003) 139–146.
27. R. Cigna, E. Proverbio, G. Rocchini, *Corrosion Science*, 35 (1993) 1579–1584.
28. M. Pandiarajan, *European Chemical Bulletin*, 2 (2013) 1-8.
29. H. Oranowska, Z. Szklarska-Smialowska, *Corrosion Science*, 21 (1981) 735–747.
30. S. Joiret, M. Keddab, X. R. Nóvoa, M. C. Pérezb, C. Rangelc, H. Takenouti,

- Cement and Concrete Composites*, 24 (2002) 7–15.
31. M. Kawamura, *ACI Special Publications*, 173 (1997) 35-54.
 32. C. Andrade, M. Keddam, X. R. Nóvoa, M. C. Pérezb, C. Rangelc, H. Takenouti, *Electrochimica Acta*, 46 (2001) 3905–3912.
 33. C. J. Kitowski, H. G. Wheat, *Corrosion*, 53 (1997) 216–226.
 34. K. Y. Ann, H. W. Song, *Corrosion Science*, 49 (2007) 4113–4133.
 35. S. Trépanier, B. Hope, C. Hansson, *Cement and Concrete Research*, 31 (2001) 713–718.
 36. L. Jiang, G. Huang, J. Xu, Y. Zhu, L. Mo, *Construction and Building Materials*, 30 (2012) 516–521.
 37. S. Rajendran, C. Nathiya, P. Prabhakar, P. Shanthi, M. Pandiarajan, *European Chemical Bulletin*, 3 (2014) 734-737.
 38. W. Morris, M. A. Vázquez, *Cement & Concrete Research*, 32 (2002) 259–267.
 39. A. Rosenberg, *Corrosion*, 56 (2000) 986–987.
 40. C. Monticelli, A. Frignani, G. A. Trabanelli, *Cement and Concrete Research*, 30 (2000) 635–642.
 41. Al-Amoudi OSB, M. Maslehuddin, A. Lashari, A. A. Almusallam, *Cement and Concrete Composites*, 25 (2003) 439–449.
 42. B. Elsener, M. Büchler, F. Stalder, H. Böhni, *Corrosion*, 56 (2000) 727-732.
 43. C. Andrade, C. Alonso, M. Acha, B. Malric, *Cement and Concrete Research*, 22 (1992) 869–881.
 44. N. S. Berke, M. C. Hicks, *Cement and Concrete Composites*, 26 (2004) 191–198.
 45. Wellea A, J. D. Liao, K. Kaiser, M. Grunze, U. Mäder, *Applied Surface Science*, 119 (1997) 185–198.

46. S. Reou, KY. Ann, *Materials Chemistry and Physics*, 109 (2008) 526-533.
47. Ryu H-S, J. K. Singh, Lee H-S, M. A. Ismail, Park W-J, *Construction and Building Materials*, 133 (2017) 387-396.
48. Ryu H-S, J. K. Singh, Lee H-S, Park W-J, *Advances in Materials Science and Engineering*, (2017) Article ID 6265184.
49. V. Ngala, C. Page, M. Page, *Corrosion Science*, 44 (2002) 2073–2087.
50. Ryu H-S, J. K. Singh, Lee H-S, M. A. Ismail, *Construction and Building Materials*, 114 (2016) 223-231.
51. M. Hassoune, A. Bezzar, L. Sail, F. Ghomari, *Journal of Adhesion Science and Technology*, 32 (2017) 68-90.
52. B. Elsener, M. Büchler, F. Stalder, H. Böhni, *Corrosion*, 55 (1999) 1155–1163.
53. N. S. Berke, *Materials Performance Magazine*, 28 (1989) 41-44.
54. N. S. Berke, M. P. Dallaire, M. C. Hicks, R. J. Hoopes, *Corrosion*, 49 (1989) 934–943.
55. M. A. Asaad, *Construction and Building Materials*, 188 (2018) 555–568.
56. V. Ganesan, *International Journal of Electrochemical Science*, 13 (2018) 9981 – 9998.
57. L. Benzina Mechmeche, *Cement and Concrete Composites*, 30 (2008) 167-173.
58. M. M. Mennucci, E. P. Banczek, P. R. P. Rodrigues, I. Costa, *Cement and Concrete Composites*, 31 (2009) 418-424.
59. P. Garcés, P. Saura, E. Zornoza, C. Andrade, *Corrosion Science*, 53 (2011) 3991-4000.
60. Xin Zhou, *Corrosion science*, 54 (2011) 193-200.
61. LijuanFeng, *International Journal of Electrochemical Science*, 7 (2011) 4064-4077.

62. Fei-long, *Construction and Building Materials*, 70 (2014) 43-53.
63. J. L. García Calvo, *Materials*, 6 (2013) 2508-2521.
64. M. A. Stern, *Corrosion*, 14 (1958) 60–64.
65. H. J. Flitt, D. P. Schweinsberg, *Corrosion Science*, 47 (2005) 3034–3052.
66. B. Elsener, *Corrosion Science*, 47 (2005) 3019–3033.
67. I. Olefjord, L. Wegrelius, *Corrosion Science*, 31 (1990) 89–98.
68. Veleva L, *Journal of Electroanalytical Chemistry*, 537 (2002) 85–93.
69. S. R. Krishnamurti, P. M. Huang, *Clays and Clay Minerals*, 39 (1991) 28-34.
70. R. Naderi, M. Mahdavian, M. M. Attar, *Electrochimica Acta*, 54 (2002) 6892–6895.
71. M. Mahdavian, R. Naderi, *Corrosion Science*, 53 (2011) 1194–1200.
72. F. Badii, N. K. Howell, *Journal of Agricultural and Food Chemistry*, 50 (2002) 2053–2061.
73. K. V. S. Ramana, *Corrosion*, 58 (2007) 873-880.
74. A. A. Almusallam, *Construction and Building Materials*, 15 (2001) 361–368.
75. H. A. F. Dehwah, M. Maslehuddin, S. A. Austin, *Cement and Concrete Composites*, 24 (2002) 17–25.
76. J. B. Aguiar, C. Júnior, *Construction and Building Materials*, 49 (2013) 478–483.
77. K. K. Sideris, N. S. Anagnostopoulos, *Construction and Building Materials*, 41, (2013) 491–497.
78. K. Sisomphon, L. Franke, *Cement and Concrete Research*, 37 (2007) 1647–1653.
79. J. Rodriguez, *Construction and Building Materials*, 11 (1997) 239–248.
80. A. Muntean, M. Böhm, J. Kropp, *Chemical Engineering Science*, 66 (2011)

538–547.

81. C. A. Apostolopoulos, V. G. Papadakis, *Construction and Building Materials*, 22 (2008) 2316–2324.
82. J. N. Enevoldsen, C. M. Hansson, B. B Hope, *Cement and Concrete Research*, 24 (1994) 1373–1382.
83. T. Vidal, A. Castel, R. François, *Cement and Concrete Research*, 34 (2004) 165–174.
84. S. Altoubat, M. Maalej, F. U. Shaikh, *International Journal of Concrete Structures and Materials*, 10 (2016) 383–391.
85. M. G. Stewart, D. V. Rosowsky, *Structural Safty*, 20 (1998) 91–109.
86. Y. Zhu, M. Free, R. Woollam, *Progress in Material Science*, 90 (2017) 159–223.
87. B. Pradhan, B. Bhattacharjee, *Construction and Building Materials*, 23 (2009) 2346–2356.
88. K. A. T. Vu, M. G. Stewart, *Structural Safty*, 22 (2000) 313–333.
89. D. Zehua, W. Shi, X. Peng Guo, *Corrosion Science*, 53 (2011) 1322–1330.
90. A. Chen, *Corrosion Science*, 66 (2013) 183–195.
91. J. A. González, C. Andrade, C. Alonso, S. Feliu, *Cement & and Concrete Research*, 25 (1995) 257–264.
92. M. G. Stewart, *Structural Safty*, 26 (2004) 453–470.
93. M. G. Stewart, A. Al-Harthy, *Reliability Engineering and System. Safty*, 93 (2008) 373–382.
94. M. G. Stewart, *Structural Safty*, 31 (2009) 19–30.
95. T. A. Söylev, M. G. Richardson, *Construction and Building Materials*, 22 (2008) 609–622.

96. J. M. Gaidis, *Cement and Concrete Composites*, 26 (2004) 181–189.
97. J. Gaidis, & A. Rosenberg, *Cement, Concrete and Aggregates*, 9 (1987) 30-33.
98. A. U. Malik, I. Andijani, F. Al-Moaili, G. Ozair, *Cement and Concrete Composites*, 26 (2004) 235–242.
99. V. Saraswathy, H.-W. Song, *Building and Environment*, 42 (2007) 464–472.
100. H. Saricimen, M. Mohammad, A. Quddus, M. Shameem, M. S. Barry, *Cement and Concrete Composites*, 24 (2002) 89–100.
101. K. K. Sideris, A. E. Savva, *Cement and Concrete Composites*, 27 (2005) 277–287.
102. P. Montes, T. W. Bremner, D. H. Lister, *Cement and Concrete Composites*, 26 (2004) 243–253.
103. F. Wombacher, U. Maeder, U. Marazzani, *Cement and Concrete Composites*, 26 (2004) 209–216.
104. M. A. Asaad, *Construction and Building Materials*, 188 (2018) 555–568.
105. V. Ganesan, *International Journal of Electrochemical Science*, 13 (2018) 9981 – 9998.
106. Neal S. Berke, *Cement and Concrete Composites*, 26 (2004) 191-198.
107. M. Ormellese, F. Bolzoni, Sara Goidanich, Maria Pia Pedefferri, *Cement and Concrete Research*, 36 (2006) 536-547.
108. D. M. Bastidas, *Cement and Concrete Composites*, 43 (2013) 31-38.
109. Zhaocai Zhang, *Construction and Building Materials*, 198 (2018) 288-298.
110. T. Zhao and G. Mu, *Corrosion science*, 41 (1999) 1937-1944.
111. J. B. Aguiar, C. Júnior, *Construction and Building Materials*, 49 (2013) 478–483.
112. L. Yohai, W. Schreiner, M. Vázquez, M. B. Valcarce, *Electrochimica Acta*,

202 (2016) 231–242.

113. J. J. Shi, W. Sun, *Cement and Concrete Composites*, 45 (2014) 166–175.

114. D. M. Bastidas, M. Criado, S. Fajardo, A. La Iglesia, J. M. Bastidas, *Cement and Concrete Composites*, 61 (2015) 1–6.

115. D. M. Bastidas, M. Criado, S. Fajardo, A. La Iglesia, *Cement & Concrete Composites*, 43 (2013) 31–38.

116. L. Yohai, M. B. Valcarce, M. Vázquez, *Electrochimica Acta*, 202 (2016) 316–324.

LIST OF PUBLICATIONS

1. **Binsi M Paulson**, Joby Thomas K, Vinod P Raphael, “Efficacies of sodium nitrite and sodium citrate–zinc acetate mixture to inhibit steel rebar corrosion in simulated concrete interstitial solution contaminated with NaCl”. *International Journal of Industrial Chemistry* (springer) Vol 9, Issue 2, 105-114, 2018
2. **Binsi M Paulson**, Joby Thomas K, Vinod P Raphael, K S Shaju, “Prevention of reinforcement corrosion in concrete by sodium lauryl sulphate– Electrochemical and gravimetric investigations”. *International Journal of Corrosion* Vol 2018, 1-10, 2018
3. **Binsi M Paulson**, Joby Thomas K, Ragi K, Sini Varghese C, “Interaction of Two Heterocyclic Schiff bases Derived from 2-acetylpyridine on Mild Steel in Hydrochloric acid- Physicochemical, Electrochemical and Quantum Mechanical Investigations”. *Current Chemistry Letters* Vol 9, 19-30, 2019
4. Sini Varghese, Joby Thomas K, Vinod P Raphael, **Binsi M Paulson**, Ragi K, “Electrochemically Synthesized Poly(2-aminobenzenesulphonic acid)-An Efficient Protection for Carbon Steel Corrosion” *Oriental Journal of Chemistry* Vol 35, 678-683, 2019
5. Ragi K, Joby Thomas K, Vinod P Raphael, Sini Varghese, **Binsi M Paulson**, “ Synthesis, cyclic voltammetric, electrochemical and gravimetric corrosion inhibition investigations of Schiff base derived from 5,5-dimethyl-1,3-cyclohexanedione and 2-aminophenol on mild steel in 1M HCl and 0.5M H₂SO₄” *International Journal of Electrochemistry* Vol 2019, 1-13, 2019

LIST OF CONFERENCE PAPERS

1. **Binsi M Paulson**, Joby Thomas K, Vinod P Raphael, Ragi K, Sini Varghese C, “Efficacy of sodium citrate-zinc acetate mixture to inhibit steel reinforcement corrosion in concrete block contaminated with NaCl” - *International Conference on Chemistry and Physics of Materials*, St. Thomas College, Thrissur, 2018
2. **Binsi. M. Paulson**, Joby Thomas K, Ragi. K, Sini Varghese C, Reeja Johnson, “Corrosion inhibition efficacy of 2-Acetylpyridine phenylhydrazone on mild

steel in acid media - Physicochemical and Electrochemical investigations”
MATCON, Cochin University of Science and Technology, 2019

3. Aby Paul, Joby Thomas K, **Binsi M Paulson**, Sini Varghese C, Reeja Johnson, “Preparation, characterization and antimicrobial studies on transition metal complexes of (Z)-2-((1H-indole-3yl)methylenamino)benzoic acid” - *UGC Sponsored National Seminar on Recent Advances in Chemistry*, St. Mary’s College, Thrissur, 2015
4. Aby Paul, Joby Thomas K, **Binsi M Paulson**, Sini Varghese C, Reeja Johnson, “VO(II), Cr(III), Mn(II) and Fe(III) complexes of (z)-3-((1H-indol-3-yl)methyleneamino)benzoic acid” - *UGC Sponsored National Seminar on Green Technologies for Green Environment*, S. N. M. College Maliankara, Ernakulam, 2015
5. Aby Paul, Joby Thomas K, Reeja Johnson, **Binsi M Paulson**, Sini Varghese C, “Synthetic, structure and antibacterial analysis of Ni(II), Cu(II) and Cd(II) complexes of (Z)-3-((1H-indole-3-yl) methyleneamino)benzoic acid”- *UGC Sponsored National Seminar on Modern Trends in Chemistry*, St. Joseph’s College, Irinjalakuda, 2015
6. Aby Paul, Joby Thomas K, Reeja Johnson, Sini Varghese C, **Binsi M Paulson**, “Studies on physicochemical and thermal properties of Mn(II) and Cu(II) chelates of 3-formylindole-2-amino-5-nitrobenzoic acid- *UGC Sponsored National Seminar on Advanced Topics in Chemistry*, SN College Nattika, 2015
7. Aby Paul, Joby Thomas K, Sini Varghese C, Reeja Johnson, **Binsi M Paulson**, “Evaluation on anticorrosive properties of 3-formylindole-2-aminobenzoic acid and 3-formylindole-3-aminobenzoic acid on copper in HCl media”- *UGC Sponsored National Seminar on Advanced Topics in Chemistry*, SN College Nattika, 2015
8. Shaju K S, Joby Thomas K, **Binsi M Paulson**, Vinod P Raphael, “Cyclic voltammetric studies of the Schiff Base 3-(anthracen-9(10H)-ylideneamino)propanoic acid and it’s Zn(II) complex in DMSO at the surface of Glassy Carbon “- *Kerala Science Congress*, 2016
9. Sini Varghese C, Joby Thomas K, Vinod P Raphael, **Binsi M Paulson**, “ Interaction of two heterocyclic oximes on copper corrosion in nitric acid: Electrochemical, surface morphological and quantum chemical investigations”- *30th Kerala Science Congress*, 2018

10. Ragi K, Joby Thomas K, Vinod P Raphael, Sini Varghese C, **Binsi M Paulson**, “Gravimetric and electrochemical investigations on inhibition of N, N’-9, 5-dimethylcyclohexanane-1,3-diyldine) dianiline on mild steel surface in 1M HCl”-*International Conference on Chemistry and Physics of Materials*, St. Thomas College, Thrissur, 2018
11. Sini Varghese C, Joby Thomas K, Ragi K, **Binsi M Paulson**, “ Corrosion inhibition investigations of 3-formylindole phenylhydrazone on copper in nitric acid medium”- *International Conference on Chemistry and Physics of Materials*, St. Thomas College, Thrissur, 2018

PAPERS COMMUNICATED/ TO BE COMMUNICATED

1. “Mitigation of Concrete Reinforcement Corrosion by Penta Sodium Triphosphate - Electrochemical and Gravimetric Investigations” (communicated)
2. “Sodium citrate-zinc acetate mixture: A potential inhibitor to steel reinforced concrete corrosion” (To be communicated)
3. “Effect of reduced form of 3-acetylpyridine thiosemicarbazone on the corrosion inhibition behaviour on mild steel in HCl and H₂SO₄ media”(To be communicated)

